APPLICATIONS OF RAY TRACING TO A PSEUDOPHAKIC EYE MODEL

by

Jason Turuwhenua

THESIS

Submitted in partial fulfillment of the requirements
for the degree of Doctor of Philosophy in Physics
University of Waikato, 2001

Hamilton, New Zealand

Abstract

The calculation of IOL power using keratometry is adversely affected by recent corneal reshaping surgeries. This thesis investigates the application of ray tracing and general anterior corneal surface modeling, for the purpose of improving ophthalmic measurements and in particular, the estimation of IOL power.

A new algorithm (based on a multi-step approach) for the recovery of the corneal height using videokeratography is presented. The method ensures a cubic recovery with continuous curvature; skew rays are treated in post-processing. The RMS height error is measured for three simulated (with two skewed) cornea. The total errors are 6.2×10^{-4} mm ignoring the skew ray error, and 1.7×10^{-4} mm accounting for it. The individual height errors are submicron in the latter case. The algorithm gives average errors of 2.5×10^{-4} mm for a set of calibration balls. The completion time is 2.3 s over all cases, using a standard desktop PC.

A new method for the recovery of the internal ocular radii of curvature is investigated. The method is used to recover the posterior corneal radii (PII) and the anterior lens radii (PIII) given several anterior cornea models (PI) in simulation. The recovered surface powers are no more than 0.1 D(PII) and 0.006 D(PIII) in error of the true surface powers.

A framework is then presented for modeling the effect of lens decenter and tilt on *perceived image quality*. The SQRI image quality metric is determined for a range of lens tilt and lens decenter values. These are compared with the statistical moments of the spot diagrams. The SQRI shows asymmetric degradation (with tilt for a particular decenter value) of imaging for a plane displaced -0.1 mm from best focus. For a plane displaced +0.1 mm from best focus, the SQRI is symmetric and improves regardless of the sign of tilt. The statistical moments suggest that skew does not necessarily imply poor imaging.

Finally, the modeling methods developed are tested on two clinically measured eyes. Minimizing the spot size, predicts the spectacle prescription to 0.0 D(OS) and 0.1 D(OD) of the mean spherical equivalent. Adding prescribed lenses to the model eye, estimates best focus to 0.03 mm and 0.02 mm of the retinal plane; consistent with better than 6/6 VA measured for OS/OD. A VisTech VCTS 6500 contrast sensitivity chart is used to verify the eye model. A 75% match with theory is found for OS, a 50% match is found for OD.

Acknowledgements

Firstly, I would like to acknowledge my supervisor, Dr. Jon Henderson for his guidance during the extent of this thesis: (i) for many "words of wisdom" (in particular *key* insights regarding the physics of light transport) (ii) careful comments, and revisions of the text (iii) for generally providing an *apprenticeship* which has significantly refined my research skills.

I am indebted to the Foundation for Research Science and Technology, for providing the financial assistance that made this work possible.

This work could not have been completed without the ophthalmologists, optometrists and other eyecare professionals who provided their time and assistance. In particular, Dr. Doug Cox and his staff at LaserSight; and the staff at Hamilton Eye Clinic. Also, thanks to Derek Gower and staff of Houston Medical, who provided the necessary initial links from which this research was possible. Also to Paul Dickson Optometrists for the use of their contrast sensitivity chart.

Finally, I would like to acknowledge friends and family, who continually supported me throughout my study (and perhaps more significantly, continue to support!). In particular, thanks to Liz Richardson and family, for her mentoring throughout the years. Finally, to the two people closest to me, Jeni-leigh who suffered and struggled tirelessly with me; and to Kura-Kakerangi, who provided the motivation to complete!

Contents

List of Figures

List of Tables

Glossary of Terms

ACD See anterior chamber depth.

Anterior chamber depth This is distance from the posterior cornea to the anterior lens. However, clinically the anterior chamber depth is the distance from the anterior corneal surface to the front lens surface, as measured by ultra-sound.

Aqueous Fluid bounded by the posterior cornea and the iris, and anterior lens.

Arc-step algorithm The standard method for reconstructing the corneal surface using videokeratography.

Astigmatism A refractive error caused by the difference in principal curvatures of the cornea.

Axial length The clinically measured distance from the anterior corneal to the retinal plane.

Axis component The angle subtended in rotating the cylindrical component of a spherocylindrical lens.

AXS See axis component

Cardinal points Points which describe an Gaussian optics system completely. These are the object and image principal points, nodal points and focal points.

Cataract A disease in which the lens becomes opaque.

Coma A refractive error characterized by a point spread function with comet like tail.

Contrast The amplitude of a sinusoidal grating, over the average of the maximum and minimum illuminances of the two sinusoids.

Contrast sensitivity function A measure of visual sensitivity, typically for sinusoidal gratings presented to the observer. It is 1/(modulation threshold).

Cornea The transparent portion of the eye that refracts light onto the retina.

Corneal apex A corneal point with no curvature. There is typically only one point on the corneal surface where this is true. For modeling purposes, this point is taken to coincide with the origin.

Corneal curvature The convention adopted here is that it is the 1-dimensional expression for instantaneous curvature, taken along a meridional plane.

Corneal height The displacement from the plane z=0, given that the corneal apex also lies in the plane z=0.

Corneal slope The first radial derivative of the corneal height.

Corneal tilt The first angular derivative scaled by $1/r$, where r is the radial distance to the point.

Corneal topography The measurement of quantities which describe the corneal area is some sense, not necessarily height.

Cylindrical component The dioptric power of a spectacle lens which describes the astigmatism.

CSF See contrast sensitivity function.

CYL See cylindrical component.

Diopter The measure of refracting ability of a surface or lens. This is 1/(focal length) and has units of m^{-1}

Entrance pupil The image of the pupil as viewed from object space i.e. through the cornea.

Exit pupil The image of the pupil as viewed from image space i.e. through the lens.

Focal points The focal points of a Gaussian optical system, are points where rays from infinity (image/object space), converge to after passing through an optical system.

Fovea Central part of the macula that provides sharpest vision.

Geometrical optics The theory of light where light energy travels along rays, in a homogenous media.

Human visual system The combination of the optics of the eye, processing in the retina and decision making criteria.

HVS See human visual system.

Image space The side of a refracting system to which light moves.

Intraocular lens An artificial lens which replaces the natural crystalline lens; typically as a surgical solution to a cataract.

IOL See intraocular lens.

Keratoconus A disease of the eye, where the cornea tends to bulge, due to corneal thinning.

Keratometry The measurement of the principal curvatures of the corneal surface.

Keratotomy (radial) See radial keratotomy.

Keratectomy (photorefractive) See photorefractive keratectomy.

Kurtosis A statistical measure of the "peakedness" of a distribution.

Landolt "C" A standard visual testing target which looks like the letter "C".

Lens An optical element used for altering the path of light rays. Generally, the intention of a lens is to produce focused images. Here, it is often meant to refer to the human crystalline lens, or an implanted intra-ocular lens, depending on context.

Line spread function The image formed by a optic system, if a line in object space.

Longitudinal error Any displacement measured *along* the optic axis.

LSF See line spread function.

Macula Small central area of the retina that provides vision for fine work and reading.

Meridional plane Any plane that contains the optic axis.

Modulation See contrast.

Modulation threshold The modulation at which a particular spatial frequency is resolved at a defined threshold level (typically 50%).

Modulation transfer function The magnitude of the optical transfer function (OTF). Describes the ratio of output spatial frequency to input spatial frequency (linear systems).

MTF See modulation transfer function.

Nodal point A point such that any ray which enters an optic system at a defined angle leaves the optic system at the same angle.

Nodal camera A camera which allows rays to pass through to the image plane via a pinhole only. Also known as a pinhole camera.

Object space The side of a refracting system from which light emanates.

OD See oculus dexter.

OS See oculus sinister.

Oculus sinister The left eye. This has also come to be known as the evil eye.

Oculus dexter The right eye.

Optical transfer function The optical transfer function describes the total magnitude and phase change that operates on a sinusoidal input spatial pattern (linear system).

OTF See optical transfer function.

Paraxial The assumption that rays travel close to the optic axis.

Photorefractive keratectomy A laser based technique for inducing shape changes in the eye.

Point spread function A function describing the distribution of light energy over the image plane. In a geometrical optics approximation, it is the density of rays.

Prescription A (non-unique) description of a spectacle lens, given in the form $SPH/CYL@AXS$.

Principal axes The azimuthal angles at which maximum and minimum curvatures of the corneal surface occur.

Principal curvatures The maximum and minimum curvatures of the corneal surface.

Principal focii The focal positions of characteristic elongations (due to astigmatism) of the point spread function.

Principal plane The plane formed when paraxial rays from object/image space are intersected with their corresponding rays which exit into image/object space.

Pseudophakic A term to describe an eye with an artificial crystalline lens.

PSF See point spread function.

Pupil The natural aperture of the eye, which restricts the amount of light that enters the eye.

Radial keratotomy A surgical procedure where radial cuts are made in the corneal surface.

Refractive error Measures of the displacement of rays from the Gaussian focal point. These errors may be measured in a transverse or longitudinal direction.

Refractive index A property of a medium in which light travels; it is the ratio of the speed of light in a vacuum, to the speed of light in the material.

Retina That part of the eye, responsible for converting light energy to electrical signals.

RK See radial keratotomy.

Schematic Eye A general term for an eye model.

Shallow angle The principal axis which subtends the smallest angle from horizontal.

Skew ray A ray that is not constrained to lie in a meridional plane.

Skewness A measure of the "tailedness" of a distribution, which for practical purposes is a description of coma.

SPH See spherical component.

Spherocylinder A lens measured as one spherical and one cylindrical surface.

Spherical component That part of a lens which gives only the magnification of the image.

Spherical aberration The refractive error which arises since a spherical lens cannot focus rays (with displacement from the optic axis) to a point.

Steep angle The principal axis which subtends the largest angle from horizontal.

Telecentric camera A nodal camera, with a lens placed one focal length in front of the pinhole. Only rays which are parallel with the optic axis will pass through to the image plane.

Transverse error Any direction perpendicular to the optic axis. A transverse plane is a plane that is perpendicular to the optic axis.

VA See visual acuity.

Videokeratography The derivation of corneal information from the images of targets, whose reflections are captured using video equipment.

Videophakometry The measurement (typically) of internal radii of curvature, for example the radii of curvature of the posterior cornea and anterior/posterior lens. Video equipment captures the required images.

Visual acuity A measurement of visual performance. Typically, letters of steadily decreasing size are presented to the observer. The point were the letters cannot be resolved is called the visual acuity.

Vitreous A gel-like substance, which fills the posterior chamber, i.e. the chamber that lies behind the lens.

VK See videokeratography.

VP See videophakometry.

Chapter 1

Introduction

1.1 Introduction

The content of this thesis arose from work done at Houston Medical, Hamilton, New Zealand[1]. Through contact with ophthalmologists, I was made aware of the use of artificial intraocular lenses (IOLs) used in cataract surgery, and the use of IOL calculations for determining the dioptric power of lenses needed to produce a desired *refraction*(or visual result). Through this contact, it became apparent that research was needed in this area. The literature has shown that there is a need to develop IOL calculation methods, in response to the advent of recent corneal refractive procedures [Seitz and Langenbucher, 2000, Celikkol et al., 1996, Hoffer, 1995]. Current methods are constrained (a) by the simplifying assumptions of the paraxial theory, and (b) the use of gross anatomic measurements of the cornea, which I believe limit the predicting power of current methods.

The initial intention of this research was to develop a method for predicting IOL power, using general corneal surface information, and ocular biometry. The approach taken would be to model the eye as an optical system consisting of a measured (calibrated) corneal surface (obtained through videokeratography), combined with IOL position and dimensions, and the axial length of the eye. However in doing so, several problems which arose in the context of videokeratography were investigated and addressed. The generality of the modeling tools developed allowed investigation of the measurement of lens radii in the eye, and modeling of IOL lens tilt and decentration.

Hence, the intention of this chapter is to support the assertion that there is a need for research in this area. This is done by describing (a) current IOL formulae in clinical use and their limitations, (b) ray-tracing as applied to the calculation of IOL power, and (c) the use

[1] A company which offers ophthalmic practice management software

of corneal topography in the context of ray-tracing. The chapter then concludes by outlining the contents of the thesis.

1.2 Background

IOL lens calculations are of two types (i) regression based, where the IOL power is the dependent variable, and (average) keratometry readings, axial length, effective lens position, target refraction and A-constant[2] are possible independent variables [Seitz and Langenbucher, 2000] (ii) theoretic formulae, based invariably on paraxial theory. The SRK I and II formulae are examples of regression based equations for clinical use [Retzlaff et al., 1990, Haigis, 2001]. Schechter [1995] gives the theoretic model equation for calculation of *emmetropia* as,

$$P_{IOL} = \frac{n}{a - k - g(t)} - \frac{n}{n/P_c - k - g(t)} \tag{1.1}$$

where P_{IOL} is the *dioptric power* of the IOL lens, P_c is the power of the cornea, n is the index of refraction of the aqueous and vitreous, a is the axial length of the eye (in meters), k is the Anterior Chamber Depth (ACD) and $g(t)$ is a function of the lens thickness. The theoretic formulae are the Haigis, Hoffer Q, Holladay 2, SRK/T and Binkhorst formula [Haigis, 2001, Holladay et al., 1988, Hoffer, 1995, Retzlaff et al., 1990]. These equations are all variations on equation (1.1), where the differences between these formulae lie in differences in the calculation of parameters such as the Anterior Chamber Depth (ACD), and the use of the A-constant. In fact, these theoretic formulae are the recommended formulae for use in current practice, and therefore define the standard in clinical practice.

These IOL calculations are adequate for the *majority* of corneas. In fact, communications with ophthalmologists revealed that refractive outcome were typically within 0.5 D of the desired result. However, the literature showed that this was not the case for *all* eyes. There appeared to be cases in which IOL calculation according to standard methods were not successful, particularly after corneal refractive procedures.

Recently, Seitz and Langenbucher [2000] have attributed errors in IOL calculation after refractive surgeries (e.g. RK, PRK and LASIK) to keratometry i.e. the gross measurement of corneal *curvature*. Maloney et al. [1993] state that measurements obtained by keratometry are unreliable for irregular corneas, and suggest that metrics obtained by videokeratography (in the context of corneal surface diagnosis) are a better option. Hoffer [1995] reached a similar conclusion, reporting that standard keratometers do not accurately measure corneal

[2]The A-constant is typically the value of IOL lens power if all independent variables are zero

power after refractive keratotomy, and suggesting that inclusion of keratometry values derived from videokeratography may be a useful in improving IOL formulae. Husain et al. [1996] mention that videokeratographically derived keratometry values are important for patients with abnormal or surgically altered corneas, though (ironically) they found that standard keratometry was more accurate for normal corneas. Celikkol et al. [1996] used videokeratography derived keratometry for the calculation of IOL power in patients with keratoconus. In that paper they found that IOL power prediction for patients with keratoconus requiring cataract extraction, appeared to be more accurate than standard keratometry. They also mentioned that IOL power calculation could be negatively affected by eyes with high/irregular preoperative astigmatism [Modorati et al., 1990, Alimisi et al., 1996], increased corneal power as well as long axial lengths. These results are evidence that there are eyes in which IOL calculations do not give accurate predictions.

A natural progression from paraxial theory is exact ray-tracing. However, the use of this theory is not wide-spread in IOL calculation. Naeser [1997] has described an IOL formula which incorporates the thickness of the lens and lens curvatures (as required by exact ray-tracing), but the method is still paraxial. Fink et al. [1996a,b] have developed a system for displaying the effect of visual aids such as glasses, contact lenses or IOL. The program casts several hundred rays for every point of a given object, from which a visual impression of the scene is generated. This program uses the Gullstrand eye model, i.e. a schematic eye with spherical eye surfaces. Takei et al. [1995] use an exact ray-tracing method to model four IOL types, in order to estimate the aberrational astigmatism they produce. They conclude that an IOL with 1:4 radii of curvature (i.e. a radii of curvature 4 times larger on the posterior surface) minimizes the aberrational astigmatism. Korynta et al. [1999] model IOL lens decentration and tilt using an exhaustive ray-tracing technique, which generates the Visual impression of the letter C. However, in all these cases, the modeling of the eye is constrained to simple model surfaces. It appears that the use of a general corneal surface representation has not been considered in IOL calculation.

The literature regarding the use of ray-tracing applied to corneal topography measurement (i.e. general surface representation) is more detailed. An early attempt at modeling the cornea is presented in Camp et al. [1990b]. They describe a method for ray-tracing corneal topography *maps*, i.e. maps of local surface dioptric *power*, utilizing the *lensmaker's* formula. This is then extended in Camp et al. [1990a], for modeling the effect of irregular corneal surface topography on corneal optical performance. They find that quite irregular corneas exist, which give good performance on 100% contrast visual acuity tests. They believe that

ray-tracing methods may be a means of differentiating irregular corneas with good optical performance, and those with bad optical performance. Maguire et al. [1991] use the methods of Camp et al. [1990b] to simulate images of Snellen "E"'s. The purpose was to show that post-operative topography can be used to determine differences in image quality, that can be reproducibly ranked by independent observers.

However, Roberts [1994], Tripoli et al. [1996], Schanzlin and Robin [1992] have shown there are drawbacks with power maps extracted from videokeratography devices, due to the non-standard definition of power, and the level of accuracy that can be obtained from these maps. The accuracy of these maps are assumed by the methods of Camp et al. [1990b]. In addition there appear to be inherent limitations Klein [1992, 1997a], Schanzlin and Robin [1992] in current reconstruction devices which limit the accuracy of corneal reconstruction devices. Therefore, it is not clear whether the maps obtained are accurate.

The modeling of visual acuity used by Greivenkamp et al. [1995a] was applied to the ray-tracing of schematic eyes. In this paper, the visual acuity was taken as the intersection of the Modulation Transfer Function (MTF) and modulation threshold of the eye, and was modeled by generating point spread functions for various de-focus levels (0 to 5 D) and pupil sizes (0.5 to 8 mm). In that paper, they find a good correlation ($r^2 = 0.909$) with actual visual acuity (for a large population data-set).

Klonos et al. [1996] use a computer model for predicting image quality (i.e. where image quality is defined by the geometric spot size) after photorefractive keratectomy. The cornea is modeled using aspheric surfaces, whilst the crystalline lens is tested with gradient index distributions. They find that the anterior corneal curvature and axial length contribute most to the image quality at the retina, though pupil size is found to affect image quality when it is larger than the *ablation* zone (i.e. the area treated).

An alternative approach is described by Hemenger et al. [1995] in which the wave-front aberration function is derived from videokeratography. Interestingly, this is the only paper, in which the data is calibrated. The reason for calibration is that wave-front aberration data is limited by the accuracy of videokeratography. Greivenkamp et al. [1995b] use ray-tracing on videokeratography data extracted from patients with radial keratotomy. The effect on the contrast sensitivity was predicted. Recently Klein and Garcia [2000], Garcia et al. [2000] have used an advanced surface modeling of the cornea based on B-Splines [Halstead et al., 1995b] to model visual acuity, but the emphasis was on the quantification of corneal irregularity, rather than IOL calculation or the synthesis of imagery.

The organization of this thesis, and a brief outline of each chapter follow:

Chapter 2 The basic concepts relevant to this thesis are introduced. The eye is introduced in terms of its physiology, and then as an optic system. The theory of paraxial optics and physical optics are described, in the context of eye modeling. Methods used to test visual performance are described.

Chapter 3 The modeling of the cornea requires detailed knowledge of the corneal surface. This chapter introduces videokeratography (VK), the method used for obtaining the corneal surface . A new method for recovery of the corneal surface is presented, which yields accurate height recovery whilst maintaining simplicity of reconstruction. Also presented is a method for calibrating data on videokeratography, which appears to improve reconstruction on actual VK devices, when the system parameters are only partially known.

Chapter 4 A MATLAB[3] toolbox RAYTRAK v1.0 (which was developed by the author) for ray-tracing the eye is described. The theory of geometric optics is considered in more detail, which then leads naturally into an explanation of the toolbox. The toolbox is applied to the problem of determining the errors incurred by the methods developed in the previous chapter.

Chapter 5 The RAYTRAK toolbox is applied to the measurement of lens radii *in-vivo*, and the modeling of lens tilt/decentration. To this end, the chapter has two distinct sections (i) a new method for recovery of the internal lens radii utilizing videokeratography (ii) an investigation of the effect of lens tilt and lens decentration on perceived image quality. This introduces novel objective measures of image quality, i.e. an image quality metric and statistical moment measures of the spot-diagram.

Chapter 6 This chapter attempts to verify the *per individual* based model, developed in this thesis. Two approaches are taken (i) objective approaches: the clinically measured *lens prescription* is compared with spot-diagrams computed from the uncorrected eye. The spectacle lens correction is predicted using objective criteria. (ii) Psychophysical approaches: the effect of spectacle lens prescription on modeled spot-diagrams is generated and compared with measured visual acuity. The CSF of an observer is measured and tested for consistency with the generated eye model.

Chapter 7 The contents of this thesis are reviewed and summarized. Suggestions for further work are made.

[3]The MathWorks, Inc.,3 Apple Hill Drive Natick, MA 01760-2098

Chapter 2

Background

2.1 Introduction

The purpose of this chapter is to provide a general introduction to modeling of the eye. A natural starting place for discussion is to introduce the eye, as a biologic entity. To this end, the eye is described in terms of the physiology of its components. Attention is restricted to those parts of the eye directly responsible for image formation and visual perception. These are the cornea, lens and aqueous humor, vitreous humor and retina.

The next section introduces the eye as an optical system, introducing paraxial optics theory in the context of eye modeling. Refractive error and eye aberrations are briefly discussed. This also requires a description of geometrical optics/wave optics theory. The eye may be considered as a linear imaging system, so this description is considered. Finally, the chapter concludes with methods used for testing the performance of the eye.

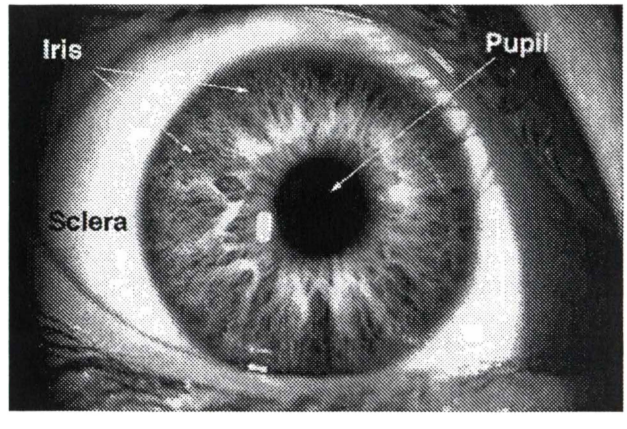

Figure 2.1: The external eye showing the pupil, iris and sclera. Picture reproduced from Avery [2001]

2.2 The Eye

2.2.1 An Overview

The eye is an approximately spherical structure (radius typically 12 mm) mounted in the *orbit* of the skull. It is controlled by six extra-ocular muscles (see Figure 2.2(a)) where each muscle pair controls movement in one of three orthogonal planes. These muscles are inserted in the sclera, the thick fibrous covering that comprises the "white" of the eye. The sclera comprises 5/6 of the envelope of the eye, the other 1/6 is covered by the cornea, the transparent window that allows light to pass into the interior of the eye. The junction of the scleral and corneal regions is called the scleral spur or limbus, which is more marked in the vertical meridia, giving the cornea an oval shape (11.7 mm horizontally and 10.6 mm vertically).

Figure 2.2(b) shows a schematic of the eye. Lining the sclera is a coat containing blood vessels called the uvea (Greek for *black grape*). This contains pigment used to absorb light that may pass through the sclera. The choroid is the posterior 2/3 of the uvea. The retina lines the interior of the choroid, and contains the retinal visual cells, which convert light energy into nervous signals. The retina is separated from the choroid by the retinal pigment epithelium.

The macula allows detailed central vision, the fovea is the central part of the macula. The macula, located close to the posterior pole is elliptical with its wider axis horizontal (approximately 2 mm). At the center of the fovea, is the foveola, which is the point upon which gaze is centered. When the image falls on the center of the fovea, or within 0.3 mm of it, the vision is said to be central or *foveal.* Posteriorly, the optic nerve exits the eye, through a cone shaped opening with diameter 1.5 mm internally, and 3 mm externally, which has its center 3 mm to 4 mm nasally, and 1 mm to 2 mm inferior to the posterior pole. The optic nerve is a collection of visual nerve fibers which collect at the optic nerve head, or optic disk. Since there are no photoreceptors in this area, there is no visual signal which gives rise to the "blind spot".

Finally, enclosed in a capsule, behind the pupil is the crystalline lens, which is suspended from the ciliary body, by ciliary fibers (or zonular fibers). These fibers produce tension on the lens body, which causes the lens to flatten and bulge as the ciliary muscles relax and contract. The lens is situated directly behind the iris, and is bounded anteriorly by the aqueous, and posteriorly by the vitreous. This is the largest part of the eye, comprising 5 cm^3 of the total 7 to 8 cm^3 volume of the globe.

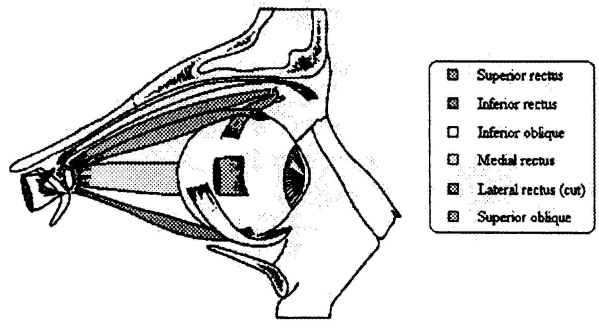

(a) Extra-Ocular Muscles

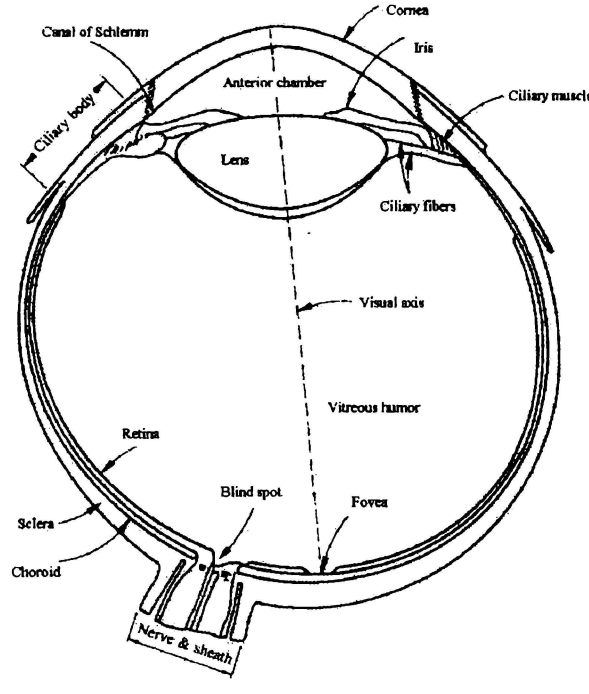

(b) A Schematic Eye

Figure 2.2: (a) The first figure shows the muscles of the eye, 3 orthogonal pairs of muscles control eye movements [Unknown, 2001]. (b) A schematic of the eye. Reproduced from Gonzalez and Woods [1992]

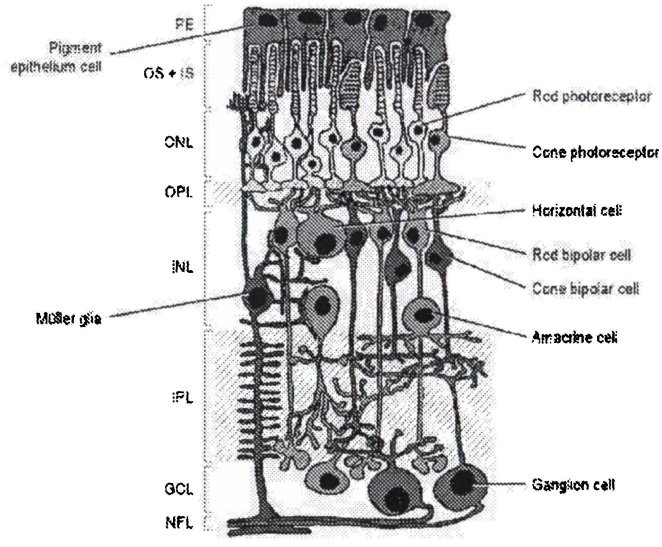

Figure 2.3: The retina in cross-section. Figure reproduced from Euler [2001]

2.2.2 The Cornea

The cornea is the transparent portion of the eye that refracts light onto the retina. It is responsible for the majority (2/3) (see section 2.3) of the refraction of the eye, and is therefore the main contributor to optical degradation. The cornea itself is roughly 0.4 mm to 0.7 mm thick. It is avascular i.e. has no blood vessels, except at the very periphery. It does possess a sensitive network of nerves, which responds (by producing a blinking reflex) to forces on the order of 20mg/mm^2, which increases to 40mg/mm^2 with age.

The cornea is composed of five layers. These are the epithelium (thickness 45μm centrally), the anterior limiting lamina (16μm centrally), the corneal stroma (about 500 μm), the posterior limiting lamina and the endothelium (6μm). In the epithelium, flattened cells create a smooth surface over the cornea. Tears fill small irregularities of the surface, the purpose of which is to (a) create a smooth optical surface (b) to nourish the cornea through absorption (c) to kill bacteria. The epithelium has a high demand for oxygen and will loses transparency if it becomes starved of oxygen [Le Grand and El Hage, 1980].

The anterior limiting lamina (or Bowman's membrane) is made up of tightly packed collagen fibers. The corneal stroma comprises the bulk of the cornea, and is formed from 50 (or so) lamellae (layers) stacked on each other. The posterior membrane is again a layer of tightly packed collagen fibers (as with Bowman's membrane). The endothelium (6μm) is responsible for pumping out aqueous humor, which the cornea absorbs. If the amount of humor absorbed increases the cornea will become opaque.

2.2.3 The Iris

The iris is an aperture, i.e. it limits the amount of light able to pass through to the retina, the size of which depends on the ambient light in the surroundings. The iris encloses the pupil, the diameter of which can vary from 1.5 mm to 10 mm. In moderate light levels, the pupil diameter is 4 mm. The magnifying effect of the cornea produces apparent pupil sizes, which are about 13% larger than the actual size of the pupil [Charman, 1995]. The size of the pupil is dictated by the sphincter pupillae, a ring of muscle 0.8 mm wide by 0.15 mm thick, formed by a ring of muscle around the iris which causes constriction of the pupil, when it contracts. The dilator pupillae on the other hand, line the posterior iris much like the spokes of a wheel, which causes the pupil to widen when they contract.

2.2.4 The Crystalline Lens

The crystalline lens provides the eye with a viewing range of distances from infinity to less than 10cm in the eye (in early adulthood) [Thibos and Bradley, 1999]. The lens is able to stretch and bulge, so that light is refracted onto the retina as required, a process known as *accommodation*. When the ciliary muscles contract, the zonular fibers (which support the lens) relax, and the lens (by virtue of its elasticity) bulges outwards. The opposite process occurs when the muscle relaxes, the zonular fibers increase in tension, and the lens is forced into a flatter shape.

A normal adult lens measures roughly 4 by 9 mm and weighs approximately 175mg. The structure of the lens has been compared to an onion, in which new layers are superimposed over old layers, much like the rings of a tree [Le Grand and El Hage, 1980]. The lens is supplied from exchanges with the aqueous humor, which are slow but essential. The lens quickly becomes opaque when blood flow ceases in the eye.

With age, the lens hardens and may become opaque. In this instance the lens is termed *cataractous*, and clinical intervention may be required. A common option is the removal of the crystalline lens, followed by insertion of an artificial intraocular lens (IOL). In this case the patient is termed, *pseudophakic*, a natural lens subject being *phakic*, whilst a subject with no lens (artificial or natural) is termed *aphakic*.

2.2.5 The Aqueous and Vitreous Humor

The aqueous humor is the fluid bounded by the posterior corneal surface, the iris, anterior surface of the lens. The aqueous humor is secreted into the posterior chamber, whereupon it moves through the pupil into the anterior chamber. At this point the fluid moves according

to convection currents in the anterior chamber. The aqueous humor is formed continuously; approximately 1% of the total volume of aqueous is produced per minute, replacing an equal amount which leaves the eye through the *canal of Schlemm.* The normal amount of aqueous fluid (0.3 cm^3) is formed in approximately 1 hour. The pressure of the aqueous fluid on the surroundings can be measured by measuring the area flattened by a given force, or the force required to flatten a given area. The normal intraocular pressure varies from 10.5 to 20.5 mm Hg in the vast majority of eyes (95.5 %).

The vitreous body is the gel-like substance, which fills the posterior chamber. The water content of the vitreous is very high (98% to 99.7%), with $7g$ NaCl/l and 0.5g/l soluble proteins. The glucose content is 0.5 to 0.6 g/l, which is lower in the posterior than the anterior vitreous body. This is attributed to the retina using glucose for its metabolism. The viscosity of the vitreous is due to Hyaluronic acid, which has its highest concentration in the cortical portion of the vitreous body.

2.2.6 The Retina

The retina is the eye's equivalent of the digital camera's Charge Coupled Device (CCD), which collects light falling on an array of photosites. The retina itself is a vascular (has blood vessels) transparent membrane. The macula located close to the posterior pole, is a yellow elliptical area (approximately 2 mm) which allows detailed central vision. The fovea (*Latin.* pit) is the central part of the macula. At the center of the fovea, is the point of fixation named the foveola. The retina consists of 10 functional levels (see Figure 2.3), where the pigment epithelium lies adjacent to the choroid (so that the photo-receptors are inverted with respect to incoming light). The functions of the various layers follow:

The epithelium layer The functions of this layer are to (a) absorb unwanted light (b) help nourish the retina and (c) to help with the functioning of the rod visual cells.

The receptor cell layer This layer consists of the functional parts of the visual cells. It consists of the rods and cones, which operate at two different operating conditions i.e. low light levels and cones at high light levels. The cones can be further divided into "long" "middle" and "short" [Charman, 1995] level cones, which corresponds to their spectral sensitivities. All rods have the same spectral sensitivity, which peaks at roughly 500nm. The physical dimensions of the cones are about 1.5μm - 3μm in the fovea. The rods function at low light levels, and reach their highest sensitivity at about 20° from the fovea [Smith and Atchison, 1997]. The rods are connected such that the output of 100 rods may combine, which gives

high sensitivity to light, but the spatial resolution is poor. In poor lighting conditions the maximum visual acuity is reached where the density of rods is the highest i.e. 20° from the fovea. The neural and blood supply to the retina enter and leave the eye at the optic disk.

The external limiting membrane This is a membrane formed by the thickening of the cell membranes of receptor cells, and *Müller* cells, which store energy.

The outer nuclear layer This contains the cell nuclei of the rods and cones.

The outer plexiform layer This is a synaptic layer, where the receptor cells terminate and meet the nerve cells (bi-polar) that carry the visual signal further.

The inner nuclear layer This consists of retinal nuclei of various cells such as Müller cells, horizontal, nerve, interplexiform and amacrine cells).

The inner plexiform layer This is another joining layer (synaptic layer) c.f. The outer plexiform layer, where the axons of bipolar cells terminate to make contact with the ganglion and amacrine cells. The ganglion cells pass the visual signal to the brain, via the optic nerve. The amacrine cells interrelate areas of the retina.

The ganglion cell layer This layer is formed by the cell bodies of these neurons.

The nerve-fiber layer This layer consists of the axons of the Ganglion cells.

The internal limiting membrane This forms the border between the neural part of the retina and the vitreous. It is absent at the optic disc.

2.3 The Eye as an Optical System

2.3.1 Paraxial Optics

The standard treatment of the eye begins with paraxial optics [Charman, 1995] i.e. the limiting case where the light rays travel close to the optic axis. In this limit, the physical structure of the eye may be replaced by six *cardinal* points, from which the (paraxial) imaging properties of the eye are determined. The concept of dioptric power, is central to this theory and arises from the equation for a spherical refracting surface,

$$\frac{n}{s} + \frac{n'}{s'} = \frac{n}{f} \tag{2.1}$$

where s is the distance from the surface to the object and s' is the distance from the image to the surface. Here, n and n' are the refractive indices of the media in which s and s' lie respectively. The focal length f for a single spherical refracting surface is given by,

$$\frac{1}{f} = \frac{n' - n}{n}\left(\frac{1}{R}\right) \tag{2.2}$$

where R is the radius of the refracting surface. All of the above quantities are subject to the following convention. Rays are assumed to travel from left to right (where possible), and are measured from the surface of interest. Distances measured to the left of the surface are taken as negative, whilst distances measured to the right are positive. Defining the (reduced) *vergence* by,

$$L = \frac{n}{x} \tag{2.3}$$

where n is the refractive index of the material and x is a distance, gives for equation (2.2),

$$L' - L = D \tag{2.4}$$

and $D = n/f$ is the *dioptric power* of the surface, L and L' are the object and image vergences respectively. The image vergence gives the point where rays converge. After this point, rays will diverge from this point, so that it is effectively an object point, with an object vergence relative to a subsequent surface. The thin lens equation is obtained by this reasoning, with form of equation (2.4) but *lens* power now given by,

$$D = \frac{1}{f} = (n' - n)\left(\frac{1}{R} - \frac{1}{R'}\right) \tag{2.5}$$

where R and R' are the front and back surface radii of curvature of the lens respectively.

There have been numerous attempts to model the eye using paraxial theory. Thibos and Bradley [1999] describe the history of schematic eyes, crediting Gullstrand (the six surface eye), Le Grand (the four surface eye), Listing (the three surface eye) and Emsley as the major contributors in the period from 1850-1950. More recently Thibos and Bradley [1999], Kooijman [1983], Liou and Brennan [1997], Escudero-Sanz and R [1999] have modeled the eye with varying levels of complexity (i.e. curved retina and aspheric surfaces). However, the standard model in use today is the Gullstrand eye [Le Grand and El Hage, 1980] based on paraxial theory, and with properties listed in Appendix A.

As mentioned, the optics of the eye may be replaced by the *cardinal points* (shown in Figure 2.4) i.e. the object and image principal points (P, P'), the object and image nodal points (N, N'), and the object and image focal points (F, F'). Rays from infinity pass through the eye (or any optical system) and converge at the image focal point, whilst parallel light rays traveling from inside the eye will converge at the object focal point. The principal planes (i.e. planes perpendicular to the optic axis, containing the principal points) are found by tracing the ray that exits the system back from the image point, until it intersects the original parallel ray from infinity that entered the eye. The nodal points are such that a

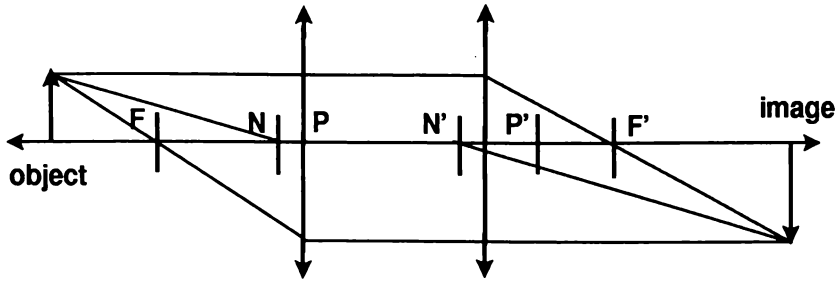

F, F' object/image focal points

P, P' object/image principal points

N, N' object/image nodal points

Figure 2.4: An optical system may be replaced by its cardinal points. Shown are the object, and resulting image. The optical system is replaced by the focal points (F, F'), principal points (P, P') and the nodal points (N, N'). The "un-primed" quantities are object space quantities, whilst the primed quantities belong to image space.

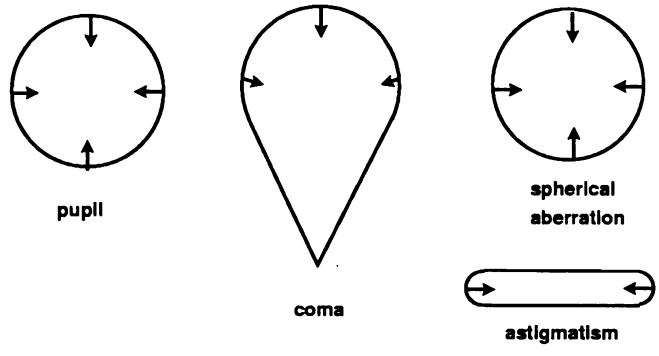

Figure 2.5: The gross effect of aberrations, showing resulting distributions of light at the image plane, given a point object.

ray from an off-axis object point, will pass through the first nodal point, and exit from the second nodal point without any angular deviation.

The relaxed eye (i.e. unaccommodated) has a total power of approximately 60 D, and the contribution of the cornea is roughly 40 D, which is 2/3 (66%) of the eye's total dioptric power. In the accommodated state, the total power of the eye increases to roughly 70 D, the corneal power is 4/7 (60%) of the total power. This increase is reflected by the second principal plane moving slightly closer to the retina. The object of furtherest position from the eye that can be focused on is at the *far point*, the closest object is at the *near point*.

2.3.2 Geometrical Aberrations

When the far point is at infinity, i.e. light from infinity focuses on the retina, then the subject is *emmetropic*, and the subject is said to have a "normal" eye. All other eyes are *ametropic*

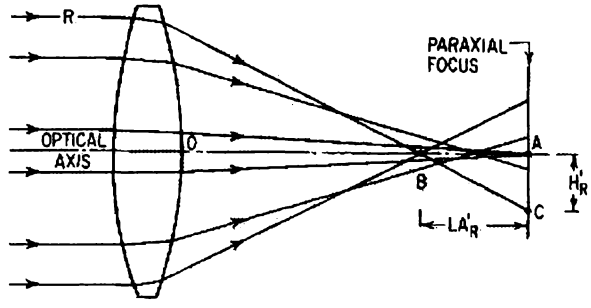

(a)

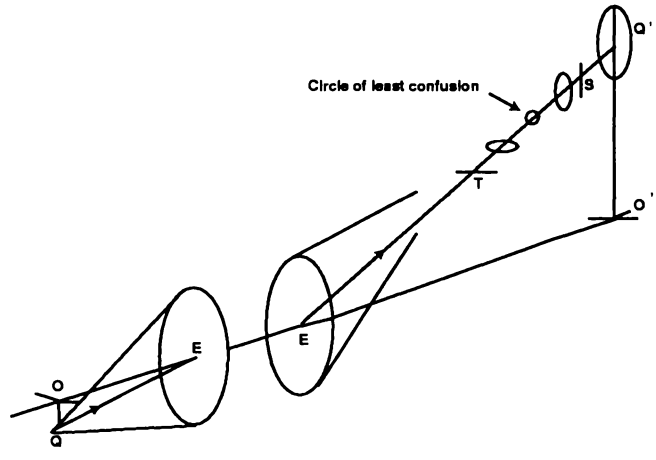

(b)

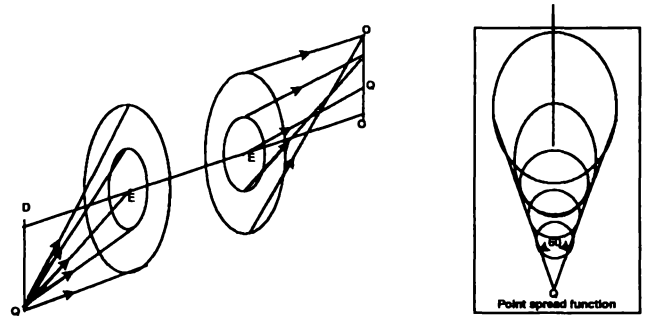

(c)

Figure 2.6: (a) Spherical Aberration, (b) Astigmatism, and (c) Coma. Figure (a) has been reproduced from Smith [1966]), whilst Figures (b) and (c) were adapted from Smith and Atchison [1997].

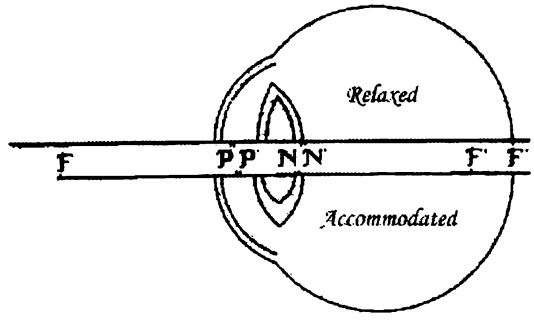

Figure 2.7: The Gullstrand schematic eye, showing cardinal points for a relaxed (upper horizontal line) and accomodated eye (lower horizontal line). Picture reproduced from Smith and Atchison [1997]

and possess *refractive error*. If light from infinity focuses in front of the retina then the subject is *myopic*. If light focuses behind the plane then the subject is *hyperopic*. This mismatch between focal plane and image plane, is *defocus*. Even when defocus is zero, there may be still be aberrations present which degrade visual performance. These aberrations are due to the fact that real lenses cannot image an object perfectly. In the eye, the main aberrations are spherical aberration, coma and astigmatism. Figure 2.5 shows spherical aberration, coma and astigmatism in terms of their gross illuminance distributions. The arrows indicate the change in shape as the pupil diameter changes. Geometrical optics easily accounts for these aberrations. Light energy travels along rays in this theory, where rays are geometric entities which (a) travel in straight lines in media of homogeneous refractive index (b) refract/reflect according to Snell's law/Law of Reflection. Figures 2.6(a)-2.6(c) show the aberrations in terms of the rays that comprise the image.

Spherical aberration produces a blur circle (illuminance distribution). From Figure 2.6(a) the rays have a focal length which depends on the height of the ray in the pupil. Therefore, a point-like PSF cannot be expected at any focal position. Astigmatism is characterized by an elliptical blur disc, which changes its shape with plane of observation. There are two positions where the PSF will form thin lines, which will be perpendicular (see Figure 2.6(b)). Decreasing the pupil decreases the size of the line, indicating the rays at the edges of the aperture are responsible for the extent of the line. Finally, coma is an off-axis aberration, in which radial zones of the pupil form displaced blur circles. The geometrical optics theory shows this again, where rays from zones form small circles on the image plane. The result is a flared PSF, with a tail due to the rays that pass through the center of the aperture, with a head due to the rays that pass through the outer aperture (see Figure 2.6(c)). Increasing the pupil size does not affect the tail.

The goal of optometry is to reduce these refractive errors. The typical example of corrections are spectacle lenses. A standard way of modeling glasses is by sphero-cylindrical lens i.e. a spherical front surface, with a cylindrical back surface. In this case, the glasses possess two axes of symmetry: one due to the combination of the spherical front surface and the plane axis of the cylindrical lens; and one axis corresponding to the spherical surface combined with the cylindrical surface. These two axes define the principal meridia of the glasses. By equation (2.5),

$$F_J = \frac{n-1}{n}\frac{1}{R_1} \tag{2.6}$$

$$F_K = \frac{n-1}{n}\left(\frac{1}{R_1} - \frac{1}{R_2}\right) \tag{2.7}$$

where F_K is the power of the *axis* meridian (i.e. corresponding to the cylindrical surface) [Bennet, 1968], and F_J is the total power of the principal meridian perpendicular to this meridian. The mean spherical equivalent is the mean focusing ability of the glasses, and is given by,

$$F_{mean} = \frac{F_J + F_K}{2} \tag{2.8}$$

In clinical practice, a standard means of writing the lens prescription is to define the spherical (SPH) and cylindrical powers (CYL) as,

$$SPH = F_J \tag{2.9}$$

$$CYL = F_J - F_K \tag{2.10}$$

which are given in the form SPH/CYL@AXS, where AXS is the angle at which the cylindrical meridian is oriented. Figure 2.8 shows an example, of how these are diagrammed in optometry. This figure shows the same prescription written in two forms (a) crossed-cylinder form, where the two principal powers are given explicitly (i.e. two cylindrical surfaces crossed at angle AXS) (b) minus cylinder form, where the front surface (S) is assumed spherical (i.e. takes on the value of the higher positive power or lower minus power) and the cylindrical (C) is determined from equation (2.10).

To end this section, a comment is made on refractive surgery procedures. The advent of refractive procedures such as Radial Keratotomy (RK), PhotoRefractive Keratotomy (PRK) and LASIK (Laser Assisted In Situ Keratomileusis) have energized research in the fields of optometry and ophthalmology. These procedures re-shape the cornea, in order to correct refractive errors. In RK, the cornea is cut radially (with a surgical blade), which causes the central cornea to flatten, for the correction of near-sightedness. In PRK, a laser is used to sculpt the surface of the cornea, rather than introducing radial cuts. The shape of the

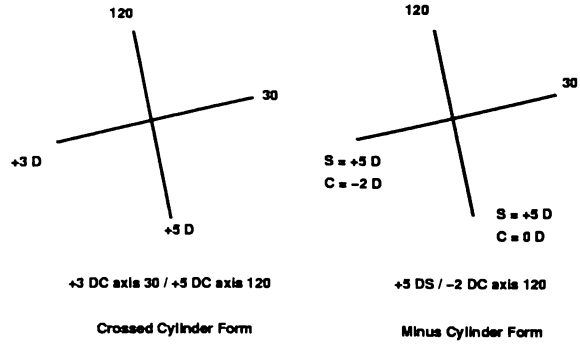

Figure 2.8: Diagrammatic representation of a spectacle prescription. The lens prescription does specify information as to the actual shape of the glasses.

sculpted area determines hyperopic or myopic correction. In addition, PRK is superior to RK, because the integrity of the cornea is maintained. In LASIK, the cornea is cut, creating a hinged flap. This flap is lifted, and the exposed cornea is treated. After this, the flap is folded back into place, which quickly seals. With the advent of these procedures, new methods of quantifying corneal shape and metrics have been devised [Schanzlin and Robin, 1992].

2.3.3 Physical Optics

Even with correction of refractive error, there are physical limits to imaging. At small pupil sizes (< 3 mm) the shape of the Point Spread Function (PSF) is dominated by diffraction, i.e. the wave characteristics of light. The PSF is given by

$$I(x,y) = E^*(x,y)E(x,y) \tag{2.11}$$

where $I(x,y)$ is the illuminance and $E(x,y)$ is the scalar electric field (i.e. ignoring polarization) at the point (x,y) in the Gaussian image plane. In the case of aberration free imaging with point source (and optical elements) aligned on the optic axis, the electric field is given by,

$$E(x,y;z_i) = -\frac{A}{i\lambda L^2} e^{-\frac{ik}{2L}(x^2+y^2)} \int\int e^{-i(2\pi/\lambda L)(xx'+yy')} dx'dy' \tag{2.12}$$

Here A is a constant, (x,y) is a point on the Gaussian image plane, L is the distance from the *exit pupil* (i.e. the Gaussian image of the pupil, as viewed from the retina) to the image plane, z_i is the position of the Gaussian image plane and k is the wave-number of a monochromatic incident wave. The integration is over the *exit pupil.* so that choosing a circular pupil in evaluating (2.12) and using the result in (2.11) gives the *Airy disk*,

$$I = \left\{ \frac{J_1(kr_0 \sin(\theta))}{kr_0 \sin(\theta)} \right\}^2 \tag{2.13}$$

where $J_1(z)$ is a Bessel function of the first kind of order 1 [Charman, 1995]. The value of I is in a relative form, where constants have been dropped, since the absolute illuminance is of secondary importance in most optical applications [Born and Wolf, 1965]. Figure 2.9(b) shows the resulting illuminance distribution, showing characteristic light and dark bands in profile. In fact, 84% of the total light energy is contained within the central peak, which is clearly contrary to geometrical optics, in which the PSF may be made arbitrarily small.

The influence of aberrations (and intervening optics) may be included by way of the *pupil function.* The form of this function is,

$$\tau_p(x', y'; z_i) = \tau_P(x', y') e^{-ikW(x', y'; z_i)} \tag{2.14}$$

where $\tau_p(x', y'; z_i)$ is the *pupil function*, $\tau_P(x', y')$ is the amplitude transmittance i.e. a weighting function over the exit pupil area and $W(x', y'; z_i)$ is the *wave aberration function.* This function measures the difference in Optical Path Length (OPL) between a reference sphere (with center at the position of interest, and with radius equal to the distance from the exit pupil to this point) and a spherical wavefront (i.e. a surface of constant optical path length) which coincide on the exit pupil, see Figure 2.9(a). Equation (2.12) is modified to give,

$$E(x, y; z_i) = -\frac{A}{i\lambda L^2} e^{-\frac{ik}{2L}(x^2+y^2)} \int\int \tau_P(x', y'; z_i) e^{-i(2\pi/\lambda L)(xx'+yy')} dx' dy' \tag{2.15}$$

where the integral may be identified as the Fourier transform of the pupil function denoted $\hat{\tau}_P$ and given by,

$$\hat{\tau}_P(u, v; z_i) = \int\int \tau_p(x', y'; z_i) e^{-2\pi i(ux'+vy')} dx' dy' \tag{2.16}$$

with $u = x/\lambda L$ and $v = y/\lambda L$. An important function is the optical transfer function (OTF) given in *normalized* form as,

$$\hat{O}(u, v; z) = \int\int \tau_P(x', y'; z_i) \tau_P^*(x' - \lambda L u, y' - \lambda L v; z_i) \frac{dx' dy'}{\sigma_P} \tag{2.17}$$

which is the *auto-correlation* function of the pupil function. The OTF embodies important modulation (i.e. the magnitude of the OTF) and phase information (i.e. the argument of the OTF), used for the assessment of visual performance, as will be seen in the following section.

To end this section a final note is made regarding computation of the PSF. The point spread function is typically generated from equation (2.17). Charman [1995] states that the

eye performs close to the diffraction limit for pupil sizes < 2 mm, so this equation is important at these pupil sizes. The balance between aberration limited performance and diffraction limited performance is optimal in the range 2.5 mm to 3.0 mm. For pupil diameters greater than this, the PSF becomes aberration dependent. This situation is shown in Figure 2.10, where the Line Spread Function (LSF) (i.e. the image of a line) is shown in comparison to the diffraction limited LSF as a function of pupil diameter. In cases of large aberrations, the use of the geometrical optics method of computing the PSF (i.e. as the density of rays [Sinclair, 1995]) is valid. This method is used throughout this thesis.

2.4 The Eye as a Linear Imaging System

For incoherent light sources, the point spread functions corresponding to points in the object plane may be summed linearly. That is, given an object source distribution I_0, the image plane irradiance distribution I_1 may be calculated by,

$$I_1(x_0, y_0) = \int\int I_0(x, y) G(x, y; x_0, y_0) dx dy \tag{2.18}$$

where (x_0, y_0) are the co-ordinates of a point on the image plane. If the point spread function is constant (i.e. isoplanatic or spatially invariant) over the region of interest then the function $G(x, y; x_0, y_0)$ may be taken as,

$$G(x, y; x_0, y_0) = G(x - x_0, y - y_0) \tag{2.19}$$

so that equation (2.18) becomes,

$$I_1(x_0, y_0) = \int\int I_0(x, y) G(x - x_0, y - y_0) dx dy \tag{2.20}$$

which in short-hand is written,

$$I_1(x_0, y_0) = I_0(x, y) \otimes G(x, y) \tag{2.21}$$

where $\otimes$ is the *convolution operator*. The process of convolution in the spatial domain is multiplication in Fourier space. Introducing spatial frequency co-ordinates (u, v) equation (2.21) becomes,

$$\hat{I}_1(u, v) = \hat{I}_0(u, v) \hat{G}(u, v) \tag{2.22}$$

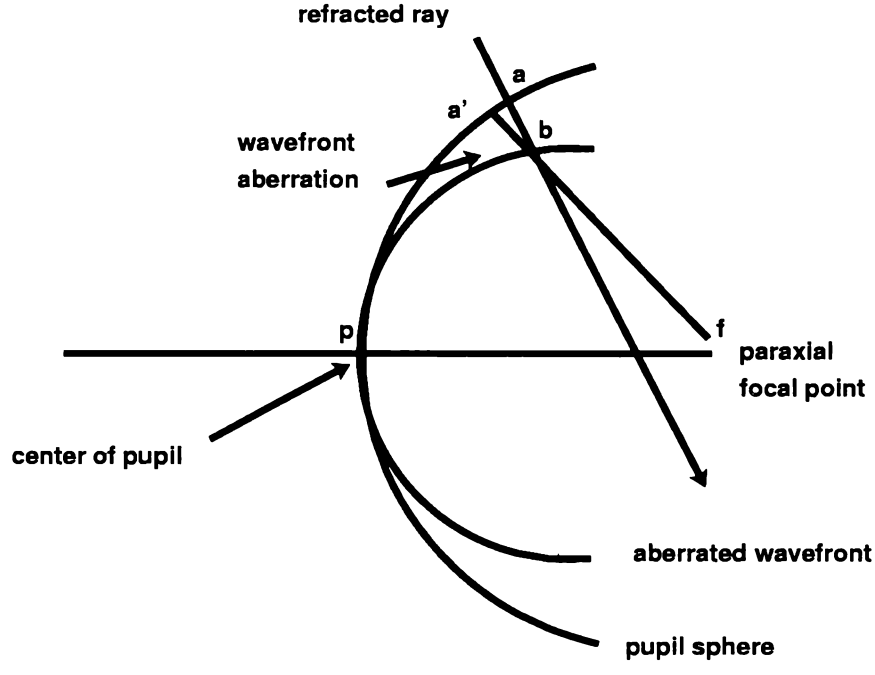

(a) Wave Aberration

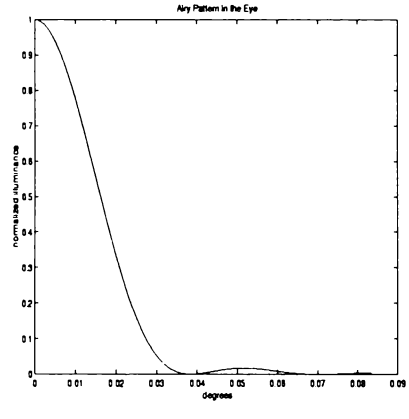

(b) Diffraction Limited PSF

Figure 2.9: (a) Wave aberration function [Salmon, 1999] (b) Diffraction limited PSF (normalized) as a function of angle relative to the optic axis.

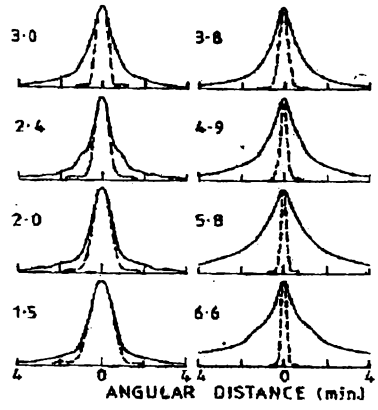

Figure 2.10: Ocular line spread functions (LSFs) with varying pupil size. The geometric aberrations become increasingly important as the pupil size increases. The diffraction limited LSF is shown for comparison. Picture reproduced from Charman [1995]

where the hatted variables are the Fourier transforms of the "hatless" variables. The function $\hat{G}(u,\omega)$ is the *unnormalized* OTF introduced in normalized form (i.e. $\hat{O}$ defined in equation (2.17)). The magnitude of $\hat{G}(u,v)$ is the (unnormalized) modulation transfer function (MTF) which is a measure of the reduction in contrast as a function of spatial frequency (and thereby a measure of performance). It is customary practice [Hecht, 1997] however, to use the *normalized* MTF. Introducing the *contrast* or *modulation*,

$$contrast(u,v) = \frac{I_{max}(u,v) - I_{min}(u,v)}{I_{max}(u,v) + I_{min}(u,v)} \tag{2.23}$$

where I_{max} and I_{min} are amplitudes of the sinusoids at the input stage (but is equally applicable to the output stage by adding primes to the I's) gives the normalized MTF as,

$$MTF = \frac{image\ contrast}{object\ contrast} \tag{2.24}$$

The phase transfer function (PTF) measures the shift in phase and is given by,

$$PTF = \phi' - \phi \tag{2.25}$$

where ϕ' is the image phase, and ϕ is the object phase. These functions combined form the normalized optical transfer function (OTF) introduced previously. In particular,

$$\hat{O} = MTF \times e^{iPTF} \tag{2.26}$$

As stated above, the MTF is a measure of the performance of the eye. Figure 2.11(a) shows the MTF for an eye under several levels of de-focus. The optical cut-off frequency of the eye is approximately 60 cyc/deg (160 cyc/mm) (which is found to correspond closely to the frequency of retinal cones at the fovea). However, the eye is generally limited by the optical aberrations of the eye to around 30 cyc/deg (80 cyc/mm). The letter "E" on the 6/6 line of a Snellen chart has an equivalent sinusoidal grating frequency of 30 cyc/deg.

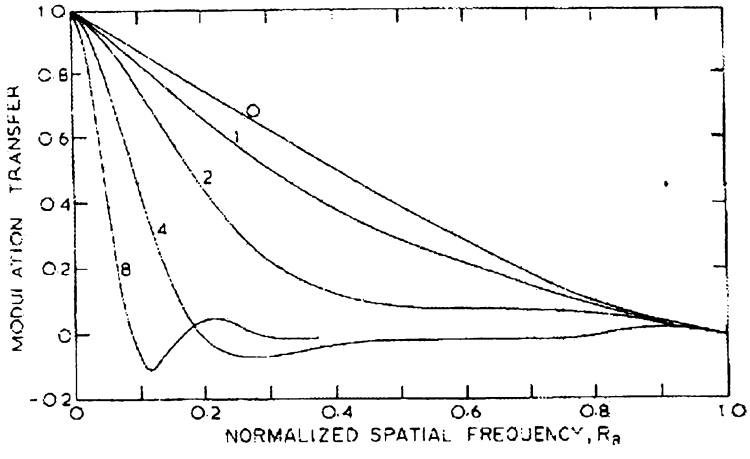

(a) Modulation transfer function

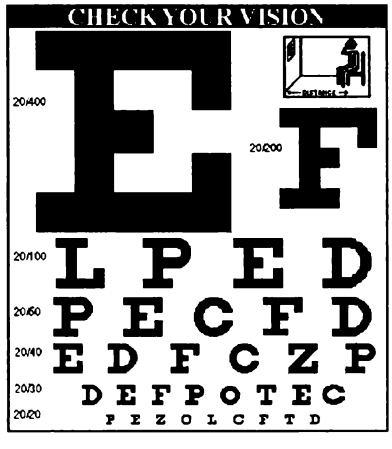

(b) Visual Acuity

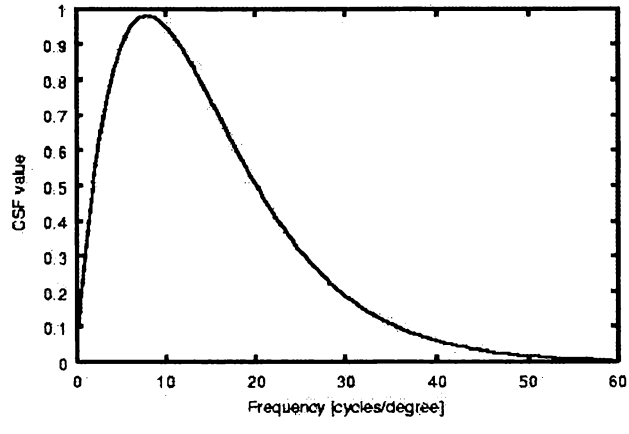

(c) Contrast Sensitivity Function

Figure 2.11: (a) Modulation transfer function (Diffraction Limited) as a function of de-focus (D). The frequency is normalized, but for the eye this maximum frequency corresponds to 60 cyc/deg (160 cyc/mm) [Charman, 1995] (b) The Snellen visual acuity is the minimum legible acuity [NEI, 2001] (c) The Contrast Sensitivity Function (CSF) measures the sensitivity to sinusoidal gratings (picture reproduced from Matkovic [1997]).

2.5 Testing the Eye

Testing of the eye's performance is hindered by the fact that the light distribution on the retina is not easily measured *in-vivo*. Objective methods do exist however, for example, the Hartmann-Schack wavefront sensor (originally applied to the eye by Liang [Salmon, 1999]), uses diffuse light reflected from the retina, which is passed through a lenslet array giving the local wave-front slope. From this information, the entire wavefront is reconstructed. The laser ray-tracing method of Losada and Navarro [1998] passes an unexpanded laser beam into the eye. From the diffusely reflected rays that return from the retina, estimates of the PSF (at the retina) are obtained.

The simplest and most widely used methods are subjective, i.e. they depend on the performance of the observer to a given visual task. The term "visual discrimination" encompasses the range of possible visual tasks shown in Table 2.1 (the table has been reproduced from Schechter [1995]). The three main discrimination tasks are: (1) Light discrimination, which involves the detection of light and color (2) Spatial discrimination, which involves distinguishing spatial objects and the relationships between the objects in space (3) Temporal discrimination, which is concerned with detecting changes in objects as a function of time.

The category of most relevance is the spatial discrimination category, since this covers the standard clinical methods. In particular, the standard visual performance measure is minimum legible acuity, commonly referred to as Visual Acuity (VA). This task involves correctly identifying the letters in a chart with gradually decreasing letter size, as shown in Figure 2.11(b). The line where 50% correct identification occurs, is usually taken as the visual threshold. The visual acuity is quantified by the "Snellen fraction", which expresses the vision of the observer with respect to normal population performance. It is defined,

$$Visual Acuity = \frac{distance\ at\ which\ letter\ is\ read}{distance\ at\ which\ letter\ is\ normally\ read} \tag{2.27}$$

For example, the 6/9 Snellen fraction means that a line which was correctly identified at a standard viewing distance of 6m, would be correctly identified by a normal observer at 9m. Thus, 6/6 vision is normal vision, but visual acuities of 6/5 i.e. better than normal, are not uncommon. The size of the letters of the chart may be computed by noting Snellen's observation, that the 6/6 Snellen letters subtended 5/60° in the eye. Thus, the size of the 6/9 letter may be determined by realizing that a letter placed at 9m will subtend the same 5/60° angle on the retina. Simple trigonometry gives the height of the letter, h, as a function of d, the Snellen denominator,

$$h(z) = 2d \tan\left(\frac{5/60°}{2}\right) \tag{2.28}$$

I. Light discrimination
A. Brightness sensitivity or the ability to detect a very weak light B. Brightness discrimination or the ability to detect threshold and their visual interactions C. Brightness contrast having to do with luminance differences at levels well above threshold and their visual interactions D. Color discrimination or the ability to detect colors
II. Spatial discrimination
A. Types of visual acuity 1. Minimum visible and perceptible acuity: the ability to detect the presence of objects in the visual field without naming or resolving them 2. Minimum separable acuity: the ability to resolve separate parts of a pattern 3. Vernier acuity: the ability to localize small displacements of one part of an object with respect to the other parts 4. Minimum legible acuity: the ability to recognize a pattern such as a letter 5. Modulation transfer function of the eye B.Distance discrimination or the ability to judge absolute or relative distances of objects C.Movement discrimination or the ability to detect relative or absolute angular motion
III. Temporal discrimination
The growth and decay of sensations caused by time-varying stimuli, such as flickering lights

Table 2.1: The term Visual Discrimination encompasses I. Light Discrimination II. Spatial Discrimination III. Temporal Discrimination [Schechter, 1995]

Unfortunately, the use of letters is a confounding factor, since it depends on psychological factors. The approach taken in research, and in clinical evaluation of diseases is to measure the Contrast Sensitivity Function (CSF) of the eye. This function is the inverse of the modulation threshold, i.e. the lowest modulation that can be detected. An example CSF is shown in Figure 2.11(c), which according to Matkovic [1997] is based on a model equation due to Mannos and Sakrison [1974]. The model function shows the general observation that the sensitivity of the eye has its highest sensitivity at frequencies below 10 cyc/deg (typically 3-7 cyc/deg), which then drops off to zero at 60 cyc/deg.

The MTF of the eye was first measured by psychophysical methods, by Campbell and Green [1965]. In their classic experiment, interference fringes were projected onto the retina, bypassing the optics of the eye. Subjective measurement of the modulation threshold (m_t) gave the threshold without contribution from the eye's optics. The subjects then viewed gratings on a monitor to give m_{ext} (i.e. including the eye's optics), which from the relation,

$$m_t = MTF_{eye} m_{ext} \tag{2.29}$$

gave MTF_{eye}. This method can be generalized, for two experimental conditions so that,

$$\frac{MTF_{eye}}{CSF_{eye}} = \frac{MTF_0}{CSF_0} \tag{2.30}$$

where MTF_0 and CSF_0 are measured under some reference condition. The equality of the sides of this equation may be used to determine the validity of MTF data.

2.6 Summary

The physiology of the eye was introduced. The basic concepts for modeling the eye as an optical system were introduced. The eye was introduced as a paraxial system, with a brief description geometrical/wave optics. The eye as a linear imaging system was introduced, which led finally into the testing of the eye clinically, and in the context of linear systems.

Chapter 3

Measuring the Corneal Surface

3.1 Introduction

The anterior cornea accounts for approximately 2/3 of the refraction of light onto the retina. Therefore it is important that a general eye model has detailed information regarding this surface. To this end, this chapter will concentrate on videokeratography (VK), the measurement of corneal surface metrics for the diagnosis of corneal surface irregularities, based on the image of a pattern reflected from the anterior cornea.

Videokeratography defines the current "state of the art" in corneal topography measurement [Applegate, 1995]. This method has been in use for over 100 years, but amazingly, its use as a practical clinical method is a relatively recent development. The current interest in refractive surgery and contact lens fitting is responsible for the interest in this method; the availability of computer processing power is certainly responsible for making this method a reality in clinical practice.

The chapter will start by giving a brief history of videokeratography. A model of a videokeratograph will then be described, including appropriate camera model equations. The resulting equations relate a measured image point (the reflection captured by the camera) to a source point (an element of the pattern presented), through the first derivatives of the corneal surface. The aim of any VK is to recover surface metrics based on this knowledge, which amounts to solving the resulting differential model equation for the corneal height. Further, clinically relevant metrics may be defined from this output.

The corneal reconstruction methods that appear in the literature are reviewed. It is found that some aspects of the problems of reconstruction have not been dealt with previously. A new arc-step corneal recovery algorithm is then presented, which is tested on three simulated cornea. The algorithm is found to perform well in the recovery of corneal height. It has a fast

execution time ($\leq 2.3s$ on a DEC-ALPHA), is *iteratively stable*, and produces results with RMS height errors that are sub-micron ($< 1 \times 10^{-3}$ mm) (in simulation). These tests show that low error height recovery is possible using a simple cubic polynomial based method, combined with skew ray error compensation.

Finally, the algorithm is tested on calibration balls using a commercially available VK[1]. It is found that the surface can be recovered to less than 1μm of RMS (height) error (for the set of calibration balls), *provided* the data is calibrated appropriately. The calibration process and rationale for the method are explained.

3.2 Background

3.2.1 History of Placido Disk Videokeratography

The idea of determining the corneal contour using images reflected from the cornea is due to Scheiner [El Hage, 1992], when he attempted to measure the cornea by comparing the images found in a subject's eye with the images in several convex mirrors. However, the main aspects of the process of *videokeratography* as it stands today, begins with the French Ophthalmologist Ferdinand Cuignet, who coined the term "keratoscopy" in the 1820s [Schanzlin and Robin, 1992]. In his system the light, target and patient were positioned so that the an observer could view the image of the object. Distortion of the reflected image, allowed qualitative assessment by the observer. This technique was hampered by alignment problems, namely in lining the system up with the visual axis.

In 1880, A. Placido introduced the standard object that is still used today, the *Placido Disk* [Schanzlin and Robin, 1992]. The disk had a hole in the center, through which an observer could see the reflected pattern from the cornea. This solved the alignment problems found in the technique of Cuignet, because the subject was aligned so that the center of the disk was aligned with the visual axis. However without magnification of the observed image it was difficult to detect small changes in the image rings.

It was E. Javal, who had the idea of capturing the image of the targets photographically in the late 1880s, and measuring the results by way of a microscope. El Hage [1992] credits A. Gullstrand for actually combining the Placido disk with a photographic system. He is also credited with developing a method for determining the radii of curvature based on measurements of the images obtained, using a *measuring* microscope.

By the 1950s keratographs were quantitated by comparing sections of the cornea to the

[1] Technomed C-SCAN

images found from sets of calibration balls [Schanzlin and Robin, 1992]. In particular, a photograph of a calibration sphere was cut in half and then placed over the keratograph. If the rings in the photo, matched those in the keratograph, then it was assumed that the radius of curvature in that region was the same as the test ball. In 1961, Charles Hendrick introduced a device for performing this task, which is known as a *comparator*. This system works by projecting the keratograph on to a screen, which is adjusted to match standard rings on the comparator screen by altering the magnification. From this process, the radius of curvature can be determined.

3.2.2 Alternative Methods for Corneal Topography

There are several ways of measuring corneal topography besides the videokeratographic method. These include the interferometric and rasterstereographic methods [Belin and Zloty, 1993, Belin et al., 1995]. The interferometry technique is based on the reflection formed by a monochromatic laser. The rasterstereographic method uses a fluorescein stain to dye the corneal tear film. A grid then illuminates the surface of the eye, which produces a diffusely emitting pattern over the eye. Standard methods of structured lighting can be applied to recover the corneal surface shape.

In fact, interferometric and rasterstereographic methods require minimal or no assumptions. This is attractive in theory, but videokeratographic methods currently define the "state of the art" because much has been published about these devices, and they have been commercially available since about 1991. This is not true for devices based on the former methods, and little has been published about their use to date [Applegate, 1995].

Therefore, when considering a suitable means of clinically obtaining corneal surface measurements, the obvious choice is videokeratography, since it is used widely and is clinically accessible. The operation of this type of device will be explained in the following sections.

3.3 A Model of a Placido Disk Videokeratograph

Figure 3.1 shows a typical VK setup. The main features of the device are a set of object rings that diffusely illuminate the cornea, a camera which forms the resultant image of the cornea, and an image capture device, typically a Charge Coupled Device (CCD) camera.

Suppose then, that every point on a VK ring is a diffuse emitter, so that an infinite number of rays leave a particular object point P. A subset of these rays will intersect the corneal surface. For those rays, an *incident ray vector* $\hat{\mathbf{i}}(r,\theta)$ (*normalized* by default) is defined, written here as a function of the corneal domain coordinates (see Figure 3.4). From

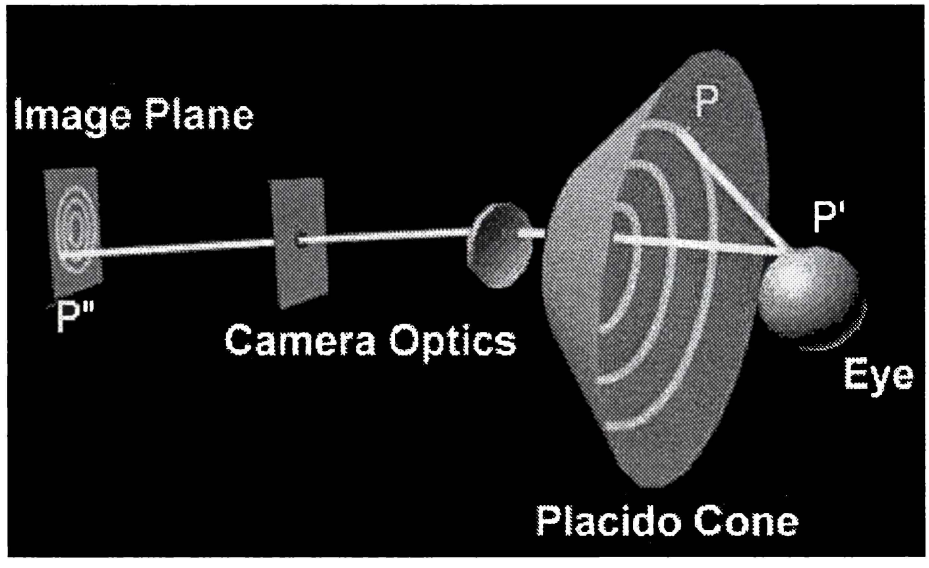

Figure 3.1: The figure shows the main elements of any VK. The object rings illuminate the cornea diffusely. The rays are reflected specularly, and the camera captures these rays to form the image. By modeling this process, we can establish a procedure for generating the corneal surface when the image and object points are known.

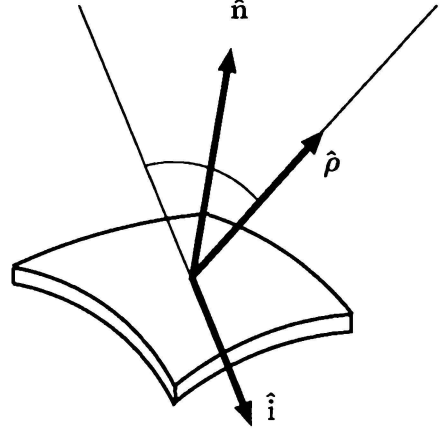

Figure 3.2: A patch of corneal surface, showing the incident, reflected and normal vectors. The normal vector is the gradient of ϕ.

geometry, the incident ray vector may be calculated by,

$$\hat{\mathbf{i}} = \frac{P' - P}{|P' - P|} \tag{3.1}$$

where P is an object point on the Placido cone, and P' is a point on the corneal surface. The rays that are incident on the corneal surface will be reflected specularly, so that every corneal point will have an associated *reflected vector* $\hat{\boldsymbol{\rho}}(r, \theta)$. The value of $\hat{\boldsymbol{\rho}}$ is determined by the vector form of the *law of reflection*,

$$\hat{\mathbf{n}} \cdot (\hat{\mathbf{i}} \times \hat{\boldsymbol{\rho}}) = 0 \tag{3.2}$$

$$\hat{\mathbf{n}} \cdot \hat{\boldsymbol{\rho}} = -\hat{\mathbf{n}} \cdot \hat{\mathbf{i}} \tag{3.3}$$

$$\hat{\boldsymbol{\rho}} \neq -\hat{\mathbf{i}} \tag{3.4}$$

which requires, in addition to the incident and reflected rays, a normal vector to the surface, chosen here to be the unit normal $\hat{\mathbf{n}}$. Figure 3.2 shows the relationship between the incident, reflected and normal vectors. Equation (3.2) expresses the co-planarity of the incident, normal and reflected ray vectors, equation (3.3) says that incident and reflected rays make the same angle with the normal. The condition (3.4) disallows the co-incident solution, i.e. the unphysical solution where the reflected ray is anti-parallel to the incident ray[2]. The normal vector is determined from the corneal surface by,

$$\hat{\mathbf{n}} = -\frac{\nabla\phi}{|\nabla\phi|} \tag{3.5}$$

where $\phi(r, \theta, z) = z - f(r, \theta) = 0$, and it has been assumed that ϕ is differentiable over the domain of the cornea. The negative sign ensures that the normal is directed out of the corneal surface, as is the convention in optical refraction/reflection problems.

Only a subset of the reflected light rays will enter the camera image space. For example, a pinhole camera will only "accept" rays that pass through the pinhole (thereby producing a CCD event at P''). This may be described by the condition,

$$\hat{\boldsymbol{\rho}}'(P'') = \hat{\boldsymbol{\rho}}(P') \tag{3.6}$$

where the reflected ray vector $\hat{\boldsymbol{\rho}}(P')$ must equal the camera condition $\hat{\boldsymbol{\rho}}'(P'')$. The intention of the camera model is to create a unique map from the object space to the image space. In practice, the two camera models used are the telecentric and nodal camera models.

[2]with the exception of the case of normal incidence

The nodal camera is a pinhole camera with an aperture (or nodal point) placed a distance d in front of the image plane (see Figure 3.3(b)). A ray from object space passes through the pinhole to the image plane, thereby creating a CCD event at P''. The distance d, will determine the magnification of the resultant image. This setup is equivalent to an in-focus thin lens camera, provided the CCD is at the focal plane. In this case the nodal point D coincides with the center of the thin lens, and all rays leaving the object point will coincide at the image plane. The image plane will be *conjugate* to the virtual image of the VK object point. This description is shown in Figure 3.3(c). In either case, simple geometry gives the relationship between the measured image point P'', and the reflected ray vector $\hat{\boldsymbol{\rho}}$ as,

$$\hat{\boldsymbol{\rho}} = \hat{\boldsymbol{\rho}}' = \frac{P'' - D}{|P'' - D|} \tag{3.7}$$

where D is the nodal point (i.e. the point a distance d from the image plane). The telecentric camera shown in Figure 3.3(a) includes a *Badal* lens [Smith, 1966], one focal length in front of the pinhole. In this case, the system accepts rays parallel to the optic axis of the camera only. By placing the image plane one focal length behind the pinhole, the magnification is unity. In this case, the camera model vector is,

$$\hat{\boldsymbol{\rho}}'(P'') = \hat{\mathbf{z}} \tag{3.8}$$

It is also clear that the corneal domain coordinates (r, θ) are then the image coordinates also. The model equations are particularly simple in this case. Provided the corneal surface is sufficiently well-behaved, a 1-to-1 map from P to P'' results. For a particularly irregular corneal surface, two (or more) rays from the same object point could cause two distinct CCD events P_1'' and P_2''. The result would be a "double image", of the object rings. However, this effect is not generally observed (Doss et al. [1981]) and so will not be considered further. Explicit equations from the description given in this section will now be given.

3.3.1 A Corneal Co-ordinate System

A corneal co-ordinate system is now described, using Figure 3.4 which shows a front-on view of the cornea. A cylindrical co-ordinate system is defined by the diagram, where the $z-axis$ points out of the page, with θ defining an angular displacement from the (positive) horizontal, r the radial distance to a point and z the axial distance. Thus, (r_s, θ_s, z_s) are the co-ordinates of the source point, (r_c, θ_c, z_c) is the intersection point of the incident ray with the cornea, and (r_m, θ_m, z_m) are image plane co-ordinates.

The angle θ defines a *meridional plane* i.e. any plane that contains the optic axis, cutting the corneal surface to form a profile view of the cornea. The *corneal normal* is the gradient

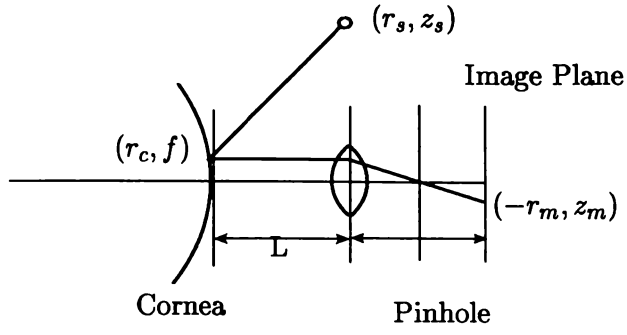

(a) Telecentric Camera

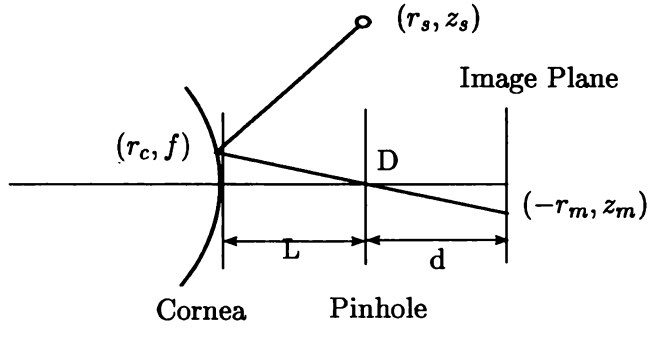

(b) Nodal Camera

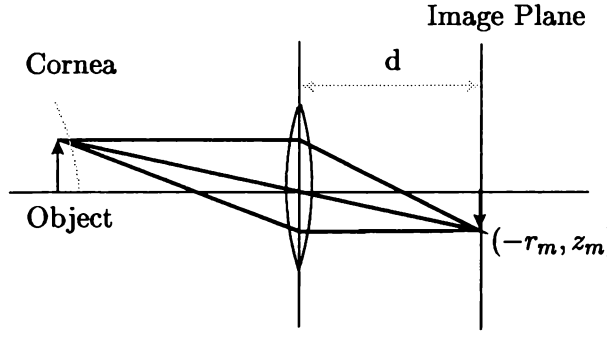

(c) Thin Lens

Figure 3.3: (a) A telecentric camera consists of a lens placed one focal length in front of a pinhole. This camera will only "accept" rays that are paraxial (b) A nodal camera is a simple pinhole, which will focus an image at any distance (c) A thin lens camera is an approximation to the nodal camera.

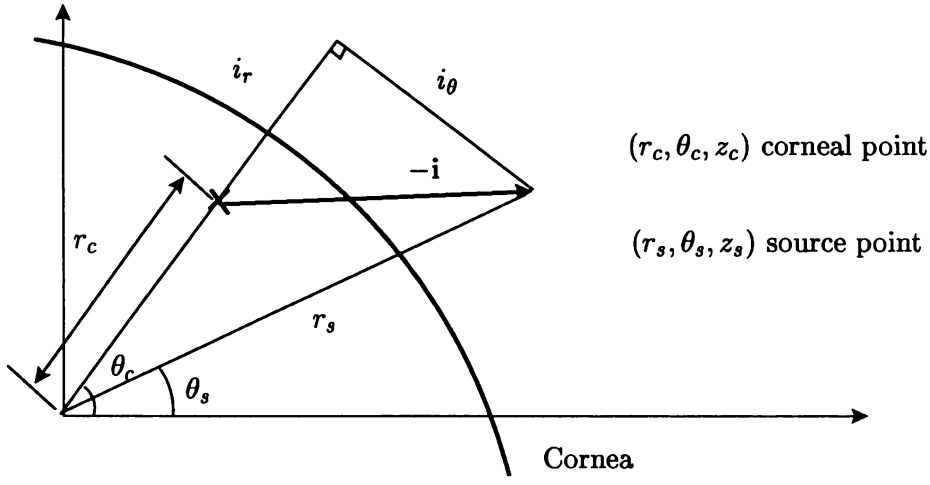

Figure 3.4: The diagram shows the cornea in a front on view. Shown are the components of the (un-normalized) incident ray vector $\mathbf{i} = (i_r, i_\theta, i_z)$, emanating from the source point (r_s, θ_s, z_s). The positive z-axis points out of the page. The intersection of the optic axis with the corneal surface defines the origin. The coordinates (r, θ) (i.e. ignoring subscripts) specifies the projection of a corneal point f, onto the x-y plane.

of the surface given by equation (3.5), or in component form,

$$\hat{\mathbf{n}} = \frac{(n_r, n_\theta, 1)}{|(n_r, n_\theta, 1)|} \tag{3.9}$$

where the components are given by,

$$n_r = -f_r \tag{3.10}$$

$$n_\theta = -\frac{1}{r} f_\theta \tag{3.11}$$

The corneal slope is $n_r = -f_r$ the first radial derivative and the corneal tilt is the first angular derivative $n_\theta = -(1/r)f_\theta$. Corneas with tilt ($n_\theta \neq 0$) are said to introduce *skew-rays* (i.e. are not constrained to meridia) which causes the *skew-ray error* in current recovery techniques, since they do not account for this possibility.

In the following sections, use will be made of the components of the incident, refracted and normal vectors. Considering the forward problem, where the corneal surface intersection $f(r_c, \theta_c)$ is known, yields the incident ray vector,

$$i_r = r_c - r_s \cos(\theta_c - \theta_s) \tag{3.12}$$

$$i_\theta = r_s \sin(\theta_c - \theta_s) \tag{3.13}$$

$$i_z = f - z_s \tag{3.14}$$

where r_c is radial position where the ray strikes the cornea. This cannot be measured directly, but is related to the position of the ray on the image plane by the camera model. For example,

in the case of a telecentric camera,

$$r_c = r_m \tag{3.15}$$

or alternatively, the nodal camera given by,

$$r_c = \left\{ \frac{L-f}{d} \right\}^{-1} r_m \tag{3.16}$$

where r_m is the radial position on the image plane and L is the distance from the corneal origin to the nodal point. These equations have been found from considering the geometry of the cameras in Figure 3.3, and will re-appear in the following section.

3.3.2 The Corneal Transform Equations

The incident vectors, reflected vector and normal vectors can be written in component form,

$$\hat{\mathbf{i}} = \frac{(i_r, i_\theta, i_z)}{|(i_r, i_\theta, i_z)|} \tag{3.17}$$

$$\hat{\boldsymbol{\rho}} = \frac{(\rho_r, 0, \rho_z)}{|(\rho_r, 0, \rho_z)|} \tag{3.18}$$

$$\hat{\mathbf{n}} = \frac{(n_r, n_\theta, 1)}{|(n_r, n_\theta, 1)|} \tag{3.19}$$

where the component ρ_θ has been set to zero, as is the case with the telecentric and nodal camera models. Substituting equations (3.17)-(3.19) in equations (3.2)-(3.4) gives,

$$n_r(i_\theta \rho_z) - n_\theta(i_r \rho_z - i_z \rho_r) - n_z(i_\theta \rho_r) = 0 \tag{3.20}$$

$$\frac{n_r i_r + n_\theta i_\theta + n_z i_z}{\sqrt{i_r^2 + i_\theta^2 + i_z^2}} = -\frac{n_r \rho_r + \rho_z}{\sqrt{\rho_r^2 + \rho_z^2}} \tag{3.21}$$

which are general relationships between the reflected, incident and normal vectors in a component form. These equations may be solved for n_r and n_θ (see Appendix C) to give,

$$n_r = \frac{i_\theta^2 \rho_r + (i_z \rho_r - i_r \rho_z)(i_z + \rho_z \psi)}{i_\theta^2 \rho_z - (i_z \rho_r - i_r \rho_z)(i_r + \rho_r \psi)} \tag{3.22}$$

$$n_\theta = -\frac{i_\theta \psi(\rho_z^2 + \rho_r^2) + \rho_z i_z + \rho_r i_r}{i_\theta^2 \rho_z - (i_z \rho_r - i_r \rho_z)(i_r + \rho_r \psi)} \tag{3.23}$$

where ψ is,

$$\psi = \frac{\sqrt{(i_r^2 + i_\theta^2 + i_z^2)}}{\sqrt{\rho_r^2 + \rho_z^2}}$$

These equations are the *general corneal transform equations* (using the terminology of Rand et al. [1997]) as functions of n_r and n_θ. Selecting values for $\hat{\boldsymbol{\rho}}$ commits to a particular camera model; the nodal camera and telecentric camera being the relevant choices. The nodal camera equation is given by,

$$\hat{\boldsymbol{\rho}} = (-r_m/\sqrt{r_m^2 + d^2}, 0, d/\sqrt{r_m^2 + d^2}) \tag{3.24}$$

where r_m is the radial image position, and d is the nodal distance from the image plane. The telecentric camera equation is given by,

$$\hat{\boldsymbol{\rho}} = (0, 0, 1) \tag{3.25}$$

where the image point r_m is also the radial distance r_c to the corneal point (by virtue of Figure 3.3(a)). Equations (3.24) and (3.25) may be substituted in equations (3.22) and (3.23) to give equations for the camera choices, but due to the rather convoluted results obtained, the reader is directed to Appendix C where corneal transform equations for corneal tilt/no corneal tilt and nodal/telecentric cameras are derived. The two equations of key interest in the mentioned appendix are the *telecentric corneal transform with no corneal tilt* given by,

$$n_r = -\frac{i_z + \psi}{i_r} \tag{3.26}$$

and the *nodal corneal transform with no corneal tilt* given by,

$$n_r = -\frac{i_z + d\psi}{i_r - r_m\psi} \tag{3.27}$$

with the additional assumptions,

$$n_\theta = 0 \tag{3.28}$$

$$i_\theta = 0 \tag{3.29}$$

$$\rho_\theta = 0 \tag{3.30}$$

$$\tag{3.31}$$

Equations (3.26) and (3.27) form the basis of commercial VK algorithms for recovery of corneal height; so that practical height recovery algorithms are the solution of these differential equations. The more general equations (3.21) are not solved for, because a given image point cannot be identified with a unique object point using continuous Placido rings. Assuming there is no tilt, allows a unique object/source point to be identified, which however, incurs the *skew-ray error* [Klein, 1997a] since this is not necessarily true. Klein [1997b] compensates for this error, by estimating tilt from solutions to equation (3.26) (i.e. initially ignoring tilt) with apparent success.

Finally, as a matter of convenience, the equations (3.26) and (3.27) will be referred to in generic form,

$$f_{r_m} = F(r_m, z) \tag{3.32}$$

where f_{r_m} is the derivative with respect to r_m and the function F represents a *generic corneal transform* equation i.e. without regard to the form of the camera model equation. This form will be useful later (see section 3.5) in the context of a corneal recovery algorithm.

3.4 A Review of Reconstruction Methods

3.4.1 Spherically Biased Methods

Mattioli and Tripoli [1997] mention that the operation of leading VK height recovery algorithms are based on finding *equivalent* spherical corneal models i.e. spheres that model the imaging of the eye. These methods are based on the method of 17^{th} century Jesuit priest C. Scheiner, who first compared images of objects in convex mirrors, to those in real eyes, as a means of describing the shape of these eyes [El Hage, 1992]. This method has been described in the context of videokeratography by Halstead et al. [1995b] (from which the following explanation has been adapted).

In particular, a set of P calibration spheres of radius M_j (where $M_1 < \ldots < M_P$) is defined, with the surface of each sphere passing through the origin. These are used to image an object ring of radius C_1 say. The result is P images of radius R_j where $R_1 < \ldots < R_P$. These are then compared against a subject's mire image of radius γ. If a value α can be found, where $0 \leq \alpha \leq 1$, such that the equation $\gamma = \alpha R_\beta + (1-\alpha)R_{\beta+1}$ is satisfied (for some β, $1 \leq \beta \leq N$), then the corresponding radius of curvature of the cornea is estimated as the corresponding linearly interpolated radius of calibration sphere,

$$m = \alpha M_\beta + (1-\alpha)M_{\beta+1} \tag{3.33}$$

where m is now the estimated radius of the cornea (or the *equivalent* calibration sphere). The corneal height at a radial position r, is the depth of the *equivalent* calibration sphere (i.e. of radius m) as shown in Figure 3.5(b).

The total corneal profile can be constructed as the result of imaging N object rings $C_1, \ldots, C_N$, which results in the set of equivalent calibration balls $m_1, \ldots m_N$. The assumption that the actual corneal shape and the fictitious sphere height are equal is called "spherical equivalence" or *spherical bias* [Mattioli and Tripoli, 1997]. Clearly, this assumption will be true only in the case of a spherical cornea. Roberts [1994] has shown that the error in the recovery of aspheric surface height is significant, while Tripoli et al. [1996] have demonstrated that *arc-step* methods are more accurate than these methods.

3.4.2 Arc-Step Algorithms

An improved approach to corneal height recovery is the method proposed by Doss et al. [1981] i.e. the *arc-step* method. In fact, the method described here is the result of improvements due to several authors, namely Klyce [1989], Wang et al. [1989], van Saarloos and Constable [1991]. In this approach, the corneal profile is determined by constructing intersecting arcs,

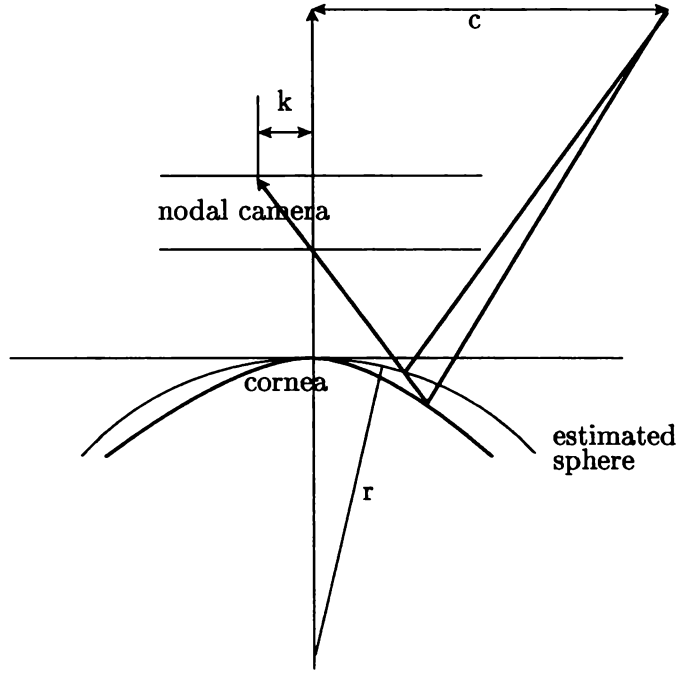

(a)

1.Find a 2^{nd} order Taylor approx. at (r_j^*, z_j^*) given (r_{j-1}, z_{j-1})
2.Calculate a cubic term, to find (r_j, z_j).
3.Calculate the slope of this polynomial
4.Calculate angle of incidence and angle of reflection
5.Adjust z_j accordingly and return to 2, or exit if done

(b)

Figure 3.5: (a) Spherical bias in a simple reconstruction scheme. (b) An outline of Klein's continuous curvature algorithm.

which form a corneal profile that extends out radially from the corneal apex. By requiring that the arc satisfy several constraints, a unique arc can be obtained. These conditions are: (a) The arc has constant curvature (i.e. is a circle) (b) The arc satisfies the *law of reflection* at the transition point from one arc to the next (c) The slope found by approaching a transition point from the left, is the same as the slope found by approaching from the right. This last constraint is a continuity condition, which means that the arc-step method generates height reconstructions which are C^1 continuous. A corneal height recovery will (in general) have discontinuous curvature. Physically this is undesirable, because the majority of corneal surfaces have at least C^2 continuity [Klein, 1992]. In addition, this derivative information is clinically relevant, since the 2^{nd}*derivative* is used to define the *instantaneous power* which has been shown to reveal optically significant shape asymmetries [Klein and Mandell, 1995, Salmon and Horner, 1995].

3.4.3 Improvements to the Arc-Step Algorithm

To improve upon the arc-step algorithm, Klein [1992], proposed a 3^{rd} order polynomial approximation. The coefficients of the polynomial up to 2^{nd} order are equal to the corresponding 2^{nd} order Taylor expansion coefficients. The cubic term is determined iteratively, by searching along the reflected ray for a point which satisfies the law of reflection. When this point is found, the slope and curvature at this point can be transferred to the next arc, which ensures C^2 continuity. The outline of the algorithm is shown in Figure 3.5(a).

Klein tested this method in simulation, with object rings set on a circle of radius 10cm, centered on the center of curvature of a sphere of radius 1cm (a spherical cornea). A pinhole was placed 9cm from the cornea. He found that the algorithm recovered the (spherical) corneal surface with height accuracy within 1μm, and curvature to better than 1%. These results were in simulation [Klein, 1992], so that it would be expected that experimental errors would introduce larger errors.

The second improvement described in Klein [1997a] and Klein [1997b] included the assumption of corneal tilt, which thereby compensated for the *skew ray error*. Klein treated this error by assuming f_θ could be approximated by,

$$f_\theta \approx \frac{f(\theta+\delta) - f(\theta-\delta)}{2\delta} \tag{3.34}$$

which was found from a first approximation to the corneal height $f(r,\theta)$ (using the no tilt assumption), and the angular distance δ between consecutive meridia. Given then the estimate for f_θ, a new corneal slope $\hat{f}_r$ was found, and hence a new estimate for the corneal height $\hat{f}$ (see Klein [1997a] and Klein [1997b] for more details). This method was tested on

a simulated corneal model (for radial keratotomy) used by Rand et al. [1997]. The surface consisted of eight "corrugations" added to a spherical base surface, denoted here by $f(r,\theta)$. In particular,

$$f(r,\theta) = \sqrt{R^2 - r^2} + g(r,\theta) \tag{3.35}$$

where,

$$g(r,\theta) = \begin{cases} \epsilon \sin(8\theta) & \text{where } r \geq 2\text{mm} \\ 2(r-1.5)\epsilon \sin(8\theta) & \text{where } 1.5 < r < 2\text{mm} \\ 0 & \text{where } r \leq 1.5\text{mm} \end{cases}$$

The surface $g(r,\theta)$ is illustrated in Figure 3.6(a). Klein [199, b] asserts that radial lines added to the Placido cone (which thereby give exact object location information) will not improve reconstruction, and are therefore un-necessary. In response to this assertion, Rand et al. [1997] point out that VK images of equation (3.35) give no indication of the undulations present in the outer segment $r \geq 2$ mm of the cornea. Therefore, the surface could correspond to a spherical surface also.

Klein agrees with this point, but adds that the model surface is continuous, so it should produce a satisfactory result in this case. The skew-ray arc-step algorithm is applied at several meridional angles to the simulated cornea. The compensation for the treatment of skew rays significantly improves results found by the arc-step algorithm he uses. The error in the arc-step algorithm is reduced from as much as $8\mu m$ in the corneal periphery, to less than $< 1\mu$m. Again, this result is produced on simulated data.

3.4.4 A B-Spline Reconstruction Algorithm

Halstead et al. [1995a,b, 1996] take a novel approach to reconstructing the corneal surface, drawing on the techniques of CAGD (Computer Assisted Graphic Design). The theory of B-Spline surfaces is used to generate polynomial approximations, which are linear combinations of *basis* spline functions (see for example Farin [1988]).

The method works in the following way: a bi-quintic solution for the surface is guessed. The normal vectors to this surface are computed, along with the *required* normal vectors, i.e. the normal vectors needed to produce the given image with the given surface. A metric is formed from this information, which is subsequently minimized using standard techniques. A unique feature of this algorithm is the addition of a subdivision phase, at which the number of control points are increased thereby increasing the degrees of freedom of the surface (the surface remains biquintic). This phase is invoked when the surface has converged to some threshold level, and by adding degrees of freedom, the surface is allowed to continue

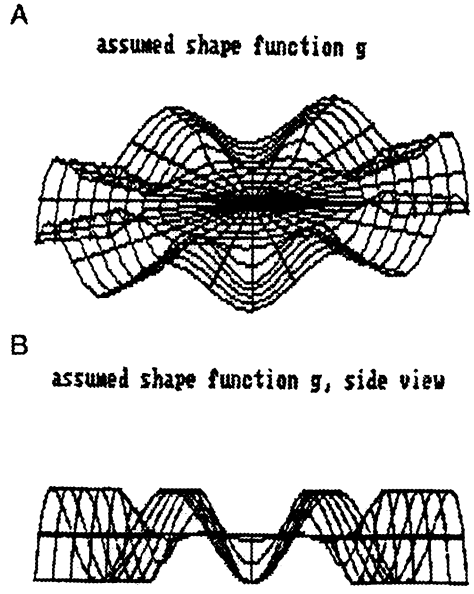

(a)

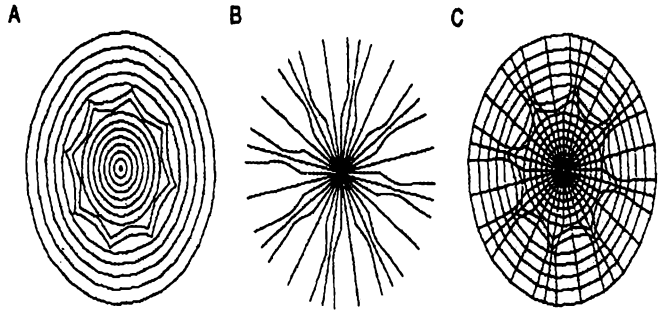

(b)

Figure 3.6: (a) The function $g(r, \theta)$ is added to a sphere. Picture taken from Klein [1997b] (b) The inclusion of radial lines allow remove ambiguity as to the slope of the corneal surface. Figure shows: a) the resulting image given ring objects only b) only radial lines are imaged c) combined radial spokes and circular rings, indicate the undulations present in the corneal periphery. Picture taken from Rand et al. [1997]

refinement.

Halstead et al. [1995b] avoid problems associated with interpolating polynomials of high order , because the B-Spline is fitted to the data using in the *constrained* least squares sense. A least squares fit results in a *fair* surface i.e. a surface which approximates the data smoothly. They find that by adding an interpolation constraint i.e. the surface must pass through the origin, a unique solution is found to the problem.

Two alternative objective functions are minimized using standard iterative methods, with respect to the control points. The first error metric is the Euclidean distance between the set of rings found by casting rays from the image plane back to the object plane, with a corneal model determined by the current set of control points for the *surface*. Halstead et al. [1995b] mention that this method is slow but accurate.

The second method, employs the Levenberg-Marquart [see for example Gill, 1981] algorithm applied to the *normal* vectors. In this case, the error metric is the Euclidean distance between the set of normal vectors of the current surface, and the hypothetical set of normal vectors that would produce the correct image. The correct surface is found when these two sets are equivalent. This method is reported to be much faster, run-times from 3s to 3min have been reported.

The error of this algorithm appears to be very low, with RMS error significantly less than sub-micron accuracy (8.5×10^{-6} mm) in simulation applied to an ellipsoid, with RMS error of 1 micron accuracy on actual spherical calibration balls.

3.4.5 Summary

This section has reviewed corneal reconstruction algorithms. Arc-step algorithms are the standard method for reconstruction, but these are not automatically more than C^0 continuous. Klein has described an iterative algorithm that has continuous curvature, which gives less than micron error in simulation. The method is not tested in experiment. Klein also presents an arc-step algorithm with compensation for the skew-ray error, but it is not iterative, and does not possess C^2 continuity. Halstead et al. have produced significant improvements by use of B-Splines (RMS height error of 8.5×10^{-6} mm).

3.5 A New Method for Recovery of Corneal Shape

3.5.1 Introduction

This section describes a new corneal height recovery algorithm, based on a *multi-step* approach [Press et al., 1992]. The method proceeds by estimating the corneal shape, which through equation (3.32) is used to estimate the corneal *slope*. A quadratic equation is then fitted to the slope data, which by integration produces a cubic representation of the height. This new estimate is then used again, until a convergence threshold is reached. A post-processing step is used to compensate for the *skew ray error*. In particular, the *corneal tilt* is estimated using the method of Klein [1997b] to give (by an additional integration step) a final estimate of the corneal height.

A supplementary condition (referred to here as the *continuous curvature condition*) is used in the above described method, to guarantee a height recovery with continuous 2^{nd} derivative (motivated by clinical requirements for continuous *curvature* [Klein, 1992]). In this case the method is shown to be *iteratively stable*. That is, convergence to a solution can be guaranteed. To the author's knowledge, a formal guarantee of convergence has not been described before for the VK model equations.

The method is tested on three simulated corneal shapes assuming a telecentric camera. Simulated VK images are generated, and the method is applied to recover the original height. The shapes tested are an aspheric with "radius" 7.5 mm and shape factor Q = -0.25, an ellipsoid (with half-axes (8,9,10) mm) originally tested by Halstead et al. [1995b] and the radial keratotomy (RK) model of Rand et al. [1997] (i.e. equation (3.35)).

Setting an RMS convergence threshold of 1×10^{-12}mm gives convergence in 7 iterations, which is achieved in 2.3s on average. The RMS height error in these cases is found to be consistently less than sub-micron (an averaged RMS error of 1.7×10^{-4} mm). These are encouraging results, given both a need for sub-micron error [Halstead et al., 1995a], and the simple implementation of the method. Interestingly, sub-micron accuracy is obtained for the aspheric and the radial keratotomy example *without* the need for skew-compensation. However, introducing skew ray compensation gives both improved sub-micron error in these two cases, and sub-micron error for the ellipsoid case also. In the present implementation, *skew ray* compensation is found to account for the majority of the total processing time (1.7s, 70%), but improves the RMS height estimation by 70%.

In section 3.6 the algorithm is tested on experimentally obtained data. In this case it is found that the RMS height error in recovery is less than sub-micron at 2.5×10^{-4} mm.

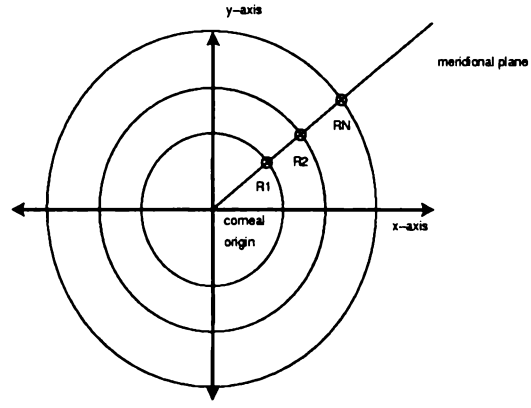

Figure 3.7: (a) Image samples are taken along a meridional plane

However, this is *provided* the output data is calibrated appropriately. In addition the testing done here *includes* the calibration set. The calibration procedure and rationale are explained.

3.5.2 Theory

Consider the image points denoted r_i (where $i = 1 \cdots N$ and N are the number of samples [3]). An initial corneal shape is chosen i.e. $f^0(r_i)$ (where the superscript denotes the j^{th} estimate) which is then used to estimate the corneal slope using the VK transformation equation (3.32), reproduced here from section 3.3.2 for convenience,

$$f'(r_i) = F(r_i, f^0(r_i)) \tag{3.36}$$

The values for $f'(r_i)$ are fitted with a quadratic polynomial, which on integrating, yields a piecewise cubic recovery $f^1(r_i)$. By repeating the process using these new estimates, the process converges to a solution (see Figure 3.7 for a diagram of these points). To this end, a numerical method and convergence properties will now be described. There are three additional issues to consider: (i) the initial conditions, i.e. the assumed values of f and its derivatives at the corneal apex, (ii) the choices for f'' that arise in deriving the numerical method as will be seen, and (iii) compensation for the skew ray error.

Initial Conditions

The following conditions are assumed at the corneal apex ($r_0 = 0$),

$$f(0) = 0 \tag{3.37}$$

$$f'(0) = 0 \tag{3.38}$$

$$f''(0) = \frac{F(h,0)}{h} \tag{3.39}$$

[3] note that r_i where i is an index, replaces r_m (where m refers to "image") used in section 3.3.1

where h denotes the distance to the first ring (i.e. $r_1 = h$). The first two conditions set the corneal apex at the origin, and the normal at the corneal apex along the optic axis. The third initial condition is found by assuming the cornea is *spherical* in the region of the first ring, i.e. with equation given by,

$$r^2 + (f(r) + R)^2 = R^2 \tag{3.40}$$

where R is the radius of curvature of the *corneal cap*. Differentiation of equation (3.40) gives at h,

$$f'(h) = -\frac{h}{f(h) + R} \tag{3.41}$$

$$\Rightarrow R \approx -\frac{h}{f'(h)} \tag{3.42}$$

since $f(h)$ is small compared to R (typically $< 0.1\%$). In addition, the effect of $f(h)$ will be small in $F(h, f(h))$ (typically $< 0.01\%$) (see also [Klein, 1997b]) so that,

$$f'(h) \approx F(h, 0) \tag{3.43}$$

Finally noting the relationship between the second derivative of a circle and the *radius of curvature*,

$$f''(0) = \frac{-1}{R} \approx \frac{F(h,0)}{h} \tag{3.44}$$

which is equation (3.39).

A Numerical Method

A numerical method is now derived for the integration described. Again, for simplicity (and with no loss of generality) consider the corneal apex and the position of the first ring. If the corneal surface is assumed cubic, the height and derivatives (up to 2^{nd}) at h are given by,

$$f(h) = ah^3 + bh^2 + ch + d \tag{3.45}$$

$$f'(h) = 3ah^2 + 2bh + c \tag{3.46}$$

$$f''(h) = 6ah + 2b \tag{3.47}$$

From Figure 3.8 the knowns may be used to determine the unknown co-efficients of the polynomial. In particular,

$$f(0) = d \tag{3.48}$$

$$f'(0) = c \tag{3.49}$$

$$f'(h) = 3ah^2 + 2bh + c \tag{3.50}$$

$$f''(0) = 2b \tag{3.51}$$

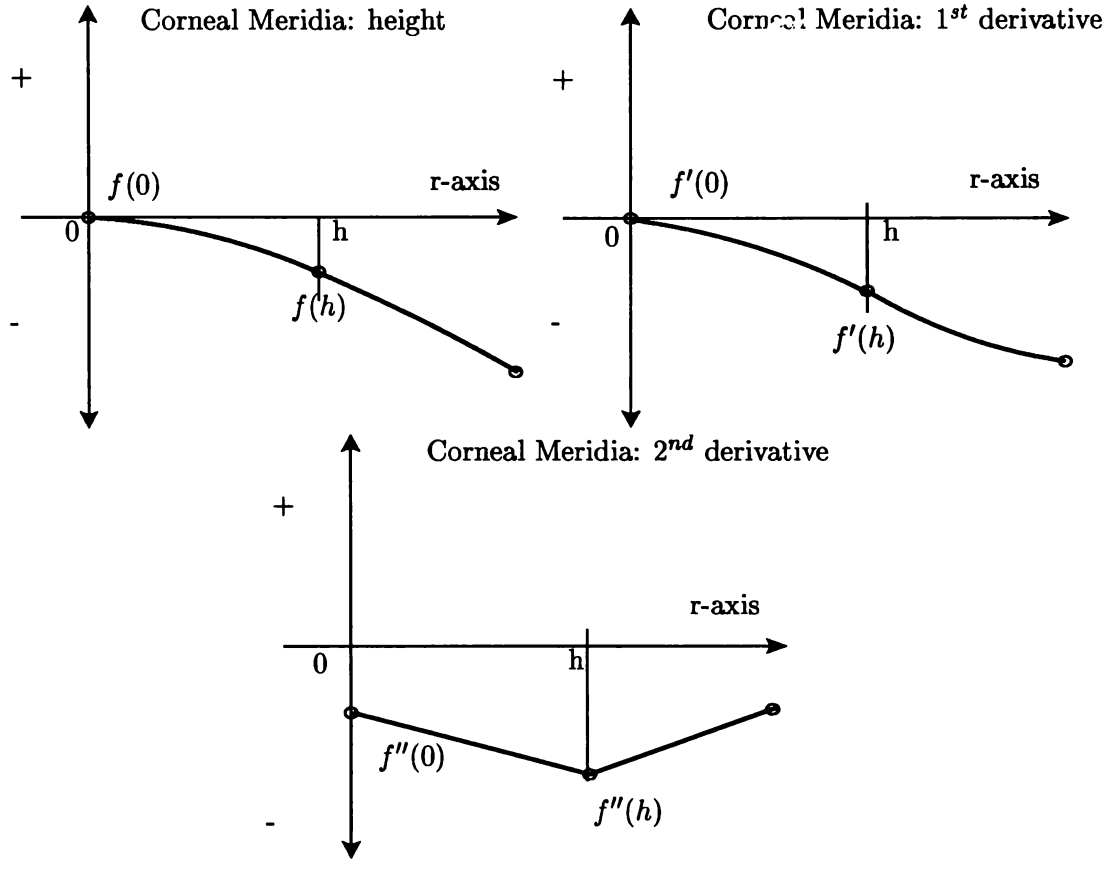

Figure 3.8: The figure shows the cornea in profile, with associated derivatives. The local curvature condition is shown, where the value of $f''(0)$ is used to calculate $f''(h)$, which is then used as the initial 2^{nd} derivative value for the next step of the integration step.

which gives for the co-efficients,

$$a = \frac{1}{3h^2}\{f'(h) - f'(0)\} - \frac{1}{3h}f''(0) \tag{3.52}$$

$$b = f''(0)/2 \tag{3.53}$$

$$c = f'(0) \tag{3.54}$$

$$d = f(0) \tag{3.55}$$

Substituting these values in (3.45) gives,

$$\begin{aligned} f(h) &= \frac{h}{3}\{f'(h) + 2f'(0)\} \\ &+ \frac{h^2}{6}f''(0) + f(0) \end{aligned} \tag{3.56}$$

which is the rule for the height at h (i.e. which integrates the quadratic over one section). Equation (3.56) may be extended to any two subsequent points r_i and r_{i+1} with associated slopes $f'(r_i)$ and $f'(r_{i+1})$,

$$\begin{aligned} f^{(j+1)}(r_{i+1}) &= \frac{h_i}{3}\left\{F(r_{i+1}, f^j(r_{i+1})) + 2f'(r_i)\right\} \\ &+ \frac{h_i^2}{6}f''(r_i) + f(r_i) \end{aligned} \tag{3.57}$$

where the super-scripted variable j represents the j^{th} guess for the corneal height (at the point r_{i+1}), and $f'(h)$ has been replaced by equation (3.36) to make clear the relationship between the current guess and the new estimate. However, it is not clear whether such a method will actually converge to a solution. The next section will addresses this issue.

Stability Criterion

Consider two consecutive estimates for $f(r_{i+1})$, $f^{(j+1)}(r_{i+1})$ and $f^{(j)}(r_{i+1})$ say. Subtracting these two estimates, gives through equation (3.57),

$$\begin{aligned} f^{(j+1)}(r_{i+1}) - f^j(r_{i+1}) &= \frac{h_i}{3}F(r_{i+1}, f^j(r_{i+1})) \\ &- \frac{h_i}{3}F(r_{i+1}, f^{(j-1)}(r_{i+1})) \end{aligned} \tag{3.58}$$

which, by the theorem of the mean [Spiegel, 1988, Chap. 4, pg.61] gives,

$$f^{(j+1)}(r_{i+1}) - f^j(r_{i+1}) = \frac{h_i}{3}\frac{\partial F}{\partial f}(\eta)\left\{f^j(r_{i+1}) - f^{j-1}(r_{i+1})\right\} \tag{3.59}$$

where it has been assumed that F is differentiable, and the variable η is some real number such that $f^j(r_{i+1}) < \eta < f^{j-1}(r_{i+1})$. The result is that convergence occurs when the absolute

value of the "un-bracketed" term on the right-hand side of equation (3.59) is less than unity i.e.

$$\left|\frac{h_i}{3}\frac{\partial F}{\partial f}\right| < 1 \tag{3.60}$$

The equality was tested by substituting the telecentric camera equation in (3.60), and entering bounding values which maximized the equality. From this procedure, it was found that,

$$\left|\frac{h_i}{3}\frac{\partial F}{\partial f}\right|_{\max} = \frac{1}{12} \tag{3.61}$$

which guaranteed that convergence would occur for the no-tilt case. The relevant calculation is given in Appendix C. In fact, this numerical method (and approach to demonstrating convergence) is a variation of an *Adams-Moulton* method which is known to have very stable convergence properties [Press et al., 1992].

A Supplementary Condition

The numerical method performs an integration in a step-wise fashion. The corneal height is necessarily adopted as the "initial condition" for the current step (which guarantees C^0 continuity), from which $f'(r_i)$ is also calculated. However, there is freedom in the choice of $f''(r_i)$. Setting the value of $f''(r_i)$ so that the 2^{nd} derivative is (piecewise) continuous is referred to here as the *continuous curvature condition.* In this case, the value of the second derivative $f''(r_i)$ is found by replacing the parameters given by (3.52)-(3.53) in (3.47) which yields,

$$f''(r_i) = \frac{2}{h_{i-1}}\left\{F(r_i, f^j(r_i)) - F(r_{i-1}, f^j(r_{i-1}))\right\} - f''(r_{i-1}) \tag{3.62}$$

This is not the only possible choice for f'', but continuity is clinically advantageous [Klein, 1992], and this choice also preserves the convergence analysis of the previous section, since it is a function of r_i.

Skew Ray Error Compensation

Skew ray error is treated in a post-processing step. After the numerical method has been applied, the resulting solution for the corneal height f is used to estimate f_θ. This yields a new estimate for the corneal slope $\hat{f}_r$, and by an additional integration, the final corneal height $\hat{f}$ is obtained. The method for estimating $\hat{f}_r$ from f_θ is due to Klein [1997b], who assumes that the presence of tilt does not alter the magnitude of normal vectors at the corneal surface appreciably. In this case,

$$f_r^2 + 1 \approx \hat{f}_r^2 + \left(\frac{1}{r} f_\theta\right)^2 + 1 \tag{3.63}$$

where f_θ is estimated by equation (3.34) from the recovered corneal surface, and thereby compensates for the skew ray error. Solving for $\hat{f}_r$ gives,

$$\hat{f}_r = \frac{f_r}{|f_r|}\sqrt{f_r^2 - \left(\frac{1}{r} f_\theta^2\right)} \tag{3.64}$$

where the root of the new estimate is that with the sign of f_r. Although equation (3.64) is very simple, a problem in estimating f_θ arises since $f(r, \theta - \delta)$ and $f(r, \theta + \delta)$ are not, generally, *sampled* points. However, they can be estimated by applying equation (3.45) with the appropriate cubic polynomial coefficients, i.e. for the particular meridian (i.e. $\theta - \delta$ or $\theta + \delta$) and radial distance r. The corresponding MATLAB code for this process is given in Appendix D.1.3.

3.5.3 Method

The algorithm was tested using a simulated VK model, with model parameters similar to the Technomed C-SCAN corneal topographer. This device has 30 mire rings (i.e. 15 object rings $\times$ 2 edges), with 360 meridia, at 1° spacing. However, less than half of the total available information was used for modeling. The rings were initially reduced to 16, to achieve a similar resolution found in VK recovery tests reported by Halstead et al. [1995b]. This was then reduced to 14 rings, which ensured that the reconstruction was limited to the central (roughly) 8 mm of the corneal surface. A total of 14 $\times$ 360 points were therefore used for recovery purposes.

A telecentric camera was assumed, and the method was tested on three simulated corneal shapes. The shapes tested were an aspheric surface with radius 7.5 mm and *shape factor* Q = -0.25, an ellipsoid (with half-axes (8,9,10) mm) originally tested by Halstead et al. [1995b], and the radial keratotomy (RK) model of Rand et al. [1997] (i.e. equation (3.35)). The VK images generated for these shapes are shown in Figure 3.9. The new method was used to recover the corneal height, slope and tilt (for both skew-ray compensation and no skew-ray compensation). Convergence was assumed to have occured when the RMS convergence threshold, ϵ_j (for the jth iteration) defined by,

$$\epsilon_j = \sqrt{\frac{\Sigma(f^j - f^{j-1})^2}{N}} \tag{3.65}$$

was less than 1×10^{-12} mm. Here $N = 14 \times 360 = 5040$ is the number of sample points, and the sum is over all N points. A plane was used as the initial estimate of the corneal

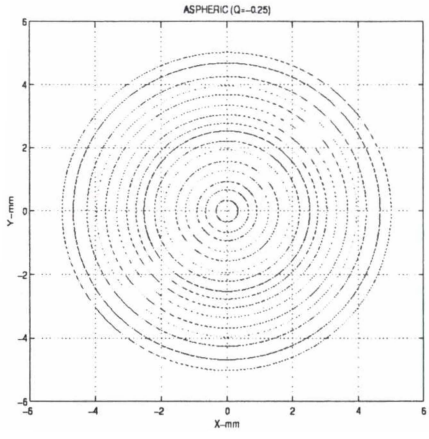

(a) Aspheric R = 7.5 mm with Q = -0.25

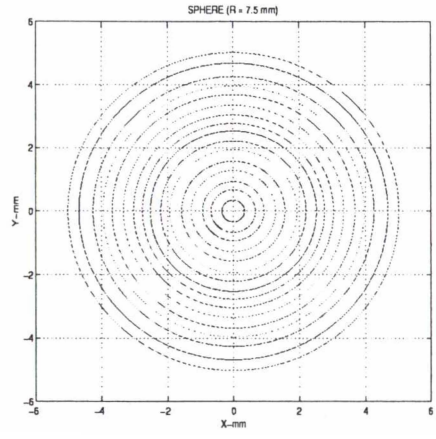

(b) Ellipsoid (8,9,10)mm

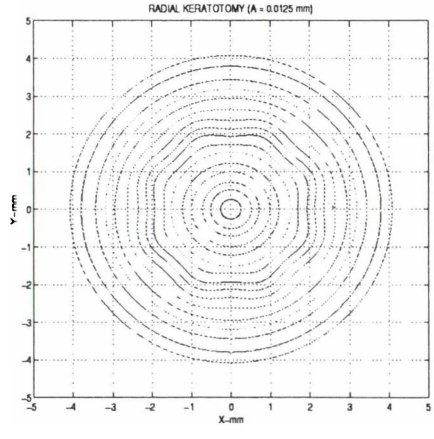

(c) Radial K. (a = 0.0125 mm)

Figure 3.9: The images produced by a telecentric camera (a) Aspheric (Q=-0.25) surface (b) an (oblate) ellipsoid with half-axes (8,9,10) mm (c) A model of radial keratotomy (RK) using equation (3.4.3) where a = 0.0125 mm is the amplitude of the sinusoidal undulations.

shape. This was primarily for simplicity, but it also tested the robustness of the method to the initial guess.

From the resulting recovery, the RMS height errors, RMS slope errors and RMS tilt errors between the entire recovered and analytic corneal surfaces were measured i.e. over the set of $N = 5040$ sample points. The number of iterations and time taken to complete were also recorded for all situations. The simulations were written in MATLAB v5.0 and ran on a DEC-ALPHA running UNIX.

3.5.4 Results

Tables 3.1(a) and 3.1(b) summarize the performance of the algorithm on the test cornea. It was found that the method converged under the RMS height tolerance of 1×10^{-12} mm, for both cases (no skew compensation and skew compensation) in exactly 7 iterations in all cases. The time taken to iterate to convergence (i.e. recovery without skew compensation) was 0.7s (on the DEC-ALPHA platform) for all cases. However, with the addition of the post-processing step, a combined total time of 2.3s to complete was found.

Table 3.1(a) shows results ignoring the contribution of skew-rays to the recovery. The average RMS height error for the three cases was found to be 6.2×10^{-4} mm. The average RMS error in the slope was 4.9×10^{-4}mm/ mm and the average RMS tilt error was 3.6×10^{-2}mm/rad. The average sub-micron results were due to particularly low errors found for the aspheric surface, but only the ellipsoid (in fact) gave height errors over a 1 micron threshold (1.4 μm). Table 3.1(b) shows results including the contribution of skew-rays. In this case, the resulting errors were consistently lower. In particular, the RMS height error dropped to 1.7×10^{-4} mm, the RMS slope error dropped to 1.1×10^{-4}mm/ mm and the RMS tilt error to 2.1×10^{-3}mm/rad. These results indicated a drop of error by factors of 3.6,4.1 and an order of magnitude (17) in the case of the height, slope and tilt respectively. The addition of skew compensation consistently improved the results obtained, and thereby justified its inclusion in the method. In fact, it was found that the RMS height error reduced by 70% in compensating for skew rays.

Finally, the accuracy of the recovered surfaces indicated that the method was not sensitive to the initial guess for the surface. Therefore, the method was very robust with respect to the initial choice of surface.

3.5.5 Discussion

The results from this testing are encouraging. It was found that a reasonably low RMS height error could be achieved (an average error of 6.2×10^{-4} mm), in small completion times (0.6s) even without compensation for the skew ray error. However, it was found that the compensation for skew improved reconstruction of corneal height, slope and tilt for all cases. In the case of the aspheric surface, it was found that the errors were very low (8.9×10^{-7}), and ensured sub-micron accuracy was achieved for all three cases. The method also produced rapid estimates (within 2.3s) with low (sub-micron) error, though these estimates were not as low as the algorithm of Halstead et al. [1995b] i.e. 8.5×10^{-6} mm).

The algorithm had a low completion time of 2.3s. There is the possibility for further im-

Shape	Iterations	RMS Height Error (mm)	RMS Error in f_r	RMS Error in f_θ	Total Time
Aspheric	7	8.9×10^{-7}	1.2×10^{-8}	0	0.7
Ellipsoid	7	1.5×10^{-3}	1.1×10^{-3}	6.8×10^{-2}	0.7
Radial K.	7	3.6×10^{-4}	3.8×10^{-4}	4.0×10^{-2}	0.7
Average	7	6.2×10^{-4}	4.9×10^{-4}	3.6×10^{-2}	0.7

(a) Results with no skew compensation

Shape	Iterations	RMS Height Error (mm)	RMS Error in f_r	RMS Error in f_θ	Total Time
Aspheric	7	8.9×10^{-7}	1.2×10^{-8}	3.4×10^{-15}	2.3
Ellipsoid	7	3.8×10^{-4}	2.5×10^{-4}	3.4×10^{-3}	2.3
Radial K.	7	1.4×10^{-4}	9.0×10^{-5}	3.0×10^{-3}	2.3
Average	7	1.7×10^{-4}	1.1×10^{-4}	2.1×10^{-3}	2.3

(b) Results with skew compensation

Table 3.1: (a) Recovery without skew ray compensation (b) Recovery with skew compensation. The results show that skew ray compensation consistently improves recovery of the corneal height. In particular, recovery is now sub-micron in all cases. However, by compensating, the time to complete increases by a factor of about 3, though the overall time taken is still low i.e. 2.3s on average

provements, particularly in the skew compensation phase, which may benefit from improved coding. However, this time already compares favorably with those reported by Halstead et al. [1995a] who cite completion times of up to 3min.

The results confirm that compensating for the skew ray error improves the recovery of the corneal surface. However, in the case of the radial keratotomy example, it was found that the RMS error was recovered to under sub-micron accuracy without compensation. This suggests also that the numerical integration method used here improves upon the method of Klein [1970], where errors on the order of microns were found ignoring tilt. Compensating for tilt causes height error reductions of 2.6 (Radial K.) and 3.9 (Ellipsoid) times respectively, which contributed to improved results.

3.5.6 Conclusion

A new method for recovery of the corneal surface was presented. The method used a continuous supplementary curvature condition, to ensure a recovery with continuous curvature.

A guaranteed convergence criterion was derived for this case. The simulated data was recovered with an average RMS height error of 6.2×10^{-4} mm ignoring skew and 1.7×10^{-5}mm including skew. This amounted to a 70% reduction in RMS height error. The inclusion of skew ray error is therefore, useful in recovery of the corneal surface. In addition, a rapid completion time time for this recovery was found (2.3 sec).

This algorithm is presented as a method which maintains the simplicity of arc-step/continuous curvature algorithms, whilst achieving low error. Based on the testing conducted here, the recovery algorithm for *local curvature* is adopted as the default recovery method used in this thesis.

3.6 Calibrating the New Method for Clinical Use

3.6.1 Introduction

This section describes the calibration of the algorithm developed in the previous section. In particular, it describes problems found in experimental measurements, and the solutions adopted to overcome these problems. After describing the processing steps introduced, the method is calibrated on manufacturer supplied calibration balls. It is found that the average RMS height can be recovered with sub-micron (and therefore sufficient) accuracy (2.7×10^{-4} mm).

3.6.2 Background

The Technomed C-SCAN[4] was used to test the recovery algorithm[5]. Manufacturer supplied calibration balls of radii 7.0 mm, 8.0 mm, and 9.0 mm respectively were imaged. The ring data for these images were subsequently output to disk as three ASCII files (for each ball), containing the radial displacement $r_i(\theta_k)$ for the i^{th} ring and k^{th} meridian (with angular displacement θ_k).

To identify the camera model which best represented the VK's operation, the telecentric and nodal camera models were used to generate simulated images of the supplied calibration balls. It was found that the telecentric camera model better fitted the measured rings c.f. a nodal model tested at several nodal point values. As a result, the telecentric camera model was adopted to represent the VK. However, it was noted on a subsequent height recovery attempt that the RMS height errors were still significantly above 1 μm.

[4]TechnoMed GmbH, Berlin, Germany

[5]Thanks to LazerSight Eye Clinic, Hamilton, New Zealand

The mean error between the measured ring data and simulated ring data was found to be 50μm. It was decided to identify possible causes of this residual error, and to identify an appropriate means of compensating for this error.

Artifacts in the Output Data

Figure 3.10 displays the raw output data over the first 5-6 rings for the 7 mm, 8 mm and 9 mm rings respectively. These figures illustrate problems found with the output data: (i) missing ring data, and (ii) "steps" in the output data. The absence of data was explained by the TechnoMed C-SCAN operating manual, as a consequence of the processing algorithm used. This problem was addressed by using cubic interpolation to fill in the gaps.

However, the steps found on close inspection of the rings were unexpected, and were not evident from video captured screen shots. This implied that these errors were due to internal VK data processing. Moreover, these steps were of a significant magnitude (roughly 20μm), and so were a possible candidate for the observed errors. It was observed that these steps were reproducible in the data for a number of test runs on the *same* calibration ball. However, the angular and radial distribution of these steps did not appear to be constant across calibration balls. Figure 3.10 illustrates the appearance of these features in calibration ball images.

To reduce the steps, the ring data was filtered. The intention was to reduce high frequency Fourier components, i.e. the sharp edges, while passing frequencies corresponding to *true* corneal features. A natural strategy is to apply filtering to each ring, i.e. to filter each r_i w.r.t. θ. However, in an attempt to preserve *true* corneal features (namely, astigmatism), the radii values were first transformed into parameterized form $x(t)$ and $y(t)$ and filtered w.r.t. this new parameter, t (see Appendix D.1.4 for details regarding this procedure).

The motivation for this choice is illustrated on a simulated image of an astigmatic cornea, shown in Figure 3.12. Figure 3.13(a) shows the magnitude of the Fourier transform of the original ring data points, which is compared to the t parameterized representation, see Figures 3.13(b) and 3.13(c). The frequency content of the radial signal $r_i(\theta)$ is *richer* (i.e. contains several non-zero frequency components) c.f. $x(t)$ and $y(t)$, which is a disadvantage. Furthermore, as astigmatism increases "leakage" into higher frequencies is observed in the former case, which does not occur in the latter. Therefore, low-pass filtering is more likely to preserve (particularly) astigmatism, which is desirable.

The low pass filter was designed with a cut-off of 30Hz, which was chosen to balance smoothing of the edges, against eliminating *true* corneal features. The filter was a zero-phase forward and reverse digital filter, which eliminated the need for phase compensation. As

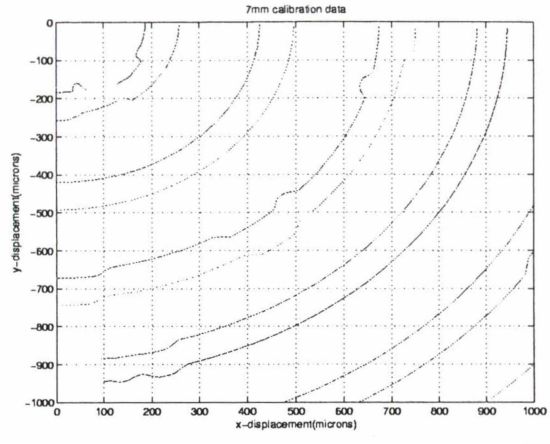

(a) 7mm

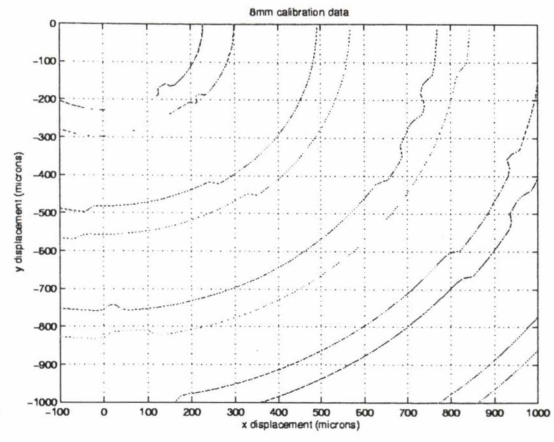

(b) 8mm

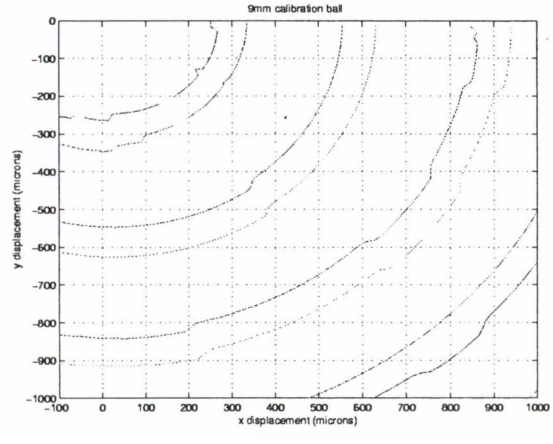

(c) 9mm

Figure 3.10: The raw output ring data, for 7 mm, 8 mm and 9 mm calibration balls. The area shown corresponds to angles 270 degrees through to 360 degrees, and radial values of about 1000 microns. Steps are jumps in the rings, which have a magnitude of roughly 20 μm. For example, steps are prominent in the fifth and sixth rings of the 8mm calibration ball (i.e. (b)) at roughly 30 degrees below horizontal. The 7 mm and 9 mm calibration balls contain these step artifacts also, and the occurence of these artifacts does not appear to have a relationship with radial distance or angle.

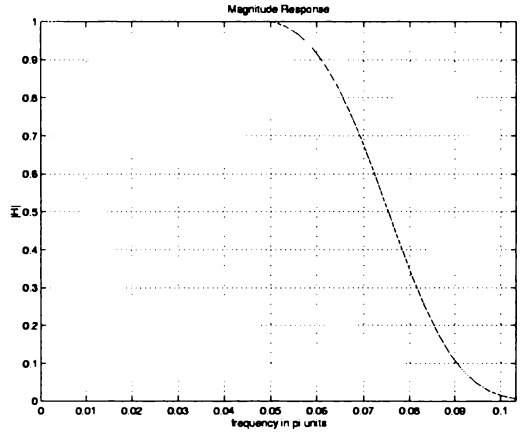

Figure 3.11: The magnitude response of the zero-phase forward and reverse digital filter applied to the x and y data. The magnitude response is the square of the uni-directional magnitude response, as a result of the forward and backward filtering. This two-way filtering process ensures zero phase.

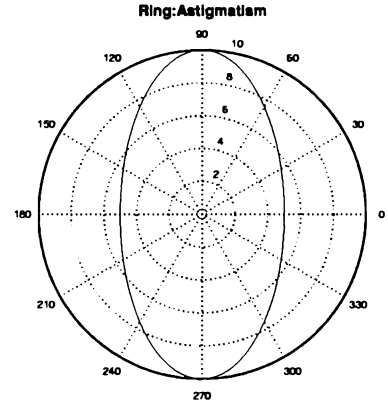

Figure 3.12: A simulated ring image (exaggerated), modeling astigmatism. It is desirable to preserve the ellipse shape, i.e. astigmatism, when filtering the ring.

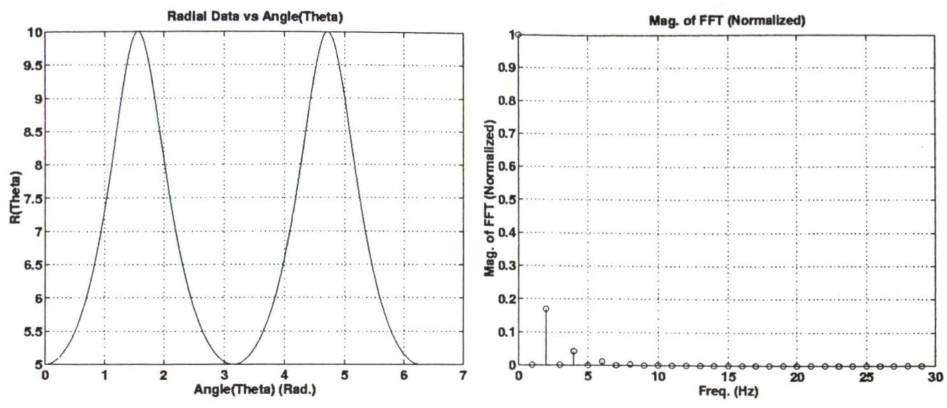

(a)

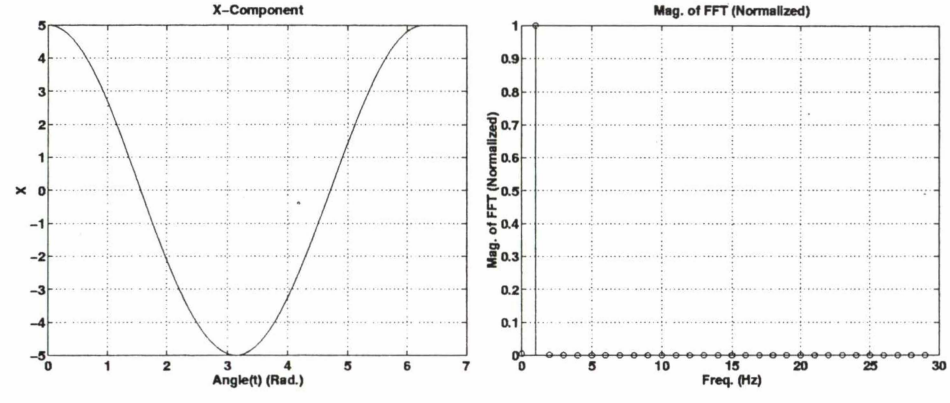

(b)

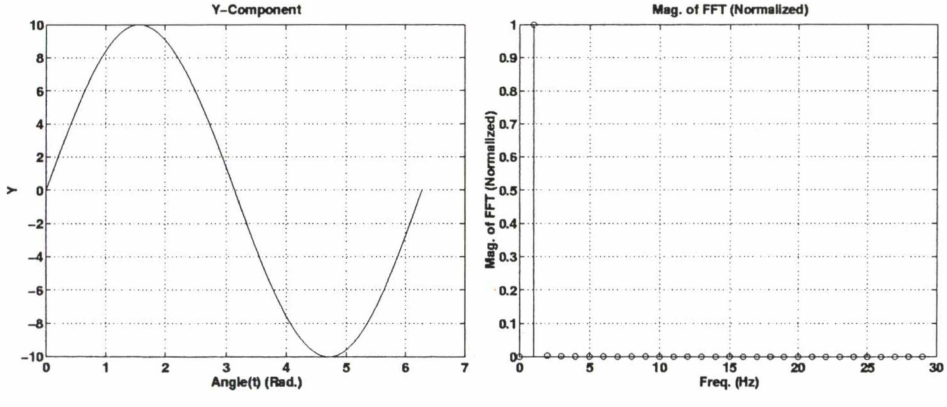

(c)

Figure 3.13: A comparison of filtering approaches, showing the fourier transform of the simulated ring data. The first panel, (a) shows the ring data in a natural polar form, whilst (b) and (c) show x and y with respect to the parameter t. The parameterization attempts to shift the components corresponding to astigmatism toward the lower frequencies.

a result for the two-pass nature of the filter, the actual magnitude is the magnitude of the forward pass squared. The frequency response has been plotted in Figure 3.12, and was easily implemented by way of MATLAB commands.

Systematic Error

The processed experimental data was compared against data points generated by the telecentric equation. At this point it was noted that there was still a discrepancy between the experimentally gathered images, and the theoretically predicted images. This error appeared to be *systematic*, the source of which is at present, unknown. It is suggested that this is likely due to the VK processing algorithms, and errors in measurement of the VK dimensions.

In order to overcome these apparent errors, calibration coefficients (i.e. for each (i,k) combination) were determined, to fit the experimental data to the theoretical data in the linear least squares sense. These values was generated by using data obtained for 3 runs of the 7 mm, 8 mm and 9 mm calibration balls (i.e. $3 \times 3 = 9$ data points for each value of i and k). This data was then multiplied with the smoothed data (i.e. on an element by element fashion) in order to obtain a calibrated and smoothed representation, $r_i'(\theta_k)$.

The variance was determined for the calibration coefficients, in order to test the "goodness" of fit to the model. It was found that the variance was large in the first ring (30% of the absolute ring radius), but it was small in all other rings (roughly 5%). As a result it was decided to leave the first ring uncalibrated, since this data could not be relied upon to produce a good fit.

3.6.3 Results

Figure 3.14 shows the results of the entire calibration procedure applied to the 8 mm and 9 mm calibration balls, where (starting from the top) the 1^{st} panels show the result of interpolating, the 2^{nd} panels show the result of smoothing the interpolated results, and the 3^{rd} panels show the calibrated,smoothed and interpolated results.

The inner ring is left uncalibrated, whilst the calibrated rings are shifted slightly from the previous panels. The figure also shows that the smoothing distorted the central two rings, due to uneven-ness outside of the picture. However, this is not critical in the central cornea, so this error is acceptable here. Alternatively, a calibration constant could be applied in this area, but it would produce much larger distortions. The RMS error in the estimation of the rings decreased on application of this procedure to 3×10^{-3} mm from the original 5×10^{-2} mm error.

Description	RMS Height Error (mm)	RMS Slope Error (mm/mm)	RMS Tilt Error (mm/ra
7 mm	2.2×10^{-4}	3.5×10^{-4}	$8.2 \times 10^{-}$
8 mm	3.4×10^{-4}	5.3×10^{-4}	$1.1 \times 10^{-}$
9 mm	2.5×10^{-4}	3.8×10^{-4}	$1.2 \times 10^{-}$
Average	2.7×10^{-4}	4.2×10^{-4}	$1.1 \times 10^{-}$

Table 3.2: The results using the calibration routine, reduce the RMS error to sub-micron levels.

The resulting method was tested on the 7 mm, 8 mm and 9mm calibration balls i.e. using them as input to the corneal height recovery algorithm. Unfortunately, these balls constituted the calibration (training) set, and no appropriate calibration balls were available for validation. Table 3.2 shows the RMS height,slope and tilt recovery errors. The resulting errors are sub-micron, which shows that accurate reconstruction of a sphere is possible by applying the described steps to the data. This method can be expected to be a reasonable method for reconstructing the corneal surface in general, at the very least for relatively spherical smooth shapes which do not exceed the limits of applicability, i.e. with complicated corneal features and curvatures outside the range of calibration balls used.

3.6.4 Conclusion

A calibration technique was employed for use in videokeratography for a case where system parameters are not fully available. By making reasonable assumptions, a height reconstruction with an average RMS height error of 2.7×10^{-4} mm was found. This method may be applicable in cases where not all system parameters are known exactly. The primary purpose of this testing was to recover accurate height models, which was achieved - on the calibration(training) set. Further testing is required to establish the accuracy of the method on a validation set. Therefore, there is some work needed to fully verify the corneal reconstruction algorithm presented in this chapter.

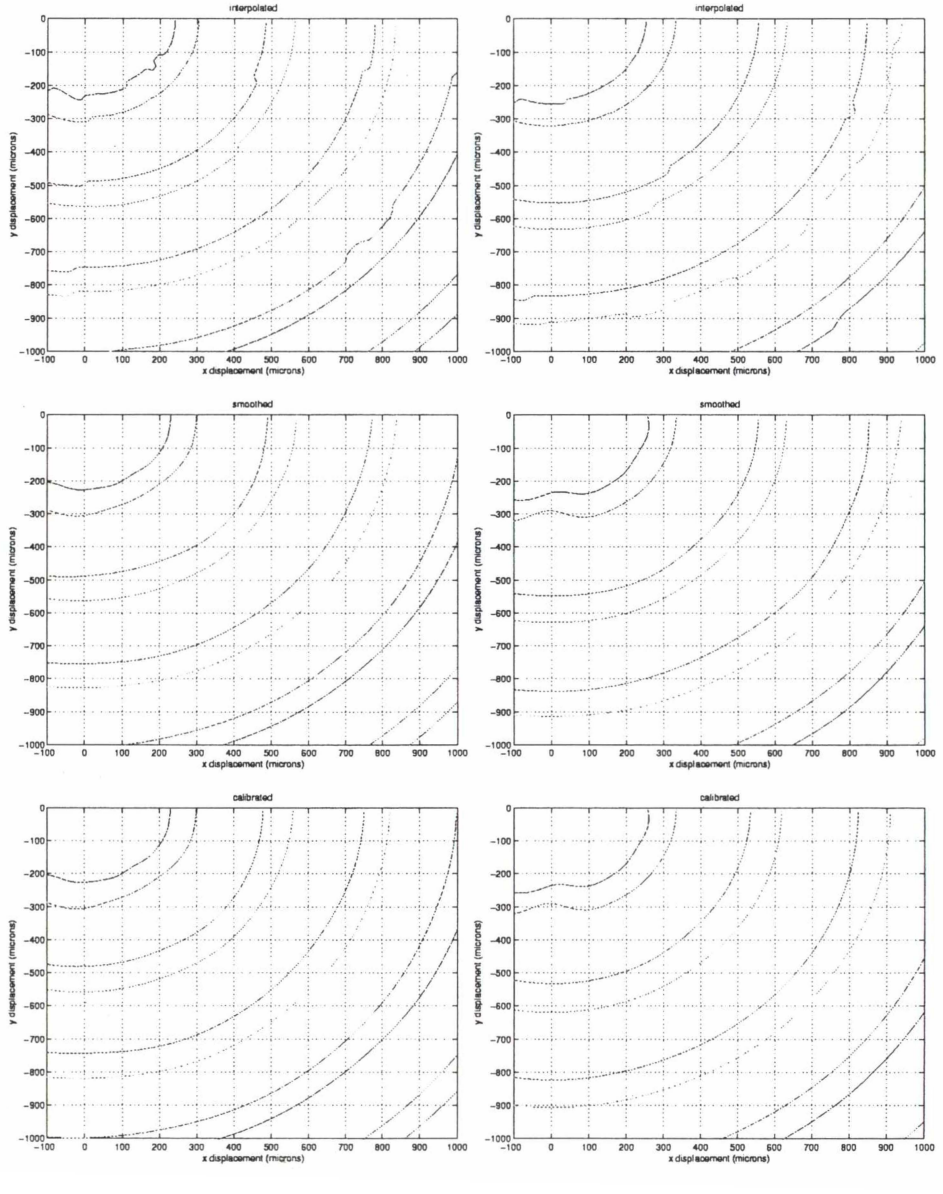

Figure 3.14: The left column shows the calibration sequence on the 8mm calibration ball, while the right column shows the 9 mm ball. The smoothing process tends to distort the inner 2 rings, but this does not occur further out. The calibration stage tends to accentuate the distortion in the inner rings. Therefore, the inner rings 2 were left uncalibrated.

Chapter 4

Implementing A Ray Tracer

4.1 Introduction

This chapter will describe the implementation and design of RAYTRAK, a set of MATLAB v5.0 routines for ray-tracing. The first section introduces the basic definitions and laws of geometric optics (on which the program is based). The approach taken is to view geometric optics as a consequence of Maxwell's equations in the high frequency limit.

With this theory in place, coding of these laws is described. Equations for intersection, refraction and reflection are given, supported by code snippets. Practical modeling problems such as vignetting, decentered and tilted lenses are also described. The next section then details the computer implementation. The ray-tracer was implemented as a *toolbox* consisting of routines that fall into roughly three functional categories: system definition, system processing and system evaluation. The structure of this section reflects this, with a description of each of these sub-topics. This section concludes with a summary of possible improvements future developments.

The next section describes testing of the ray tracer on recovered corneal surfaces. Rays were traced through the recovered simulated surfaces, and the (transverse) displacements between analytically determined and recovered spot diagrams were measured. These errors were found to be relatively small in simulation, with RMS errors ranging from 4.1×10^{-5} mm to 3.2×10^{-3} mm . This analysis was repeated with the calibration ball data, and it was found that the errors were on the order of 4×10^{-3} mm. The ray tracing analysis was used again, to determine the amount of error in estimating the point of best focus (longitudinal error), which was found to correspond to errors of roughly 0.1 mm (0.1 D).

4.2 Geometrical Optics

4.2.1 Introduction

This section will introduce the theory of geometrical optics and in particular, the laws that comprise the geometric theory i.e. the laws of rectilinear propagation, refraction and reflection. The content of this section is a summary largely adapted from Born and Wolf [1965], who view geometric optics as a limiting case of Maxwell's equations for high frequency light, or short wavelength. This is an attractive approach for two reasons: (a) the mathematical entities of geometric optics theory (i.e. rays and wavefronts) arise from the physically fundamental concept of the *electromagnetic* field, and (b) the rays are given practical meaning, i.e. they can be related to physically measurable quantities.

4.2.2 A Development from Maxwell's Equations

Consider a charge/current free and *isotropic* medium, with Maxwell's equations in time independent form i.e. with the time dependent term $e^{-i\omega t}$ removed. Then,

$$\nabla \times \mathbf{H}_0 + i\omega\epsilon\mathbf{E}_0 = 0 \tag{4.1}$$

$$\nabla \times \mathbf{E}_0 - i\omega\mu\mathbf{H}_0 = 0 \tag{4.2}$$

$$\nabla \cdot \epsilon\mathbf{E}_0 = 0 \tag{4.3}$$

$$\nabla \cdot \mu\mathbf{H}_0 = 0 \tag{4.4}$$

where $\mathbf{E}_0$ and $\mathbf{H}_0$ are the spatial parts of the electric and magnetic field vectors respectively, ϵ is the electric permittivity, μ is the magnetic permeability. The form of $\mathbf{E}_0$ and $\mathbf{H}_0$ is assumed to be of form,

$$\mathbf{E}_0 = \mathbf{e}(\mathbf{r})e^{ik_0L(\mathbf{r})} \tag{4.5}$$

$$\mathbf{H}_0 = \mathbf{h}(\mathbf{r})e^{ik_0L(\mathbf{r})} \tag{4.6}$$

which are therefore, general trial solutions. The variable k_0 is the wave number; $\mathbf{e}$, $\mathbf{h}$ and L are all functions of position, but $\mathbf{e}$ and $\mathbf{h}$ are (in general) complex, whilst L is scalar. The physical fields are understood to be the real parts of equations (4.5) and (4.6). Substituting these trial solutions in equations (4.1)-(4.4) gives,

$$\nabla L \times \mathbf{h} + c\epsilon\mathbf{e} = -\frac{1}{ik_0}\nabla \times \mathbf{h} \tag{4.7}$$

$$\nabla L \times \mathbf{e} - c\mu\mathbf{h} = -\frac{1}{ik_0}\nabla \times \mathbf{e} \tag{4.8}$$

$$\mathbf{e} \cdot \nabla L = -\frac{1}{ik_0}(\mathbf{e} \cdot \nabla \log(\epsilon) + \nabla \cdot \mathbf{e}) \tag{4.9}$$

$$\mathbf{h} \cdot \nabla L = -\frac{1}{ik_0}(\mathbf{h} \cdot \nabla \log(\mu) + \nabla \cdot \mathbf{h}) \tag{4.10}$$

where $c = \omega/k_0$ (the *speed of light*) has been introduced to make it clear there is no k_0 dependence on the left hand side. The high frequency limit is found for large values of k_0, so letting $k_0 \to \infty$ gives,

$$\nabla L \times \mathbf{h} + c\epsilon\mathbf{e} = 0 \tag{4.11}$$

$$\nabla L \times \mathbf{e} - c\mu\mathbf{h} = 0 \tag{4.12}$$

$$\mathbf{e} \cdot \nabla L = 0 \tag{4.13}$$

$$\mathbf{h} \cdot \nabla L = 0 \tag{4.14}$$

where the equations (4.13) and (4.14) are already satisfied by the first two equations (4.11) and (4.12) so need not be solved for simultaneously. This means that $\mathbf{h}$ say, may be eliminated from equations (4.11) and (4.12) to give,

$$(\mathbf{e} \cdot \nabla L)\nabla L - \mathbf{e}(\nabla L)^2 + c^2\mu\epsilon\mathbf{e} = 0, \tag{4.15}$$

which on account of (4.13) (and the fact that $\mathbf{e}$ is not everywhere zero) becomes,

$$(\nabla L)^2 = n^2 \tag{4.16}$$

where $L(\mathbf{r})$ is a scalar function of position called the *eikonal* and $n(\mathbf{r})$ is the refractive index i.e. the experimentally determined ratio of material velocity to vacuum velocity $n = c/v = \sqrt{\epsilon\mu/\epsilon_0\mu_0}$. The equation (4.16) is the *eikonal equation*, which on reminding ourselves that ∇L is a vector, can be written in expanded form as,

$$\left(\frac{\partial L}{\partial x}\right)^2 + \left(\frac{\partial L}{\partial y}\right)^2 + \left(\frac{\partial L}{\partial z}\right)^2 = n^2(x, y, z) \tag{4.17}$$

Solutions for the electromagnetic field of form given by equations (4.5) and (4.6) must satisfy this *scalar* equation to be consistent with Maxwell's equations.

An important question at this point is: "how is the eikonal related to measurable quantities?". The answer is, through the Poynting vector $\mathbf{S}$, which describes the instantaneous magnitude and direction of flow of energy density in an electromagnetic field. Due to the high frequencies of visible light (on the order of 10^{14} Hz), the magnitude of the time averaged Poynting vector is the physically measured quantity given by,

$$\langle \mathbf{S} \rangle = \frac{1}{2}\Re(\mathbf{E}_0 \times \mathbf{H}_0^*) \tag{4.18}$$

which by substitution of the trial solutions for $\mathbf{E}_0$ and $\mathbf{H}_0$ gives,

$$\langle \mathbf{S} \rangle = \frac{c}{n^2} \langle w_e \rangle \nabla L \tag{4.19}$$

where $\langle w_e \rangle$ is the time averaged electric energy density. Introducing the normalized direction vector $\hat{\mathbf{s}}$,

$$\hat{\mathbf{s}} = \frac{\nabla L}{|\nabla L|} \tag{4.20}$$

equation (4.19) becomes,

$$\langle \mathbf{S} \rangle = v \langle w_e \rangle \hat{\mathbf{s}} \tag{4.21}$$

by equation (4.16) and $n = c/v$. It is now clear that the eikonal determines the direction of energy flow, through equation (4.20). The factor $v \langle w_e \rangle$ is the magnitude of the time averaged energy density. The surfaces of L such that,

$$L(\mathbf{r}) = constant \tag{4.22}$$

are called *geometrical wave-fronts* and are everywhere perpendicular to $\langle \mathbf{S} \rangle$ by virtue of (4.20). The *geometrical light rays* are the *orthogonal trajectories* to the geometrical wavefronts, so that energy flows *along* rays (see Figure 4.1). By this description, a light ray is the result of repeatedly stepping out along differential sections of length ds in the direction of the Poynting vector $\hat{\mathbf{s}}$. If the path of such a ray is described by a function $\mathbf{r}(s)$ then the differential change in $\mathbf{r}$ must be $d\mathbf{r} = \hat{\mathbf{s}} ds$. Using this fact, the equation of a ray is,

$$n \frac{d\mathbf{r}}{ds} = \nabla L \tag{4.23}$$

which reinforces the idea that a geometric ray path $\mathbf{r}(s)$ is the path orthogonal to the geometrical wavefronts at all parts of the region. It is noted at this point that from the relation,

$$\frac{dL}{ds} = \frac{d\mathbf{r}}{ds} \cdot \nabla L \tag{4.24}$$

that,

$$\frac{dL}{ds} = \frac{d\mathbf{r}}{ds} \cdot \nabla L = n = \frac{c}{v} \tag{4.25}$$

taking the dot product of both sides of (4.23) with $d\mathbf{r}/ds$. The eikonal changes as a function of the distance along a ray. The *Optical Path Length* (OPL) is defined as the integral of dL over a section of the light ray say i.e.

$$\Delta L = \int_{P_1}^{P_2} n ds = L(P_2) - L(P_1) \tag{4.26}$$

or,

$$\Delta L = c \int_{P_1}^{P_2} dt \tag{4.27}$$

where the light ray passes from P_1 to P_2. This shows that the OPL is also the vacuum velocity multiplied by the time taken to traverse the ray. The OPL links the theory of rays with physical optics, since it appears in scalar diffraction theory.

For isotropic media, with large frequencies, solutions to Maxwell's equations must satisfy the *eikonal equation* (given by equation (4.16)). The solution to the equation is the *eikonal* and defines the meaning of the terms *wave-front*, and *ray*. In this context, wavefronts are constant surfaces of the eikonal function. The rays are the trajectories that are orthogonal to the wavefronts. The trajectory of these rays is the trajectory of the flow of energy density.

4.2.3 The Laws of Geometrical Optics

The laws of geometrical optics follow easily from consideration of equation (4.23). Differentiating both sides of this equation with respect to s gives,

$$\frac{d}{ds}\left(n\frac{d\mathbf{r}}{ds}\right) = \nabla n \tag{4.28}$$

which has the advantage that the explicit dependence on L has been removed. In a *homogeneous medium* $n = constant$ so this equation becomes simply,

$$\frac{d^2\mathbf{r}}{ds^2} = 0 \tag{4.29}$$

which is solved by the equation,

$$\mathbf{r} = \mathbf{a}s + \mathbf{b} \tag{4.30}$$

where $\mathbf{a}$ and $\mathbf{b}$ are constant vectors. Hence in homogeneous media, a light ray will travel in a straight line. This is the law of *rectilinear propagation.*

The laws of reflection and refraction describe how the time averaged Poynting vector changes at a discontinuity in n. Taking the curl of both sides of equation (4.23) gives,

$$\nabla \times (n\hat{\mathbf{s}}) = 0 \tag{4.31}$$

which is the requirement that the field defined by $n\hat{\mathbf{s}}$ has zero circulation. An alternative form for *circulation* is that,

$$\oint_C (n\hat{\mathbf{s}}) \cdot d\mathbf{l} = 0 \tag{4.32}$$

for any closed curve C in the region of interest. Suppose a closed curve such as in Figure 4.2, is placed over the interface between two media of refractive index n_1 and n_2, which contains a small planar area $\delta\mathbf{A}$. The legs that straddle the boundary are chosen so their contribution is negligibly small. Evaluating (4.32) yields,

$$\begin{aligned}
\oint_C (n\hat{\mathbf{s}}) \cdot d\mathbf{l} &= (n_1\hat{\mathbf{s}}_1) \cdot \delta\mathbf{l} - (n_2\hat{\mathbf{s}}_2) \cdot \delta\mathbf{l} \\
&= (n_1\hat{\mathbf{s}}_1 - n_2\hat{\mathbf{s}}_2) \cdot \delta\mathbf{l} \\
&= (n_1\hat{\mathbf{s}}_1 - n_2\hat{\mathbf{s}}_2) \cdot (\hat{\mathbf{n}} \times \delta\mathbf{A}) \\
&= -\hat{\mathbf{n}} \times (n_1\hat{\mathbf{s}}_1 - n_2\hat{\mathbf{s}}_2) \cdot \delta\mathbf{A} = 0
\end{aligned}$$

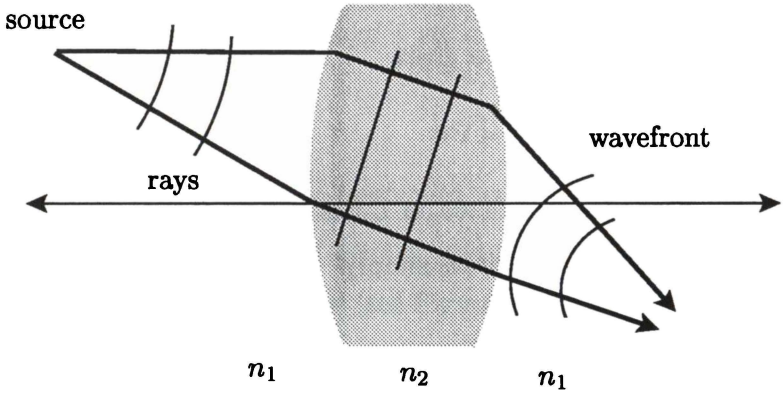

Figure 4.1: The wavefronts are curves of constant eikonal. Geometric rays are curves that are everywhere perpendicular to the wavefronts.

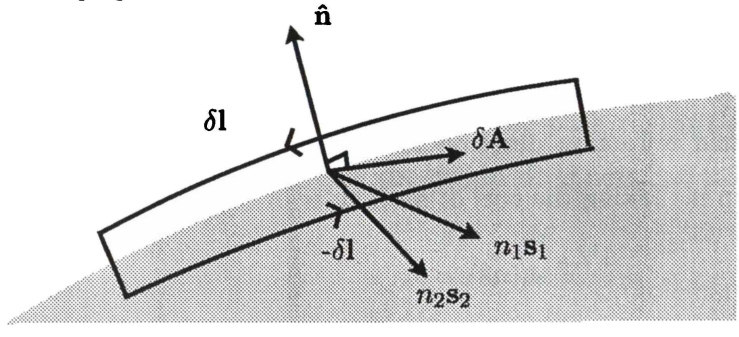

Figure 4.2: The refractive index is discontinuous at a boundary, which causes rays to change direction abruptly.

which will remain true regardless of the orientation of $\delta\mathbf{A}$ so that,

$$\hat{\mathbf{n}} \times (n_1\hat{\mathbf{s}}_1 - n_2\hat{\mathbf{s}}_2) = 0 \tag{4.33}$$

which simply states that the tangential component of $n\hat{\mathbf{s}}$ is continuous across the interface. This immediately gives,

$$n_1 \sin(\theta_1) = n_2 \sin(\theta_2) \tag{4.34}$$

which is the *law of refraction*, or *Snell's law*. The *law of reflection* is obtained by requiring a solution in which $n_1 = n_2$, thus

$$\theta_1 = \pi - \theta_2 \tag{4.35}$$

the *law of reflection*.

4.3 Geometrical Aspects of Ray Tracing

4.3.1 Overview

From section 4.2.3, the three "operations" for ray tracing are: rectilinear propagation, refraction and reflection. RAYTRAK implements these rules in the following simple (pseudo-coded) algorithm,

```
Get initial ray position and direction
while (not last element) {
    Get next optical element information
    Propagate ray to the next optical element
    If (not successful) stop
    Apply refraction/reflection to ray
}
```

which is *sequential* ray-tracing, since the order of optical surfaces traversed is known beforehand. By convention, rays initially travel from left to right, which will change if the system contains a reflective surface for example. Each surface has an associated refractive index n, which determines the index of refraction of the current medium (i.e. generally to the left of the surface to be traced). A surface may be decentered, or oriented with respect to the optic axis. Each surface also has an associated aperture, which will block rays that pass outside of its extent. Figure 4.3 illustrates these points for three rays passing through an arbitrary optical system. The figure also illustrates possible outcomes for rays: (a) ray A traverses the entire system (b) Ray B is blocked by the aperture of the 3^{rd} optical surface (i.e. lands outside of the "I" bars) (c) ray C leaves the system prematurely.

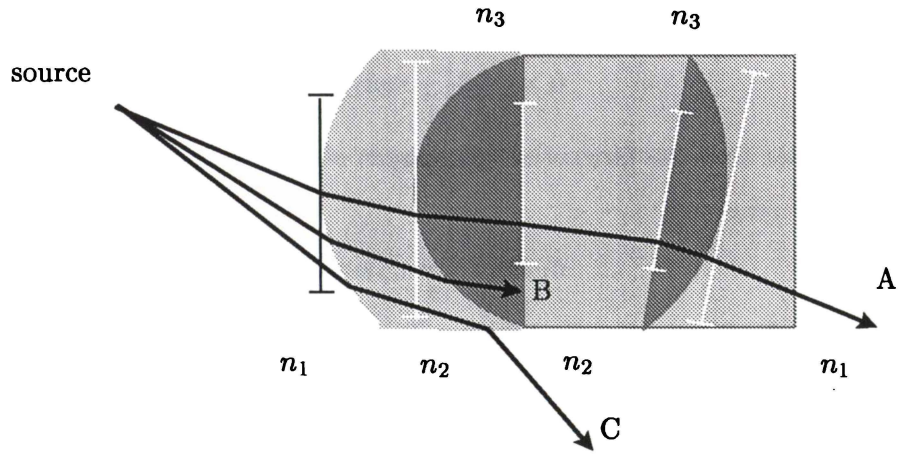

Figure 4.3: A system of refracting surfaces, with apertures. Rays that traverse the system may be pass through successfully, be blocked or leave the system prematurely.

The majority of the computation time is spent propagating rays to the next optical element. To this end, equations for this process will be derived. Propagating rays amounts to intersecting the ray with the next optical surface or *geometric primitive*. The plane, ellipsoid, Bi-Cubic and B-Spline surfaces are the *geometric primitives* implemented by RAYTRAK.

4.3.2 Intersecting a Plane

A plane (see Figure 4.4(a)) is defined by the equation,

$$(\mathbf{y} - \mathbf{y}_p)^T \mathbf{n} = 0 \tag{4.36}$$

where $\mathbf{y} = (x, y, z)^T$ is a point on the plane, $\mathbf{y}_p = (x_0, y_0, z_0)^T$ is the *origin* of the plane and $\mathbf{n}$ is the normal to the surface. A particularly simple expression is obtained if the optical system is centered on the origin with normal parallel to the optic axis. In this case, $\mathbf{y}_0 = (0,0,0)^T$, $\mathbf{n} = (0,0,1)^T$ and equation (4.36) becomes,

$$\mathbf{y}^T (0,0,1)^T = 0 \tag{4.37}$$

which on substituting the ray equation (4.30) becomes,

$$\begin{aligned} & (\mathbf{a}s + \mathbf{b})^T (0,0,1)^T = 0 \\ \Rightarrow \quad & (\mathbf{a}^T (0,0,1)^T) s + (\mathbf{b}^T (0,0,1)^T) = 0 \\ \Rightarrow \quad & w_0 s + z_0 = 0 \\ \Rightarrow \quad & s = -\frac{z_0}{w_0} \end{aligned} \tag{4.38}$$

where $\mathbf{a}^T = (u_0, v_0, w_0)$ and $\mathbf{b}^T = (x_0, y_0, z_0)$ have been used. This trivial result can then be substituted in (4.30) for the intersection point. Section B.1.1 of Appendix B.1 shows the code

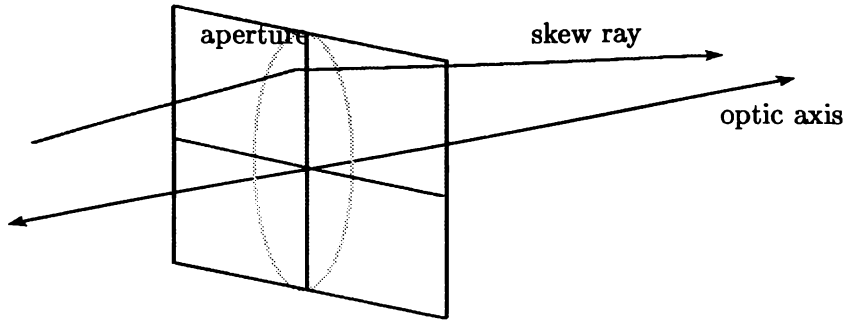

(a)

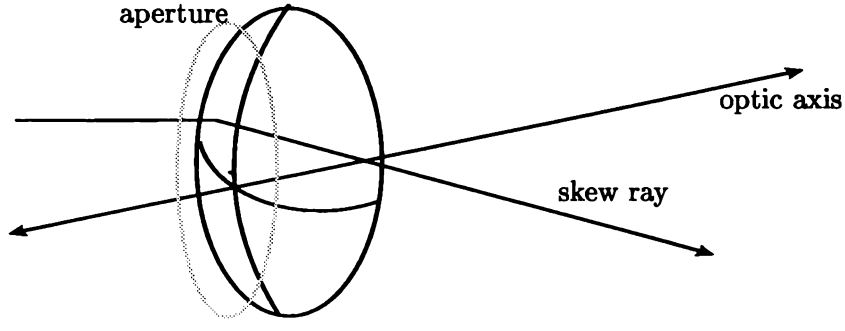

(b)

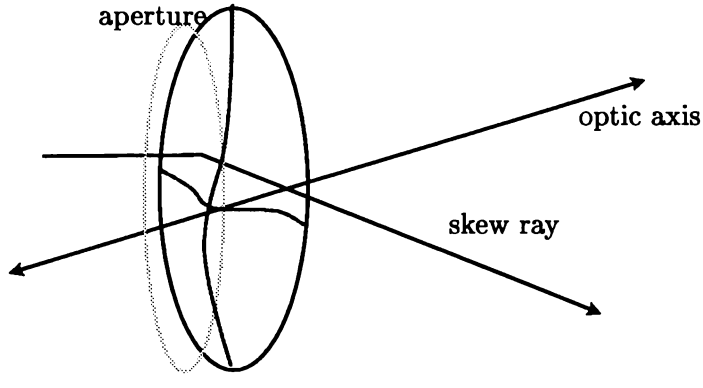

(c)

Figure 4.4: (a) A plane is centered on the optic axis. Also shown is the entrance pupil . Rays outside of this pupil are blocked (b) An ellipsoid with entrance pupil (c) A general surface i.e. Bi-Cubic/ B-Spline surface allows general surfaces to be represented

snippet for this equation. The code also shows that rays which fall outside of the aperture are discarded.

It is an easy matter to extend this procedure so that it applies to planes with general $\mathbf{n}$ and $\mathbf{y}_0$. The idea (mentioned in Hanrahan [1997] for example) is to transform the co-ordinate system so that equation (4.38) is valid. This amounts to transforming the rays by shifting and rotating them appropriately. After intersection testing is performed, the ray intersection and required vectors may be transformed back into the original coordinate system. The details of this process are given in section 4.3.6, but suffice to say, this is a convenient approach which applies to any other surface with no modifications.

4.3.3 Intersecting an Ellipsoid

The ellipsoid intersection point is found in the same way as a plane. Consider an ellipsoid with half-axes (a,b,c) as shown in Figure 4.4(b) in the (x,y,z) co-ordinate space. Choose a co-ordinate system scaled by $(1/a, 1/b, 1/c)$ respectively, so that the ellipsoid takes the equation of a sphere,

$$\phi(\mathbf{y}') = (\mathbf{y}' - \mathbf{y}'_P)^T(\mathbf{y}' - \mathbf{y}'_P) - 1 = 0 \tag{4.39}$$

where $\mathbf{y}' = (x', y', z')$ are *normalized* coordinates of the ellipsoid, related to the original system co-ordinates (x, y, z) by,

$$x' = x/a \tag{4.40}$$

$$y' = y/b \tag{4.41}$$

$$z' = z/c \tag{4.42}$$

The vector $\mathbf{y}'_P = (0, 0, z'_0)$ determines the curvature of the surface that passes through the origin. In particular, when $z'_0 = -1$, the surface is concave, and for $z'_0 = 1$ the surface is convex. A normal vector in this system may be found by computing the gradient of ϕ, which gives,

$$\begin{aligned} \mathbf{n}' &= -\nabla\phi(\mathbf{y}') \\ &= \left(\frac{x'}{z' - z'_0}, \frac{y'}{z' - z'_0}, 1\right) \end{aligned} \tag{4.43}$$

for any $\mathbf{y}'$ satisfying (4.39). Substituting equation (4.30) into (4.39) gives the intersection point,

$$\begin{aligned} & (\mathbf{a}'s + \mathbf{b}' - \mathbf{y}'_P)^T(\mathbf{a}'s + \mathbf{b}' - \mathbf{y}'_P) - 1 = 0 \\ \Rightarrow\ & (\mathbf{a}')^2 s^2 + 2(\mathbf{a}')^T(\mathbf{b}' - \mathbf{y}'_P)s + (\mathbf{b}' - \mathbf{y}'_P)^2 - 1 = 0 \end{aligned} \tag{4.44}$$

where $\mathbf{a}'$ and $\mathbf{b}'$ are the ray slope and ray positions in the normalized co-ordinate system. The roots s_i are given by,

$$s_i = -(\mathbf{a}')^{-2}\left\{(\mathbf{a}')^T(\mathbf{b}' - \mathbf{y}'_p) \pm 2\beta^{1/2}\right\} \tag{4.45}$$

which are substituted in equation (4.30) to give $\mathbf{y}'_i$ for the intersection point, and then in equation (4.43) for $\mathbf{n}'_i$. The product 2β is the discriminant with β given by,

$$\beta = (\mathbf{a}')^T(\mathbf{b}' - \mathbf{y}'_P))^2 - (\mathbf{a}')^2((\mathbf{b}' - \mathbf{y}'_P)^2 - 1) \tag{4.46}$$

and is used to determine whether the ray leaves the system prematurely. When $\beta < 0$ the ray will not intersect the ellipsoid. If $\beta = 0$ then the ray grazes the surface, and is treated by allowing it to pass unmodified. If $\beta \geq 0$ then the ray intersects the surface at two positions, and equation (4.45) gives the two path lengths at which these intersections occur. The correct path length depends on the surface required by the user, i.e. the convex or concave surface (relative to the optic axis). A simple test that works well in this application is to determine the distance of the two intersection points, from the origin of the surface. The origin of the surface is a point defined by the user, on which the required convex/concave surface is centered. The intersection with minimum distance from the surface origin is the required intersection point. This method works well, provided a ray strikes the convex side say, and then the concave side. If the ray enters at such a steep angle, as to intersect the ellipsoid twice on the convex/concave side then this algorithm will fail. However, since this situation is not found in practice, this possibility is safely ignored. Section B.1.2 of Appendix B.1 shows the implementation of the ellipsoid intersection in MATLAB.

Finally, the reader is reminded that the equations are in normalized co-ordinates, so that once the intersection and normals are found, the transformations (4.40)-(4.42) need to be applied to transform $\mathbf{n}'_i$ and $\mathbf{y}'_i$ into their "un-primed" counterparts.

4.3.4 Intersecting a General Surface

The videokeratographic height data recovered via the method of chapter 3 (section 3.5) was modeled (in RAYTRAK) using two methods (to be explained presently): (i) a combined cubic and linear interpolation method (which will hereby be referred to as the cubic/linear interpolation method) and, (b) B-Spline surfaces. The purpose of these approaches were to determine *interpolated* data points and associated normals for computing refracted/reflected rays.

The cubic/linear interpolation method utilized the cubic corneal profile information obtained from the recovery algorithm. Given a requested point (r, θ), the method first located

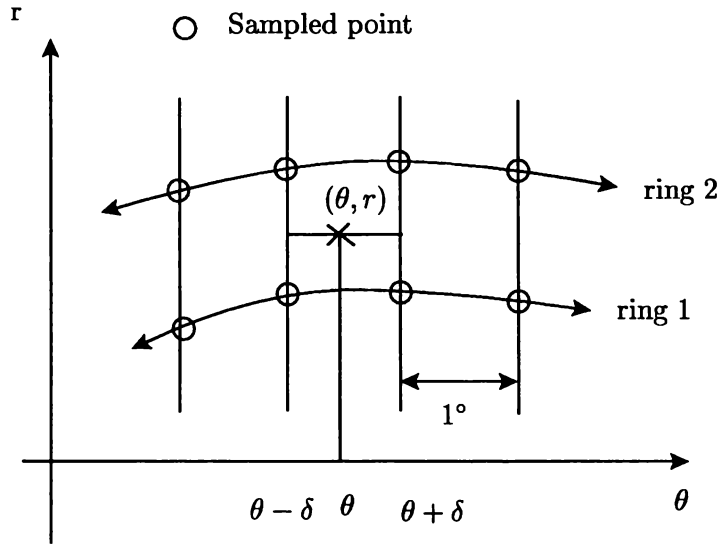

Figure 4.5: The cubic/linear interpolation method. The cubic information from the corneal recovery algorithm of chapter 3 (section 3.5) is used to determine the height, or radial slope at radial distance r along the meridia adjacent to θ (spaced at an angular distance $\delta = 1°$). A subsequent linear interpolation (i.e. in the angular dimension) uses this information to determine the height, slope or tilt at θ.

the meridia adjacent (i.e. spaced at δ radians) to the requested angle, θ. The height/radial slope along these meridia was then determined, from their cubic polynomial representations. A subsequent linear interpolation in the angular dimension gave estimates of height, slope, or tilt at (r, θ). The method is shown in Figure 4.5. Here the sampled points are shown as circles, with the angular direction along the x-axis, and the radial direction on the y-axis. The z-axis points out of the page. Smooth curves have been drawn through the sampled points, which represent images of the source rings. The vertical lines are meridia, which are therefore spaced at $\delta = 1°$ intervals.

A final detail: since the data was periodic (in θ), the boundaries were "wrapped" so that the data belonging to $\theta = 359°$ was placed before the $\theta = 0°$ data, and conversely $\theta = 0°$ was placed after the $\theta = 359°$ data. This ensured that interpolation would succeed for the entire range of angles, i.e. $0° \leq \theta \leq 360°$.

The B-Spline surface is constructed from a linear combination of B-Spline basis functions. These basis functions are piecewise continuous, and are non-zero only over a segment of the real line. The non-parametric B-Spline is written in the form,

$$z(x, y) = \sum_{ij} c_{ij} N_i(x) M_j(y) \tag{4.47}$$

where z is the height of the cornea. In this case c_{ij} have a simple interpretation. In particular, they are control points which mimic the shape of the surface [see Farin, 1988, for details].

It was found that a non-parametric (i.e. an explicit representation as given in equation

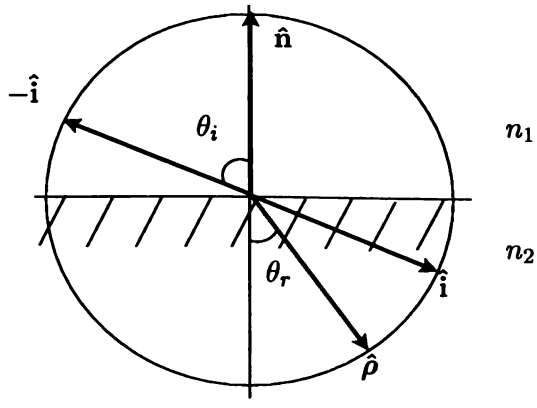

Figure 4.6: The refracted ray is found from the above setup.

(4.47)) cubic B-Spline with uniform knot sequence gave robust/accurate fitting. A 24×24 control point matrix was chosen, since this appeared to give an adequate fit in surface cases tested. The surface had guaranteed continuity of its derivatives to the 2^{nd} derivative. The B-Spline representation fitted the reconstructed height data in a least squares sense (i.e. it was fitted with more data points than control points). This produced a *fair* surface which approximated the data smoothly, in order to avoid *rippling* found in interpolating methods of high order. It was also possible to impose an interpolation constraint on the surface, namely that the corneal surface should pass through the origin.

Performing intersection testing on such surfaces has been described by several authors, with varying levels of complexity [Sherstyuk, 1999, Tuy and Tuy, 1984]. A routine based on a simple binary search along the ray was implemented, for calculating intersections with arbitrary surfaces. The distance between a test point and the surface (along the z-axis) was minimized. This method was found to be adequate (70-100 rays/sec) for the application, and it was coded so that many rays were minimized *simultaneously* i.e. rather than the standard MATLAB minimization functions, which (to the Author's knowledge) could minimize only one ray at a time. The code is included in section B.1.3 of Appendix B.1.

However, in cases where the anterior corneal surface was the only arbitrary surface traced, intersection points could be chosen initially, and the corresponding rays then constructed from these points. It was found that this method caused slightly different output, due to the fact that the surface vectors where determined from surface points initially, rather than searched for. However, these errors were small due to the large source point distances (i.e. 3m - 6m) and the small radial area of the cornea traced (i.e. approximately 4 mm).

4.3.5 Modeling Refraction/Reflection

Heckbert and Hanrahan [1984] describe a method for computing the refracted ray vector, found by constructing the refracted ray from orthonormal vectors in the plane defined by the incident and normal rays. In particular, the refracted ray is found from the equation,

$$\begin{aligned}\hat{\boldsymbol{\rho}} &= \sin(\theta_r)\hat{\boldsymbol{\rho}}_\perp + \cos(\theta_r)\hat{\boldsymbol{\rho}}_{||} \\ &= \sin(\theta_r)\hat{\boldsymbol{\rho}}_\perp - \cos(\theta_r)\hat{\mathbf{n}} \end{aligned} \tag{4.48}$$

where $\hat{\boldsymbol{\rho}}$ is the refracted ray vector, θ_r is the angle of refraction, $\hat{\boldsymbol{\rho}}_\perp$ is the unit vector perpendicular to the normal $\hat{\mathbf{n}}$ (but co-planar with the normal and incident vectors) and $\hat{\boldsymbol{\rho}}_{||} = -\hat{\mathbf{n}}$ is the unit vector (anti-)parallel to the normal. This setup is shown in Figure 4.6. From simple geometry $\hat{\boldsymbol{\rho}}_\perp$ can be written in terms of the incident ray vector $\hat{\mathbf{i}}$ as,

$$\begin{aligned}\hat{\boldsymbol{\rho}}_\perp &= \frac{(-\hat{\mathbf{i}}\cdot\hat{\mathbf{n}})\hat{\mathbf{n}} + \hat{\mathbf{i}}}{\sin(\theta_i)} \\ &= \frac{\cos(\theta_i)\hat{\mathbf{n}} + \hat{\mathbf{i}}}{\sin(\theta_i)} \end{aligned} \tag{4.49}$$

where θ_i is the angle of incidence. The numerator of the fraction defines a vector parallel to $\hat{\boldsymbol{\rho}}_\perp$, whilst the $\sin(\theta_i)$ term ensures it is of unit length. Substituting this result in equation (4.48) gives,

$$\begin{aligned}\hat{\boldsymbol{\rho}} &= \frac{\sin(\theta_r)}{\sin(\theta_i)}\left(\cos(\theta_i)\hat{\mathbf{n}} + \hat{\mathbf{i}}\right) - \cos(\theta_r)\hat{\mathbf{n}} \\ &= \frac{n_i}{n_r}\left(\cos(\theta_i)\hat{\mathbf{n}} + \hat{\mathbf{i}}\right) - \cos(\theta_r)\hat{\mathbf{n}} \\ &= \left(\frac{n_i}{n_r}\cos(\theta_i) - \cos(\theta_r)\right)\hat{\mathbf{n}} + \hat{\mathbf{i}}\frac{n_i}{n_r} \end{aligned} \tag{4.50}$$

where Snell's law (4.34) has been used to eliminate the sine terms. By the fact (from the diagram) that $\cos(\theta_i) = -\hat{\mathbf{i}}\cdot\hat{\mathbf{n}}$ and

$$\begin{aligned}\cos(\theta_r) &= \sqrt{1-\sin^2(\theta_r)} \\ &= \sqrt{1-(n_i/n_r)^2\sin^2(\theta_i)} \\ &= \sqrt{1-(n_i/n_r)^2(1-(\hat{\mathbf{i}}\cdot\hat{\mathbf{n}})^2)} \end{aligned} \tag{4.51}$$

we obtain an explicit equation for the refracted ray in terms of the incident vector and normal,

$$\hat{\boldsymbol{\rho}} = -\left((n_i/n_r)\hat{\mathbf{i}}\cdot\hat{\mathbf{n}} + \sqrt{1-(n_i/n_r)^2(1-(\hat{\mathbf{i}}\cdot\hat{\mathbf{n}})^2)}\right)\hat{\mathbf{n}} + \hat{\mathbf{i}}\frac{n_i}{n_r} \tag{4.52}$$

If the quantity under the square root sign is negative, then there will be no refracted ray. This corresponds to total internal reflection. Some care is required in the case of total internal reflection, since RAYTRAK will attempt to trace the ray to the next surface in the lens prescription, even though that ray never reaches it. It is important that the sequence surfaces the ray travels is known *a-priori* to account for this possibility.

4.3.6 Decentration and Surface Orientation

A convenient method for modeling intersections with decentered/tilted objects, is to change co-ordinate systems in order to simplify the intersection equations. If the surface is originally displaced by an amount $\mathbf{r}_0$, and a rotation R of the surface about this point is required, then we can model this change by setting the origin of our new co-ordinate system at $\mathbf{r}_0$ and rotating the coordinate axes R^{-1} about this point. The equation for a ray in the new coordinate system is,

$$\begin{aligned} \mathbf{r}'(s) &= R^{-1}(\mathbf{r}(s) - \mathbf{r}_0) \\ &= R^{-1}(\mathbf{a}s + \mathbf{b} - \mathbf{r}_0) \\ &= (R^{-1}\mathbf{a})s + R^{-1}(\mathbf{b} - \mathbf{r}_0) \\ &= \mathbf{a}'s + \mathbf{b}' \end{aligned} \tag{4.53}$$

where $\mathbf{a}'$ and $\mathbf{b}'$ are the ray slope and ray position vectors in the new co-ordinate system, and R is a 3×3 rotation matrix[1]. The transformation of co-ordinate systems is shown in Figure 4.7, which shows the situation in the optic axis based system (i.e. the standard laboratory based system), and the surface based system. Ray-tracing is carried out using the simple intersection formulae e.g. (4.36) and (4.39), in the surface based system, which can be subsequently returned to the original co-ordinate system by applying the inverse transformation R. Some care is required at this point, since finite rotations do not *commute*[2]. However, following the convention that rotation proceeds about the x-axis, followed by the y-axis and then the z-axis circumvents this problem. The inverse matrix R^{-1} is found by doing the inverse rotations in the reverse order.

This method is convenient for several reasons. Firstly, transformations on rays are simple, but transformations on surfaces can be difficult and introduce unnecessary coding. This in turn improves the readability of the code. Another useful feature is that the surface aperture will behave as if it were rotated also, as required. This is a rather more complicated feat in the original co-ordinate system. Finally, this method is independent of the surface representation, so that it is applicable to general surface models.

---

[1] It is customary to distinguish points (e.g. b) and vectors (e.g. a) via homogeneous coordinates (x,y,z,w) where $w = 1$ corresponds to a point, and $w = 0$ corresponds to a direction. In this case, decentering and rotation may be represented by the linear 4×4 transformation matrix. However, this method will be disregarded for the *computationally* expedient approach given here.

[2] infinitesimal rotations however do, see for example Kleppner and Kolenkow [1984]

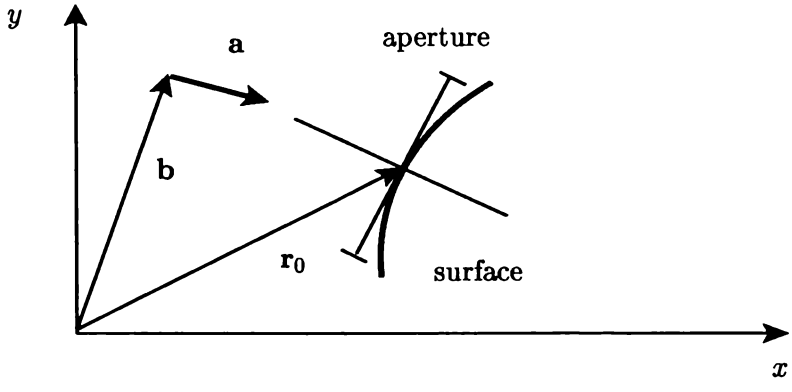

(a) Laboratory based system

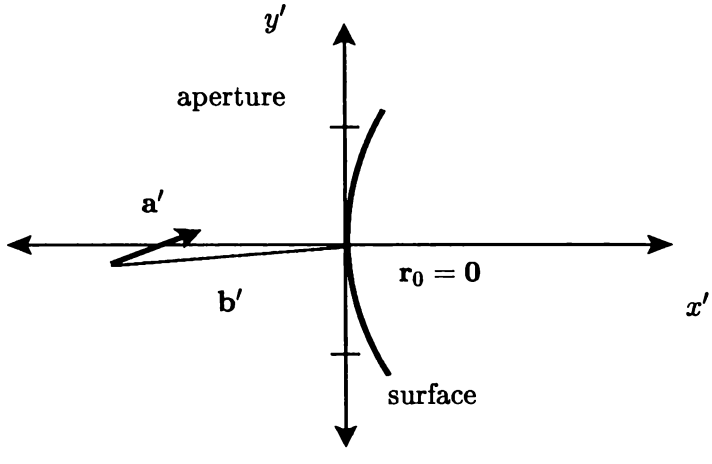

(b) Surface based system

Figure 4.7: Lens decentering and tilt are handled by transforming to a surface based system, so that decentering and tilt is applied to the *rays* rather than the surfaces. This method is independent of surface representation, so is generally applicable.

4.4 Implementation Details

4.4.1 Overview

The RAYTRAK toolbox consists of functions which fall in three categories i.e. system definition, system processing, and system evaluation. System definition encompasses functions that process input files used for defining individual rays, collections of rays and the lens prescription. System processing refers to functions that directly support, and do the work of tracing rays. Finally, system evaluation refers to reporting/evaluation routines for displaying spot diagrams, aberration metrics, and other performance measures such as the PSF and MTF. The set of evaluation functions were kept small, because the emphasis of the toolbox was to model, rather than evaluate the performance of the eye.

4.4.2 System Definition

System definition is either *interactive* or *non-interactive*. The *non-interactive* method involves writing and then parsing a ray/lens definition file, whose parsed output is a matrix of ray values. The advantage is that ray/lens definitions can be stored in an easily editable form (i.e. as files). The *interactive* method bypasses the file creation step, so that rays are created "on the fly" using ray definition routines. The output of these routines are again, a matrix of ray values.

The lens prescription may be generated in the same way, but it was found for most tasks, that the lens prescription was best written to file. In this way, a record of the optical system was retained. This was not critical for the ray definition step, it was found convenient to generate rays "on the fly". This is because evaluating the system requires flexibility in the rays, e.g. different field positions, different numbers of rays, different configurations of rays.

Figures 4.8 and 4.9 show example ray files and lens prescription respectively. The example ray file shows three commands. The first command is for a single ray. The second command defines a collection of rays (termed here a *node*) that spreads out over a square grid, while the third line defines a collection of *nodes* arranged to form the letter "C" (Note this is the brute force method of Korynta et al. [1999] for generating synthetic images of the Landolt-C in the eye).

The lens prescription starts by defining the index of refraction of the medium in which the rays start propagating, the first surface is then defined, followed by the index of refraction of the next medium, and so on. The image plane is a plane surface, but it need not be, since the output of the ray-tracer are the intersection points on the final surface.

```
// ---------------------------------------
// EXAMPLE RAY FILE
// RAY  = A single ray
// SOU  = A grid of rays
// LD2  =   Landolt C: A collection of SOU
//          shaped like the letter C
// ---------------------------------------
RAY 0,0,6000,0,0,1
SOU 10,0,3000,1
LD2 0,0,6000,10,12,0
```

Figure 4.8: An example ray file.

```
// -----------------------------------------------
// EXAMPLE LENS PRESCRIPTION
// IND = Refractive index to the left of surface
// RSP = Ellipsoid surface
// STP = Stop
// PLA = Plane
// -----------------------------------------------
IND 1.000
RSP 0,0,0,-7.7,-7.7,-7.7, 5,1,0, 0,0,0,0,0,0
IND 1.376
RSP 0,0,-0.5,-6.8,-6.8,-6.8,5,1,0, 0,0,0,0,0,0
IND 1.336
STP 0,0,-3.7,5,0,1
IND 1.336
RSP 0,0,-4.1,-5.90,-5.90,-5.90, 3,1,0,0,0,-3.945, 0,0,0
IND 1.495
RSP 0,0,-4.80,28,28,28, 3,1,0, 0,0,-3.945, 0,0,0
IND 1.336
PLA 0,0,-22.3,50,0,1
IND 1.336
```

Figure 4.9: An example lens file.

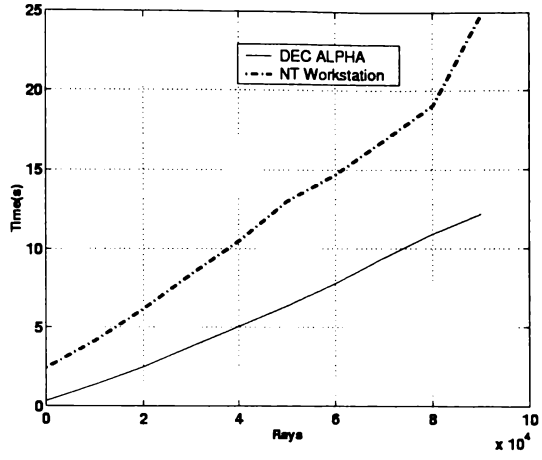

Figure 4.10: Timing results for a 7 surface eye-model on two different platforms. The DEC ALPHA running UNIX is approximately 2 times faster than the WIN NT workstation. Both timing tests give computation times that should be acceptable for clinical use.

4.4.3 System Processing

The core routines of the ray-tracer have been explained in section 4.3. An example of timing results for RAYTRAK found on a DEC-ALPHA and WIN-NT system running MATLAB v5.0 are shown in Figure 4.10. The number of rays traced are increased from 1K to 100K rays in steps of 10K rays, where tracing is through a seven surface optical system i.e. the Gullstrand eye. The time taken increases in a roughly linear fashion, the graph indicates a work rate of roughly 1×10^4 rays/sec on the DEC-ALPHA, with a rather lower work rate of about 5×10^3 rays/sec on the WIN-NT work-station. However, given that the number of rays required for tracing is at most 3×10^4 rays, this equates to less than 10 sec of delay. This is a clinically acceptable number of rays considering that a corneal topographer is typically supported by a fast Pentium-like PC.

4.4.4 System Evaluation

Evaluation routines take rays and produce output based on the resultant ray-trace. Several simple evaluation routines were implemented, adapted largely from O'Shea and Harrigan [1995], Smith [1966]. These routines were simple geometric aberration routines, wave aberration (i.e. diffraction calculations) and paraxial routines for determining the cardinal points of an optical system. It was found that extending the program was made relatively simple due to the extensive set of analysis functions provided in MATLAB. The following list explains the core routines of RAYTRAK (there are routines for manipulating rays, producing spot diagrams, producing images which have not been included here):

RAY2PSF Produce PSF from the traced rays.

RAYSTATS	Compute Spherical Aberration(LSA), Transverse Coma(TC) and Ray-Intercept Curves.
RAYOTF	Generate OTF, MTF, directly from rays or PSF.
RAYWAVE	Determine the wave aberration function and PSF by equation (2.17).
RAYCARD	Determine the cardinal points, by an exact ray-tracing method.
RAYPARAX	Determine focal points by single surface equation (2.1) implemented in a ray tracing loop.

The accuracy of RAYCARD and RAYPARAX were assessed by comparing with the schematic eye data given in Appendix 3 of Smith and Atchison [1997]. Agreement to the accuracy (4 dp) of the data was found. Agreement was always found between the two methods, for all on axis cases. These two methods can be expected to deviate for decentered optical elements, in which case, RAYPARAX ignores this information. Figure 4.11 shows an example of some the output capabilities of RAYTRAK.

4.4.5 Conclusion

This section has presented RAYTRAK, a prototypic MATLAB toolbox for ray-tracing. The toolbox includes functions for modeling rays, and simple measures of ray error. The main advantage of this toolbox, is that it provides a flexible framework for research applications. In particular, it is useful for applications in which non-standard ray-tracing tasks are required, as will be demonstrated in following chapters (see in particular 5.3).

4.5 Ray-Tracing Errors due to Corneal Height Maps

4.5.1 Introduction

It is essential that ray-tracing of the cornea (in particular) is accurate. This is because it has the greatest influence on the imaging of the eye. This section assesses ray-tracing errors due to recovered corneal height maps. The testing is carried out for the two general surface methods implemented by RAYTRAK, i.e. cubic/linear (to be explained soon) interpolation and a B-Spline interpolation [3].

[3]This testing was influenced by the historical implementation of RAYTRAK. Originally, the toolbox included a cubic/linear spline interpolation, after-which B-Spline routines were implemented

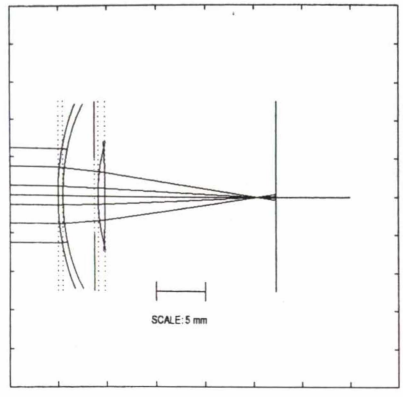

(a) System Display

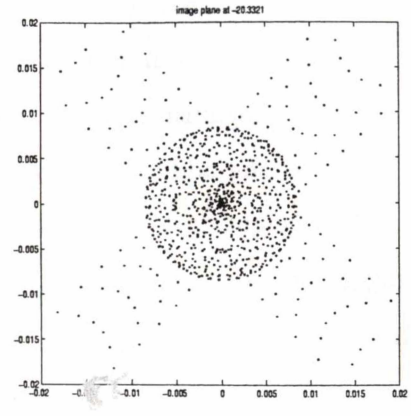

(b) Spot Diagram

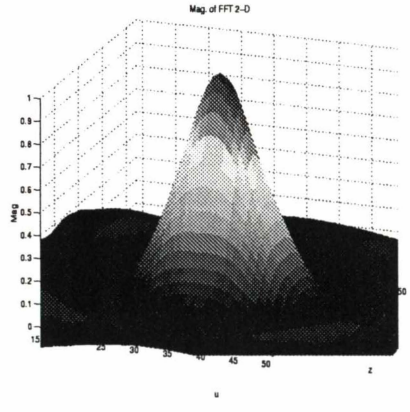

(c) MTF (2-D)

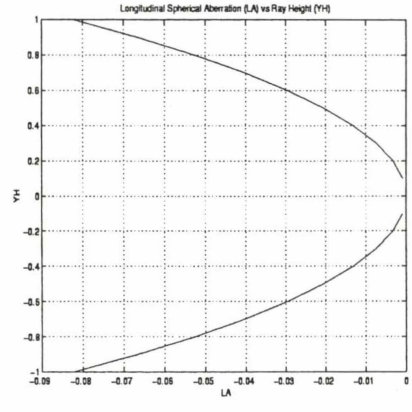

(d) Spherical Aberration

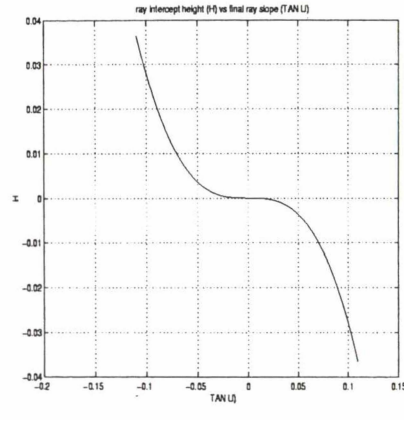

(e) Ray Intercept Curve

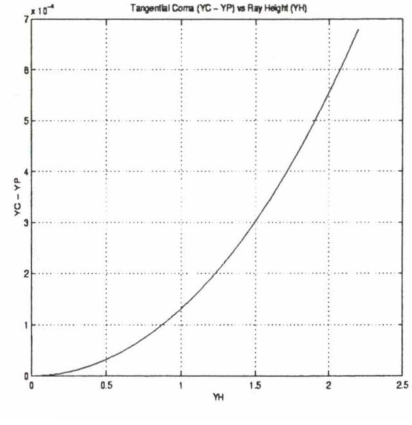

(f) Coma

Figure 4.11: An example of the system evaluation routines available in the RAYTRAK toolbox.

The necessary surface information for tracing rays are surface normals and surface intersections. The error in generating surface normals by the two methods above are compared. From this comparison it is found that the B-Spline method gives lower RMS error in the height, slope and tilt (against analytic model results) then the cubic/linear method. The B-Spline method has the additional advantage that it does not use any information, other than the recovered height data-points. This method is therefore used as the default method for ray-tracing general surfaces.

The ultimate test of accuracy is the amount of transverse (i.e. in the image plane) error and longitudinal (focal) error, that results from tracing rays. Of particular importance is the estimation of focal length, since this is a clinically important quantity. Using simulated data, gives small focal errors (no greater than 0.05 mm (0.2 D)) and transverse RMS (spot-diagram) errors no greater than 1.5×10^{-3} mm (i.e. 1 retinal cone). The B-Spline method is then tested on calibration ball data, obtained from section 3.6. The resultant errors incurred are on average 6.5μm (4 retinal cones) in the image plane, and on average, 1.4×10^{-2} mm (0.1 D) axially. These are acceptably low errors, given that a typical spot diagram will be of much larger dimension ($< 50\mu$m) in the transverse plane; and the focal error is well under a *just noticeable error* of 0.25 D as stated by Lang et al. [1994]. This is evidence that the current accuracy of the experimentally obtained *corneal* data, is sufficient to model the PSF within the tolerance of Human perception.

4.5.2 Method

To assess the cubic/linear and B-Spline methods of section 4.3, the analytic and (simulated) recovered spherical, ellipsoidal and radial keratotomy models of section 3 were added (in turn) to the Le Grand eye model (see section A.2 of Appendix A for details) as the anterior corneal surface. A *node* of 512 rays was created, by generating a square grid of 512 rays over the central 5 mm of the Le Grand eye. The node was positioned at 6m (along the axis) in object space. The cubic/linear and B-Spline methods were then used to determine the normals at the intersection of these rays with the cornea (see section 4.3.4 for details). In order to test the efficacy of the interpolated reconstruction at these points, the RMS error between the height,slopes and tilts of the recovered and exact surface were determined.

The B-Spline generated rays were subsequently traced to the plane of best focus, and the transverse RMS error in spot diagram positions (i.e. between the simulated and exact surfaces) was determined at the image plane. A transverse displacement diagram was generated, showing the errors between the two representations as a displacement from the origin

Description	Height (mm)	Slope (mm/mm)	Tilt(mm/rad)
Asphere	6.6×10^{-7}	4.4×10^{-6}	5.7×10^{-15}
Ellipsoid	2.8×10^{-3}	1.6×10^{-3}	1.2×10^{-1}
Keratotomy	6.7×10^{-4}	8.1×10^{-4}	1.1×10^{-1}
Average	1.2×10^{-3}	8.0×10^{-4}	7.7×10^{-2}

(a) Cubic/linear spline interpolation: RMS height, tilt and slope errors for a node of 512 rays

Description	Height Error (mm)	Slope Error(mm/mm)	Tilt Error (mm/rad)
Asphere	7.2×10^{-7}	4.8×10^{-6}	4.2×10^{-6}
Ellipsoid	3.9×10^{-4}	2.9×10^{-4}	3.5×10^{-4}
Keratotomy	2.6×10^{-4}	3.5×10^{-3}	1.4×10^{-3}
Average	2.2×10^{-4}	1.3×10^{-3}	5.9×10^{-4}

(b) B-Spline interpolation: RMS height, tilt and slope errors for a node of 512 rays

Table 4.1: The two tables show the RMS errors in height, slope and tilt between interpolated and analytic model surfaces. The B-Spline method gives better results, and is therefore chosen in preference to the cubic/linear method. In addition the B-Spline method does not use any other information other than the recovered height.

(in the plane of best focus). The axial position of the plane of best focus was determined by minimizing the objective function,

$$E = \sqrt{\frac{\sum_{i=1}^{N} \{(x_i - \bar{x})^2 + (y_i - \bar{y})^2\}}{N}} \tag{4.54}$$

where (x_i, y_i) are the co-ordinates of the i^{th} ray (of $N = 512$ rays) over the image plane, and $(\bar{x}, \bar{y})$ are the means. This was used to estimate of the shift in focus due to modeling errors, by determining the difference with analytic results. The ray-tracing process was repeated on calibration ball data of section 3.6. This gave an estimate of experimental errors in corneal reconstruction for spherical eyes. The recovered 7 mm, 8 mm and 9 mm spheres were added to the Le Grand eye model, spot diagrams were generated and transverse/longitudinal RMS errors were calculated.

Description	Method	Spot RMS Error (mm)	Focal Error(mm)(D)
Asphere	B-Spline	1.1×10^{-4}	$2.5 \times 10^{-3}0$ (0.0 D)
Ellipsoid	B-Spline	1.5×10^{-3}	4.6×10^{-2} (0.2 D)
Keratotomy	B-Spline	1.3×10^{-3}	8.7×10^{-3} (0.0 D)
Average		1.0×10^{-3}	0.019 (0.1 D)

Table 4.2: Rays are traced to the image plane using the B-Spline method for modeling the cornea. The RMS error between the 512 rays generated by analytic surface models, and recovered surface models are shown. Also shown are the focal plane displacement error (mm) with an estimated dioptric error (D).

Description	Method	Spot RMS Error (mm)	Focal Error(mm)
7 mm	B-Spline	4.0×10^{-3}	0.016 (0.1 D)
8 mm	B-Spline	5.8×10^{-3}	0.015 (0.1 D)
9 mm	B-Spline	9.8×10^{-3}	0.012 (0.0 D)
Average	B-Spline	6.5×10^{-3}	0.014 (0.1 D)

Table 4.3: Rays are traced to the image plane using the B-Spline method for modeling the cornea. The RMS error between the 512 rays generated by analytic surface models, and recovered surface models are shown. Also shown are the focal plane displacement error (mm) with an estimated dioptric error (D).

4.5.3 Results

Tables 4.1(a) and 4.1(b) summarize the results found for the RMS height, slope and tilt errors after interpolating the corneal surface at the ray intersection points. Whilst the errors are low in both cases, the tables show that the B-Spline outperforms the cubic/linear method implemented here. In particular, the height is consistently sub-micron, and the tilt estimation is two orders of magnitude lower than in the cubic/linear case. The slope error is slightly higher in the case of B-Spline interpolation, but the difference between the two methods in this case is small. For these reasons, the B-Spline method was adopted as the default surface modeling method.

Subsequent ray-tracing of the Le Grand eye model verified the efficacy of the modeled rays in simulation. The rays were traced to the plane of best focus for the particular surface. The resulting spot diagrams for the B-Spline method is shown in 4.12. The left column shows the actual spot diagrams generated at the image plane, whilst the right hand column shows *error* diagrams between analytic and surface generated results. The transverse RMS errors and longitudinal focal errors are summarized in Table 4.2. The average transverse RMS errors are no larger than the dimensions of a retinal cell (1.5μm), whilst the focal errors are much less

than a *just noticeable difference* of 0.25 D [Lang et al., 1994]. These results are encouraging, given the accuracy of the results *and* from an implementation point of view, the fact that the representation was determined from height values only.

The B-Spline method was used to test the 7 mm, 8 mm and 9mm calibration balls, using the same method used previously. The resulting spot-diagrams are shown in Figure 4.13. The results for these calibration balls are summarized in Table 4.3. In this case, the errors increased to an averaged RMS error of 6.4×10^{-3} mm. The error for each calibration ball increased steadily from 4.0×10^{-3} mm to 9.8×10^{-3} mm over the calibration balls. This implied that the accuracy of the spot-diagrams would be most accurate for smaller spherical corneas. However, in this case again, the point of best focus was found to shift an average of 0.015mm(0.05 D), from the analytic result. These, again are certainly below a tolerable displacement of 0.25D as described in Lang et al. [1994]. This is evidence that reconstruction of corneal shape will produce accurate measures from general measurements.

4.5.4 Conclusion

The cubic/linear and B-Spline interpolation methods were initially tested on simulated data. It was found that both methods performed well on the recovered simulated data. However, the B-Spline was (across height and tilt) more accurate. From an implementation point of view, the B-Spline method was also preferable, since the B-Splines were generated from height data only. This method was therefore adopted as the standard.

The transverse RMS error (on the image plane) between simulated and analytic spot-diagrams were measured. Computing the point of highest spot density was used as means of estimating the position of best focus. The average transverse RMS error on the image plane for simulated data was less than a retinal cone, at 1.0×10^{-3} mm. A retinal cone limits the accuracy of resolution, so this was an encouraging result. A corresponding average focal error of 0.019 mm (0.1 D) was found for simulated data. This was encouraging, since focal errors were well within a tolerable error of 0.25 D.

In the case of experimental data, the average transverse error increased to 6.5×10^{-3} mm. The error therefore increased to a distance on the order of 4 retinal cones. Considering that spot diagrams would be generated for large (50μm) defocused cases, implied that this error would be acceptable. In this case, the focal error was again found to be 0.014mm(0.1 D), which was evidence that at least for experimentally obtained (spherical) eyes, prediction of focal length would be accurate (ignoring errors in measurement of other optical elements).

The results implied that the corneal recovery and subsequent B-Spline interpolation

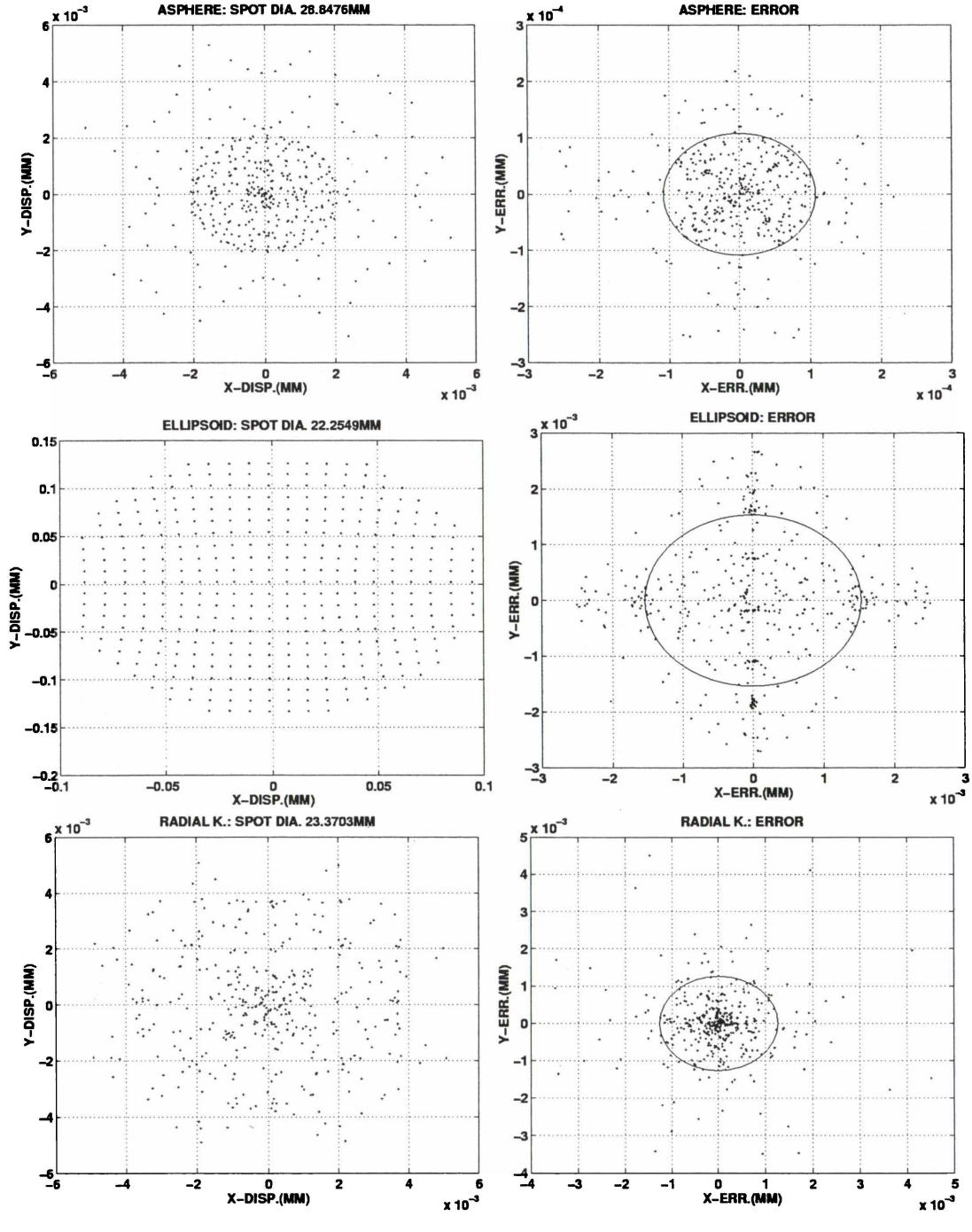

Figure 4.12: The figures in the left column show the spot diagrams generated through ray-tracing an aspheric, ellipsoidal and radial keratotomized anterior cornea, when added to a Le Grand eye model. The column on the right shows the errors between the analytic and generated surfaces. The interpolation method used here is the B-Spline method.

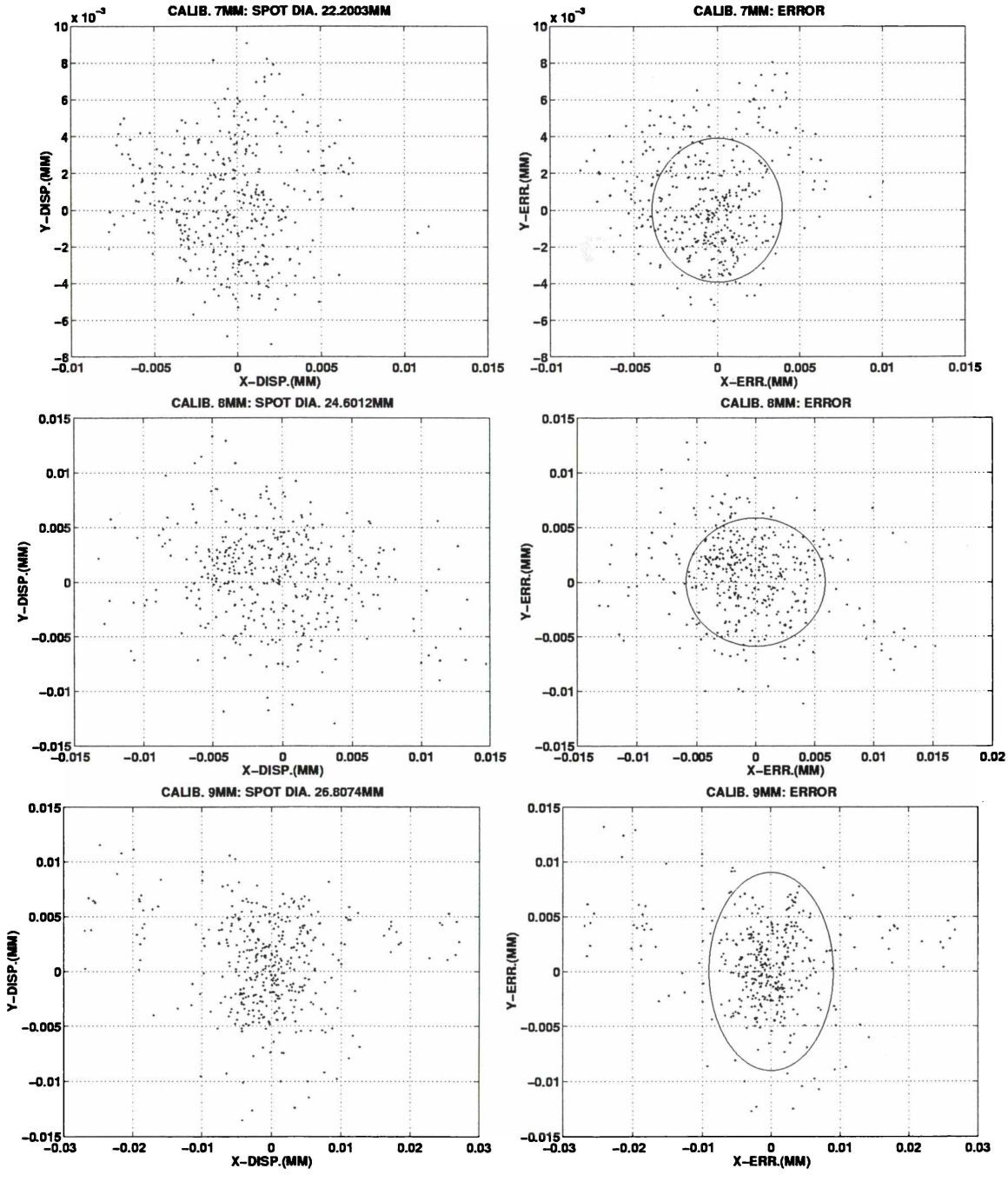

Figure 4.13: The figures in the left column show the spot diagrams generated by ray-tracing calibration balls of radius 7 mm, 8 mm and 9 mm, added to the Le Grand eye model. The results show a maximum RMS error of not more than 10 μm. This will result in errors in reconstruction on the order of 7 retinal cells. The focal error is no more than 0.16 mm (0.05 D).

method, combined with ray-tracing, would be of sufficient accuracy to produce valid spot-diagrams. This analysis assumed that errors in the assumed quantities (refractive indices, posterior cornea model) and measured distances (axial distance to lens, manufacturer provided quantities) were negligibly low, so did not consider the possible contributions of these errors.

Chapter 5

Measurement of Internal Ocular Radii and Modeling Lens Tilt and Decenter

5.1 Introduction

The theme of this chapter is the application of ray-tracing to: (i) the measurement of the internal ocular radii, and (ii) modeling the effect of IOL decentering and tilt. The chapter therefore contains two distinct sections which deal with the two separate problems.

The first section looks specifically at the measurement of the radii of curvature of ocular surfaces internal to the eye (i.e. the posterior corneal curvature and lens radii of curvature). Under the hypothesis that the methods of videokeratography are applicable to videophakometry, a new method of determining the internal radii is presented. The approach taken extends on methods which utilize the *Purkinje-Sanson* images, the externally measured reflections from the internal ocular surfaces.

The method consists of three steps: (a) ray-tracing is used to model the images of point sources in object space, (b) a linear model relates the images to the internal parameters, and (c) the model is then inverted to give a formula for estimating the internal parameters given clinically measured image points.

The method itself is the analogy of the method of *spherical equivalence* (see section 3.4.1) used in VK, but it was originally inspired by the eye modeling work of Barry et al. [1997b]. The method is tested using the Le Grand eye model (see Appendix A for details) as used in Barry et al. [1997b]. The recovery of the posterior cornea and anterior lens radii are tested. The recovery of these parameters is found to be accurate, but slow.

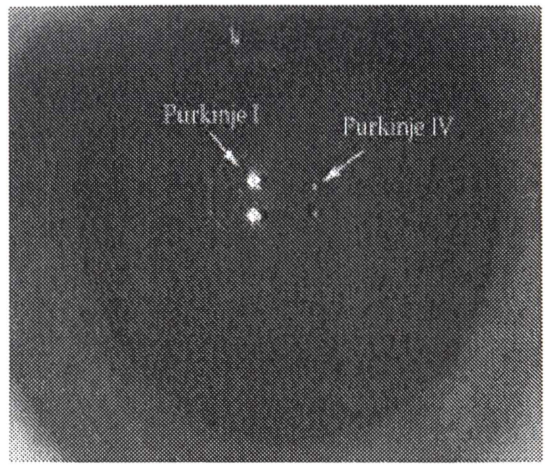

Figure 5.1: A Picture showing PI and PIV [Friedman, 2000]

The discussion describes how the method may be improved upon in the future. It is suggested that existing video-keratographic algorithms may be modified for video-phakometric purposes. To the author's knowledge, the equipment needed to take full advantage of such an approach has not been developed. Hardware requirements and the potential limiting factors on the method, are briefly described.

In the second section of this chapter, attention is turned to modeling the optical effect of lens decentering and tilt on IOL patients. The Le Grand eye model is retained, but the lens is replaced with an artificial IOL. Spot diagrams on the retinal plane are produced and geometrical PSFs are computed from these representations. Image quality is determined objectively by use of the SQuare Root Integral (SQRI) image quality metric. A novel method for quantifying the source of the image quality is also presented, namely by way of statistical moment measures. The results found are discussed.

Taken together, these metrics form a means of determining both the total perceptual image quality and the cause of the image quality. The results are also evaluated by visual inspection.

5.2 A New Method for Recovery of Internal Ocular Radii

5.2.1 Background

Videophakometry (VP) is the measurement of the crystalline lens parameters (tilt, decenter, radii of curvature) using the *Purkinje-Sanson* (or simply the *Purkinje* images) [Schwiegerling, 2000][1]. These are the images of external sources, reflected from the internal ocular surfaces.

[1]The term *phakometry* is used to refer to measurement of the anterior/posterior corneal surface, and IOL lens surfaces also.

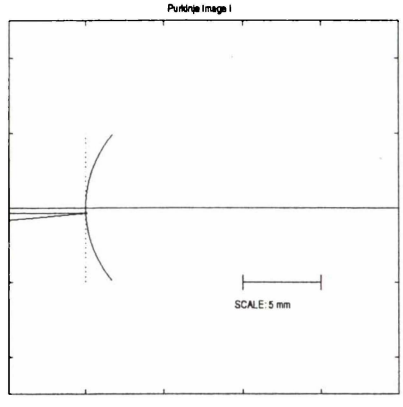

(a) Purkinje Image I

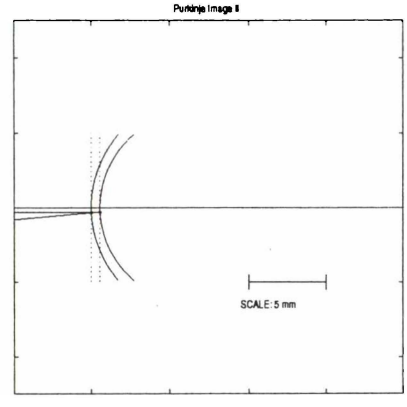

(b) Purkinje Image II

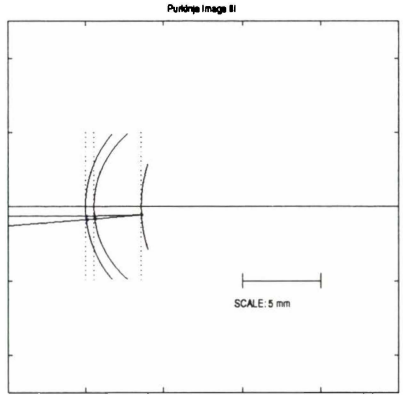

(c) Purkinje Image III

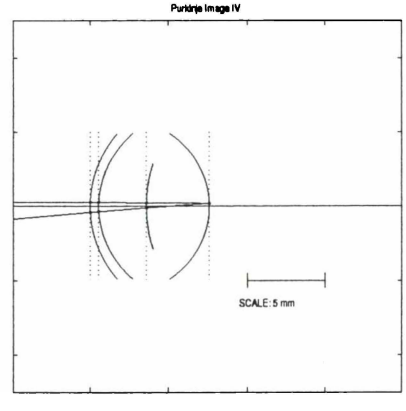

(d) Purkinje Image IV

Figure 5.2: Purkinje Images for the Le Grand Schematic Eye. The source point is below the axis at (50,-50,500) mm. The x-component is not visible in the diagram, since the x-axis points out of the page. The camera is telecentric, so the exit ray always exits the cornea parallel to the optic axis.

Figure 5.2 shows raytraced examples of the Purkinje images PI - PIV, reflected from the anterior corneal surface (PI), posterior corneal surface (PII), anterior lens (PIII) and posterior lens (PIV) respectively. The source has been positioned below the optic axis, and the reflected light is captured by an axially centered camera. Figure 5.1 shows a photographic example [Friedman, 2000] of PI and PIV, where a pair of lights separated vertically are the objects. From the distance between the two images, an estimate of internal parameters (typically the surface decentering and radii may be obtained [Philips et al., 1988]).

The standard method for calculating the internal ocular dimensions, is by way of the *equivalent mirror* theorem [Le Grand and El Hage, 1980] which states that an optical system consisting of refracting surfaces, followed by a reflecting surface, can be replaced by an *equivalent mirror*. The radius of this mirror is determined from the measured heights of PI and PIII. The vertex and center of curvature of this equivalent mirror, are conjugates to the real anterior lens vertex and radii. Garner and Smith [1996] utilize this method, for measuring the radius of curvature of the anterior lens, including techniques which avoid the need to re-focus the camera for different Purkinje images, and accounting for targets at finite distances.

However, the use of videophakometry is not restricted to the measurement of the lens parameters. Quick and Boothe [1992] use the displacement between the reflected images of PI and PIV as a means of determining the direction of gaze of an eye. The horizontal misalignment of the images (PI and PIV) is the horizontal direction of gaze, and the vertical misalignment is the vertical gaze direction. More recently, Barry et al. [1994a,b] have described the computational principles and equipment for measuring angles of gaze for detection of strabismus (i.e. angular misalignment of the eyes).

Dunne et al. [1996] have described a technique for measuring astigmatism of the internal ocular surfaces. This technique combines VK, A-scan ultrasonography, autorefractometry and multi-meridional (i.e. many point sources arranged in a half-circle) phakometry for determining the principal powers of the posterior cornea, anterior cornea and posterior crystalline lens. The method of *meridional analysis* is used to locate the principal axes of the surfaces, which measures the dioptric power as a function of meridional angle.

It appears that phakometry techniques have not employed the *methods* of VK to date. Dunne et al. [1996] use VK, but the measurements taken are the steepest and flattest radii for the cornea, i.e. keratometric measurements. There are advantages to using *complete* (i.e. position, slope and tilt information) corneal surface information, because accurate knowledge of the corneal surface has the potential to improve techniques which attempt to measure the internal ocular surfaces. In addition, such an approach is an ideal application for a toolbox

such as RAYTRAK.

Barry et al. [1997a] use ray-tracing routines [Clement et al., 1987] based on 2^{nd} order aspheric surfaces model surfaces to model the effect of eye parameters on the Purkinje images. In particular, the camera image plane positions of PI, PIII and PIV are determined as a (linear) function of total eye rotation, lens rotation and lens decentration. The ray which enters the camera is found by adjusting the angle of the incident ray (from the source in 0.003° increments), until it intersects the image plane 2.5 mm from the camera position. The apparent location of the returning ray (i.e. the exit ray) is taken as the intersection point with the cornea (i.e. a telecentric assumption). The analysis is limited to 2^{nd} order aspheric surfaces, and requires a compromise between the time taken and the pupil area sampled.

5.2.2 Theory

The new method presented here is inspired by the work of Philips et al. [1988] and Barry et al. [1997b] who fit a linear model to determine the effect of ocular parameters on the Purkinje images. However in this case the resulting linear model is inverted for the internal ocular parameters. This method is analogous to the method of *spherical equivalence* of videokeratography, described by Mattioli and Tripoli [1997], Halstead et al. [1995b]. In that method the anterior cornea radii were determined by linearly interpolating the images of pre-imaged calibration balls.

In this case, the pre-imaged calibration surfaces (i.e. for the posterior cornea say) are instead simulated, and subsequently ray-traced (for the image positions). This requires a general method for determining the ray which enters the telecentric camera, i.e. for computing images. Such a search routine is described in the following section. The linear interpolation of the *spherical equivalence* method is implemented by fitting a linear model to the simulated images (as a function of the eye parameters). After the model is fitted to the data, it is then inverted to give estimates of the internal radii based on measured images. The search routines and linear modeling taken together form a new method which has not been investigated previously.

Simulating Telecentric Camera Images

The method employed here for determining the exit ray (i.e. the ray which exits the eye and enters the camera) is based on a triangle based subdivision search. The algorithm searches the cornea by tracing rays through the vertices of triangular patches, from which exiting rays can be used to further refine the search.

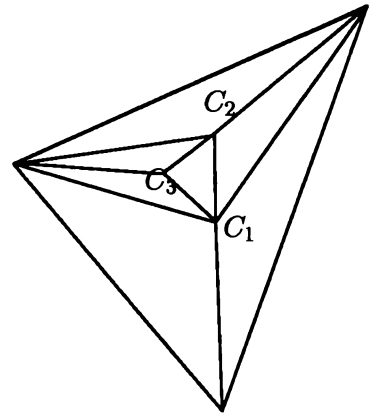

(a) Recursion

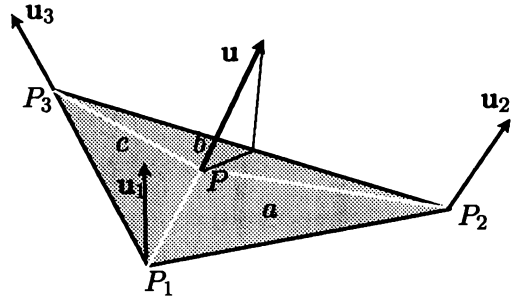

(b) Geometric interpretation of co-ordinates (a, b, c)

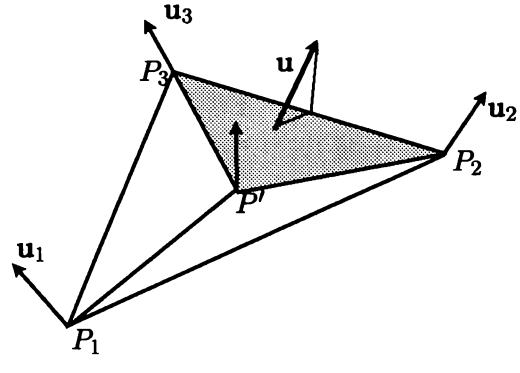

(c) Subdivision Rule

Figure 5.3: (a) The recursion aspect of the sub-division algorithm, showing three levels of recursion, (b) a geometric interpretation of the co-ordinates (a, b, c), where they are proportions of the entire triangular area, (c) A sub-triangle is chosen by testing whether it can be constructed from the ray directions at the vertices.

Suppose for now, a triangle of incident rays has been found, which produces exit rays that bound the required (telecentric) ray. That is, the triangle of incident rays *encloses* the required incident ray. Consider the intersection points of the incident rays on a plane which lies in the (x-y) plane and passes through the origin say. Form a triangle from the resulting intersection points i.e. spot-diagram, and subdivide it into three sub-triangles (by finding the centroid of this triangle), and test these sub-triangles for *enclosure*. This will locate the ray to within one of the smaller triangles. Repeating the subdivision will eventually locate the ray to a desired tolerance. The Figure 5.3(a) shows three levels of recursion, where the centers of each sub-divided triangle are denoted C_1, C_2, C_3. The general method of subdivision is a reliable technique, used widely in the context of surface intersection algorithms [see Dokken, 1995, for example].

The algorithm starts by estimating the *first entrance pupil*. This is the area (in the x-y plane at the origin) defined by the convex hull of rays that pass through the pupil. This is approximated by casting a finite grid of rays over an area known to be larger than the actual first entrance pupil of the eye. The convex hull of the surviving rays thereby forms an approximation to the first entrance pupil. Using a *delaunay* triangulation and sequentially testing each resultant triangle for *enclosure*, ensures that a large proportion of the entrance pupil is searched.

Figure 5.3(c) illustrates enclosure, where intuitively, the required ray $\mathbf{u}$ appears bounded by the exit ray vectors at the vertices of triangle $P'P_2P_3$. The actual decision rule for enclosure was the following. Suppose, the exit rays have directions given by the unit vectors $\mathbf{u}_1$, $\mathbf{u}_2$ and $\mathbf{u}_3$. Then the vector $\mathbf{u}$ is considered to be enclosed if it can be constructed by "blending" the exit rays via,

$$\mathbf{u} = a\mathbf{u}_1 + b\mathbf{u}_2 + c\mathbf{u}_3 \tag{5.1}$$

where

$$a + b + c = 1 \tag{5.2}$$

and

$$0 \leq a, b, c \leq 1 \tag{5.3}$$

The condition (5.2) is explained by Figure 5.3(b) which shows that the co-ordinates (a, b, c) may be interpreted as the fractional areas of sub-triangles formed by the point P(a,b,c). Therefore all points within the triangle have coordinates (a, b, c) which are positive and less than unity. The code for this algorithm has been included in Appendix E.

The advantage of this method is that it is general, i.e. it can be used to search surfaces such as a VK obtained cornea. There is the possibility that the method can fail, if the cornea

is extremely irregular, or the Purkinje image lies outside of the computed entrance pupil, but these cases should be rare. Naturally, the computation time can be expected to increase in order to handle the complexity of the surface modeled - but this is a surface intersection issue, rather than a surface search issue.

The initial triangle was found by casting 16 rays through the optic system which covered the corneal surface. The incident spot-diagram was found, and a *delaunay* triangulation was constructed from these points. This is a common triangular meshing technique, easily facilitated by MATLAB. It was found that random noise ("fuzz") aided the technique, since the edges of the mesh lay *exactly* on the point being searched for, typically the y-axis. This was due to the exact positioning of the simulated sources, but this should not occur in practice, since noise will naturally cause required points to lie *within* triangle domains.

This method was tested on a DEC-ALPHA running UNIX, and was found to produce sub-micron accuracy $< 10^{-4}$ mm on the image plane in times ranging from 3sec (PI) to 10sec (PIV). At this accuracy, the algorithm ran to about 20 levels of recursion, i.e. 20 extra rays were traced in order to find the best estimate. In addition, the surrounding exit ray vectors could be used to determine the image locations. The algorithm appears adequate, but was not optimized for speed. It is also noted that the algorithm was tested for a telecentric camera model only.

The method searches the *entire* corneal surface using a similar number of rays as Barry et al. [1997a] (i.e. about 21) whilst maintaining reasonable execution times. Provided the corneal surface is smooth, which Doss et al. [1981], Klein [1992] point out is clinically observed for the majority of corneas, the method will successfully complete. The method is based completely on native MATLAB code, and the RAYTRAK toolbox, see Appendix E.

A Linear Model for Recovery of Ocular Parameters

The problem of generating images corresponding to a particular set of ocular parameters is addressed by the method of the previous section. Assuming a linear relationship between these parameters, and the resulting image points (or more importantly, *distances* between these points) is a means of determining the ocular parameters. In particular, by simply inverting the relationship and using actual measurements (e.g. distance between the image points), estimates of the ocular parameters can be found.

This linear modelling method is now described in more detail, including the possibility of many point sources, and many ocular parameters. To start, a *feature* is defined as some scalar function of the image plane points. A feature generalizes the idea of measuring *distances*

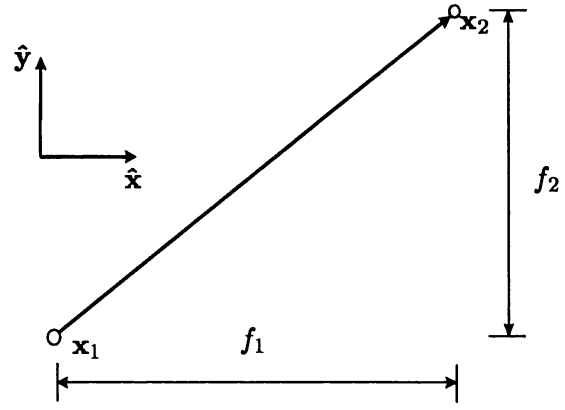

Figure 5.4: The diagram shows the positions of two horizontally oriented sources relative to the center of the image plane co-ordinated system (0,0). The horizontal and vertical components of the displacement vector between the two image points are *features* f_1 and f_2. A linear model will therefore require at least two model parameters in order to yield a unique solution.

between image points. The i^{th} feature may be written,

$$f_i(\mathbf{v}) = F_i(\mathbf{x}_1(\mathbf{v}), \cdots, \mathbf{x}_P(\mathbf{v})) \tag{5.4}$$

where F_i represents the relationship between the model parameters and the i^{th} feature, $\mathbf{v} = [v_1, \cdots, v_N]^T$ are the N model parameters, and $\mathbf{x}_1(\mathbf{v}), \cdots, \mathbf{x}_P(\mathbf{v})$ are the P image plane points. Figure 5.4 gives a simple example with two image plane points $\mathbf{x}_1, \mathbf{x}_2$ (i.e. $P = 2$) where the two features $f_1 = |(\mathbf{x}_1 - \mathbf{x}_2).\hat{\mathbf{x}}|$ and $f_2 = |(\mathbf{x}_1 - \mathbf{x}_2).\hat{\mathbf{y}}|$ are the horizontal and vertical distances between the two points.

Defining a feature vector $\mathbf{f} = [f_1, \cdots, f_N]^T$ and hence, assuming a linear $N \times N$ model matrix $\mathbf{A}$ for the F_i gives,

$$\mathbf{f} = \mathbf{A}\mathbf{u} \tag{5.5}$$

or in inverted form,

$$\mathbf{u} = \mathbf{A}^{-1}\mathbf{f} \tag{5.6}$$

i.e. the model parameters are now a function of the observed features. Each row $\mathbf{a}_j = [a_{j1} ... a_{jN}]$ of the matrix $\mathbf{A}$ is found by using $M \geq N$ observations of model parameters, and linear regression to determine each row of N coefficients. In the cases given here, the number of features were low, i.e. $N \leq 3$, and the number of observations were typically ≤ 30. It was found that a typical fit to the data took from 2 mins (II) to 6 mins (IV), where the major speed limitations were imposed by the non-optimized search method of the previous section. This time increased dramatically with the number of model parameters, but once training was complete, the method was fast.

5.2.3 Method

The method was tested using two point sources, placed at (-50,-50,500) mm and (50,-50,500) mm respectively. The Le Grand schematic eye model was chosen as the basis for the simulation, with the modifications listed in Table 5.1. The anterior cornea was initially chosen to be spherical (case (i)), but was replaced by an ellipsoidal surface with half-axes (7.6,7.8,7.6) mm. This ellipsoid was oriented at 0° (case (ii)) and 30° degrees (case (iii)) to the horizontal. In addition, a videokeratographically obtained anterior corneal surface of the author's own eye was included and tested for the recovery of PIII (case (iv)).

The posterior corneal surface was initially spherical (with radii of curvature r_I) for cases (i)-(iii). The feature (corresponding to the one model parameter) was taken to be the horizontal distance between the PII images of the two source objects, i.e.

$$f_1 = (\mathbf{x}_2 - \mathbf{x}_1).\hat{\mathbf{x}} \tag{5.7}$$

In the case of the spherical posterior surface, the model was fitted to (posterior corneal) radii of curvatures ranging from 6.0 mm to 7.0 mm in steps of 0.05 mm. An R^2 value (of 0.8) was found on fitting this data with the linear model. The fit was subsequently tested by choosing 5 random posterior radii in this range (6 mm - 7 mm), and testing the accuracy of the recovery by recording the absolute errors. This was repeated in the case of the tilted ellipsoidal cornea (i.e. with 30° tilt) which produced equivalent (to 1dp) fitting results ($R^2 = 0.8$).

The tilted anterior cornea was then used with an ellipsoidal posterior cornea (cases (iv)-(v)), with principal axes aligned *with* the co-ordinate system axes (half axes (r_{Ih}, r_{Ih}, r_{Iv}), *and* axes oriented over a moderate range of angles $0 < \phi_{II} < 30$. The range of posterior radii of curvature ranged from 6.2 mm to 6.6 mm (in 0.05 mm steps), which were based on the observations of Tscherning [Le Grand and El Hage, 1980, pg.50].

The choice of features in the case of the ellipsoidal posterior surface with half-axes *aligned* with the axes were,

$$f_1 = \mathbf{x}_1.\hat{\mathbf{x}} - \mathbf{x}_2.\hat{\mathbf{x}} \tag{5.8}$$

$$f_2 = \mathbf{x}_1.\hat{\mathbf{y}} - \mathbf{x}_2.\hat{\mathbf{y}} \tag{5.9}$$

which were the horizontal and vertical displacements of the Purkinje images. In the case of posterior surface half-axes *tilted* with respect to the axes the following features were defined,

$$f_1 = \mathbf{x}_1.\hat{\mathbf{x}} - \mathbf{x}_1.\hat{\mathbf{y}} \tag{5.10}$$

$$f_2 = \mathbf{x}_1.\hat{\mathbf{y}} + \mathbf{x}_2.\hat{\mathbf{y}} \tag{5.11}$$

$$f_3 = \mathbf{x}_1.\hat{\mathbf{y}} + \mathbf{x}_2.\hat{\mathbf{x}} \tag{5.12}$$

Case	Anterior Cornea	Posterior Cornea	Anterior Lens	Posterior Lens
i	Spherical	Spherical		
ii	Ellipsoid at 0°	Spherical		
iii	Ellipsoid at 30°	Spherical		
iv	Ellipsoid at 30°	Ellipsoid at 0°		
v	Ellipsoid at 30°	Ellipsoid (several ϕ_{II})		
vi	VK example	Spherical	Spherical	
vii	Spherical	Spherical	Spherical	

Table 5.1: This table summarizes the conditions under which the method was tested

where these transformations were chosen (in this testing) because of their large R^2 statistics. As a result, these selections did not exploit the relationships between the features and model parameters, and so should not be considered optimal. This would be an area of further investigation.

A spherical Le Grand eye model and videokeratographically obtained surface model were used to illustrate the method for the recovery of anterior lens radius of curvature (via PIII). The feature chosen was that of equation (5.7). PIV was not tested in this application. It was assumed that the distances between the optical surfaces were known i.e. they were measurable by available methods [Garner and Smith, 1996, Dunne et al., 1996], and that the anterior and posterior cornea were centered on the optic axis. In practice, this would be evident from the relative alignment of the PI and PII images.

5.2.4 Results

The results for the five randomly chosen radii of curvature for test cases (i)-(iii) are shown in Table 5.2. The left most column shows the randomly chosen radii, the resultant recovered radii follow to the right. From that table, the recovered spherical posterior cornea radii was found to have a mean absolute error of 0.045 ± 0.032 mm. Using an anterior ellipsoidal surface aligned with the co-ordinate system axes, gave an error of 0.035 ± 0.075 mm, whilst orienting this surface produced errors of 0.017 ± 0.014 mm. Including an extra feature Orienting the surface appeared to improve the fit of the model to the data. The maximum error in estimation could be expected to be 0.11 mm, which was less than 2% of the surface radius. Due to the small change of index of refraction between the cornea and aqueous, this amounted to a maximum surface power error of 0.1 D.

This was an encouraging result, given that the method was chosen for expediency rather than accuracy. Figure 5.2.4 shows the image camera points used to generate the linear model, in the case of the tilted ellipsoid. These points show the 10 different posterior cornea radii, taken in steps of 0.05 mm radii of curvature steps.

A spherical surface and videokeratographically obtained surface was added as the anterior cornea to the Le Grand eye, in order to test the recovery of anterior lens radius using PIII i.e. cases (vi)-(vii). The method nominally used the recovered value R=6.481 mm for the true value of R=6.493 mm (see Table 5.2 for the posterior corneal radius). The method was tested again with good results, see Table 5.3. A mean error of 0.001mm was found for the spherical eye, and an error of 0.007 mm for the video-keratographically obtained eye. This amounted to less than 0.1% of the total radius of the surface, with a total error in surface power of 0.006 D. These were very small errors.

The method was tested for cases (iv) and (v). Table 5.4 shows the results for case (iv), i.e. a tilted anterior cornea, with a posterior cornea with principal axes aligned with the x and y axes respectively. Low error was obtained, with a maximum error of 0.064 mm, which represents a 1% error in estimation of the radii of curvature, or 0.06D in surface power. However, extending the modeling to case (v), where the posterior astigmatism PII was given an orientation ϕ_{II} with $0 < \phi_{II} < 30$, was not successful. Good R^2 values were found i.e. $R^2 = (0.8, 0.8)$ for the radii of curvature, but the tilt angle was not predicted with accuracy. Over a set of five random parameters, the mean absolute errors in R_1 and R_2 were 0.3 ± 0.23 mm and 0.2 ± 0.28 mm respectively, but the error in tilt was much larger, i.e. $1284° \pm 1°$. Apparently, the reason for this failure was that choosing the angular tilt as an independent model parameter was not an appropriate choice given the features.

5.2.5 Discussion

The method was tested for a class of model surfaces, chosen to illustrate recovery of the internal radii of curvature of the posterior cornea and anterior lens. The method appears successful on this class of surfaces, which indicates that further research is justified.

It is is (initially) slow, because it requires calibration on an individual's ocular surfaces. However, this speed issue is certainly a result of the non-optimized surface search routines. One alternative is to assume gross models of the corneal surface i.e. ellipsoidal, or toroidal surfaces. It may be possible to pre-calibrate the method for use on a large population of patients in this case.

Only two points were used. Dunne et al. [1996] measures astigmatism using additional

Theory (mm)	Le Grand Sph (mm)	Le Grand Ast. 0° (mm)	Le Grand Ast.30° (mm)
6.088	6.037	5.920	6.072
6.235	6.198	6.235	6.261
6.493	6.481	6.494	6.485
6.925	7.020	6.923	6.961
6.363	6.336	6.364	6.363
mean error	0.045	0.035	0.017
std error	0.032	0.075	0.014

Table 5.2: Results for the Purkinje II image testing based on the Le Grand eye, with spherical and ellipsoidal anterior corneal surfaces. The theory column shows the actual radii of curvature of the posterior cornea (PII), the other columns show the recovered estimates using the new method. In particular, the first column shows results for a spherical front surface, column two shows results for an ellipsoidal front surface with no orientation, and finally, column three shows an ellipsoid with a 30° orientation.

Theory (mm)	Le Grand Sph (mm)	Theory (mm)	Video-K. (mm)
9.886	9.867	10.142	10.139
10.6645	10.664	10.202	10.198
9.7812	9.781	9.897	9.914
10.6875	10.686	10.350	10.343
10.3249	10.327	10.022	10.020
mean error	0.001	mean error	0.007
std error	0.001	std error	0.006

Table 5.3: Results for Purkinje III images tested using a Le Grand eye with spherical anterior corneal surface, and a video-keratographically obtained surface obtained from the author, added to the Le Grand eye. The theory columns show the actual radii of curvature, the other columns show the recovered estimates.

Theory (mm,mm)	Recovered (mm,mm)
(6.475,6.476)	(6.435, 6.461)
(6.665,6.514)	(6.612, 6.484)
(6.456,6.672)	(6.401, 6.641)
(6.526,6.724)	(6.463, 6.685)
(6.499,6.324)	(6.481, 6.327)
mean error	(0.046, 0.023)
std error	(0.018, 0.015)

Table 5.4: Results for the Purkinje II images using an astigmatic posterior cornea, added to a Le Grand eye with spherical cornea. The ellipsoid has half-axes (r_{Ih}, r_{Ih}, r_{Iv}), so the third ellipsoid parameter is not shown.

point sources. Therefore, the natural progression would be to introduce more points to this method. However, as more parameters are used, the manual process of choosing appropriate features becomes more complicated. Rather than attempting to determine the appropriate features and model variables, a better approach *may* be to employ a neural network. In fact, neural network methods exist [Specht, 1991] which naturally generalize the linear reqression used here.

In analogy with videokeratography, this method represents the most basic of those algorithms (i.e. the algorithm of spherical equivalence). Therefore the method proposed here may be easily implemented, but may have limited applicability. The "smarter" methods of corneal topography may prove applicable to this situation, though the implementation becomes more involved.

To implement a video-keratographic method would require many more sampling points, or a suitable reduction in order of interpolating polynomial. Dunne et al. [1996] mentions that the amount of light due to many light sources causes pupil constriction, which affects the measurable area of lens. However Applegate [1995] points out that it is possible to capture (PI) images over a very short time period, using banks of Light Emitting Diodes (LEDs) timed to emit in series. This may allow image capture over very short time period, i.e. faster than the pupil/eye can respond. An appropriate sequencing e.g. radially toward the center, would allow more time still. However, this would then affect the required exposure times, since Schwiegerling [2000], Le Grand and El Hage [1980] mention that the amount of reflected light from the internal ocular surfaces is small (2 %). It is evident that further research will be required to fully realize the analogy between videokeratography and videophakometry.

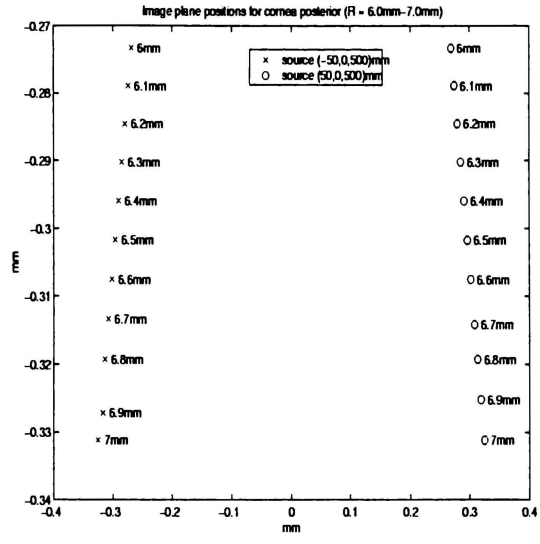

Figure 5.5: The corresponding image plane points are shown here as the posterior radius of curvature changes

An important point is made in mentioning such a device. The Author is not aware of calibration data pertaining to any such a device. That is, the experimental accuracy of other methods is unknown. Therefore, whilst in simulation, this method appears to give low error, it is difficult to compare the ability of this method with the "gold standard". There is certainly a case for constructing a model eye say, and testing such a method on such an eye.

5.2.6 Conclusion

The work of Barry et al. [1997b] was extended, with the capability of tracing skew rays into a meridional camera. The method appeared to be robust, and worked well over the space of parameter values used in this test. The maximum error of tracing was 1×10^{-4} mm with a trace time of $2, 4, 6$ or 8 seconds depending on the Purkinje image required (PI - PIV). The method suggests an improvement over existing techniques for phakometry; a "proof of concept" demonstration was used to illustrate the idea.

In particular, given knowledge of the corneal surface, the radius/radii of the posterior corneal surface and the anterior lens was determined. This was achieved by fitting a linear model to the observed output values, using the surface parameters as the independent parameters. The results were encouraging. The error in recovery was 0.1D and 0.006D (surface powers) for PII and PIII respectively. It is suggested that further research may improve on the method presented here, particularly by employing the methods of videokeratography and producing calibrated data.

5.3 Modeling Lens Tilt and Decenter

5.3.1 Introduction

This section investigates the effect of *lens tilt* (not to be confused with corneal tilt) and *lens decentration* on retinal plane images (see Figure 5.6). The approach taken here is that of Korynta et al. [1999] who evaluate the effect of decenter and tilt by generating synthetic images of the Landolt "C", and describe the resulting effects on image quality subjectively. To that end, synthetic images are tested by visual inspection.

However, this investigation differs by (i) using objective measures of total image quality, and (ii) looking at planes which pass through the focal plane. In the former case, two objective measures are investigated: the *statistical moments* of the spot-diagram and an *image quality metric*, the SQuare Root Integral (SQRI) metric [Barten, 1987]. In the latter case, this analysis reveals that the sign of the displacement from the plane of best focus must be taken into account when considering the effects of tilt and decenter on perceived images. The discussion suggests improvements for the future.

5.3.2 Background

The paper of Korynta et al. [1999] uses subjective evaluation of synthetic Landolt "C"'s in order to verify the work of Atchison [Atchison, 1989a,b]. In those papers, the aim is to determine optimum spectacle correction at the cornea [Atchison, 1989a], and to provide objective measures for image quality assessment [Atchison, 1989b]. However, one aspect of this testing is that the *subjective* ability of the observer to detect images is not addressed. This means that the extent to which the changes in the PSF are noticeable is largely unknown.

However, it is also true that methods exist whereby the ability of the Human Visual

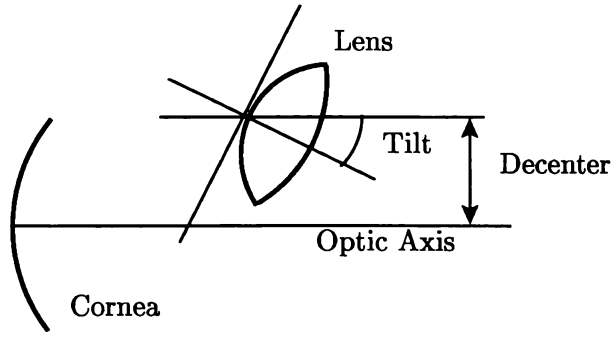

Figure 5.6: Lens tilt and decenter. Tilt (as used here) is the angular displacement from the horizontal. Negative tilt is a clockwise rotation of the lens about the front surface apex, whilst positive tilt is an anti-clockwise rotation. Positive decenter is a displacement in a transverse direction above the optic axis, and is the only decenter considered here.

System (HVS) to identify/evaluate images presented may be estimated. These are the (i) model observer approach and the (ii) image quality metric approach. In the former method, the processing structures of the eye (e.g. the retina) are modeled ([for example Barrett et al., 1993, Watson, 1987, Jackson et al., 1997]); whereas in the latter method, the performance of the eye is determined by over-all system measures, i.e. typically the combined MTF of the entire eye/VDU system.

An important difference between these two approaches is that the intention of the model observer is generally to *identify* a particular signal, e.g. to identify the letter "E" in the given image [Watson and Fitzhugh, 1989], whilst in the latter, the intention is to get an over-all measure of image quality independent of the stimulus [Rohaly et al., 1995]. It appears that the actual content of an image is not an important factor in *total* image quality assessment [Barten, 1999].

A number of such metrics for this purpose are reviewed in Barten [1999], namely the Modulation Transfer Area (MTFA) due to Charman and Olin [1965], Snyder [1973] (which according to Gerfelder and Miler [1994] has been the American image quality standard since 1988), Integrated Contrast Sensitivity (ICS) [van Meeteren, 1973], Subjective Quality factor (SQF) [Granger and Cupery, 1972], Discriminable Difference Diagram (DDD) [Carlson and Cohen, 1972] and SQuare-Root Integral (SQRI) [Barten, 1987]. These are equations of generic form,

$$J = \int j(u) d(\ln u) \tag{5.13}$$

where u is spatial frequency, and the units of J are jnds or *just noticeable differences*[2]. The integration with respect to $d(\ln u)$ in equation (5.13) arises from the observation of Granger and Cupery [1972] that subjective image quality is weighted inversely with u. The function $j(u)$ depends on the metric used, and are summarized in Table 5.5. From this table it can be seen that the MTFA is the area difference between the modulation threshold and the MTF, the ICS is the weighted area under the "threshold normalized" MTF[3]. The SQF is the weighted area under the MTF, whilst the SQRI is the weighted area under the square root of the "threshold normalized" MTF.

Barten [1999] has shown that the SQRI metric improves on the other metrics mentioned. This is justified by the experimental observation that there is a linear correlation

[2]A jnd is a unit of perceptual difference. If the modulation of a sinusoidal grating is changed until it is just noticeably different from its original modulation, then 1 jnd has been subtended. The actual modulation difference subtended depends on the absolute modulation according to *Weber's Law*. This law states that the modulation difference δm is given by $\delta m = 0.05m$, where m is the absolute modulation.

[3]i.e. the MTF is normalized by the modulation threshold m_t, see Appendix F for details

Metric	$j(u)$
MTFA	$j(u) \propto (MTF(u) - m_t(u))u$
ICS	$j(u) \propto MTF(u)/m_t(u)$
SQF	$j(u) \propto \frac{1}{ln4} MTF(u)$ for 3 cyc/deg $< u <$ 12 cyc/deg
DDD	n/a
SQRI	$j(u) = \frac{1}{ln2}\sqrt{MTF(u)/m_t(u)}$

Table 5.5: The functions which define the metric used. Here $m_t(u)$ is the modulation threshold, the minimum modulation required for resolution of a grating of spatial frequency u (see Appendix F for example). The result of the DDD is a map rather than a single value, so it does not apply.

between the number of jnds in an image, and the square root of the normalized modulation $\sqrt{MTF(u)/m_t(u)}$. In addition, the natural units of the SQRI are jnd's, whereas the original units of the other metrics are not. Therefore, the other metrics (except for the DDD) are not in perceptual units. Pappas and Safranek [1999] agree that the SQRI performs well under restricted circumstances. Gerfelder and Miler [1994] use the SQRI and point out that a 3 jnd difference between an image and the original is a significant distortion, while 10 jnds is a substantial departure. A jnd of < 1 is un-noticeable. The explicit SQRI metric follows,

$$SQRI = \frac{1}{ln2} \int_{u_{min}}^{u_{max}} \sqrt{\frac{MTF(u)}{m_t(u)}} \frac{du}{u} \tag{5.14}$$

which will now be adopted as the measure of perceptual image quality.

Statistical Moments

In order to quantitatively identify shape changes in the PSF, *statistical* descriptors of the distribution, i.e. the central moments of the spot-diagram distribution, were computed. These descriptors were used to estimate the position of/size of the geometric blur-disc, astigmatism and coma, by way of the mean, standard deviation, skew and peakedness(kurtosis) of the PSFs. In particular, for the mean,

$$\mu = \langle x \rangle \tag{5.15}$$

for the standard deviation,

$$\sigma = \left\langle (x - \mu)^2 \right\rangle \tag{5.16}$$

The skewness indicates the degree of asymmetry in the distribution, and is given by

$$\mu_2 = \frac{\langle (x - \mu)^3 \rangle}{\sigma^3} \tag{5.17}$$

The sign of the skewness is negative if the distribution has many points to the left of the mean, a positive skewness has most points to the right of the mean. Any symmetric distribution will have zero skewness. The skewness is a measure of *coma*. The kurtosis is given by,

$$\mu_3 = \frac{\langle (x-\mu)^4 \rangle}{\sigma^4} \tag{5.18}$$

and is a measure of the peakedness of a distribution, and therefore indicates the concentration of rays in the spot-diagram. From the discussion in section 2.3.2, the effect of the de-focus is to increase the geometrical size of the blur-disc. This may be quantified by the standard deviation of the distribution. The astigmatism may be quantified by the *aspect ratio*, i.e. the ratio σ_x/σ_y respectively. Finally, the coma may be quantified by the skewness. The kurtosis does not have a direct analogy in optics. Note that, the kurtosis and skew used in this investigation were re-defined from equations (5.17) and (5.18) to give,

$$\mu_2' = \left\{ \frac{\langle (x-\mu)^3 \rangle}{\sigma(0,0)^3} \right\}^{1/3} \tag{5.19}$$

$$\mu_3' = \left\{ \frac{\langle (x-\mu)^4 \rangle}{\sigma(0,0)^4} \right\}^{1/4} \tag{5.20}$$

so that the results would be relative to the spot-diagram produced by assuming zero tilt and decenter, i.e. (tilt, decenter) = (0,0). Taking the third and fourth roots in equation (5.19) and (5.20) respectively ensured the values obtained would span roughly one order of magnitude. For convenience, equations (5.19) and (5.20) will still be referred to as skew, and kurtosis, but should be understood to be modified.

5.3.3 Method

The eye model chosen was the Le Grand eye model (see Appendix A). Spot diagrams were generated over the model parameter space found by varying the tilt from -5.0° to 5.0° in steps of 2.5° combined by varying the decenter from 0 mm to 0.8 mm in steps of 0.2 mm. In this testing, this led to a set of 25 different (tilt, decenter) parameter combinations. Spot-diagrams were also computed for three focal planes (displacement ±0.1 mm and 0 mm from best focus, giving a total of 75 combinations of (tilt, decenter, focal plane) values.

The lens parameters were chosen to model a commercially available IOL lens, and the details, i.e. surface radii, index of refraction and lens thickness were taken from the lens information sheet. The image plane was set at 24.15 mm behind the anterior cornea, which coincided with the plane of best focus.

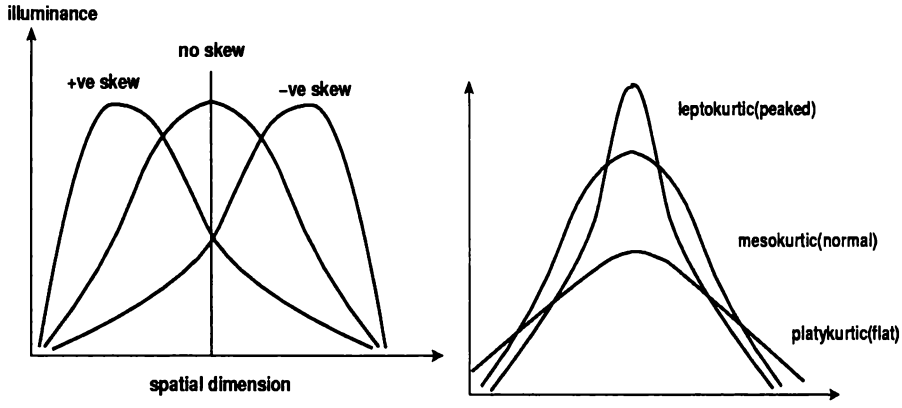

(a) Skewness (b) Kurtosis

Figure 5.7: (a) A negative skew indicates the data is spread out to the left, a positive skew indicates the data is spread out to the right. Any symmetric distribution has no skew (b) Kurtosis is a measure of peakedness. A normal distribution has a kurtosis of 3 (mesokurtic), a peaked distribution has kurtosis greater than 3 (leptokurtic) and a flat distribution has kurtosis less than 3 (platykurtic).

Spot diagrams were generated using a grid of 50 × 50 rays. The statistical moment measures of the raw spot diagrams were taken in order to assess the resultant shape of the PSF. The geometrical spot size was then used as an indicator of image quality.

The spot diagram information was used to compute the geometrical PSFs. These were found by taking the density of rays over a grid of retinal cells of size 0.003 mm ×0.003 mm. The MTF of the resulting PSF was computed by taking the (normalized) magnitude of the FFT, which was then weighted by the diffraction limited PSF [Smith, 1966]. The resulting MTF was then used to compute the SQRI for the combinations of model parameters tested. The actual SQRI was measured for all combinations tested, but the differences ΔSQRI from the standard were taken to highlight the change in *image quality* against the standard reference condition (i.e. best focus with no tilt and no decenter). The data was arranged to show the effect of image quality with image plane held constant. This approach was in contrast to Korynta et al. [1999] where tilt was held constant, and decenter and focal plane were varied. The aim in case, was to simulate the possible range of images observed, with target fixed at constant distance. Finally, synthetic images of the letter "E" were generated, as a means of verifying the objective results obtained. These were prepared by magnifying the letter to 50 × 50 pixels, so that the coarseness of the retinal sampling would not be evident.

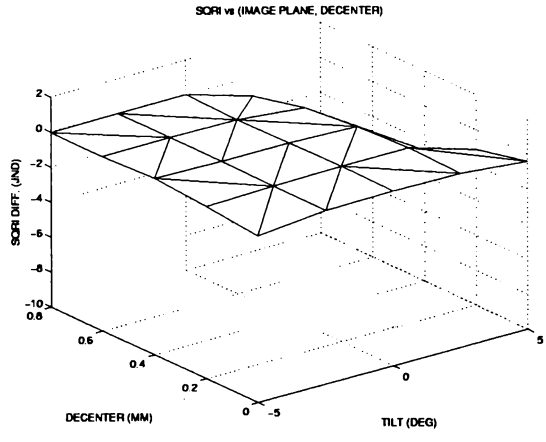

(a) SQRI values for best focus

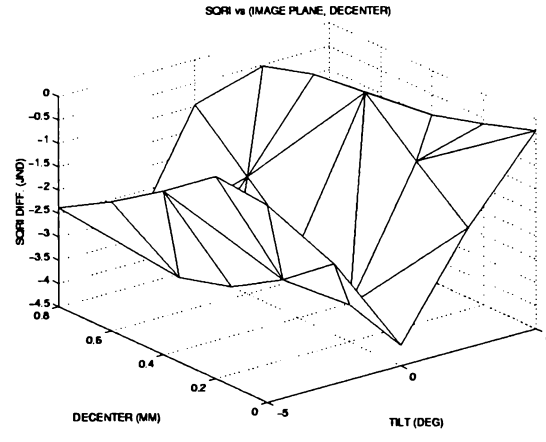

(b) ΔSQRI values for -0.1mm

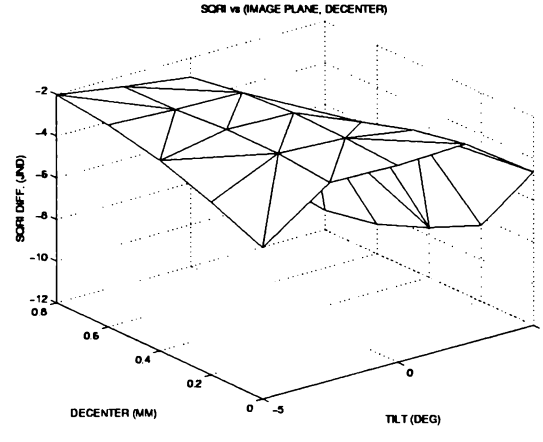

(c) ΔSQRI values for +0.1mm

Figure 5.8: The above diagrams summarize the image quality of the system as a function of tilt and decenter at three image planes (a) The image quality at the position of best focus (relative to SQRI(0°, 0mm)) (b) ΔSQRI, the difference between the reference surface and SQRI values computed at -0.1 mm from best focus (a) ΔSQRI for the case where the image plane is displaced +0.1 mm from best focus.

5.3.4 Results

Testing with Focal Plane Held Constant

Figures 5.8(a)-5.8(c) summarize ΔSQRI, the SQRI values relative to SQRI(0°,0 mm). Inspection of Figure 5.8(a) shows that the magnitude of the SQRI is generally < 1 jnd, indicating that image quality is not significantly affected by tilt and decenter in this case (i.e. in the plane of best focus). The important exception to this observation, is the case where anti-clockwise tilt (i.e. $t = 5°$) combines with increasing decenter (≥ 0.2 mm) to cause significant differences ranging from -3 jnd to -8 jnds below zero (approaching severe degradation). This asymmetry only becomes apparent for anti-clockwise tilt of the lens, combined with increasing decenter.

Figures 5.8(b) and 5.8(c) show that the variation of image quality over the image plane, depends on the sign of the displacement from the plane of best focus. The former has a "V" (valley) shape over the tilt dimension, the latter is an inverted "U". The latter (i.e. Figure 5.8(c)) appears to be an exaggerated version of the best focus case i.e. a generally constant (but in this case noticeable at ≈ -2 jnd) ΔSQRI, with the exception of anti-clockwise tilt combined with decenter. In this case the image degradation tends from -5 jnd to -10 jnd (for $t = 5°$).

The ΔSQRI values for Figure 5.8(b) indicate that imaging *improves* (i.e. relative to the "no tilt" case, for a -0.1 mm displaced image plane), irrespective of the sign of tilt. This is evident by the "V" (valley) shape over the tilt dimension. In addition, the image quality is improved with clockwise tilt (i.e. $t = -5°$) over anti-clockwise tilt (i.e. $t = 5°$). Comparing with Figure 5.8(c) again, shows the sign of the displacement from best focus has an important influence on subjective image quality.

Visual inspection of synthetic images (see Figure 5.9 - 5.11) was used to check whether these observations were *consistent* with subjective observations. In this case, good imaging was inferred by subjectively comparing the reference "E" (i.e. found by setting $t = 0, d = 0$ at the point of best focus) and the candidate "E" (for a given (tilt,decenter) pair). The meaning of "good" was determined primarily by the size of the letter. If a letter was of a comparable size to the reference, then the next criteria was the sharpness of the letter.

It appeared that visual inspection (under these criteria) confirmed the predictions of the SQRI metric values. Figure 5.9 shows the asymmetry in the image quality with tilt, where the "E"'s generated with anti-clockwise tilt (positive tilt) are obviously smaller than those with clockwise tilt (negative tilt). Interestingly, the corresponding SQRI values are relatively constant and small (i.e. $<$ 1jnd) for anti-clockwise tilt, indicating that any subjective differences

seen in the prepared images are not experimentally noticeable differences.

The images in Figure 5.10 are of comparable size to those in Figure 5.9, but are not easily identifiable as letter "E"'s. Therefore, the images are subjectively worse than in the plane of best focus. However, in line with the expected improvement in imaging with tilt (regardless of sign) the "E"'s in Figure 5.10 are larger for non-zero tilt, indicating that the imaging is better under these conditions (relative to best focus).

The images in Figure 5.11 are consistently smaller than those in the previous figures, so that the imaging is consistently worse in all cases at this displacement from best focus. If the letters are of comparable size, then it is certainly true that Figures 5.11 are more difficult to identify. This again is consistent with the observation that imaging was consistently worse than for the other two cases.

Spot Diagram Analysis by Moments

Figures 5.12 - 5.14 show corresponding spot-diagrams for the plane of best focus, followed by spot-diagrams for the displaced planes (-0.1 mm, 0.1 mm). The observations common to all three diagrams are that (i) with no decenter, tilt appears to increase the coma-like aberration (ii) increasing decenter tends to compensate the coma-like aberration when $t < 0°$ but increases skew when $t > 0°$ (iii) the compensation/skew (depending on the sign of the tilt) increases as decenter increases.

Figures 5.12 and 5.14 are similar in appearance, so that displacing +0.1 mm simply appears to increase the size of the PSF as might be expected. The coma-like aberration varies with tilt and decenter in a similar fashion in both cases. However, the results in Figure 5.13 are subjectively different. In this case, the most apparent feature of the spot-diagram is an 8-10 μm blur circle, which (in the case of $t > 0°$) becomes both increasingly skewed and astigmatic with decenter.

These subjective observations are supported quantitatively by Figures 5.15 - 5.17 where the moment measures summarize the shape of the spot-diagrams. Figure 5.15(b) shows that the skew (coma-like aberration) quickly becomes positive with tilt at $t = -2.5°$. This positive skew increases rapidly as a function of increasing tilt. The distribution also flattens and astigmatism increases when anti-clockwise tilt combines with decenter. The results of Figure 5.11 are similar to 5.9, the main differences being that skew and kurtosis are reduced, and the standard deviations of the distributions are increased. This suggests that the imaging is affected by the increased blur circle, produced by shifting to this new image plane.

Figure 5.10 is quantitatively different from the previous cases. In particular, the standard

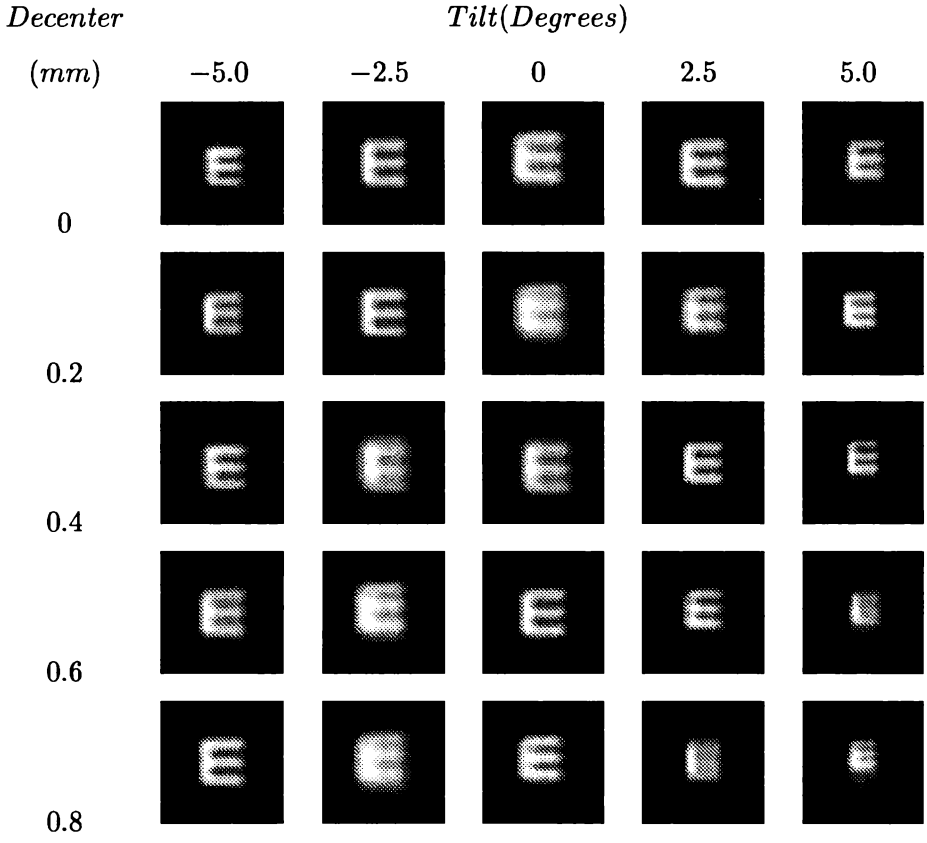

Figure 5.9: Synthetic images generated at the plane of best focus (24.15 mm), varying decenter from 0 to 1.0 mm (0.2 mm steps), and tilt from -5° to 5° in 2.5° steps. This diagram shows the subjective asymmetry caused by the combination of non-zero decenter with tilt i.e. the left hand columns are easier than the right hand columns to identify.

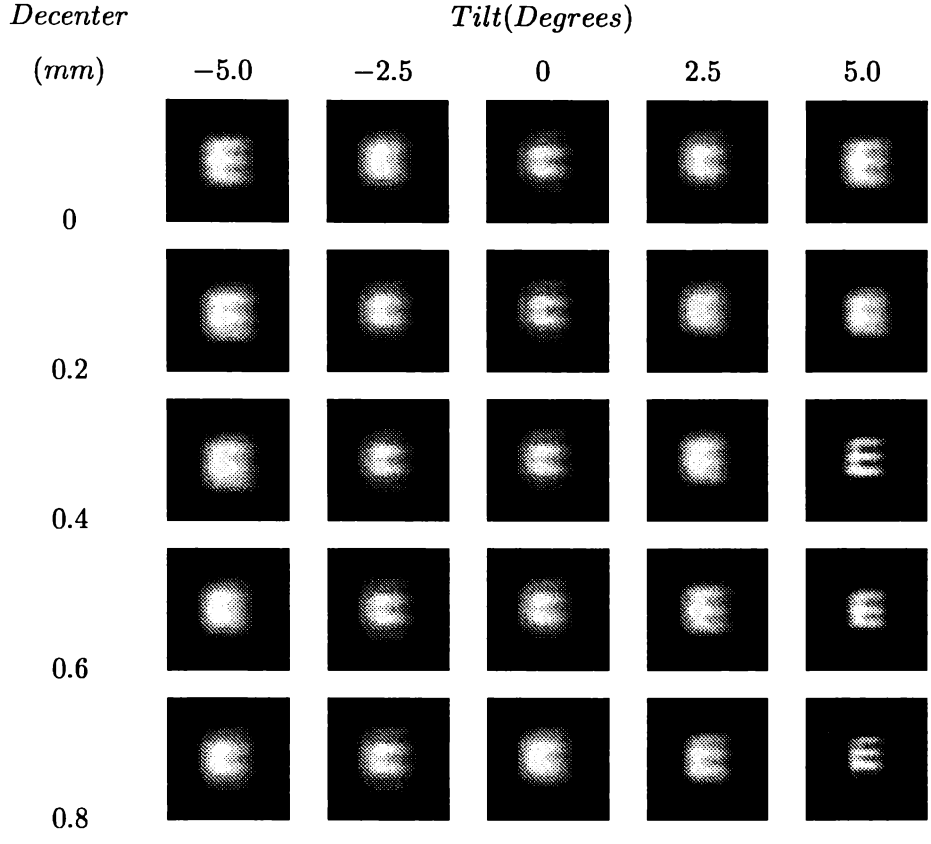

Figure 5.10: Synthetic images generated -0.1 mm from the plane of best focus (24.04 mm), varying decenter from 0 to 1.0 mm (0.2 mm steps), and tilt from -5° to 5° in 2.5° steps. In this case, the images are of subjectively similar size (to those with no tilt). However, the identification of the images is easier, with the addition of tilt (regardless of the sign). Therefore, the imaging can be expected to improve, with the addition of tilt (regardless of sign).

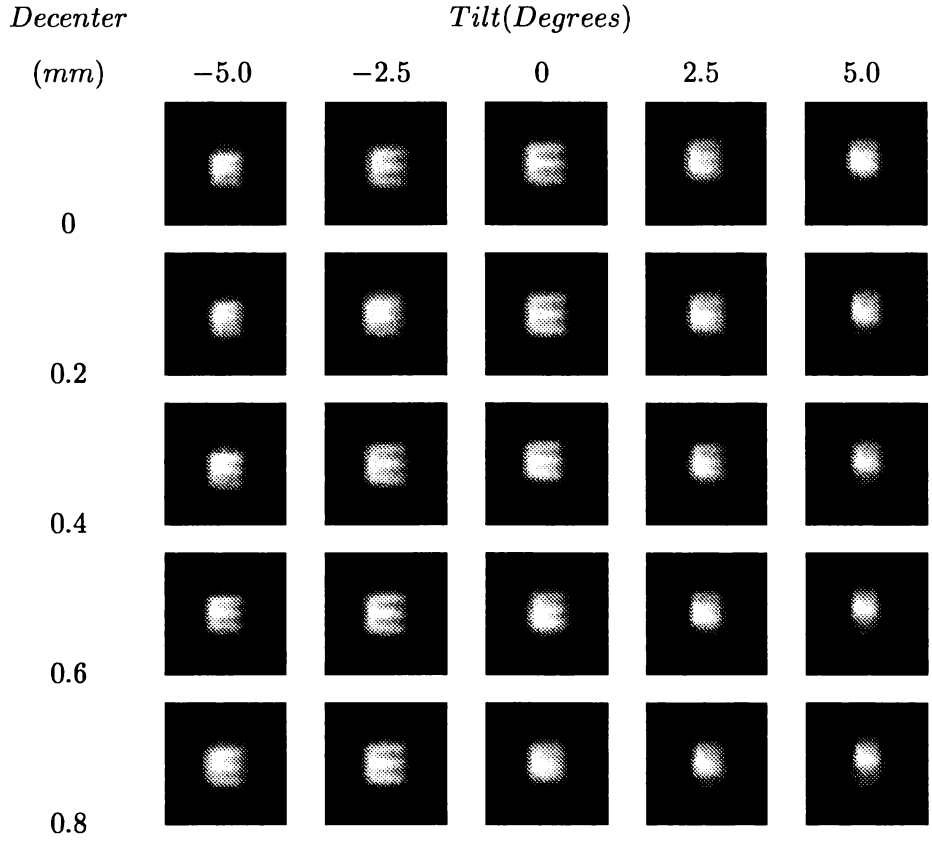

Figure 5.11: Synthetic images generated at a plane +0.1 mm from best focus (24.25 mm), varying decenter from 0 to 1.0 mm (0.2 mm steps), and tilt from -5° to 5° in 2.5° steps. This case is similar to the best focus case, in that there is an apparent asymmetry in the subjective images. In particular, for clockwise tilt (negative tilt values) the images are somewhat larger than for the anti-clockwise tilt (positive tilt) counterparts. However, these images are consistently smaller (and therefore worse) than in the best focus plane.

deviation curves show that the astigmatism has changed into the horizontal plane. In addition the blur circle is elevated, whilst the kurtosis and skew are depressed.

An interesting observation is that skew and kurtosis are largest in the case of best focus, yet the image quality is not adversely affected. The likely reason for this is that there is a dense central core of rays, which subserves the imaging, even though the skew may be large. This appears to suggest that the displacement from the plane of best focus (which increases the size of the blur spot) is the major factor in determining image quality. The worst imaging results occur in cases where the skew and kurtosis are relatively small, but the geometric spot size is larger relative to that found in the plane of best focus.

5.3.5 Discussion

There is evidence that the SQRI is well suited to determining total perceived image quality. However, experimental verification should be carried out to verify the results presented here. A direct approach would be to measure a patient with decentered and tilted IOL, using the pre-operative data for the axial length of the eye, combined with measurements of the tilted and decentered IOL (determined via methods described in the first section of this chapter).

One possible alternative solution would be to move a target across the visual field of an eye with known dimensions. An IOL patient could be used for example. Subjective comparison of presented targets with image quality results would then verify the applicability of the SQRI metric. This would then provide evidence for the validity of the results found in this case.

Assuming a model distribution is a means of attributing meaning to the values obtained. Using the normal distribution in equations (5.20) gives a kurtosis of 3. Values higher than this indicate the distribution is less peaked, or spreads out relative to the normal distribution. A value less than 3 indicates the distribution is peaked (relative to the normal distribution). Similarly, substituting the normal distribution in (5.19) gives zero. A negative skew indicates the data is spread out to the left of the mean, whilst a positive skew indicates a spread to the right. In fact, any symmetric distribution has zero skew. The quantities defined above are summarized in Figure 5.7. The equations (5.15)-(5.20) are 1-dimensional, so these equations are applied to the x and y co-ordinates separately.

Replacing an optically relevant standard, such as the Airy function (physical optics) or a step-function (geometrical optics) in equations (5.15)-(5.20) is a possible improvement over the normal distribution, as a means of obtaining intuition about the shape of the PSF. However, these alternatives were not investigated. This was primarily because the combination of the SQRI image quality metric and these statistical moment measures could answer the

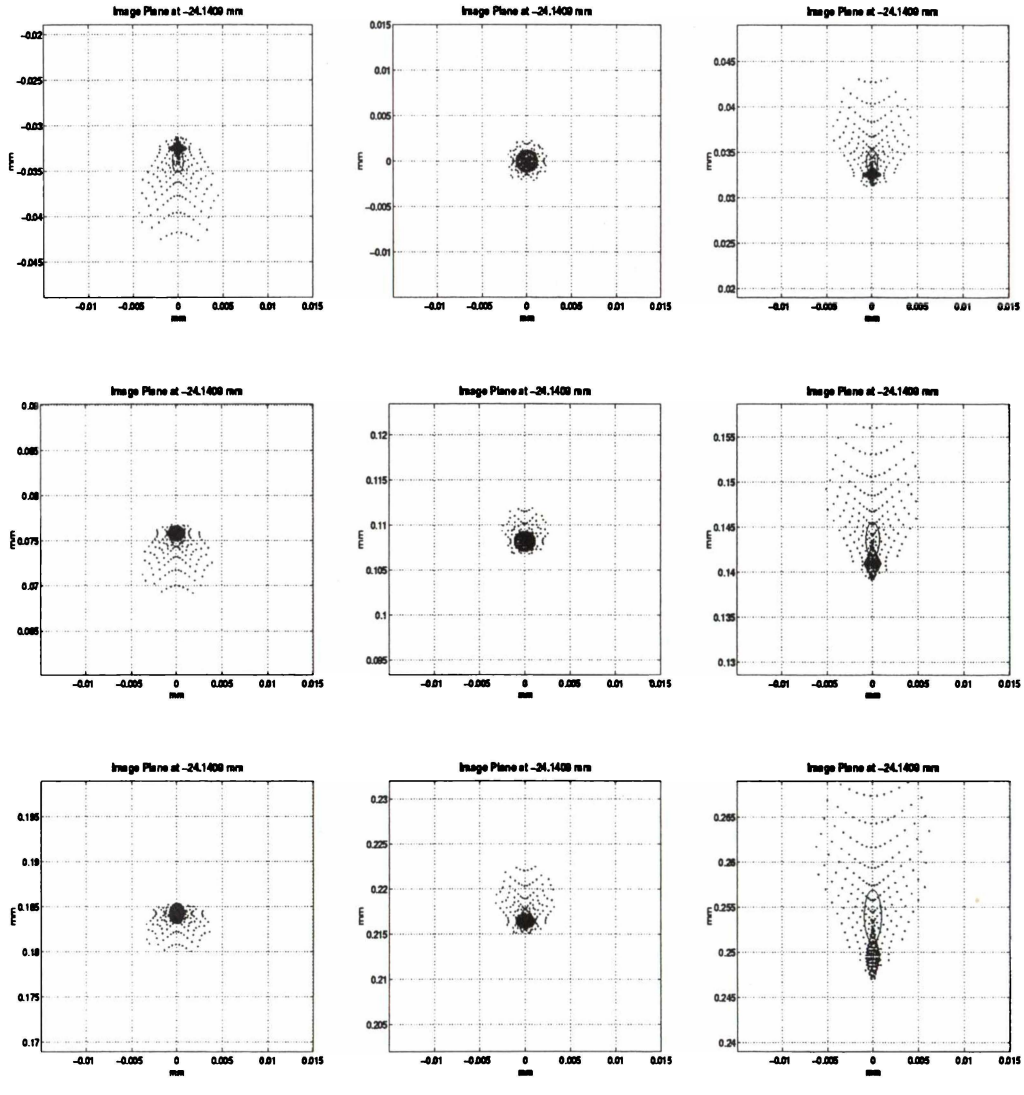

Figure 5.12: Spot diagrams for the plane of best-focus, show the effects of decenter and tilt in this plane. The figures show the spot-diagrams generated, where tilt goes from negative to positive across the columns, whilst decenter increases with the row. The main effect of decenter is to increase the skew, whereas tilt will compensate for or compound existing skew (caused by the decenter) depending on its sign. For example, in this case, clockwise (negative) tilt will compensate for skew, whilst anti-clockwise (positive) tilt will compound the skew.

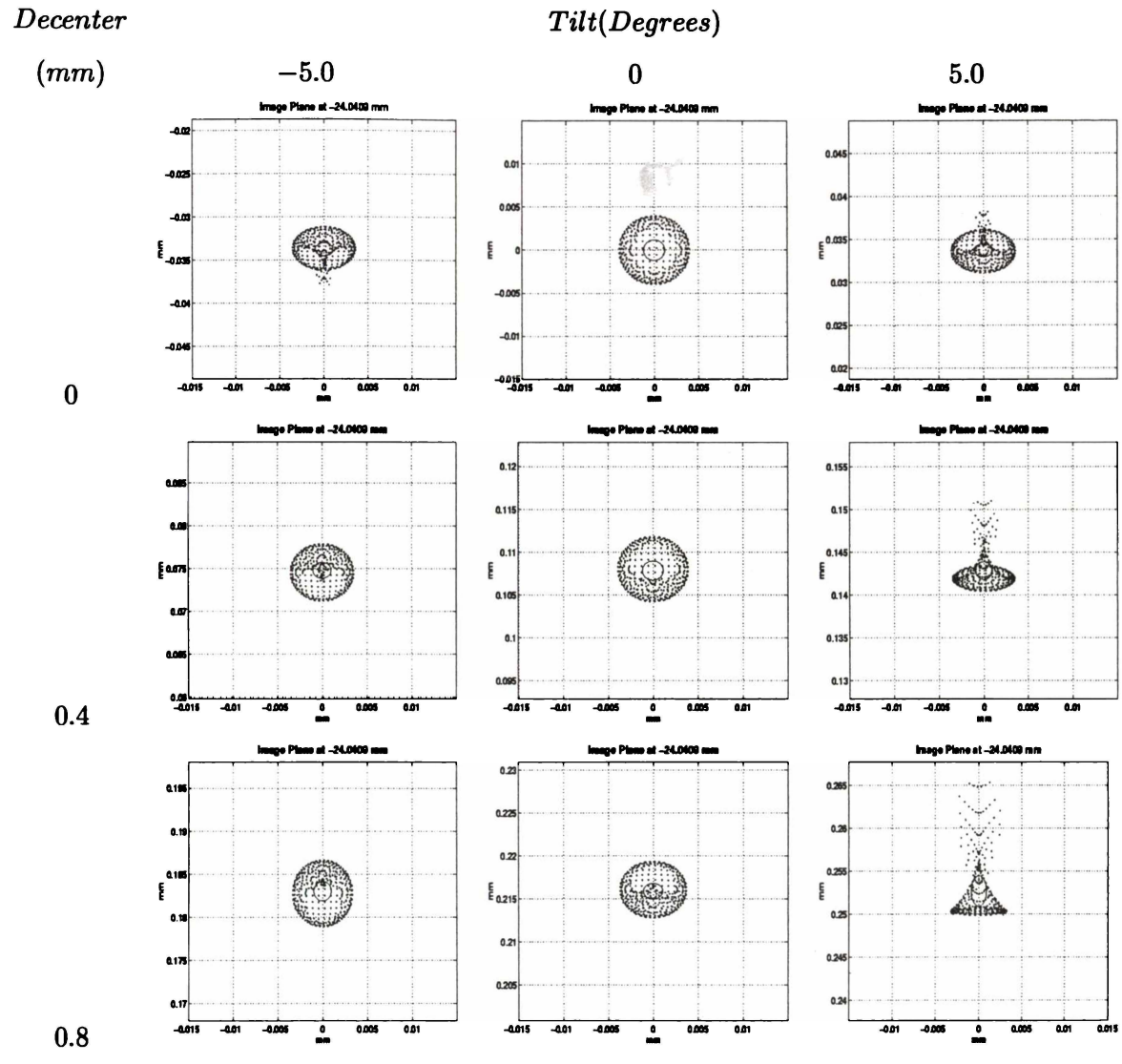

Figure 5.13: Spot diagrams -0.1 mm from the plane of best-focus, showing the effects of decenter and tilt. In this case, there is an asymmetry in the diagrams (as for the case of best focus), but the spot-diagrams (for zero and clockwise tilt) are dominated by a blur circle (roughly 5μm radius). In fact, the rays remain concentrated in this blur circle in all cases. However, in the case of anti-clockwise tilt, the blur circle takes an astigmatic shape, combined with a skewed tail.

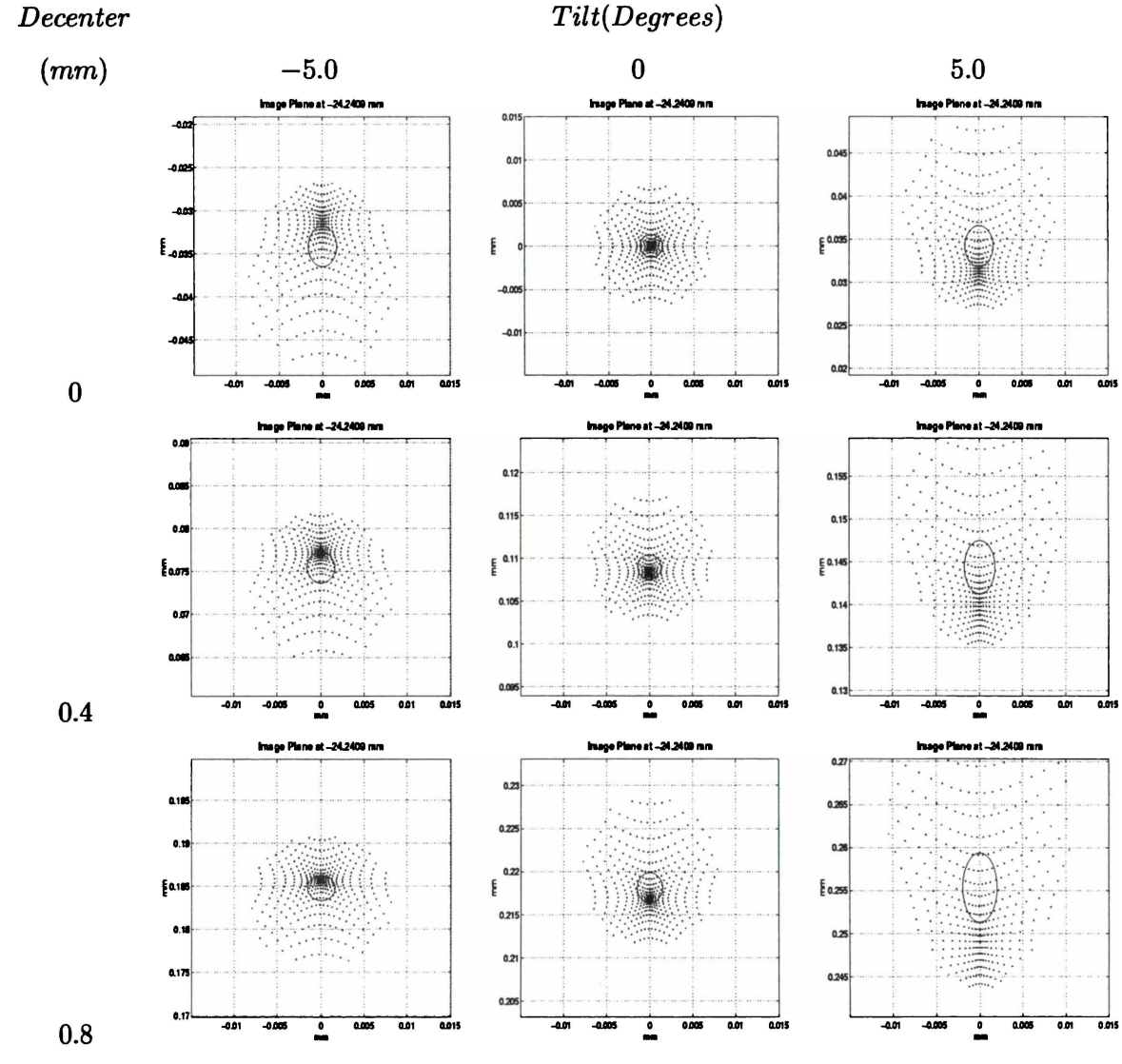

Figure 5.14: Spot diagrams generated +0.1 mm from the plane of best-focus, showing the effects of decenter and tilt. The spot-diagrams are similar in appearance to those found for best focus, but in this case, the spot-diagrams are spread out over a larger area.

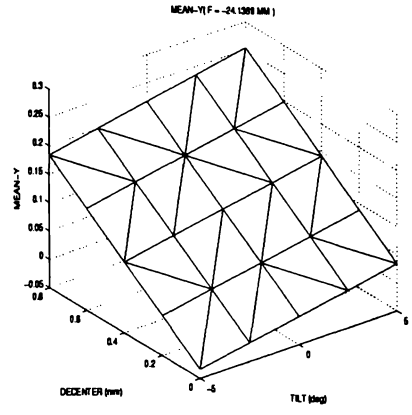

(a) Y-Mean

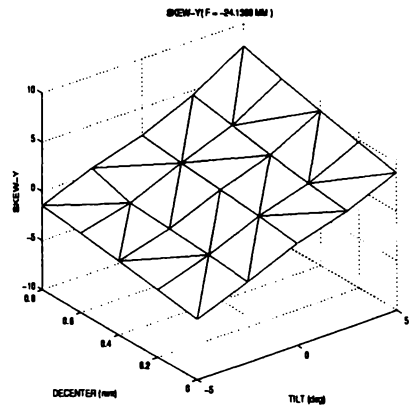

(b) Y-Skew

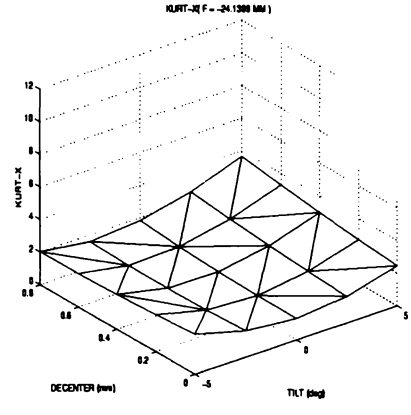

(c) X-Kurtosis

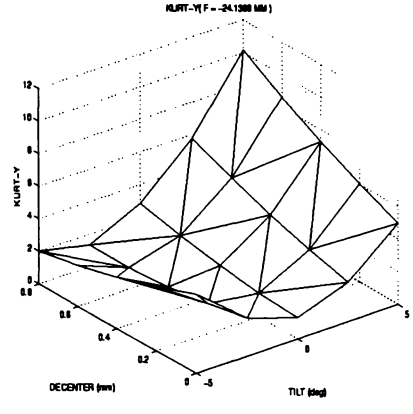

(d) Y-Kurtosis

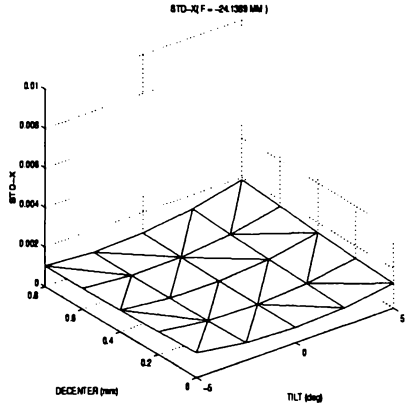

(e) X-Std

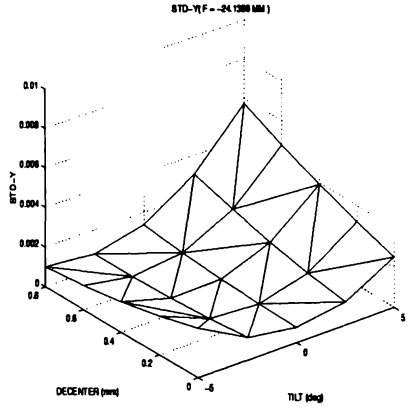

(f) Y-Std

Figure 5.15: Statistics summary at the plane of best-focus. The spot diagram information is summarized by plotting spot-diagram statistics over the (x-y) plane.

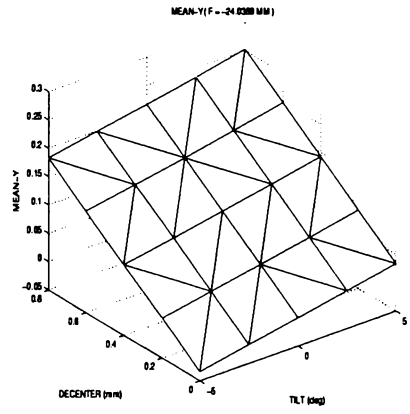

(a) Y-Mean

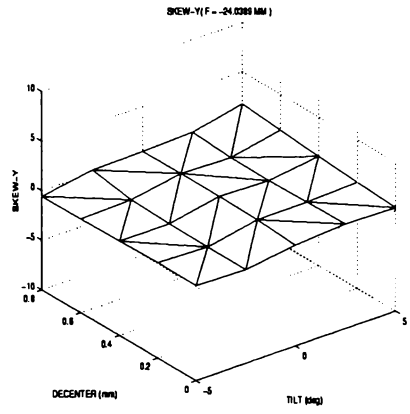

(b) Y-Skew

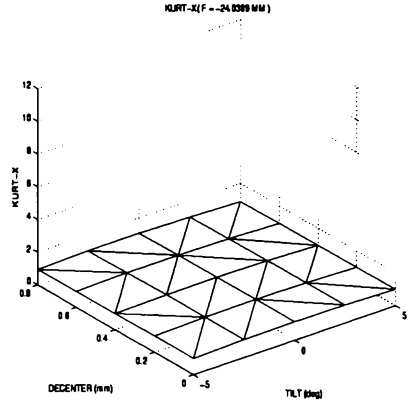

(c) X-Kurtosis

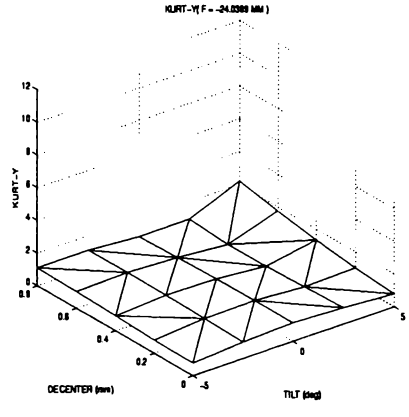

(d) Y-Kurtosis

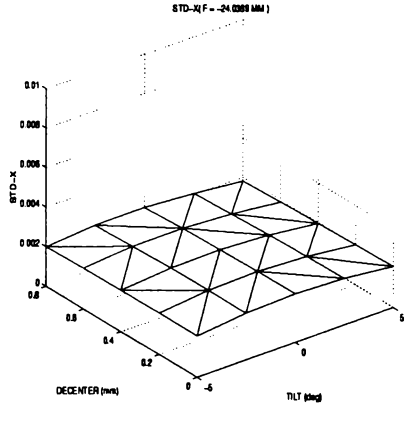

(e) X-Std

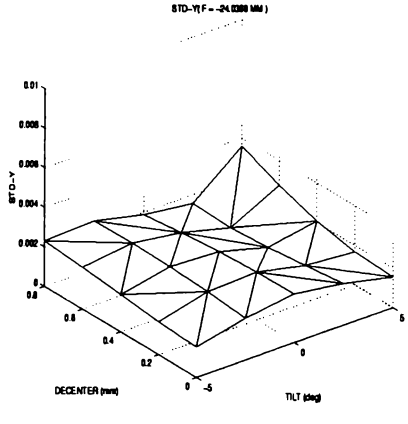

(f) Y-Std

Figure 5.16: Statistics summary -0.1 mm from the plane of best-focus. The spot diagram information is summarized by plotting spot-diagram statistics over the (x-y) plane.

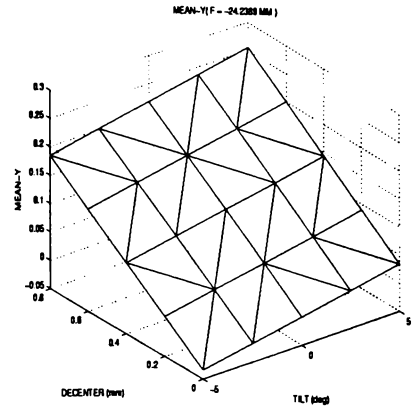

(a) Y-Mean

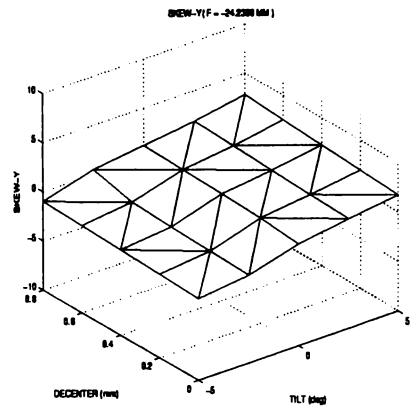

(b) Y-Skew

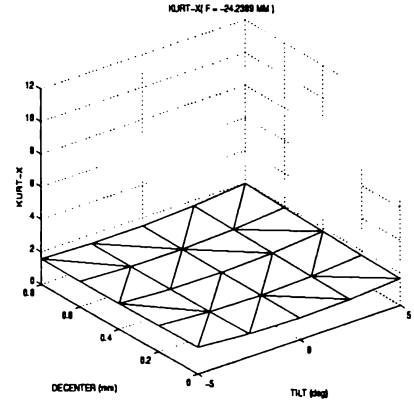

(c) X-Kurtosis

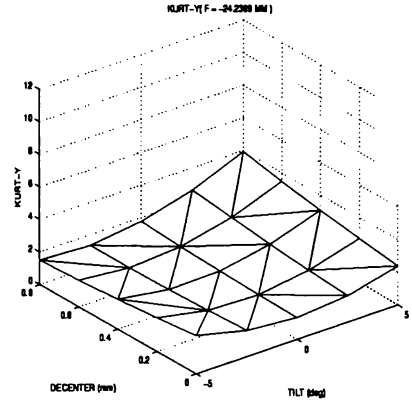

(d) Y-Kurtosis

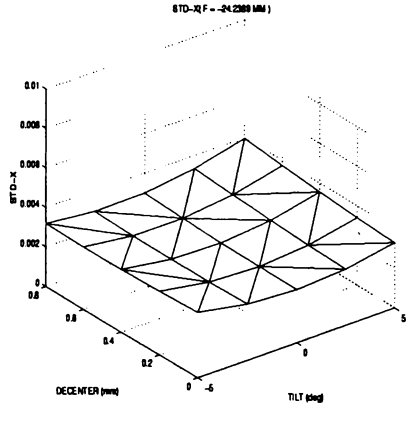

(e) X-Std

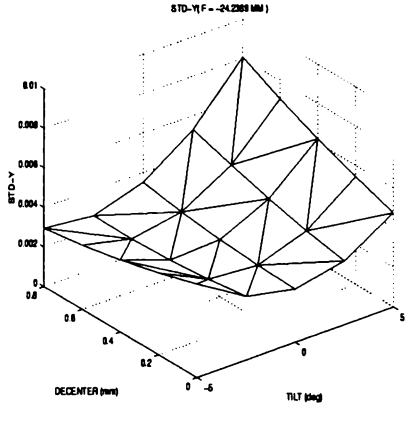

(f) Y-Std

Figure 5.17: Statistics summary +0.1 mm from the plane of best-focus. The spot diagram information is summarized by plotting spot-diagram statistics over the (x-y) plane.

question: "how much skew/kurtosis is too much?". This question was more important than the question: "what is the value of the skew/kurtosis relative to the standard distribution".

5.3.6 Conclusion

A framework for modeling the effect of IOL tilt and decentration was presented. A perceptual image quality metric, the SQRI, was used to model the decision process of an observer, which incorporated the geometrical MTF and the modulation threshold. The metric implied that decenter compensated for the addition of anti-clockwise tilt, but that it degraded imaging when tilt was clock-wise. The degradation became noticeable for $t = 5°$ but remained under 10 jnds.

This observation was also supported by subjective evaluation of synthetic images. Displacing the image plane produced results which were similar in the case of +0.1 mm, but which differed in a plane -0.1 mm (from best focus). Therefore, the position of the image plane was an important factor in deciding the form of image quality.

The underlying causes of the given image quality were attributed by way of statistical moment measures. It was observed that the tilt introduced skew in the spot-diagrams, which was compensated by the addition of decenter. An unexpected result was that these moment measures did not correlate with the image quality in all cases. In particular, it was found that the skew in the plane of best focus was larger in the other cases, but this did not significantly affect the image quality. The most probable explanation for this occurence is that there was a high concentration in energy, combined with a tailed distribution.

The statistical measures are presented as a means of gaining intuition about the role of lens tilt and decenter on the shape of the PSF. The SQRI provides intuition as to how the observer perceives these changes.

Chapter 6

Clinical Verification of a Pseudophakic Eye Model

6.1 Introduction

This chapter describes clinical testing of the eye modeling methods developed in this thesis. The testing involved modeling of two eyes, using videokeratographically measured corneal surface dimensions, ocular biometry (i.e. axial length, lens position) combined with implanted IOL lens information (lens radii of curvature, thickness, refractive index).

The testing of the model was approached in two ways: (a) by modeling the effect of spectacle correction on the observed uncorrected astigmatism and defocus, and (b) by measuring the ability of the Human Visual System (HVS) to resolve sinusoidal gratings via the Contrast Sensitivity Function (CSF). In method (a) the model was tested for *consistency* with the clinically measured refraction (i.e. astigmatism and de-focus) by preparing spot-diagrams and observing the resultant plots. The orientation of the PSF at the manually determined principal focii were measured, and compared with the clinically measured keratometry values (i.e. the principal radii of the anterior corneal surface and their orientation). The effect of the clinically prescribed spectacle correction was then modeled, and the resultant effect on the spot diagrams was observed for consistency with the experimentally measured correction.

As an objective test, a MATLAB program was written, which modeled the process of *refraction* i.e. the *subjective* process of prescribing spectacles by using test lenses and the reports of the patient. A range of sphero-cylindrical lenses[1] were added to the eye model and the lenses minimizing the RMS spot size at the retinal plane were used to infer the best

[1]Spectacle lenses with spherical front surface and cylindrical back surface are called sphero-cylindrical lenses. These lenses have two powers in perpendicular principal planes, which are used to eliminate astigmatism

correction (as used by Klonos et al. [1996]). These results were then compared with the prescribed lenses, which were clinically found to give near optimal performance on a Snellen visual acuity test (i.e. gave better than normal vision (6/6) in both eyes). In the (b) set of tests, attention was turned to the inclusion of the Human Visual System (HVS), by using the Contrast Sensitivity Function (CSF) . The CSF tested the discrimination of (near/exactly) vertical sinusoidal gratings (over the spatial frequency range 0 to 20 cyc/deg). The model was validated by testing the equality,

$$CSF_g \times MTF_{ng} = CSF_{ng} \times MTF_g \tag{6.1}$$

where CSF_g and CSF_{ng} were CSFs for the subject wearing/not wearing glasses, and MTF_g, MTF_{ng} were the MTFs for the subject wearing/not wearing glasses (see Section 2.5 of Chapter 2 for more details). These MTFs were generated from geometric PSFs (as produced by Korynta et al. [1999]). Finally, an attempt to predict the measured VA was made, by determining the intersection of the modulation threshold ($1/CSF$) with the MTF of the eye as used by Greivenkamp et al. [1995a]. This gave the point of highest resolution on viewing high contrast gratings. The results are discussed, and suggestions for further improvements are made.

6.2 Method

6.2.1 Gathering Clinical Data

Permission for the testing was given by the Waikato University Ethics Committee. Cooperation for the testing was given by the Hamilton Eye Clinic[2] and Lazersight[3] refractive surgery clinic. A request to participate was sent to 20 patients identified as potential candidates by LazerSight staff, however only 1 reply was received in the time allocated.

Therefore, testing was restricted to one subject who had undergone cataract surgery in both eyes. The subject had undergone cataract surgery 1 year and 3 years previously, with no surgical complications, and had no family history of ocular diseases. The subject was known to have corneal astigmatism and defocus, and used bi-focal spectacle correction for reading/long distance vision.

Measurements on the subject were performed by a Technician at LazerSight. Keratometry and refraction of the eye were performed, using a NIDEK ARC-900 Refractometer/Keratometer. This gave the lens prescription and the radii of curvature of the central

[2]Thanks to staff of Hamilton Eye Clinic, Hamilton, New Zealand

[3]Thanks to staff at LazerSight, Anglesea Clinic, Hamilton, New Zealand

cornea for both eyes. However, it was found that the refraction output of this device (i.e. the required lens prescription) did not print to hard-copy, which was reportedly due to the effect of the IOL implants. The refraction readings were therefore substituted by the lens prescription given by the subject's optometrist[4].

This procedure was followed by three (for each eye) videokeratographs taken using a Technomed C-SCAN. The output data from this device were ring image data (over the cornea), which were subsequently used to generate height reconstructions. This data was processed off-line, after all measurements had been made.

The subject's CSFs were measured using a VisTech 6500 Contrast Sensitivity Chart[5] provided by a local optometrist[6]. The chart is comprised of 5×9 (i.e. 5 spatial frequencies $\times$ 9 levels of contrast) circular patches of diameter 7.5 cm, with a viewing distance of 3m. Each patch is oriented slightly to the left of vertical, right of vertical, exactly vertical or blank. The chart was illuminated with a diffuse 75W bulb, placed to ensure even illumination over the chart area as per the instructions.

The subject was asked to identify the orientation of each of the patches (i.e. left of vertical, right of vertical, vertical or blank) for the left eye (OS) and right eye (OD), with and without glasses on. The responses were recorded on a patient data sheet for later analysis. After this, the patient was given a standard Snellen visual acuity test, at a standard test distance of 6m. The line at which 50% correct identification of the letters on a particular line was taken as the visual threshold, and 1 was subtracted from the denominator of the Snellen fraction, so that this fraction represented the line at which identification was above threshold. As with the VisTech chart, this was repeated for glasses on and off, and left (OS) and right (OD) eyes. The pupil diameter was then recorded by placing a ruler in front of each eye. The measured distance was subsequently reduced by 13% to allow for optical magnification caused by the cornea [Smith and Atchison, 1997, Charman, 1995].

The final task was the measurement of the axial length measured post-operatively, using a NIDEK A-SCAN US 800. Interpretation of the data was difficult due to spurious spikes in the output. These were again attributed (as with the refraction values) to the effect of IOL on the equipment. Therefore, the pre-operative axial length information was used. This was consistent with the use of this program as a means of predicting post-operative outcome, from pre-operative measurements (i.e. as an IOL lens predictor) though Hoffer and others [Schechter, 1995] have found evidence to show that there is no significant difference in axial

[4]Thanks to Paul Rose Optometrists, Hamilton, New Zealand

[5]VisTech Consultants Inc., Dayton, Ohio

[6]Thanks to Paul Dickson optometrist, Hamilton, New Zealand

length pre- and post-operatively.

6.2.2 Analysis of the Data

The RAYTRAK toolbox and MATLAB were used to model the VK corneal surface data off-line. Firstly, the VK obtained corneal height fields were reconstructed using the algorithm of section 3.5. The recovered height fields were processed into B-Spline form for use with the eye model. It was verified that the surfaces generated were consistent, by determining the difference between the surfaces at randomly chosen points. The surfaces were found to agree to micron accuracy. A final surface was then generated by averaging the recovered height data, and then processing this into B-Spline form.

6.2.3 Consistency Check with Measured Data

Spot-diagrams consisting of approximately 1000 rays were generated at several image plane positions, for both eyes with glasses on/off. The rays were cast from a position on the axis, 6m (standard eye chart viewing distance) from the anterior cornea. These diagrams were used to identify the principal focii and the orientation of astigmatism at these points, and were to be verified against the clinically measured keratometry values. The characteristic elongation of the spot diagram was used as a means of manually identifying the axial positions of the principal focii, whilst the actual angles of astigmatism were measured from print-outs. The position of best focus was determined automatically, using the RMS spot size as the criteria for minimization. The difference between this point and the retinal plane determined whether the patient was hyperopic or myopic, as well as furnishing an estimate of refractive error.

Glasses were added to the eye model, approximated by a sphero-cylindrical lens (with principal axes oriented as per prescribed lenses). The back vertices of the glasses were positioned (nominally) 12 mm from the eye (though the actual magnitude influenced the overall results negligibly). The glasses were given a nominal thickness of 0.5 mm, and the index of refraction was set to 1.59. These values were taken from values quoted in Smith and Atchison [1997], Bennet [1968]. The resulting spot-diagrams were then checked against the experimentally measured VA results, which indicated clinically optimal imaging (since they were measured at better than normal 6/6 vision for both eyes). In addition, the best focus point was measured, and compared with the retinal plane position, since these two planes could be expected to co-incide for optimal imaging.

6.2.4 Objective Prediction of the Spectacle Prescription

A MATLAB program was written to scan through values of spherical and cylindrical powers in the range $SPH = [-2.25D \cdots -0.25D]$ and $CYL = [-2.25D \cdots -0.25D]$ in 0.25 D steps, in order to find the spectacle correction that would minimize the spot size at the retinal plane [Klonos et al., 1996]. Minimization was suggested by the optimal VA results obtained. This asked the question: "does the model prescribe lenses consistent with what an optometrist would prescribe?". This was subsequently verified against the optometrist provided spectacle prescription.

The radii of curvature for the modeled glasses were determined from the candidate lens prescription and the assumption of a thin sphero-cylindrical lenses. Given a lens prescription in the form SPH/CYL@AXS, the front surface radius R_1 is found from the thin lens equation,

$$R_1 = \left(\frac{n_1 - 1}{n_1}\right) SPH \tag{6.2}$$

i.e. the "sphero" part of the lens, whilst the radius R_2 of the cylindrical back surface is found from the formula,

$$\frac{1}{SPH + CYL} = \left(\frac{n_1 - 1}{n_1}\right)\left(\frac{1}{R_2} - \frac{1}{R_1}\right) \tag{6.3}$$

by substituting the result (6.2) in equation (6.3) and solving for R_2. The orientation of the cylindrical surface was taken from the lens prescription. Spot-diagrams were generated for each combination of (R_1, R_2) and the geometrical spot size was computed at the retinal plane. The smallest spot size indicated the glasses which reduced the blur; the aspect ratio (σ_x/σ_y) was measured to quantify any astigmatism in the resulting spot-diagrams.

6.2.5 Incorporating MTF and CSF Measurements

The MTF was generated at the retinal plane for glasses on/off. This was used to test the equality of equation (6.1), using the measured CSF information for glasses on/off. The form of the sinusoidal gratings (i.e. near vertical/veretical), implied the use of MTF values corresponding to vertical sinusoidal gratings. The chart tested the subject at the spatial frequencies 1.5, 3, 6, 12 and 18 cyc/deg.

The crossing of the MTF with the modulation threshold for a standard person was taken as an estimate of VA. These results were finally supplemented by generating simulated images of letter "E"s. These provided a means of visualizing the modeled optical degradation as seen by patients.

6.3 Results

6.3.1 Consistency Check with Measured Values

Figures 6.1 and 6.2 show resulting spot diagrams generated for OS/OD for three different axial positions. The positions shown are the principal focii (found by visual inspection) and the retinal plane . The orientation and error in the measurement of the astigmatism were measured from the resulting plots. Table 6.2 summarizes the keratometry values found from the surface model, and the clinically measured keratometry. The principal angles were found to be 34 ± 6, 135 ± 8 for OD, and 33 ± 2, 133 ± 7 for OS. These were compared with the clinically obtained keratometry readings, and were found to agree within the stated error in the shallow meridia, but not within the stated error in the steep meridia. However, this observation was consistent with the common practice of calculating the steep angle as the shallow angle + 90°. The Author's and Technician's keratometry also differed by exactly 90°, adding weight to this assertion. It is likely that this is the case, but without calibration on a suitable surface (with principal meridia at obtuse or acute angles) or confirmation from the manufacturer, this cannot be settled conclusively.

The position of best focus was determined by minimizing the RMS spot size, and, as expected, this position fell between these two astigmatic positions, consistent with the fact that the circle of least confusion falls between the two principal focii. These values were also consistent with the short-sightedness of the patient. The position of best focus fell 0.5mm(OS) and 0.6mm(OD) short of the retinal plane. A "rule of thumb" measurement ($0.3 \text{ mm} \approx 1D$) indicated that the dioptric error was roughly 1.7 D(OS) and 2.0 D(OD). These were within 0.3 D(OS) and 0.25 D(OD) of the mean spherical equivalent lens prescription. This indicated that this position was at least consistent (to within a rule of thumb measurement) with the lenses prescribed.

To further test this, sphero-cylindrical spectacles were added to the eyes, with dimensions given by equations (6.2) and (6.3). The positions of best focus were now +0.03mm (OS) and -0.02 mm (OD) from the retinal plane. These were errors of 0.01 D (OS) and 0.007 D (OD) respectively, which compare with a 0.25 D minimum detectable difference as reported by Lang et al. [1994]. The good correction of these lenses were also consistent with the results of Visual Acuity testing (see Table 6.4), which gave better than normal ability (i.e. 6/6 VA) to discriminate letters on a Snellen VA test. The spot diagrams shown in Figure 6.2 were generated at the same axial positions as Figure 6.1 but with glasses on. It was found that the astigmatism was now reduced, the spot diagrams at the retinal plane were now circular,

and reduced in RMS radius from 0.038mm(OS/OD) to 0.023mm(OS)/0.017mm(OD). These results indicated an improvement over the no glasses case.

6.3.2 Objective Prediction of the Spectacle Prescription

As an objective test, a MATLAB program was used to model the refraction process. For OD, the automatic refraction program gave a lens prescription of -1.5/-0.25@90, compared to the clinically prescribed -1.5/-0.5@90 lens prescription. The mean spherical equivalent lenses (i.e. the average powers) differed by 0.1 D which is an un-noticeably small amount. The RMS spot sizes predicted for the two lens prescriptions differed by 4×10^{-3} mm, so was very nearly identical according to the objective criterion. The aspect ratios (i.e. a measure of astigmatism) for the two cases were measured and were identical in both cases i.e. 1.0. For OS, the automatic lens prescription was -1/-0.75 @ 120 , compared with -0.75/-1.25 @ 120 which were not identical, but had identical mean spherical equivalent powers of 1.38 D. Therefore, it appeared that the spherical component of the lens was shifted to the cylindrical component. The spot size differences between the predicted and clinically presecribed spectacles were small, i.e. 1×10^{-3} mm, but the aspect ratios were raised (1.60) in the case of the clinically prescribed lens, compared to objectively prescribed case (1.17). This suggests that the objectively prescribed lenses could reduce residual astigmatism in the eye, c.f. the clinically prescribed lenses. These results have been summarized in Table 6.3.

6.3.3 Incorporating MTF and CSF Measurements

The measured CSFs are shown in Figure 6.3 for both eyes (OS/OD) with glasses on/off. The graphs show contrast sensitivity (i.e. the inverse of the modulation threshold) against spatial frequency (cyc/deg) plotted on a semi-log graph. Figures 6.4 and 6.5 show the corresponding MTFs computed from the PSFs generated at the retinal plane, again for OS/OD and glasses on/off. These results were used to test for the equivalence of the sides of equation (6.1).

Figure 6.6 shows the results of plotting the left and right hand sides of equation (6.1). The two resulting curves followed the same general trend. The mean difference between the two curves was 3 units for OS/OD. The bounding curves showed the expected result if the thresholds were taken to be the CSF values either side of the measured CSF point. This plots accuracy bounds due to the coarseness of the chart. For example, if the line fell entirely between these bounds, then the comparison curve could be regarded as equivalent to within the coarseness of the chart.

Unfortunately, the chart was too coarse to give estimates for 18 cyc/deg OS/OD. There-

Description	OS (Clin)	OD (Clin)
Axial Length (mm)	23.57	23.60
Thickness (mm)		
Cornea	0.55	0.55
Aqueous	3.32	2.88
Pupil diameter (mm)	4.00	4.20
Lens Power (D)	20.5 D	20.5 D
Refractive Index		
Cornea	1.3771	1.3771
Aqueous	1.3774	1.3774
Vitreous	1.3360	1.3660
ACD (mm)	3.87	3.43
Keratometry (°)		
Shallow Meridia	33 ± 1	36 ± 1
Steep Meridia	124 ± 1	126 ± 1

Table 6.1: A summary of the clinically measured and assumed eye model details.

Description	OS (Sim)	OS (Clin)	OD (Sim)	OD (Clin)
Shallow Meridia (°)	33 ± 2	33 ± 1	34 ± 6	36 ± 1
Steep Meridia (°)	133 ± 6	124 ± 1	136 ± 7	126 ± 1

Table 6.2: The orientations of astigmatism measured from the spot diagrams (simulated) compared with the values as reported by keratometry.

Eye: OS	Prescribed	Modeled
Prescription(D)	-0.75/-1.25 @ 120	-1/-0.75 @ 120
Sph. Equivalent(D)	1.375	1.375
RMS Spot Size (mm)	0.030	0.029
Aspect Ratio	1.67	1.31

(a)

Eye: OD	Prescribed	Modeled
Prescription(D)	-1.5/-0.5 @ 90	-1.5/-0.25 @ 90
Sph. Equivalent(D)	1.75	1.625
RMS Spot Size (mm)	0.024	0.023
Aspect Ratio	1.02	1.00

(b)

Table 6.3: (a) OS, prescribed spectacles vs model prescribed spectacles. The axis of astigmatism was set to equal the prescribed lenses (b) same as for (a) but now for OD.

Eye	glasses	no glasses
OD	6/24 (6/14)	6/5 (6/7)
OS	6/18 (6/36)	6/4 (6/5)

Table 6.4: Experimentally measured Snellen visual acuities. The measuring distance was 6m. The acuities with glasses on exceed those of an average person. Shown also are the predicted VA in brackets. Whilst the predictions with glasses are within 2 lines of the actually measured, the results without glasses do not match the experimentally measured acuities.

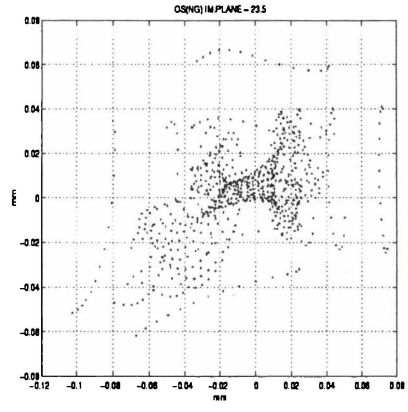

(a) OS (Shallow)

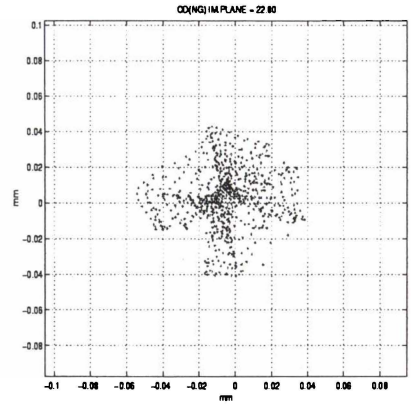

(b) OD (Shallow)

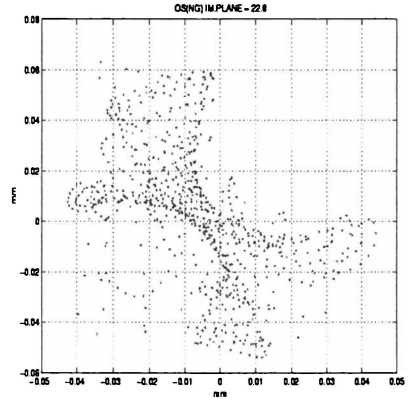

(c) OS (Steep)

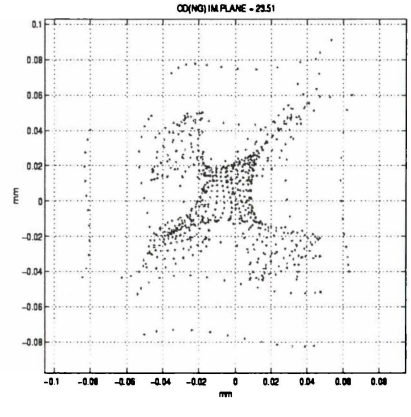

(d) OD (Steep)

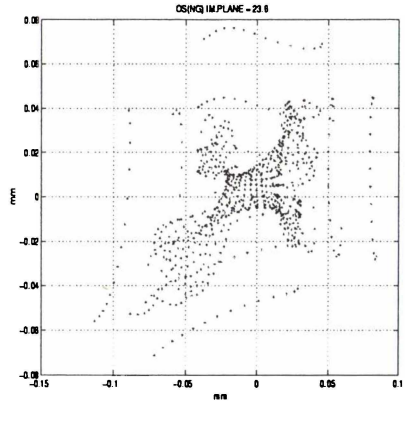

(e) OS (Retinal)

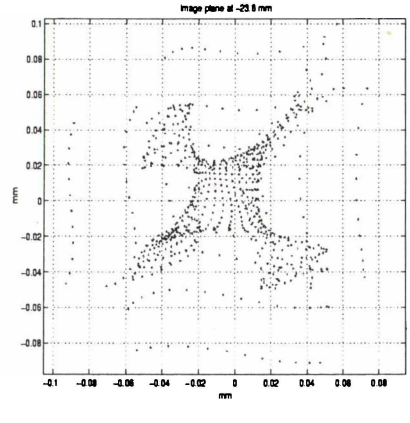

(f) OD (Retinal)

Figure 6.1: Spot diagrams generated for OS/OD for three axial positions (with glasses). These diagrams show the shallow and steep meridia of the astigmatism in the eye. Also shown is the distribution at the retinal plane. The astigmatism in OD was more difficult to quantify, since it did not have the distinct elongation of OS. This was consistent with the lens prescription, which showed that there was less astigmatism in that eye.

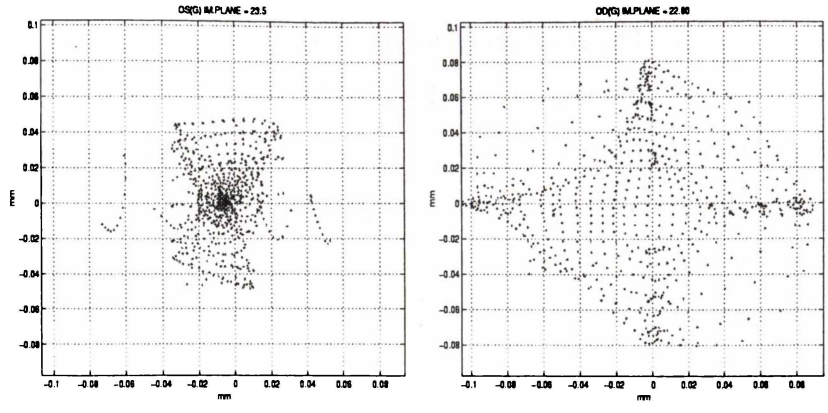

(a) OS (Shallow) (b) OD (Shallow)

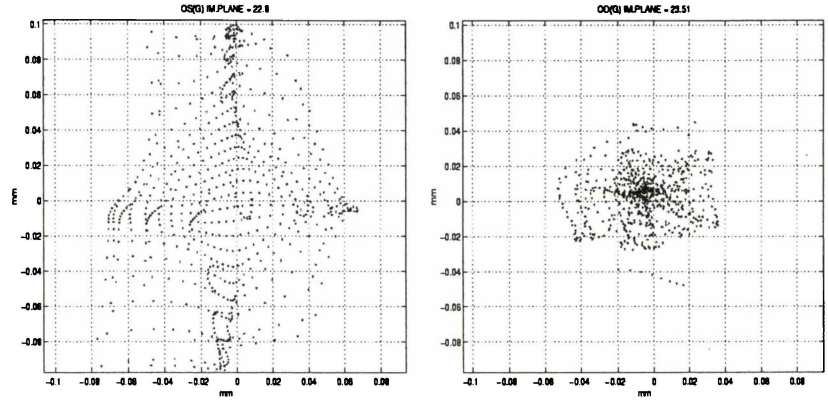

(c) OS (Steep) (d) OD (Steep)

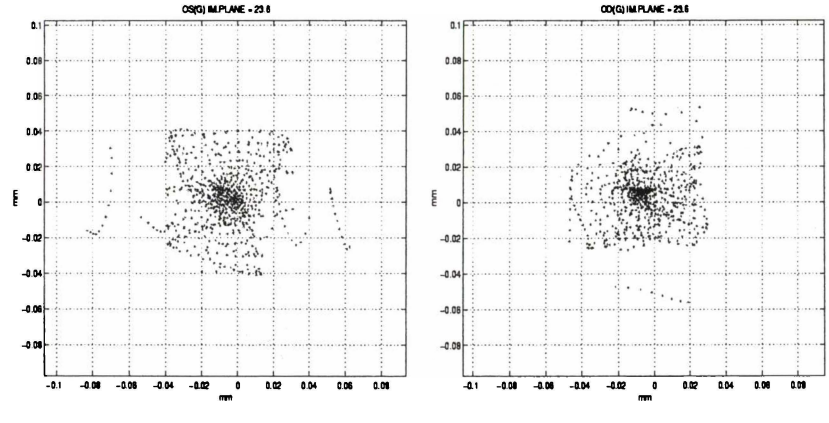

(e) OS (Retinal) (f) OD (Retinal)

Figure 6.2: Spot diagrams generated for OS/OD for three different axial positions (without glasses). These diagrams are the same as Figure 6.1 but with glasses. The astigmatism at retinal plane is replaced with a uniform blur circle, and the spot size at the retinal plane is significantly reduced.

fore, these points were not included in the analysis. For OS, the bounding lines indicated agreement between the two curves, to within the accuracy of the chart for the lower frequencies i.e. 1.5,3,6 cyc/deg. The resultant lines did not agree at 12 cyc/deg, indicating that the coarseness of the chart could not account for this discrepency at this point. There was therefore, a 75% agreement in this case. For OD, a match was found for the lower frequencies, i.e. 1.5,3 cyc/deg, with an apparently spurious point at 6 cyc/deg. The lines did not match to within the coarseness of the chart at the 12 cyc/deg point. This gave only a 50% agreement within the coarseness of the chart. The discussion briefly discusses possible improvements to the method used.

The MTFs for the eye were difficult to assess, since the point spread function was not symmetric. With glasses on, there was increased symmetry over the azimuthal angle, but a wide range of threshold values were observed without glasses. Using the modulation transfer function, as an estimator of visual acuity gave 6/7 (OD) and 6/5 (OS) with glasses on, which agreed to within two and one lines of the VA chart measurements. However, this was not the case without glasses. Agreement was not found using the current indicators.

Figures 6.7 to 6.10 show synthetic imagery, which illustrates the predicted visual impression of the letter E. It should be noted that the size of these letters have been normalized, so that in reality, a steady decrease in the letter size would be observed.

6.4 Discussion

There appeared to be agreement between the model and the experimentally measured values. The clinically observed features of the subjects vision were observed in modeling, and the positions of these features were consistent with what was expected. In particular, the astigmatism agreed to within error bounds. The steep meridia did not agree, but this was very probably due to the method used to determine the steep meridia in keratometry.

The refraction program used to test the recovery gave results in agreement with the model. For the OD, the model predicted the actual glasses used to under 0.25 D of the cylindrical component. The mean equivalent power of these spectacles differed by 0.1 D, which is typically an unnoticeable amount.

In the case of OS, the error between the spherical and cylindrical components was larger, i.e. 0.25 D for the spherical and cylindrical components. Even so, the mean spherical equivalent was exact, indicating that this 0.25 D error was due to a shift in the spherical, with an equal decrease in the cylindrical. Therefore these lenses were identical to within the mean spherical equivalent. The aspect ratio indicated a slightly lower astigmatism in the predicted

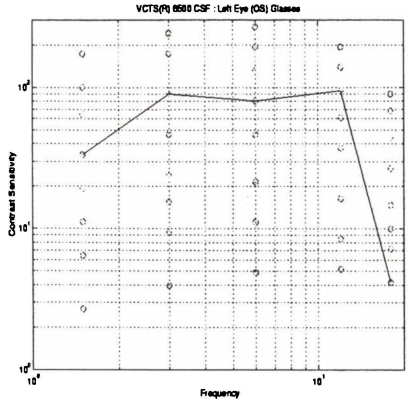

(a) CSF(OS) glasses

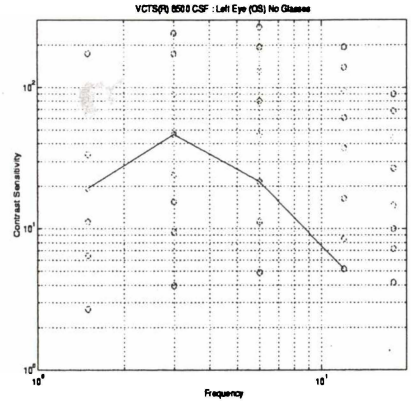

(b) CSF(OS) no glasses

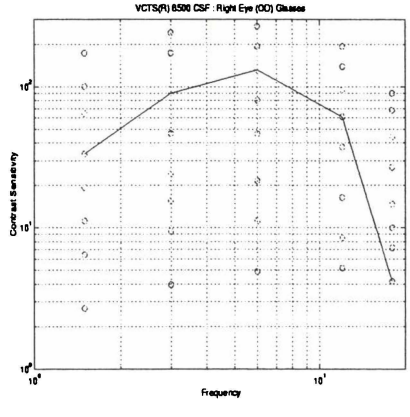

(c) CSF(OD) glasses

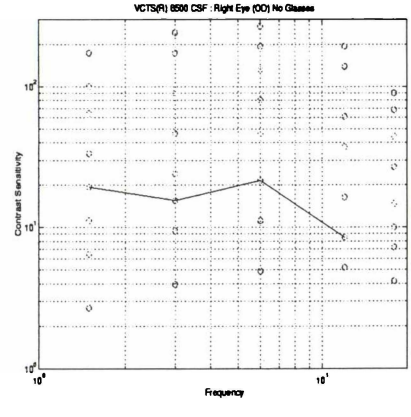

(d) CSF(OD) no glasses

Figure 6.3: (a) Experimentally measured CSF for OS with and without glasses (b) Experimentally measured CSF for OD with and without glasses.

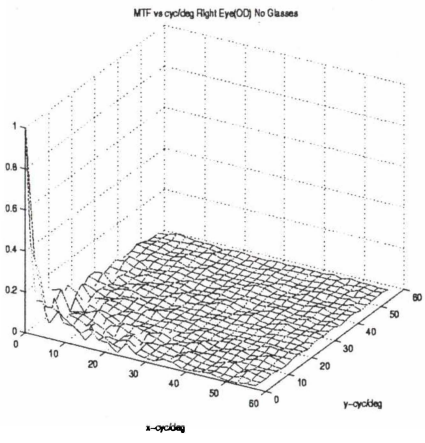

(a) MTF(OD) no glasses

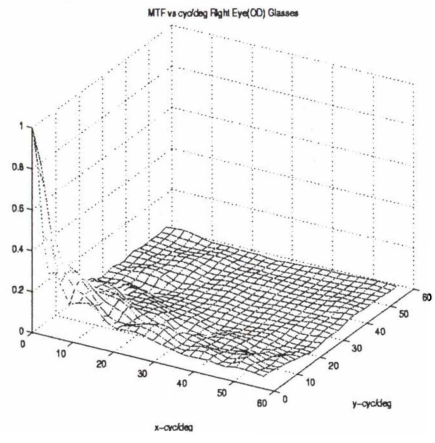

(b) MTF(OD) with glasses

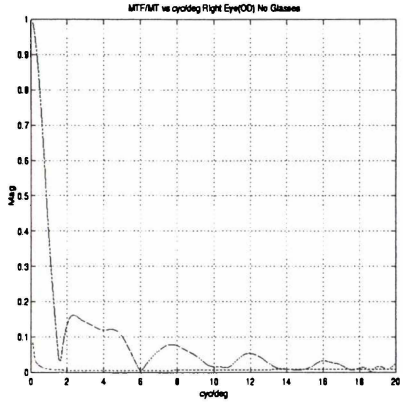

(c) MTF/MT(OD) no glasses

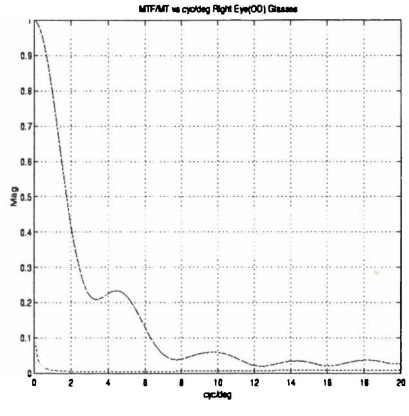

(d) MTF/MT(OD) with glasses

Figure 6.4: The figures show modulation transfer functions as a function of x/y-spatial frequencies for OD. The bottom figures are the one dimensional MTF taken along the x-direction, corresponding to vertical sinusoidal gratings. These were tested by the VisTech Contrast Sensitivity chart. Shown also are the expected modulation thresholds for a normally sighted person.

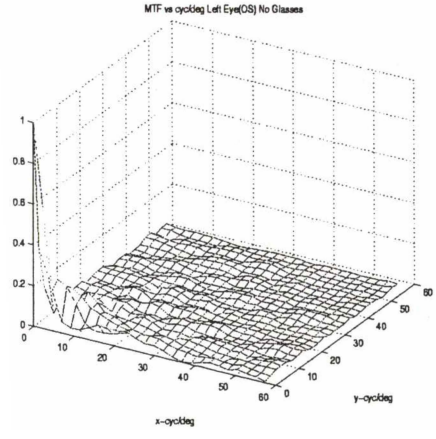

(a) MTF(OS) no glasses

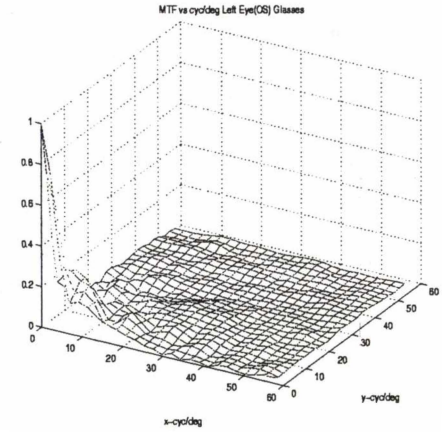

(b) MTF(OS) with glasses

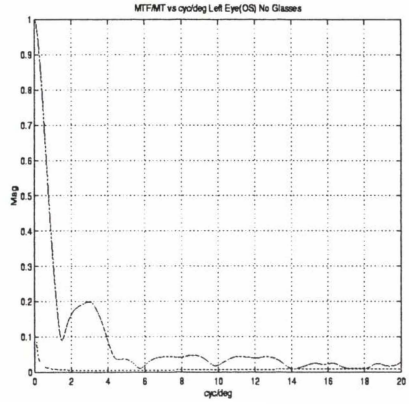

(c) MTF/MT(OS) no glasses

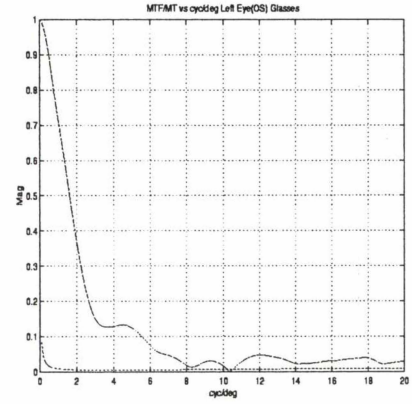

(d) MTF/MT(OS) with glasses

Figure 6.5: The figures show modulation transfer functions as a function of x/y-spatial frequencies for OS. The bottom figures are the one dimensional MTFs taken along the x-direction, corresponding to vertical sinusoidal gratings. These were tested by the VisTech Contrast Sensitivity chart. Shown also are the expected modulation thresholds for a nprmally sighted person.

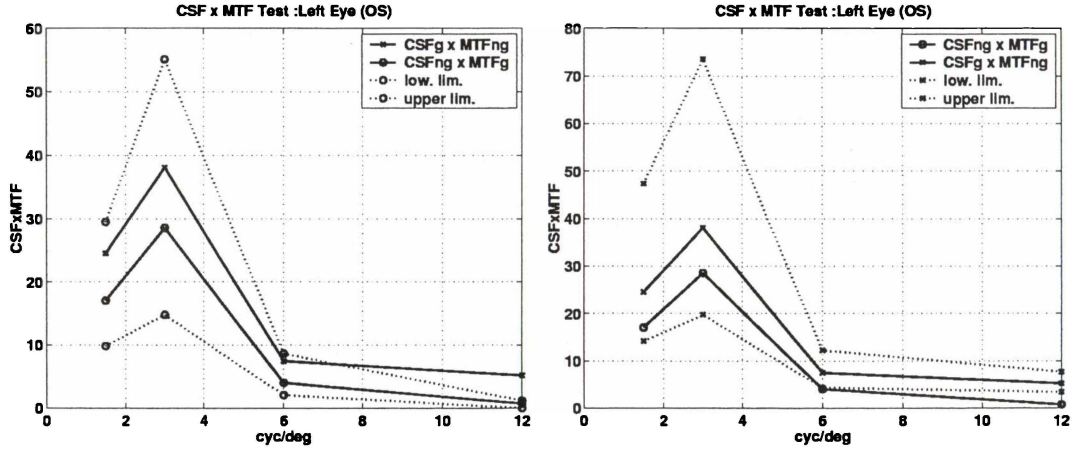

(a) CSF×MTF(OS)

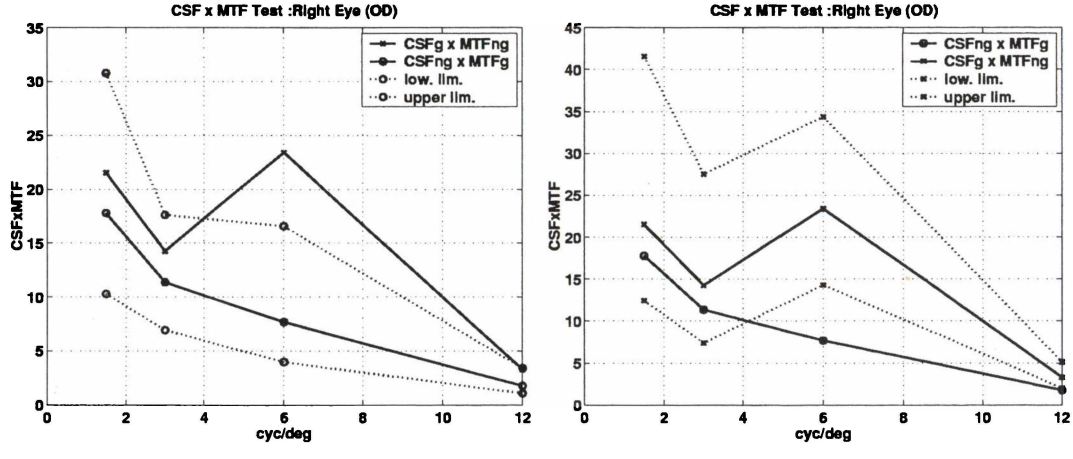

(b) CSF×MTF(OD)

Figure 6.6: The figures plot the sides of the equality $CSF_g \times MTF_{ng} = CSF_{ng} \times MTF_g$ (i.e. left to right) for OS/OD (i.e. top vs bottom panels), plotted over the 0 to 12 cyc/deg spatial frequency range. The dotted lines show the errors in each term, implied by the coarseness of the chart. Accordingly, the curves have a 75% agreement for OS, and a 50% agreement for OD.

results, indicating that the prescribed glasses could be improved by considering this 0.25 D shift. Visual inspection of the corresponding spot-diagrams appeared to support these findings. The objective criterion were very close to each other, indicating that the difference between the selections found and the experimental findings were small.

Attention was then turned to the measured CSFs, and the comparison MTF data, through equation (6.1). There appeared to be reasonable agreement between the two curves (for OS). In the OS case, the curves did not agree to within the accuracy of the chart at 12 cyc/deg. However, the graphs overall indicated that the modulation transfer information was consistent with the visually measured outcomes. However, for OD, the match was not as close. In this case there was agreement at $1.5, 3$ and 18 cyc/deg. But the graphs did not match at 6 cyc/deg or 12 cyc/deg. A possible improvement is to utilize better techniques for determining psychophysical thresholds. For example, in this case, the subject's modulation threshold was determined by guessing the orientation of the patches of decreasing contrast. However, using decreasing estimates is known to produce conservative results [Gescheider, 1985]. In addition, there are a variety of psychophysical techniques, which are aimed at removing such biases and obtaining accurate estimates [Gescheider, 1985, MacMillan and Creelman, 1991].

Finally, VA was predicted by looking at the crossing of the MTF with the CSF. However, the MTF was irregular for the situations without glasses, which made correct estimation difficult. The visual acuity was predicted to 2 lines (OD) and 1 line (OS) of the chart with glasses on, but without glasses the MTF was found to vary with meridional angle, so there would need to be a better decision criteria to address this issue. In fact, [Greivenkamp et al., 1995b], also point out difficulties in predicting VA by this method (although they use physical optics).

Though these results are encouraging, there is more work required to establish the correctness of these findings, and to improve the experimental method. One aspect of the testing that needs to be looked at, is error contributions due to the measured ocular surfaces. For example, the literature points out that 0.24mm error may be incurred by axial length measurements, due to the ultrasonic probe depressing the cornea. Such an error was not observed in these tests.

There may have been some interplay between the measured dimensions, canceling this effect out. From the analysis in section 4.5, it is assumed that the error in focal position will be 0.015 mm (0.05 D) (i.e. due to corneal topography error, the focal point will be short by this much). The thickness of the cornea, introduces very little defocus error (± 0.07 mm produces negligible defocus), but it may have an influence due to its radius. Assuming a

radius from 6.2 mm to 6.7 mm, spans a total error of 0.37 D diopter error in the position of best focus. There is the potential for noticeable amounts of error.

In fact Rengstorff [1985] found that a 10% change in each component of the eye gave the following errors i.e. anterior corneal curvature (4.87 D) index of refraction (1.87 D), depth of anterior chamber (1.20 D), posterior corneal curvature (0.62 D) and corneal thickness (0.01 D). Refractive changes were the sum of these individual changes. Therefore, it is important to know the parameters of the optical elements, in order to estimate errors in the predictions.

The effect of tilt and decentering was not measured/tested in this eye, but should be attempted in order to estimate its influence. To this end, the methods of the previous chapter should be useful. Another possible solution would be to examine the errors using an actual physical model eye, such as constructed by Rudnicka et al. [1992]. Again, there are several improvements which can be made.

6.5 Conclusion

A test of an IOL patient was conducted. It was found that the eye model was consistent with observation, in that astigmatism and positions of best focus were consistent with the clinically measured parameters. In addition, the spectacle prescriptions were predicted objectively, to within 0.0 D (OS) and 0.1 D (OD) of the mean spherical equivalent refraction.

There was reasonable agreement between the ratio of CSFs and MTFs, for OS, so that the results are consistent with theory. However, in the case of OD, the match was less convincing, so there is the possibility for improvement with the inclusion of alternative psychophysical techniques.

The intersection of the MTFs with the CSFs were used to estimate VA. The VA was estimated to 2 lines(OD) and 1 lines(OS) of the clinically observed result, for glasses on, but did not predict accurately for glasses off. It is suggested that more work in this area is required, for example, a robust decision criteria may be needed.

There is evidence that further testing would be productive. The number of patients will need to be increased in the future, and it is suggested that more sophisticated psychophysical tests be used.

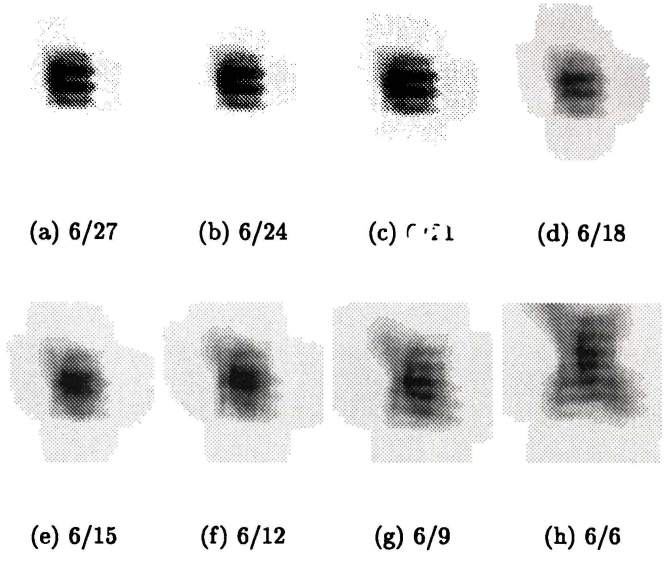

(a) 6/27 (b) 6/24 (c) 6/21 (d) 6/18

(e) 6/15 (f) 6/12 (g) 6/9 (h) 6/6

Figure 6.7: Example letter "E"s generated from the point spread function for the left eye (OS) at the retinal plane, simulating vision *without* glasses. In reality, the letters will be progressively smaller, but they have been equalized here to show the details of the images.

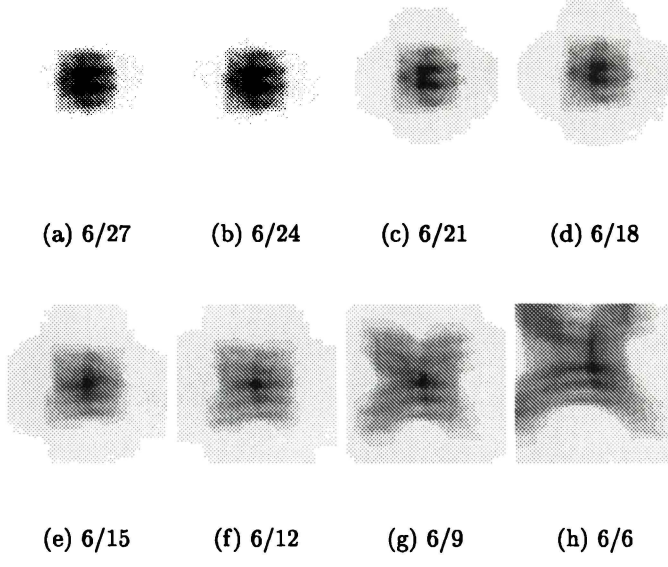

(a) 6/27 (b) 6/24 (c) 6/21 (d) 6/18

(e) 6/15 (f) 6/12 (g) 6/9 (h) 6/6

Figure 6.8: Example letter "E"s generated from the point spread function for the right eye (OD) at the retinal plane, simulating vision *without* glasses. Subjective comparison of the above figure and this figure show that the imaging appears to be worse for the right eye.

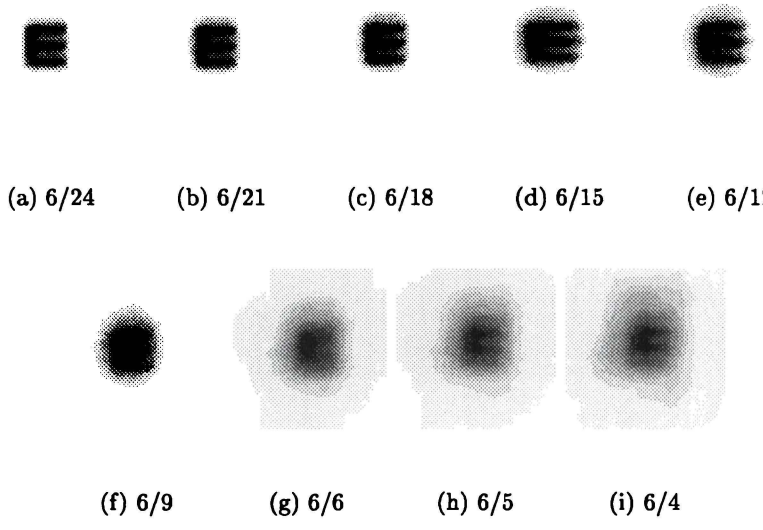

(a) 6/24 (b) 6/21 (c) 6/18 (d) 6/15 (e) 6/12

(f) 6/9 (g) 6/6 (h) 6/5 (i) 6/4

Figure 6.9: "E"s generated from the point spread function for the left eye (OS) at the retinal plane, simulating vision *with* glasses. Each letter has been magnified to equal height, in order to show the detail of the letters.

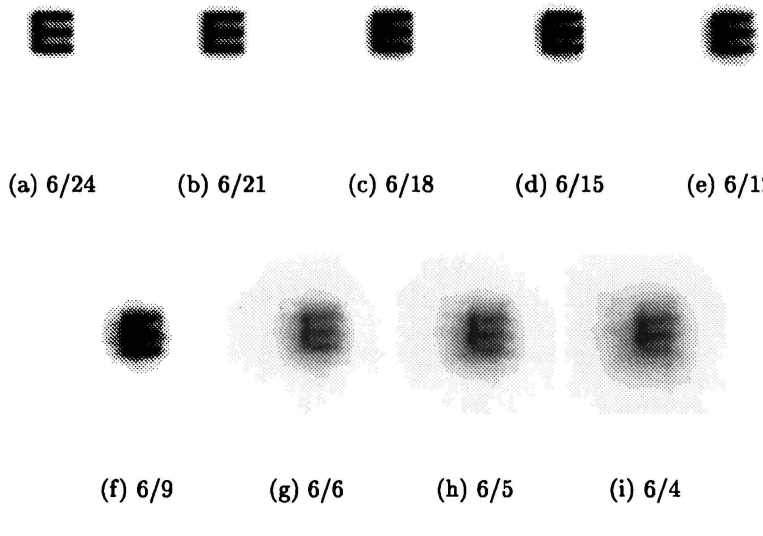

(a) 6/24 (b) 6/21 (c) 6/18 (d) 6/15 (e) 6/12

(f) 6/9 (g) 6/6 (h) 6/5 (i) 6/4

Figure 6.10: "E"s generated from the point spread function for the right eye (OD) at the retinal plane, simulating vision *with* glasses. Each letter has been magnified to equal height, in order to show the detail of the letters.

Chapter 7

Conclusions

The aim of this thesis was to investigate the idea of generalizing the modeling of light transport in the eye, in an attempt to overcome the limitations of current models for predicting IOL power. This involved: (i) modeling of the cornea to high precision, (ii) exact ray-tracing of eye, and (iii) experimental verification of the resulting model.

To this end, a new VK algorithm was presented. It was simple, yet gave good height recovery results in simulation (i.e. sub-micron error) for an aspheric surface and two surfaces with tilt. An average RMS height error of 6.2×10^{-4} mm and a maximum error of 1.5×10^{-3} mm (ellipsoid) was found *without* skew compensation. *With* skew ray error compensation the average RMS height error was reduced to 1.7×10^{-4} with a maximum error of 3.8×10^{-4}mm (ellipsoid). These results (i.e. in the skew ray error case) were below an RMS height error tolerance of 1×10^{-3} mm for all cases tested. The completion times (for an RMS convergence error of 1×10^{-12} mm) were 0.6s (no skew) and 2.3s (skew). Compensation for skew therefore accounted for a four-fold increase in completion time. However, this was acceptable given the accompanying 70% reduction in error. The number of iterations taken to complete was exactly 7 for all cases.

These results supported the contention that skew-ray error is an important part of recovery. However, given that the error was low *without* skew ray compensation, the indication is that the numerical method used here is itself capable of producing low error recoveries. Therefore, the approach taken here appears to improve on arc-step algorithms presented in the literature.

Problems with experimentally obtained data were observed. An attempt was made to remove these errors without destroying information pertaining to *true* corneal features. In particular, a double-pass low-pass filtering was applied, with the aim of preserving astigmatism and other low frequency features. This smoothing process was followed by an *element-by-*

element multiplication with a calibration matrix derived by least squares fitting to calibration ball data (7 mm, 8 mm and 9 mm).

This approach reduced an initial average RMS error between theoretically simulated rings of 5×10^{-2} mm to 3×10^{-3} mm over the first 20 rings. Subsequent height recovery (on these processed rings) resulted in average RMS height errors of 2.7×10^{-4} mm. These results were obtained for a calibration set (7 mm, 8 mm and 9 mm calibration balls); an appropriate (within the range of calibration balls) validation set was not available - so this did not test the algorithm conclusively. However, it was expected that the methods developed would work at least for spherical cornea within the range 7 mm - 9 mm.

A ray-tracing toolbox (RAYTRAK v1.0) was developed in MATLAB v5.0 for use in Ophthalmic applications. The primary purpose of this toolbox was to provide flexibility in the modeling of rays. To this end, basic geometric primitives, along with basic functions required by a sequential ray-tracer were implemented. A cubic/linear interpolation was compared against bi-cubic B-Spline (non-parametric uniform knot spacing with 24×24 control points) interpolation as a candidate general surface model. It was found that the B-Spline method gave lower error (over the cubic/linear method) in interpolating height, and tilt values. In particular, the average RMS height error was reduced from 1.2×10^{-3} mm to 2.2×10^{-4} mm ; RMS tilt error from 7.7×10^{-2} to 5.9×10^{-4} (whereas the RMS slope was raised slightly from 8.0×10^{-4} to 1.3×10^{-3}). These two advantages coupled with the ease of implementation of B-Spline surfaces, meant that this surface model was adopted as default.

The resulting B-Spline surfaces were used to estimate the errors (from the analytic models) incurred in predicting the focal length and transverse ray errors in the plane of best focus. For the simulated cornea, it was found that the average transverse RMS errors (on the plane of best focus) were 1.0×10^{-3} mm. These errors were on the order of retinal cone dimensions (i.e. 1.5×10^{-3} mm). The error in the focal length was 0.015mm(0.1 D), which was well under a just noticeable difference of 0.25 D.

This testing was repeated for the 7 mm, 8 mm and 9 mm calibration balls, whereupon an average transverse RMS error of 6.5×10^{-3} mm and error in best focus of 0.015 mm (0.1 D) was found. The average transverse error was on the order of 4 retinal cells, which was deemed acceptable, particularly given that the size of a typical spot diagram would be found to be on the order of 5×10^{-2} mm. The focal error, was again less than noticeable. These were encouraging results, particularly since they gave estimates of likely errors given corneal topography data.

Two applications of the RAYTRAK toolbox were investigated: (i) the measurement of

the internal ocular radii, and (ii) the modeling of lens tilt and decentration in the eye. In the former, a new method for the recovery of the internal ocular radii was presented. In particular, the method used ray-tracing to determine image plane positions as a function of the eye parameters, and then imposed a linear model to relate the image plane positions to the internal parameters.

The method was tested on a Le Grand eye, with a variety (7 cases) of arrangements of the anterior cornea, posterior cornea and anterior lens. For each test case, 5 randomly generated internal radii were chosen, from which recovery was then attempted (of the posterior(PII) and anterior(PIII) lens). This method was found to produce dioptric errors that were never greater than 0.1 D (PII) and 0.006 D (PIII) from exact results (in simulation). This was encouraging, given the variety of situations modeled (e.g. an experimentally obtained VK surface, ellipsoidal and spherical surfaces oriented at 30° to the axis) and the fact that the method was chosen for ease of implementation rather than high accuracy. It is also remarked that this method allows a unification between the methods of videokeratography and videophakometry which has not been exploited previously.

In the second case (ii), the effect of lens tilt and decentration were modeled. PSFs were produced at a range of decenter (0 to 0.8 mm in 0.2 mm steps) and tilt values ($-5°$ to $5°$ in $2.5°$ steps), from which image quality (via the SQuare Root Integral (SQRI) image quality metric) and statistical moment measures were taken. In particular, the SQRI was computed for the plane of best focus, afterwhich ΔSQRI was plotted (differences from best focus), for displaced image planes. To the knowledge of the author, neither of these metrics (i.e. image quality and statistical moments) have been applied to this modeling situation previously, thereby providing a novel solution/framework for modeling image quality as a function of tilt and decenter.

The results indicated the importance of displacement from best focus, in determining the effect of lens tilt and decenter on *subjective* image quality. It was found that the SQRI for the plane of best focus, and ΔSQRI for +0.1 mm from that plane were qualitatively similar. They were inverted (i.e. imaging degraded with tilt) and asymmetric (i.e. imaging degradation increased with positive tilt). In the former case, the SQRI was consistently under 1 jnd for negative tilt (regardless of decenter), indicating *un-noticeable* amounts of change in these cases. This SQRI value became noticeable (-3 jnd to -8 jnd) for positive ($5°$) tilt combined with decenter (consistent with lens decenter compounding skew at the image plane). The results in the latter case, indicated moderate (-2jnd to -4jnd) image degradation (for negative tilt), which decreased to from -5jnd to -8jnd for positive $5°$ tilt combined with

increasing decenter. However, in a plane -0.1 mm from best focus, ΔSQRI was qualitatively different. In particular, the resulting curve was valley shaped (an ΔSQRI low of -4 jnd with no tilt) with increases to as much as -0.5 jnd as tilt increases, thereby indicating image quality improvements regardless of the sign of tilt. These results were also supported by visual inspection of resulting synthetic images.

The spot-diagrams were further summarized by the statistical moment measures (i.e. kurtosis, skewness and standard deviation) of the spot diagrams. It should be noted that these measures were re-defined in this modeling (from standard definitions) to reveal shape *changes* from the spot diagram generated in the plane of best focus for zero tilt and decenter. The results were supported by visual inspection of spot-diagrams. For example, in the case of best focus, the skew increased with decenter; which was reduced/compounded by the subsequent addition of tilt (depending on sign).

An interesting result was that skew was largest in the case of best focus. However, the image quality via the SQRI, was largely unaffected and in fact indicated near normal image quality. This suggested that (i) the SQRI is not sensitive to the skew in the spot-diagram or (ii) large skew does not necessarily imply degraded imaging. However, given the results of Atchison [1989b] which utilize the MTF in the context of skewed spot-diagrams; suggests the latter is true.

The aim of the final chapter, was to test the ability of the model to predict the imaging of the eye. Two eyes were tested, using two approaches (i) the model was tested for consistency with the clinically measured refractive error. Secondly, the validity of the model was tested by way of the CSF and MTF measures, and equation (6.1); and also by attempting to predicting VA as the intersection of the MTF with the 1/CSF (the modulation threshold).

For approach (i), agreement between clinically measured astigmatism and modeled astigmatism was found in the shallow meridia. The results were consistent with the short-sightedness of the patient, with an error in the mean spherical equivalent power c.f. prescribed lenses of 0.3D (OS/OD). Adding the prescribed lenses gave errors in focal length prediction of +0.03 mm and -0.02 mm. These translated to errors of 0.01 D(OS) and 0.007 D(OD), which were small. An objective lens prescription program gave spherical mean equivalent powers of 0.0 D (OS) and 0.1 D (OD) of the clinically measured, where the RMS spot size was used as the objective criterion for minimization. The use of this minimization was supported by the clinical result that vision was (near) optimal.

Testing the equality of equation (6.1) was only partially successful. The number of spatial frequencies tested were limited by the coarseness of the chart at 18 cyc/deg. For OS, the

equality was within error bounds for 3 of the 4 tested spatial frequencies (75%). However, for OD, a match was found for 2 of the 4 tested spatial frequencies (50%). In particular, a spurious measurement appeared in the resulting graph for OD. It was suggested that the psychophysical methods used to test this equality could be refined to produce better estimates. In particular, the method used to determine the threshold may have been too simple. Finally, the VA was predicted to within 1 and 2 lines (on a Snellen acuity chart) respectively for glasses on. However VA was not predicted accurately for glasses off.

In summary, it was found that the spot diagrams, and modeled focal lengths were consistent with the subject eyes. However, when attempting to make a more detailed analysis of the spot-diagram, only a partial match with theory was found. It is suggested that better methods of testing the mentioned psychophysical equality (which were not available here) are required, along with larger numbers of patients, and potentially better criterion for determining VA are required.

7.1 Discussion and Further Work

The new algorithm worked effectively on a range of surfaces. The method showed not only the importance of the *skew ray error* but the potential gains from the numerical approach adopted here. An accurate and fast algorithm was developed, which met the requirements for ray-tracing.

An important development would be to utilize the method on spherical/non-spherical calibration surfaces. However, to test such surfaces requires reliably calibrated equipment, which was not available during this testing.

For improved results, a further development would be equipment based on non-Placido targets. It would then be possible to experimentally test situations where the surface tilt becomes an important factor in surface recovery, without post-processing for skew-rays.

In addition, a non-Placido based device may be suitable for the measurement of Purkinje images and therefore the internal surfaces of the eye. This statement alludes to the possible unification of videokeratography and videophakometry proposed in section 5.3. Such a device, would incorporate methods for recovery of internal surfaces of the eye as well as the anterior corneal surface.

It was found that no published data exists regarding the calibration of Video-Phakometers (VPs). This is in contrast to the VK literature, where calibration information has been published extensively. There is a need for calibration data to be published regarding VPs, in order to assess (experimentally) the ability of potentially extended methods, e.g. neural

network methods and ray-tracing/VK methods alluded to in the discussion on these methods.

The eye model was tested on two eyes with some success. However, the model must be tested with many more patients. The *potential* of the method was explored in this thesis. An additional test, not used here would be to model the IOL used and target refraction, and then predict the IOL power that would be optimal. An improvement in the testing used here, would be to employ sophisticated methods of *psychophysics* for dealing with CSF measurement; in addition the relationship of the ocular parameters could be dealt with in more detail in the future.

In conclusion, the work carried out here provides a solid foundation for continuing research. The methods and results are both promising and novel, but further work is needed to establish the true value of these methods in clinical practice. In particular, more experimental work and detailed calibration information is required. There is certainly the possibility of developing new technologies from this work, and thereby, potential improvement of outcomes for visually impaired patients.

Appendix A

Schematic Eyes

A.1 Introduction

This section gives data for the Le Grand and Gullstrand eyes (accomodated/relaxed), which has been adapted from [Smith and Atchison, 1997, Appendix 3]. In particular,

Section A.2 Le Grand full theoretical eye (relaxed)

Section A.3 Le Grand full theoretical eye (accommodated)

Section A.4 Gullstrand number 1 eye (relaxed)

Section A.5 Gullstrand number 1 eye (accommodated)

The information for the schematic eyes are summarized in four tables. The first table gives the sequence, position and radius of curvature of the ocular surfaces, The index of refraction of the media separating the surfaces is also given. The second table gives the paraxial powers of the individual surfaces, and groups of surfaces (cornea, lens and complete eye). The third table gives the cardinal points for the eye, and the final table shows the *pupil* positions.

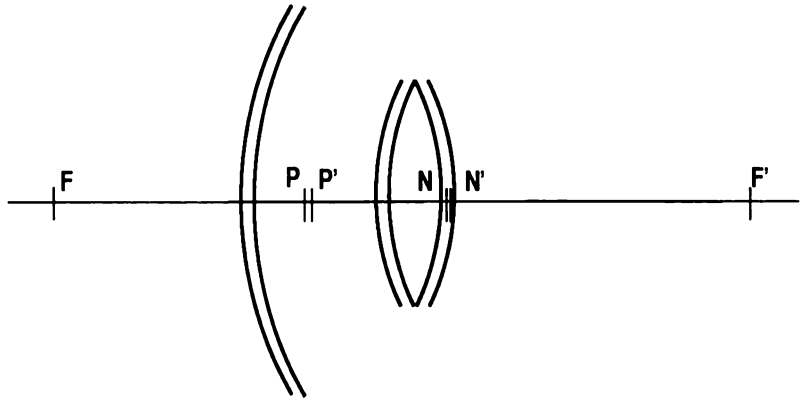

Figure A.1: Schematic of the Le Grand eye. Shown are the approximate positions of the focal points (F, F'), principal planes (P, P') and nodal points (N, N'). Here the "prime" refers to quantity in image space, whereas the "un-primed" quantity refers to object space.

A.2 Le Grand Full Theoretical eye: Relaxed

A.2.1 Surface Parameters

Surface	n	r(mm)	d(mm)	*d(total)*(mm)	
	1.0000				
1		7.800			
	1.3771		0.5500	0.5500	cornea
2		6.500			
	1.3374		3.0500	3.6000	aqueous
3		10.200			
	1.4200		4.0000	7.6000	lens[1]
4		-6.000			
	1.3360				vitreous

A.2.2 Equivalent Powers

Cornea:	Front surface	48.346 D
	Back surface	-6.108 D
	Complete	42.356 D
Lens:	Front surface	8.098 D
	Back surface	14.000 D
	Complete	21.779 D
Eye:	Complete	59.940 d

Eye length 24.197mm

A.2.3 Cardinal Point Positions

	Front	Back
Focal points (mm)	-15.089	24.197
Principal points (mm)	1.595	1.908
Nodal points (mm)	7.200	7.513

A.2.4 Pupils

	Entrance	Exit
Positions (mm)	3.038	3.682
Radii (mm)	4.000	3.682
Magnification	1.131	1.041

A.3 Le Grand Full Theoretical Eye: Accommodated

A.3.1 Surface Parameters

Surface	n	r(mm)	d(mm)	*d(total)*(mm)	
	1.0000				
1		7.800			
	1.3771		0.5500	0.5500	cornea
2		6.500			
	1.3374		2.6500	3.2000	aqueous
3		6.000			
	1.4270		4.5000	7.7000	lens(aperture)
4		-5.500			
	1.3360				vitreous

A.3.2 Equivalent Powers

Cornea:	Front surface	48.346 D
	Back surface	-6.108 D
	Complete	42.356 D
Lens:	Front surface	14.933 D
	Back surface	16.545 D
	Complete	30.700 D
Eye:	Complete	67.677 D

Eye length 24.197mm

A.3.3 Cardinal Point Positions

	Front	Back
Focal points (mm)	-12.957	21.932
Principal points (mm)	1.819	2.192
Nodal points (mm)	6.784	7.156

A.3.4 Pupils

	Entrance	Exit
Positions (mm)	2.660	3.255
Radii (mm)	4.000	3.785
Magnification	1.115	1.055

A.4 Gullstrand Number 1 Eye: Relaxed

A.4.1 Surface Parameters

Surface	n	r(mm)	d(mm)	*d(total)*(mm)	
	1.0000				
1		7.700			
	1.376		0.500	0.500	cornea
2		6.800			
	1.336		3.100	3.600	aqueous
3		10.000			
	1.386		0.546	4.146	lens: cortex (aperture)
4		7.911			
	1.406		2.419	6.565	lens: core
5		-5.760			
	1.386		0.635	7.200	lens: cortex
6		-6.000			
	1.336				vitreous

A.4.2 Equivalent Powers

Cornea:	Front surface	48.831 D
	Back surface	-5.882 D
	Complete	43.053 D
Lens cortex	Front surface	5.000 D
Lens core	Front surface	2.528 D
	Back surface	3.472 D
Lens cortex	Back Surface	8.333 D
Lens:	Complete	19.111 D
Eye:	Complete	58.636 D

Eye length 24.385mm

A.4.3 Cardinal Point Positions

	Front	Back
Focal points (mm)	-15.706	24.385
Principal points (mm)	1.348	1.601
Nodal points (mm)	7.078	7.331

A.4.4 Pupils

	Entrance	Exit
Positions (mm)	3.047	3.665
Radii (mm)	4.000	3.638
Magnification	1.133	1.031

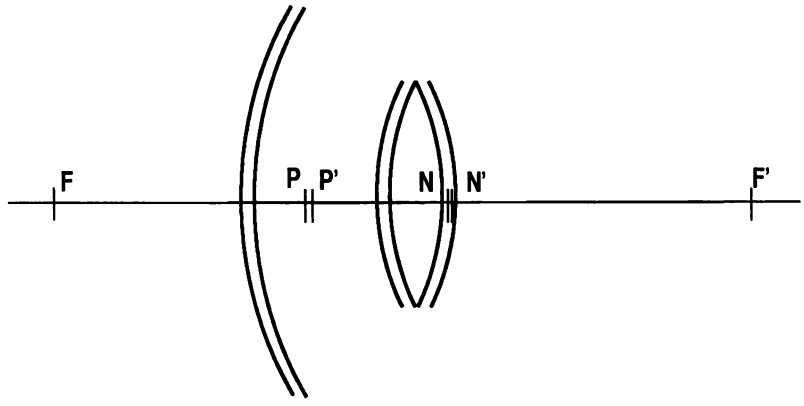

Figure A.2: Schematic of the Gullstrand eye. Shown are the approximate positions of the focal points (F, F'), principal planes (P, P') and nodal points (N, N'). Here the "prime" refers to quantity in image space, whereas the "un-primed" quantity refers to object space.

A.5 Gullstrand Number 1 Eye : Accommodated

A.5.1 Surface Parameters

Surface	n	r(mm)	d(mm)	*total* d(mm)	
	1.0000				
1		7.700			
	1.376		0.5000	0.5000	cornea
2		6.800			
	1.336		2.7000	3.2000	aqueous
3		5.333			
	1.386		0.6725	3.8725	lens: cortex (aperture)
4		2.655			
	1.406		2.6550	6.5275	lens: core
5		-2.655			
	1.386		0.6725	7.2000	lens: cortex
6		-5.333			
	1.336				vitreous

A.5.2 Equivalent Powers

Cornea:	Front surface	48.831 D
	Back surface	-5.882 D
	Complete	43.053 D
Lens cortex	Front surface	9.376 D
Lens core	Front surface	7.533 D
	Back surface	7.533 D
Lens cortex	Back Surface	9.376 D
Lens:	Complete	33.057 D
Eye:	Complete	70.576 D

Eye length 24.385mm

A.5.3 Cardinal Point Positions

	Front	Back
Focal points (mm)	-12.397	21.016
Principal points (mm)	1.772	2.086
Nodal points (mm)	6.533	6.847

A.5.4 Pupils

	Entrance	Exit
Positions (mm)	2.668	3.212
Radii (mm)	4.000	3.762
Magnification	1.177	1.051

Appendix B

RAYTRAK Code Examples

B.1 Code Examples

This section contains several code snippets used in RAYTRAK. The code snippets are for:

- Plane Intersection
- Ellipsoid Intersection
- B-Spline Intersection

B.1.1 Plane Intersection

The following code intersects a ray with a plane.

```
function [a,b,I] = plane(a, b, dr, I)

% PLANE.M return intersection of rays with a plane centered on
% the optic axis, with normal vector oriented along the
% axis [0 0 1].
%
% function [anew,bnew,I] = plane(a, b, dr, <I>)
%
% where a = ray slopes  [ u0 v0 w0 ; u1 v1 w1 ; ... ; uN vN wN ]
%       b = ray initial [ x0 y0 z0 ; x1 y1 z1 ; ... ; xN yN zN ]
%       I = optional ray id index
%
% this function may fail in the following circumstances:
%   0) rays must be unit length
%   1) no rays parallel to plane
%   2) no rays anti-parallel to plane
%   3) zero'ed w0

u0  = a(:,1); v0  = a(:,2); w0 = a(:,3);    % dirn. components
x0  = b(:,1); y0 = b(:,2); z0 = b(:,3);     % posn. components
L   = abs((z0 - cz)./w0);                   % path length

rx = u0.*L+x0; ry = v0.*L+y0;               % bad rays?
```

```
dE  = sqrt(rx.^2+ry.^2);
id   = find(dE < dr);

% discard bad rays
x0 = x0(id); y0 = y0(id); z0 = z0(id);

u0 = u0(id); v0 = v0(id); w0 = w0(id); L  = L(id);

if  exist('I'),
    I = I(id);
end

% return
b = [ u0.*L+x0 v0.*L+y0 w0.*L+z0 ];
a = [ u0 v0 w0 ];
```

The above code snippet shows how rays that cannot intersect the plane are discarded. The aperture discarding is shown.

B.1.2 Ellipsoid Intersection

The following code intersects a ray with an ellipsoid.

```
% ELLIPSOID.M return intersection of rays with an ellipsoid
% centered on the optic axis, with normal vector oriented along
% the axis [0 0 1].
%
% function [anew,bnew,I] = ellipsoid(a, b, dr, <I>)
%
% where a = ray slopes  [ u0 v0 w0 ; u1 v1 w1 ; ... ; uN vN wN ]
%       b = ray initial [ x0 y0 z0 ; x1 y1 z1 ; ... ; xN yN zN ]
%       I = optional ray id index
%
% this function may fail in the following circumstances:
%   0) rays must be unit length
%   1) no rays parallel to plane
%   2) no rays anti-parallel to plane
%   3) zero'ed w0
%
% ELLIPSOID INTERSECTION
%

DXC  = (X0 - C(ones([nlen 1]),:)); a1 = (M.*M)*A; b1 =
2*(M.*DXC)*A; c1 = (DXC.*DXC)*A - 1; disc   = b1.^2 - 4.*a1.*c1;
if     any(disc<=0),

       % missed ellipse completely
       It      = find(disc<0);
       XD      = X0(It,:);
       MD      = M(It,:);
       ID      = It;

       % remove missed rays from processing
       It     = find(disc>0);
       a1      = a1(It);
```

```
        b1      = b1(It);
        disc    = disc(It);
        I1      = I1(It);
        M       = M(It,:);
        X0      = X0(It,:);
        P0      = P0(It,:);
else
        ID = [];
end

disc    = sqrt(disc); l1     = (-b1 + disc)./(2*a1);

l2      = (-b1 - disc)./(2*a1);

L       = [ l1 l2 ];

l1      = l1(:,[1 1 1]); l2 = l2(:,[1 1 1]);


% only take the root closest to the vertex
P1  = M.*l1 + X0; P2     = M.*l2 + X0;
N(1,:)  = sqrt(sum(((P1-P0).^2)'));
N(2,:) = sqrt(sum(((P2-P0).^2)'));
[ dummy Imin ] = min(N); N = N'; dummy = []; J = (1:length(Imin))';
Imin = Imin'; ind  = sub2ind(size(N),J,Imin); L    = L(ind); L =
L(:,[ 1 1 1 ]);

% compute the intersect position
Z = M.*L + X0;

% identify rays out of extent
DR  = (Z - P0); DR  = sqrt(sum((DR(:,1:2).^2)'))';

if  any(DR>dr),

    It  = find(DR>dr);
    Z(It,1:3)   = X0(It,1:3);
    M(It,1:3)   = M(It,1:3);

end }
```

B.1.3 B-Spline Intersection Routines

The following code intersects a ray with a B-Spline:

```
function [ Xout, Iout, eee ] = IntersectBSpline2(X, M, InInfo,II,
err_tol),

% INTERSECTBSPLINE2.M intersection with b-spline
% surfaces.  Implements a simple subdivision
% rule. Has the advantage of bulk processing rays.
%
% function [ M III ] = IntersectBSpline2 ...
%                         (X, M, InInfo,  nType, err_tol ),
```

```
%
% where P     = ray vectors (split into X M)
%       nType = type of surface to intersect 'bspline'
%       C     = Information
%       M     = Intersection
%       III   = index to intersection points
%
% also assume that the b-spline has been shifted so that
% its centered on the origin
%
%  SOME TIDYING UP COULD BE DONE HERE ... BUT OK FOR NOW


% intialize
C  = InInfo.M; ap = InInfo.aperture;

if  ~exist('err_tol'),
    err_tol = 1.0e-5;
end

nType = 'bspline';  % HARDCODED BSPLINE

% eliminate rays outside of the aperture
s        = abs(X(:,3)./M(:,3)); s        = s(:,ones([1 3]));
X0       = M.*s + X;                        % intersection point
r        = sqrt(X0(:,1).^2 + X0(:,2).^2);
ind      = find(r <= ap);                   % clear aperture
if       ~isempty(ind),
          mdisp('aperture');
          X        = X(ind,:);                        % valid rays
      M        = M(ind,:);
      II       = II(ind,:);                      % indexes
end


% initialize
Xout = [];  % intersection points
Iout = []; % ray indexes
PP   = [];  % ray data      - mdebug('on') only
SS   = [];  % ray parameter - mdebug('on') only
eee  = [];  % errors
acum = 0;   % accumulated work


% [ X M ]
% input('wait...');

switch(nType)

  case 'bspline'

       mdisp('warning: please wait ... this may take some time');
       mdisp('warning: bspline assumed at origin');
       mdisp('completed ,.. 0%');

       % normalize P so that s is the distance along the axis
       M = M./abs([ M(:,3) M(:,3) M(:,3) ]);
```

```
% initialize
l     = size(M,1);

% best first guess
s1new    =   5*ones([ 1 1 ]) + X(:,3);  s1new = s1new(:);
s2new    =  -5*ones([ 1 1 ]) + X(:,3);  s2new = s2new(:);

% disp('entering main...');
k        = 1;
while(k < 100),

 s1  = s1new;      % ray parameter
 s2  = s2new;      % thang parameter

 % find mean position
 s   = 0.5*(s1 + s2);

 % error between new point surface and ray
 xtest0   = M.*[ s s s ]  + X;              % mean
 ztest0   = getbspline(C, xtest0(:,1), xtest0(:,2) );
 e0       = ztest0 - xtest0(:,3);


 temp    = abs(e0) <= err_tol;
 I       = find(temp); % members that have terminated
 if      ~isempty(I),
          Inot = find(~temp);

          acum = acum + length(I);
          mdisp([ 'completed ' ...
              num2str(100*(acum/l)) '  %' ]);

      % accumulate the answers
      Xout  = [ Xout ; xtest0(I,1:2) ztest0(I) ];
      Iout  = [ Iout ; II(I) ];
      eee   = [ eee ; e0(I) ];

      % full([ Xout Iout ])
      % input('extractor');

      if  mdebug,
          PP      = [ PP  ; X(I,:) M(I,:) ];
          SS      = [ SS  ; s(I) ];
      end


     if      isempty(Inot),

             % full([ Xout Iout ])
             % input('wait mon...');
             mdisp('done.');

         [ Iout I ] = sort(Iout);
         Xout       = Xout(I,:);
         % Iout       = Iout(I,:);
         % input('extractor');
         eee        = eee(I,:);
```

```
            if  mdebug,
                disp('objective error report');
                PP = PP(I,:);
                SS = SS(I);
                ztest1 = getbspline(C, Xout(:,1), Xout(:,2));
                ztest2 = PP(:,6).*SS + PP(:,3);
                full([ ztest1(:) ztest2(:) ])
                er     = abs(ztest1 - ztest2);
                disp([ 'objective error mean/max  :' ...
                 num2str(mean(er)) ' ' num2str(max(er)) ]);

            Iout
            Xout
                input('wait...');
            end
            return
        end

        s1      = s1(Inot);
        s       = s(Inot);
        s2      = s2(Inot);
        X       = X(Inot, :);
        M       = M(Inot, :);
        II      = II(Inot);

        ztest0  = ztest0(Inot, :);
        xtest0  = xtest0(Inot, :);
        e0      = e0(Inot,:);
        % e1      = e1(Inot,:);
        Inot    = [];
    end


% ray points and cooresponding b-spline height
xtest1    = M.*[ s1 s1 s1 ] + X;                % point
ztest1    = getbspline(C, xtest1(:,1), xtest1(:,2) );
e1        = ztest1 - xtest1(:,3);

% subdivide the remaining rays
temp  = (e0.*e1 <= 0);
i1    = find(temp);        % s1 -> s
i2    = find(~temp);       % s  -> s2

% problem must be here!!
s1new = [ s1(i1) ; s(i2) ];  s2new = [ s(i1) ; s2(i2) ];

% I think P has to be re-arranged as well
X     = [ X(i1,:) ; X(i2,:) ];
M     = [ M(i1,:) ; M(i2,:) ];
II    = [ II(i1,:) ; II(i2,:) ];
k     = k + 1;

if ~mod(k,20)
    disp([ 'Iterations ' num2str(k) ]);
end

  end
```

```
      disp('warning: partial termination only');

  end

return


function ztest0 = getbspline(X, x, y);

 % use different methods depending on number of rays
 l = length(x);

 % [ x y ]
 if   ( l < 2),
      ztest0 = bspnp2d( X, x, y );
 else
      ztest0 = bspgetbig( X, x, y );
 end


return


function OnTerminate

     % collect terminating rays
     err_tol = 0.0001;
     I       = find(abs(e) <= err_tol);
     if      ~isempty(I),

             disp([ 'completed ' ...
               num2str(100* (length(I)/l) ) '  %' ]);
             M       = [ M ; ...
                 xtest(I,1:2) ztest(I) II(I) e(I) P(I,:) ];

             % get the rays which didnt terminate this time around
         Inot    = find(e > err_tol);

         if      isempty(Inot)
                 disp('fully terminated');
             [ l I ] = sort(M(:,4));
             M = M(I,:);

             disp('coordinates');
             M

             ztest1 = full( bspgetbig(C, xtest(:,1), xtest(:,2)) )
             ztest2 = P(:,6).*s + P(:,3)

             disp('comparison');
             [ ztest1(:) ztest2(:) ]

             return
         end

         s1      = s1(Inot);
         s       = s(Inot);
```

```
        s2      = s2(Inot);
        P       = P(Inot, :);
        ztest0  = ztest0(Inot, :);
        xtest0  = xtest0(Inot, :);
        Inot    = [];
    else
            xtest = [];
    end

return
```

Appendix C

Derivation of Corneal Transform Equations

C.1 Introduction

This appendix derives the following model equations,

The general corneal transform

$$n_r = \frac{i_\theta^2\rho_r + (i_z\rho_r - i_r\rho_z)(i_z + \rho_z\psi)}{i_\theta^2\rho_z - (i_z\rho_r - i_r\rho_z)(i_r + \rho_r\psi)} \tag{C.1}$$

$$n_\theta = -\frac{i_\theta(\psi(\rho_z^2 + \rho_r^2) + \rho_z i_z + \rho_r i_r)}{i_\theta^2\rho_z - (i_z\rho_r - i_r\rho_z)(i_r + \rho_r\psi)} \tag{C.2}$$

The nodal corneal transform (with tilt)

$$n_r = -\frac{i_\theta^2 r_m + (i_z r_m + i_r d)(i_z + d\psi)}{i_\theta^2 d + (i_z r_m + i_r d)(i_r - r_m\psi)} \tag{C.3}$$

$$n_\theta = -\frac{i_\theta\{\psi\eta^2 + d i_z - r_m i_r\}}{i_\theta^2 d + (i_z r_m + i_r d)(i_r - \psi r_m)} \tag{C.4}$$

The telecentric transform (with tilt)

$$n_r = -i_r\frac{(i_z + \psi)}{i_\theta^2 + i_r^2} \tag{C.5}$$

$$n_\theta = -i_\theta\frac{(i_z + \psi)}{i_\theta^2 + i_r^2} \tag{C.6}$$

The nodal transform (no tilt)

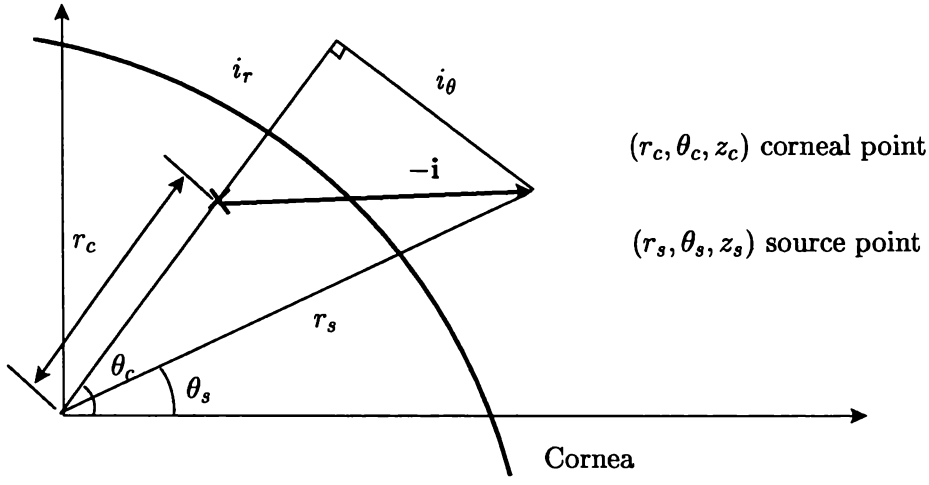

Figure C.1: The diagram shows the cornea in a front on view. Shown are the components of the (un-normalized) incident ray vector $\mathbf{i} = (i_r, i_\theta, i_z)$, emanating from the source point (r_s, θ_s, z_s). The positive z-axis points out of the page. The intersection of the optic axis with the corneal surface defines the origin. The coordinates (r, θ) (i.e. ignoring subscripts) specifies the projection of a corneal point f, onto the x-y plane.

$$n_r = -\frac{i_z + d\psi}{i_r - r_m\psi} \tag{C.7}$$

$$n_\theta = 0 \tag{C.8}$$

The telecentric transform (no tilt)

$$n_r = -\frac{i_z + \psi}{i_r} \tag{C.9}$$

$$n_\theta = 0 \tag{C.10}$$

where,

$$\psi = \sqrt{\frac{i_r^2 + i_\theta^2 + i_z^2}{\rho_r^2 + \rho_z^2}} \tag{C.11}$$

$$\eta = \sqrt{r_m^2 + d^2} \tag{C.12}$$

C.2 Derivation of Corneal Transform Equations

The incident, reflected and normal vectors are given by,

$$\hat{\mathbf{i}} = \frac{(i_r, i_\theta, i_z)}{|(i_r, i_\theta, i_z)|} \tag{C.13}$$

$$\hat{\boldsymbol{\rho}} = \frac{(\rho_r, 0, \rho_z)}{|(\rho_r, 0, \rho_z)|} \tag{C.14}$$

$$\hat{\mathbf{n}} = \frac{(n_r, n_\theta, n_z)}{|(n_r, n_\theta, n_z)|} \tag{C.15}$$

where

$$n_r = -f_r \tag{C.16}$$

$$n_\theta = -\frac{1}{r} f_\theta \tag{C.17}$$

$$n_z = 1 \tag{C.18}$$

$$i_r = r_c - r_s \cos(\theta_c - \theta_s) \tag{C.19}$$

$$i_\theta = r_s \sin(\theta_c - \theta_s) \tag{C.20}$$

$$i_z = f - z_s \tag{C.21}$$

f_r and f_θ are the first derivatives of f (the corneal height), (r_s, θ_s, z_s) is a point on the object ring, and (r_c, θ_c, z_c) is a point on the corneal surface (see Figure C.1). The following equations apply at the corneal surface,

$$\hat{\mathbf{n}} \cdot (\hat{\mathbf{i}} \times \hat{\boldsymbol{\rho}}) = 0 \tag{C.22}$$

$$\hat{\mathbf{n}} \cdot \hat{\boldsymbol{\rho}} = -\hat{\mathbf{n}} \cdot \hat{\mathbf{i}} \tag{C.23}$$

$$\hat{\boldsymbol{\rho}} \neq -\hat{\mathbf{i}} \tag{C.24}$$

Entering the definitions (C.13) - (C.15) in equations (C.22) gives,

$$\begin{aligned} & (n_r, n_\theta, n_z) \cdot \{(i_r, i_\theta, i_z) \times (\rho_r, 0, \rho_z)\} = 0 \\ \Rightarrow \quad & (n_r, n_\theta, n_z) \cdot (i_\theta \rho_z, -(i_r \rho_z - i_z \rho_r), -i_\theta \rho_r)) = 0 \\ \Rightarrow \quad & n_r(i_\theta \rho_z) - n_\theta(i_r \rho_z - i_z \rho_r) - n_z(i_\theta \rho_r) = 0 \end{aligned} \tag{C.25}$$

Similarly, for equation (C.23),

$$\frac{n_r i_r + n_\theta i_\theta + n_z i_z}{\sqrt{i_r^2 + i_\theta^2 + i_z^2}} = -\frac{n_r \rho_r + n_z \rho_z}{\sqrt{\rho_r^2 + \rho_z^2}} \tag{C.26}$$

Equations (C.25) and (C.26) may be collected into matrix form,

$$\begin{bmatrix} a_1 & a_2 \\ a_3 & a_4 \end{bmatrix} \begin{bmatrix} n_r \\ n_\theta \end{bmatrix} = \begin{bmatrix} b_1 \\ b_2 \end{bmatrix} \tag{C.27}$$

where the co-efficients of the matrix are given by,

$$a_1 = i_\theta \rho_z \tag{C.28}$$

$$a_2 = i_z \rho_r - i_r \rho_z \tag{C.29}$$

$$a_3 = \frac{i_r}{\sqrt{i_r^2 + i_\theta^2 + i_z^2}} + \frac{\rho_r}{\sqrt{\rho_r^2 + \rho_z^2}} \tag{C.30}$$

$$a_4 = \frac{i_\theta}{\sqrt{i_r^2 + i_\theta^2 + i_z^2}} \tag{C.31}$$

$$b_1 = i_\theta \rho_r \tag{C.32}$$

$$b_2 = -\left\{ \frac{i_z}{\sqrt{i_r^2 + i_\theta^2 + i_z^2}} + \frac{\rho_z}{\sqrt{\rho_r^2 + \rho_z^2}} \right\} \tag{C.33}$$

which may be inverted to give n_r and n_θ,

$$\begin{bmatrix} n_r \\ n_\theta \end{bmatrix} = \frac{1}{a_1 a_4 - a_2 a_3} \begin{bmatrix} a_4 b_1 - a_2 b_2 \\ a_1 b_2 - a_3 b_1 \end{bmatrix} \tag{C.34}$$

Introducing the definitions,

$$I = \sqrt{i_r^2 + i_\theta^2 + i_z^2} \tag{C.35}$$

$$P = \sqrt{\rho_r^2 + \rho_z^2} \tag{C.36}$$

and evaluating the determinant part gives,

$$\begin{aligned} a_1 a_4 - a_2 a_3 &= (1/I)(i_\theta \rho_z) i_\theta - (i_z \rho_r - i_r \rho_z)(i_r/I + \rho_r/P) \\ &= (1/IP)\left\{ i_\theta^2 \rho_z P - (i_z \rho_r - i_r \rho_z)(i_r P + \rho_r I) \right\} \end{aligned} \tag{C.37}$$

the elements of the column vector can be evaluated,

$$\begin{aligned} a_4 b_1 - a_2 b_2 &= (i_\theta^2 \rho_r)(1/IP) + (i_z \rho_r - i_r \rho_z)(i_z P/IP + I\rho_z/IP) \\ &= (1/IP)\left\{ i_\theta^2 \rho_r P + (i_z \rho_r - i_r \rho_z)(i_z P + \rho_z I) \right\} \end{aligned} \tag{C.38}$$

$$\begin{aligned} a_1 b_2 - a_3 b_1 &= -i_\theta \rho_z (i_z/I + \rho_z/P) - (i_r/I + \rho_r/P) i_\theta \rho_r \\ &= (-i_\theta/IP)(\rho_z(i_z P + I\rho_z) + (P i_r + I\rho_r)\rho_r) \end{aligned} \tag{C.39}$$

which gives,

$$n_r = \frac{i_\theta^2\rho_r + (i_z\rho_r - i_r\rho_z)(i_z + \rho_z\psi)}{i_\theta^2\rho_z - (i_z\rho_r - i_r\rho_z)(i_r + \rho_r\psi)} \tag{C.40}$$

$$n_\theta = -\frac{i_\theta(\psi(\rho_z^2 + \rho_r^2) + \rho_z i_z + \rho_r i_r)}{i_\theta^2\rho_z - (i_z\rho_r - i_r\rho_z)(i_r + \rho_r\psi)} \tag{C.41}$$

where the variable ψ given by

$$\psi = \sqrt{\frac{i_r^2 + i_\theta^2 + i_z^2}{\rho_r^2 + \rho_z^2}} \tag{C.42}$$

has been introduced.

C.2.1 Nodal Camera Equations

The nodal camera is given by the equation,

$$\boldsymbol{\rho} = (-r_m, 0, d) \tag{C.43}$$

Substituting the definition for $\boldsymbol{\rho}$ in the equations (C.40)-(C.41) gives,

$$\begin{aligned} n_r &= \frac{i_\theta^2\rho_r + (i_z\rho_r - i_r\rho_z)(i_z + \rho_z\psi)}{i_\theta^2\rho_z - (i_z\rho_r - i_r\rho_z)(i_r + \rho_r\psi)} \\ &= -\frac{i_\theta^2 r_m + (i_z r_m + i_r d)(i_z + d\psi)}{i_\theta^2 d + (i_z r_m + i_r d)(i_r - r_m\psi)} \end{aligned} \tag{C.44}$$

Similarly for n_θ

$$\begin{aligned} n_\theta &= -\frac{i_\theta(\psi(\rho_z^2 + \rho_r^2) + \rho_z i_z + \rho_r i_r)}{i_\theta^2\rho_z - (i_z\rho_r - i_r\rho_z)(i_r + \rho_r\psi)} \\ &= -\frac{i_\theta\{\psi\eta^2 + d i_z - r_m i_r\}}{i_\theta^2 d + (i_z r_m + i_r d)(i_r - \psi r_m)} \end{aligned} \tag{C.45}$$

where

$$\eta = \sqrt{r_m^2 + d^2} \tag{C.46}$$

summarizing gives,

$$n_r = -\frac{i_\theta^2 r_m + (i_z r_m + i_r d)(i_z + d\psi)}{i_\theta^2 d + (i_z r_m + i_r d)(i_r - r_m\psi)} \tag{C.47}$$

$$n_\theta = -\frac{i_\theta\{\psi\eta^2 + d i_z - r_m i_r\}}{i_\theta^2 d + (i_z r_m + i_r d)(i_r - \psi r_m)} \tag{C.48}$$

which is the nodal corneal transform with tilt. Assuming there is no corneal tilt, i.e. $i_\theta = 0$ gives,

$$n_r = -\frac{i_z + d\psi}{i_r - r_m\psi} \tag{C.49}$$

$$n_\theta = 0 \tag{C.50}$$

C.2.2 Telecentric Camera Equations

For the telecentric camera,

$$\boldsymbol{\rho} = (0, 0, \rho_z) \tag{C.51}$$

where the value of ρ_z is not important, since it vanishes on substituting in equations (C.40)-(C.41). For n_r,

$$\begin{aligned} n_r &= -\frac{i_r(i_z + \psi)}{i_\theta^2 + i_r^2} \\ &= -\frac{i_r(i_z + \psi)}{\psi^2 - i_z^2} \\ &= -\frac{i_r(i_z + \psi)}{(\psi + i_z)(\psi - i_z)} \\ &= -\frac{i_r}{\psi - i_z} \end{aligned} \tag{C.52}$$

and in the same way for n_θ,

$$\begin{aligned} n_\theta &= -\frac{i_\theta(i_z + \psi)}{i_\theta^2 + i_r^2} \\ &= -\frac{i_\theta}{\psi - i_z} \end{aligned} \tag{C.53}$$

Assuming that $i_\theta = 0$ i.e. telecentric with no tilt,

$$n_r = -\frac{i_z + \psi}{i_r} \tag{C.54}$$

$$n_\theta = 0 \tag{C.55}$$

C.3 Convergence of the Numerical Method

Consider two subsequent image points r_i and r_{i+1} along a particular meridian (i.e. two values of r_m). Take the equation for the numerical method,

$$f^j(r_{i+1}) = \frac{h_i}{3}\left\{F(r_{i+1}, f^{j-1}(r_{i+1})) + 2f'(r_i)\right\} + \frac{h_i^2}{6}f''(r_i) + f(r_i) \tag{C.56}$$

Subtract two successive estimates $f^{j+1}(r_{i+1})$ and $f^{j}(r_{i+1})$ to give,

$$f^{j+1}(r_{i+1}) - f^{j}(r_{i+1}) = \frac{h_i}{3}\left\{F(r_{i+1}, f^{j}(r_{i+1})) - F(r_{i+1}, f^{j-1}(r_{i+1}))\right\} \tag{C.57}$$

which by the Mean Value Theorem,

$$\frac{\partial F}{\partial f}(\eta_0) = \frac{F(r_{i+1}, f^{j}(r_{i+1})) - F(r_{i+1}, f^{j-1}(r_{i+1}))}{f^{j}(r_{i+1}) - f^{j-1}(r_{i+1})} \tag{C.58}$$

where $f^{j}(r_{i+1}) < \eta_0 < f^{j-1}(r_{i+1})$ gives,

$$\left\{f^{j+1}(r_{i+1}) - f^{j}(r_{i+1})\right\} = \frac{h_i}{3}\frac{\partial F}{\partial f}(\eta_0)\left\{f^{j}(r_{i+1}) - f^{j-1}(r_{i+1})\right\} \tag{C.59}$$

where it has been assumed that F is differentiable. Convergence will occur provided,

$$\left|\frac{h_i}{3}\frac{\partial F}{\partial f}(\eta_0)\right| < 1 \tag{C.60}$$

is true. Differentiating the transform equation F with respect to f, and substituting values to maximize the LHS of (C.60) will indicate whether the method converges or not.

C.3.1 Convergence for a Telecentric Camera

Take the telecentric camera model with no tilt,

$$f' = F(r_m, f) = \frac{i_z + \sqrt{i_r^2 + i_z^2}}{i_r} \tag{C.61}$$

where $i_z = f - z_s$ and $i_r = r_c - r_s = r_m - r_s$. The intention is to establish that (C.60) holds for this camera model equation . Differentiating w.r.t.f gives,

$$\begin{aligned}\frac{\partial F}{\partial f} &= \frac{1}{i_r}\left\{\frac{di_z}{df} + \frac{\partial\left(\sqrt{i_r^2 + i_z^2}\right)}{\partial f}\right\} \\ &= \frac{1}{i_r}\left\{1 + \frac{i_z}{\sqrt{i_r^2 + i_z^2}}\right\}\end{aligned} \tag{C.62}$$

Now, the maximum value of the LHS of equation (C.60) is estimated by substituting (C.62) into (C.60) which gives,

$$\begin{aligned}\left|\frac{h_i}{3}\frac{\partial F}{\partial f}\right|_{\max} &= \left|\frac{h_i}{3}\right|\left|\frac{1}{i_r}\right|\left|1 + \frac{i_z}{\sqrt{i_r^2 + i_z^2}}\right| \\ &\leq \frac{1}{6}.\frac{1}{4}.2 \\ &= \frac{1}{12} < 1\end{aligned} \tag{C.63}$$

Description	Variable	Lower Bnd(mm)	Upper Bnd(mm)
Object radius	r_s	5.0	16
Object position	z_s	4.0	65
Image radius	r	0.2	4.0
Image position	f	0.0	3.0
Step-size	h	0.05	0.5

Table C.1: Bounding values placed on the corneal transformation equations. Note that all measurements are inmm

where $h_i = \frac{1}{2}$ mm, and $i_r = -4$ mm have been taken from Table C.1. These values maximize the value of the LHS of the inequality (whilst remaining within the limits of possible values for the VK). The factor of 2, is a conservatively chosen factor based on the observation that,

$$0 \leq \left| 1 + \frac{i_z}{\sqrt{i_r^2 + i_z^2}} \right| \leq 2 \tag{C.64}$$

though for the majority of corneas it will be that $i_z < 0$ or a small +ve value $\ll 1$ (and hence, in practice, much lower than 2). In any case, the result is that the LHS is less than 1 (i.e. 1/12), and so convergence is guaranteed.

Appendix D

Corneal Reconstruction Algorithm

D.1 A Corneal Reconstruction Algorithm

D.1.1 Code for a Reconstruction Algorithm

```
function [ f, fr ] = vkrecoversurf(RK),

%
% VKRECOVERSURF    recover the height component given
% the radial samples
%
% [ f fr ] = vkrecoversurf(RK,my_flag)
%
% where        f            recovered height
%              fr           recovered radial derivative
%              RK           [360 x 16] radial sample points
%              h0,hphi0,hr0 give stats against these values
%
% note: some internal variables hardcoded
%       based on cf_recon/getrecon.m
%



% initialize
nAng              = size(RK,1)-1; nRing             = 16;
convergence_error = 2e-7;

% setup data
PHI = (0:1:nAng)'; PHI = PHI(:,ones([1 nRing])); RADII   = RK;

if ~exist('my_flag'),

  % technomed videokeratograph
  disp('original technomed');
  u1    = [ 0 15 23 31 36 41 44 47 49 51 53 55 56.5 58 60 61.5 ];
  rs    = 4.75  + 0.177.*u1;
  zs    = 64.49 - 0.984.*u1;
```

```
end


its = 0; eold = 0; er  = 1;
[ X Y ]
=pol2cart(degtorad(PHI),RADII);


zs0     = zs(ones([360 1]),:); rs0     = rs(ones([360 1]),:);
theta_i = degtorad(PHI);

my_err  = inf; f       = zeros(size(PHI)); f_old  = f;


while(my_err > convergence_error ),

        tic,

    ir    = RADII - rs0;
    iz    = f - zs0;
    fr    = - ( sqrt( (ir./iz).^2 + 1 ) - 1 )./(ir./iz);

    % fr    = Ftcentric(RADII, f, rs0, zs0);

    % e = max(abs(fr - fr11))
    % e
    % input('wait...')


    % reconstruct HTEST
    f   = my_integrate(PHI, RADII, fr);
    hinitr  = f(:,1);
    its = its + 1;

    a = toc;
    l = f(:) - f_old(:);
    I = find(~isnan(l(:)));
    my_err = std(abs(l(I)));

    f_old = f;
    disp([ 'c.err = ' num2str(my_err) ' ti. ' num2str(a) ]);

end


return


% ----------
% integrate
% ----------

function H = my_integrate(phi,rr,hr),

  nAng  = size(phi,1)-1;
  nRing = size(phi,2);

  % hinitr = hinitr(:); % make sure it points down
```

```
  H = zeros([ nAng+1 nRing ]);
  for l=1:(nAng+1),
    htemp  = ctintpp2d([ 0 rr(l,:) ], [ 0 hr(l,:) ], rr(l,:) );
    H(l,:) = htemp';
    % H(l,:)
    % input('wait...');
  end

return
```

D.1.2 Routine for Integrating the Corneal Slope

This routine integrates the corneal slopes to give the corneal height

```
function YI = ctintpp2(X, Y1, XI )

%
% INTEGRAL OF THE SPLINE THAT PASSES THROUGH THE GIVEN POINTS
%
% CTINTPP2D.M
%
% return integral of the cubic piecewise
% polynomial - derivatives supplied.  Use
% estimated derivatives for the hard part!
%
%
%
% X - MATRIX OF X VALUES
% Y1    - Y(X)
% XI    - fine grid
% y0    - initial
%

X      = X(:); Y1     = Y1(:); XI     = XI(:); knots  = size(X,1);

%%%%%%%%%%%%%%%%%%%%%
%                   %
% ESTIMATE DY/DX    %
%                   %
%%%%%%%%%%%%%%%%%%%%%

dy1     = diff(Y1);         % difference
len     = size(dy1,1);
dy2     = [ dy1(2:len) ; 0 ];
dy      = dy1
+ dy2; dy(len)     = 0;
dx1     = diff(X);
len     = size(dx1,1);
dx2     = [ dx1(2:len) ; NaN ];
dx      = dx1 + dx2;
dx(len)     = dx(len-1);            % last x displacement



% jasons method
rs    = 4.75; zs    = 64.49;
```

```
K    = Ftcentric(X(2),0,rs,zs) /
(X(2));


% derivatives of tranformation equation
dydx  = [ K ; dy./dx ];


XI  = XI'; Y   = Y1; AA  = [];

fxb     = K; for i = 1:1:knots-1,

    xa = 0;
    xb = X(i+1) - X(i);
    fxa  = dydx(i);

    if  (i > 1),
        fxb  = (2/(X(i)-X(i-1)) )*( dydx(i) - dydx(i-1) ) + fxb;
    else
         % K
         fxb  = K;
         % input('wait...');
    end

    ya = Y(i);
    yb = Y(i+1);

    % local curvature polynomial
    % F = [ yb fxa ya ]';
    % B = [  xb^2 xb 1 ; 0 1 0 ; 0 0 1 ];

    % continuous curvature polynomial
    % F = [ yb fxb ya ]';
    % B = [  xb^2 xb 1 ; 0 1 0 ; 0 0 1 ];

    A = B\F;
    AA = [ AA ; A'];
end

%%%%%%%%%%%%%%%%%%%%%%%%%%%%%%%%%%%%%%%%%%%%%%%%%%%%%%%%%%%%%%%%%%%%%%%%%%%%%%%%
% GOT PIECEWISE POLYNOMIALS - DETERMINE INTEGRAL    %
%%%%%%%%%%%%%%%%%%%%%%%%%%%%%%%%%%%%%%%%%%%%%%%%%%%%%%%%%%%%%%%%%%%%%%%%%%%%%%%%

ordAA   = size(AA,2);       % order of integral polynomials
rowAA   = size(AA,1);       % number of pieces
temp1   = ordAA:-1:0;       % explicit order vector
temp1(ordAA+1) = 1;


y0      = 0;
y   = y0;           % initialize
BB  = [];

% add an extra bit on for the intial point

for j=1:rowAA,

    bb  = [ AA(j,:) y0 ]./temp1;    % current piece polynomial
```

```
    pp1 = mkpp([X(j) X(j+1)],bb);
    y0  = ppval(pp1,X(j+1));        % what is the end-point?
    y   = [ y ; y0 ];           % accumulate into vector
    BB  = [ BB ; bb ];
end

YI  = []; pp3 = mkpp(X',BB); YI1 = ppval(pp3,XI); YI  = [ YI ; YI1
];


YI  = YI';

return
```

D.1.3 Routines for Compensating for Skew-Rays

The following code accounts for skew-rays. The main routines described are:

revise returns the revised slope $\hat{f}_r$ and tilt f_θ estimates, i.e. the slope taking skew-rays into account, and the tilt from which the estimate was made.

mkbigpp returns a collection of piecewise polynomial objects, i.e. a radial piecewise polynomial object for every meridian.

getangular returns estimates of the angular derivative f_θ.

```
% REVISE revise the estimate for dfdr
%
% [ dfdr, dfdt ] = revise(r,rs,zs,f,dfdr,a,b,c,d),
%
% where r       = radial image ring values matrix
%       rs      = radial object position matrix
%       zs      = axial object position matrix
%       f       = original corneal height matrix
%       dfdr    = original corneal slope matrix
%       a,b,c,d = polynomial co-efficients matrices
%


function [ dfdr, dfdt ] = revise(r,rs,zs,f,dfdr,a,b,c,d),


   % Create an object for storing all cubic pieces and the
   % end points of these pieces for the recovered corneal surface
```

```
   F            = mkbigpp(r(:,2:end),a,b,c,d);

   % Determine dfdt based on the corneal surface object F
   % for the requested distances r
   dfdt         = getangular(F,r);

   % Estimate the revised slope dfdr see eqn (3.64)
   % remove first column which are zeros
   dfdt0        = dfdt(:,2:end);
   r0           = r(:,2:end);
   dfdr0        = dfdr(:,2:end);
   dfdr0        = sqrt(dfdr0.^2 - ((1./r0).*dfdt0).^2);

   % Here is the revised estimate for dfdr
   dfdr(:,2:end)    = sign(dfdr(:,2:end)).*dfdr0;

return

%
%  HELPER FUNCTIONS
%


function F = mkbigpp(r,a,b,c,d),

% MKBIGPP create a corneal surface object.
%
% F = mkbigpp(r,a,b,c,d)
%
% r = breaks of the polynomial
% a = a coefficients
% b = b coefficients
% c = c coefficients
```

```
% d = d coefficients
%
% please note: this will append leading zeros to the
% include leading zeros

  F.r = [ r(:,1)*0 r(:,1:(end-1)) ];
  F.a = a;
  F.b = b;
  F.c = c;
  F.d = d;

return



function fphi = getangular(F,r),

% GETANGULAR determine the tilt
%
% use F = mkbigpp returned function
%       t = theta
%       r = radial values

F1.r    = rollu(F.r); F1.a    = rollu(F.a); F1.b    = rollu(F.b);
F1.c    = rollu(F.c); F1.d    = rollu(F.d); y2      = bigpp(F1,r);

F1.r    = rolld(F.r); F1.a    = rolld(F.a); F1.b    = rolld(F.b);
F1.c    = rolld(F.c); F1.d    = rolld(F.d); y1      = bigpp(F1,r);

fphi    = (y2 - y1)/(2*pi/180);

return
```

```
function A = rolld(A)

% ROLLD shift matrices down a row replacing first
% row with the last row

     A = [ A(end,:) ; A(1:(end-1),:) ];
return

function A = rollu(A)

% ROLLU shift matrices up a row replacing last
% row with the first row

     A = [ A(2:end,:) ; A(1,:) ];
return

function [ y, h ] = bigpp(F,rnew),

% BIGPP determine values for a big polynomial.
% take rnew and determine the height as the point r
% determine the piece which rnew is in
%
% r should have leading zeros


   nangles  = size(F.r,1);
   nrings   = size(F.r,2);
   npoints  = size(rnew,2);

   % build coefficients
   h     = zeros(size(rnew));
   a     = zeros(size(rnew));
   b     = zeros(size(rnew));
   c     = zeros(size(rnew));
```

```
d     = zeros(size(rnew));

for i=1:nangles,

   % columns are for each data point
   % rows are possible slots

   rlower = F.r(i,:)';
   rlower = rlower(:,ones([1 npoints]));

   rupper = [ F.r(i,2:end) inf ]';
   rupper = rupper(:,ones([1 npoints]));

   % set up each data point (nrings+1 x npoints)
   rtest  = rnew(i,:);
   rtest  = rtest(ones([ nrings 1  ]),:);
   itot   = ((rlower <= rtest).*(rtest < rupper));

   h(i,:) = sum((rtest - rlower).*itot);

   % h
   % rtest
   % rlower
   % itot

   % coefficients for each piece
   a0    = F.a(i,:)'; a0 = a0(:,ones([1 npoints]));
   b0    = F.b(i,:)'; b0 = b0(:,ones([1 npoints]));
   c0    = F.c(i,:)'; c0 = c0(:,ones([1 npoints]));
   d0    = F.d(i,:)'; d0 = d0(:,ones([1 npoints]));

   % size(itot)
   % size(a0)
```

```
    a(i,:) = sum(a0.*itot);
    b(i,:) = sum(b0.*itot);
    c(i,:) = sum(c0.*itot);
    d(i,:) = sum(d0.*itot);

end

% determine co-efficients
y = a.*(h.^3) + b.*(h.^2) + c.*h + d;

return
```

D.1.4 Calibration Filtering

The rationale for the filtering procedure of section 3.6 will now be described in detail. It is desirable to preserve astigmatism of the cornea when filtering, since this is a clinically important surface feature. This amounts to preserving the astigmatism in the *image* of a ring (denoted here by $r(\theta)$), formed by reflection from an astigmatic cornea. The fourier transform of $r(\theta)$ (see Figure 3.11) has several non-zero spectral components, which increase in number as astigmatism increases.

However, by re-parameterizing, it is to possible to preserve the spectral content corresponding to astigmatism. In particular, introducing the ellipse parameter t, the astigmatic cornea can be represented in parameterized form $x(t)$ and $y(t)$ as,

$$x = a\cos(t) \tag{D.1}$$

$$y = b\sin(t) \tag{D.2}$$

which has a very clean fourier transform (see Figures 3.13(b) and 3.13(c)). Comparing this equation with the corresponding equations for x and y as determined from the measurements $r(\theta)$, i.e.

$$x = r\cos(\theta) \tag{D.3}$$

$$y = r\sin(\theta) \tag{D.4}$$

gives the re-parameterization,

$$t = \tan^{-1}\left(\frac{a}{b}\tan(\theta)\right) \tag{D.5}$$

found by setting equation D.1 equal to D.3, equation D.2 equal to D.4 and dividing the results. The ratio between a/b can be determined directly from the data.

A final note: fourier transforming and filtering the data requires interpolating the data over a uniformly spaced grid. This is achieved using linear interpolation, which is a standard MATLAB command.

Appendix E

A Subdivision algorithm

E.1 A Subdivision Algorithm

```
function [ p, x1, x2, x3 ] =
findray(tbopt1,rho,err,S,target,dy,dbug);

% FINDRAY.M search the surface for the incident position which
% corresponds to the required exit ray is found.
% The method uses triangular subdivision, the initial search
% is sequential and has not been optimized.
%
% function p = findray(tbopt1,rho,err,source,target,dy,dbug)
%
% where   tbopt1 = lens prescription (RAYTRAK)
%         rho    = desired exit ray
%         err    = error
%         source = light source
%         target = default target for light source
%         dy     = grid dimensions (dy x dy) about target point
%         dbug   = debug option 'on' 'off'
%


% DEFAULT DATA
if ~exist('tbopt1'),

   mdebug('off');
   % input('here?');

  imz    = 0;
  ap     = 1000;

  sou_z  = 200;
  sou_y  = 20;
  S      = [ 0 sou_y sou_z ];
  rho    = [ 0.2 0.2 1 ];  rho = rho/norm(rho);
  target = [ 0 0 0 ];          % initial target
  dy     = 9;

  % nrays  = 16;
```

```
  % GET THE OPTIC TABLE
  % NEED TO ADD THE IMAGE OF
  % THE OPTIC SYSTEM - SO
  % THAT RAYS ARE TRACED OUT
  % OF THE EYE .
  tbopt  = getLeGrand;
  tbopt1 = reflectatlevel(tbopt,4);
  tbopt1 = tackonplane(tbopt1,imz,ap);

  err = 1.e-4;

end

if exist('dbug'),
   mdebug(dbug);
end


nrays = 16;

% generate initial triangulation
[ exitr gp ] = firetestrays(tbopt1, S, target, nrays, dy);

if isempty(exitr),
   error('Rays must exit system to continue search');
   return
end

[ p1 p2 p3 u1 u2 u3 ] = triangulate(gp,exitr);
l      =
size(p1,1); estart = clock;

mdisp([ 'triangles ' num2str(l) ]);

for k = 1:l,

  % set up the current triangle
  x1  = p1(k,:); x2 = p2(k,:); x3 = p3(k,:);
  w1  = u1(k,:); w2 = u2(k,:); w3 = u3(k,:);

  % determine if the required ray is within the element limits
  % recursively search triangles
  [ p x1 x2 x3 ] = precurse(tbopt1,x1,x2,x3,w1,w2,w3,rho,err,S);

  if ~isempty(p),

     % found
     if mdebug

        mdisp('-----------------------------------------------------');
        mdisp('intersection point found');
        area           = gettriarea(x1,x2,x3);
        mdisp([ 'entrance coord  ' num2str(p) ]);
        mdisp([ 'with bnd, area  ' num2str(area) ] );
        mdisp([ 'err. radius     ' num2str(sqrt(area/pi)) ]);

        tbrays   = getray(S,p,'source');
```

```
        X        = tray42(tbopt1,1,tbrays,0);  % trace these rays
        mdisp([ 'rho error       ' num2str(norm(rho - X(4:6))) ]);
        mdisp([ 'time            '
            num2str(abs(etime(estart,clock))) ]);

      end
      return

    end

end

disp([ 'no ray found in grid' ]);
% input('wait...');
p = []; return

% ------------------------
% create the triangulation
% ------------------------

function [p1, p2, p3, u1, u2, u3 ] = triangulate(gp, X0),

  % gp = surviving grid points
  % X0 = surviving exit rays

  % surviving grid points and rays at these points
  x       = gp(:,1);
  y       = gp(:,2);
  z       = gp(:,3);
  ux      = X0(:,4);
  uy      = X0(:,5);
  uz      = X0(:,6);

  % points on the convex hull
  % k       = convhull(x,y);
  % x       = x(k);
  % y       = y(k);
  % z       = z(k);
  % ux      = ux(k,:);
  % uy      = uy(k,:);
  % uz      = uz(k,:);

  % initial mesh using convex hull points only
  tri     = delaunay(x,y);

  % each tri contains indices to the (x,y) vectors
  % tri1 = index of the 1st triangle point
  % tri2 = index of the 2nd triangle points
  % tri3 = index of the 3rd triangle points
  tri1 = tri(:,1);
  tri2 = tri(:,2);
  tri3 = tri(:,3);

  p1 = [ x(tri1) y(tri1) z(tri1) ];
  p2 = [ x(tri2) y(tri2) z(tri2) ];
  p3 = [ x(tri3) y(tri3) z(tri3) ];

  u1 = [ ux(tri1) uy(tri1) uz(tri1) ];  1 = ...
```

```
    sqrt(u1(:,1).^2 + u1(:,2).^2 + u1(:,3)); u1 = u1./[ l l l];
  u2 = [ ux(tri2) uy(tri2) uz(tri2) ];  l = ...
    sqrt(u2(:,1).^2 + u2(:,2).^2 + u2(:,3)); u2 = u2./[ l l l ];
  u3 = [ ux(tri3) uy(tri3) uz(tri3) ];  l = ...
    sqrt(u3(:,1).^2 + u3(:,2).^2 + u3(:,3)); u3 = u3./[ l l l ];

%  clf;
%  trimesh(tri, x,y,0*x); view([0 90]);
%  size(tri)
%  input('wait...');

return


function x1   = fuzz(x1),

 efuzz = 1.e-4;
 x1    = x1 + efuzz*(rand(size(x1)) - 0.5)

return


function area = gettriarea(p1,p2,p3),

  % error
  A    = p2 - p1; % A = A*100;
  B    = p3 - p2; % B = B*100;
  C    = p1 - p3; % C = C*100;
  area = abs( 0.5*( A(1)*B(2) + B(1)*C(2) ...
            - A(2)*B(1) - B(2)*C(1) ) );

return


function [ L, X, Y, ln, wd] = getgridandrays(rayspernode, epupil,
gridinfo, T, S0),

  [ X Y ]  = getgrid(rayspernode, epupil, gridinfo, T, 'matrix');
  ln       = size(X,1);
  wd       = size(X,2);
  X        = reshape(X,[ ln*wd 1 ]);
  Y        = reshape(Y,[ ln*wd 1 ]);
  I0       = (1:1:(ln*wd))';
  L        = getray(S0, [ X Y 0*X ], 'source');

return

% ------------------------------------------------------
%
% FIRE TEST RAYS
%
%  ------------------------------------------------------


function [ X, tbrays1, tbrays ] ...
     = firetestrays(tbopt, source,target, nrays, dy),

% FIRETESTRAYS.M launch test rays and return
```

```
% the rays that succeeded in passing through
% the system.
%
% function [ X, tbrays1, tbrays ] ...
%    = firetestrays(tbopt, source, target, nrays, dy)
%
% where tbopt  = optic table
%       source = source point
%       target = target point
%       nrays  = rays to test
%       dy     = grid dimensions
%
% returns: X = []   all rays missed
%          X = full all rays passed
%          X = some some rays were blocked


  % create a square grid
  gridinfo.type = 'square';


  % nrays
  % dy
  % gridinfo
  % target

  tbrays1        = getgrid(nrays,dy,gridinfo,target);
  tbrays1(:,1:2) = fuzz(tbrays1(:,1:2));
  tbrays         = getray(source, tbrays1, 'source');
  nlen1          = size(tbrays,1);

  % send it through the system
  [ X I ] = tray42(tbopt,1,tbrays,0);
  tbrays1 = tbrays1(I,:);
  tbrays  = tbrays(I,:);


  % if all rays were unsuccessful, then the point source
  % needs better aim
  if isempty(I)
      % disp('error: no rays survived  ...
      % - must have some succeed to continue');
      X = [];
      return
  end

return


function x1   = fuzz(x1),

 efuzz = 1.e-5;
 x1    = x1 + efuzz*(rand(size(x1)) - 0.5);

return


% ------------------------------------------
```

```
%
% PRECURSE.M
%
% ------------------------------------------


function [ p,s1,s2,s3 ] =
precurse(tbopt,p1,p2,p3,u1,u2,u3,rho,err,source),

% PRECURSE.M recursively search for the
% bounding triangle.
%
% p1,p2,p3 = entrance grid points
% u1,u2,u3 = exit ray vectors

[ encl al be ga ] = isenclosed(u1,u2,u3,rho);

mdisp('testing enclosure') if  isempty(encl),
    mdisp('---- not enclosed');
    p  = [];
    s1 = [];
    s2 = [];
    s3 = [];
    return
end

% bounding triangles (OK)
% if area is small enough then return answer
A    = p2 - p1; % A = A*100;
B    = p3 - p2; % B = B*100;
C    = p1 - p3; % C = C*100;
area = abs( 0.5*( A(1)*B(2) + B(1)*C(2) - A(2)*B(1) - B(2)*C(1) )
); mdisp([ 'parent triangle area  ' num2str(area) ] ); if   area <
err,
     p = p1*al + p2*be + p3*ga;
     % p = pmean;
     s1 = p1;
     s2 = p2;
     s3 = p3;
     return
end


mdisp('... testing subtriangles'); mdisp([ 'est. search position
' num2str([al be ga]) ]);

% find new mean point
pmean = mean([ p1 ; p2 ; p3 ]);


% trace an extra ray
tbray = getray(source,pmean,'source'); u     =
tray42(tbopt,1,tbray,0); u     = u(4:6);


% recurse on new triangles
mdisp('--subtriangle 1'); [ p s1 s2 s3 ] =
precurse(tbopt,p1,p2,pmean,u1,u2,u,rho,err,source);
```

```
if isempty(p),
   mdisp('--subtriangle 2');
   [ p s1 s2 s3 ] = ...
         precurse(tbopt,pmean,p2,p3,u,u2,u3,rho,err,source);
   if isempty(p)
      mdisp('--subtriangle 3');
      [ p s1 s2 s3 ] = ...
        precurse(tbopt,p1,pmean,p3,u1,u,u3,rho,err,source);
      if isempty(p),
     disp('warning: unbound warning');
         % input('wait...');
      end
      return
   end
end


return
```

Appendix F

The Modulation Threshold

This appendix presents the model of Barten for the modulation threshold $m_t(u)$ used in the SQuare Root Integral (SQRI) metric. The modulation threshold is the modulation required for 50% identification of a sinusoidal grating presented to an observer under the particular experimental conditions. The reciprocal of this function is the Contrast Sensitivity Function (CSF), which is denoted $S(u)$ in the following equation,

$$S(u) = \frac{1}{m_t(u)} = \frac{M_{opt}(u)/k}{\sqrt{\frac{4}{T}\left(\frac{1}{X_0^2} + \frac{1}{X_{max}^2} + \frac{u^2}{N_{max}^2}\right)\left(\frac{1}{\eta p E} + \frac{\Phi_0}{1-e^{-(u/u_0)^2}}\right)}} \tag{F.1}$$

M_{opt} is the optical MTF derived from modeling the eye; k is the signal-to-noise ratio, with signal presented at the retinal level. The integration time T, is the time over which an object is presented. X_0 is the angular extent of the object in degrees; X_{max} being the maximum angular size of the integration area. u is the spatial frequency for which the CSF is required, and u_0 is the maximum cut-off spatial frequency for lateral inhibition ceases (an apparent high-pass filtering by the neural system). N_{max} is the maximum cycles over which the eye can integrate information. Φ_0 is the spectral density of the neural noise (sec deg^2). Finally, η is the quantum efficiency of the eye which describes photon losses between the retina and the anterior cornea, p is the photon conversion factor for the light source, and E is the retinal illuminance in Troland. The constants in the model have the following typical values:

$k = 3.0$	$\eta = 0.03$	$u_0 = 7$cycles/deg
$T = 0.1$sec	$\Phi_0 = 3 \times 10^{-8}$sec deg^2	
$X_{max} = 12$degrees	$N_{max} = 15$cycles	

Bibliography

S. Alimisi, D. Miltsakakis, and S. Klyce. Corneal topography for intraocular lens power calculations. *Journal of Refractive Surgery*, 12(2):S309–S311, February 1996 1996.

R. A. Applegate. Noninvasive measurement of corneal topography. *IEEE Engineering in Medicine and Biology*, pages 30–42, 1995.

D. A. Atchison. Optical design of intraocular lenses. iii. on-axis performance in the presence of lens displacement. *Optometry and Vision Science*, 66(10):671–681, 1989a.

D. A. Atchison. Refractive errors induced by displacement of intraocular lenses within the pseudophakic eye. *Optometry and Vision Science*, 66(3):146–152, 1989b.

Paul Avery. Physics 3400 light, color and holography. Last accessed, April 2001. URL `www.phys.ufl.edu/avery/course/3400/gallery/gallery_vision.html`.

H. H. Barrett, J. Yao, J. P. Rolland, and K. J. Myers. Model observers for assessment of image quality. *Proceedings of the National Academy of Sciences*, Vol.90:9758 - 9765, 1993.

Jean-Cyriaque Barry, Klaus Branmann, and Mark C. M. Dunne. Catoptric properties of eyes with misaligned surfaces studied by exact ray tracing. *Investigative Ophthalmology and Visual Science*, 38(8):1476 - 1484, July 1997a.

Jean-Cyriaque Barry, Backes C, A. Pongs, U. M. Kirschkamp, and M. C. M. Dunne. Improved computing scheme for measuring eye alignment with Purkinje images I and IV. *Ophthalmic Physiologic Optics*, Vol.17:433 - 440, 1997b.

Jean-Cyrique Barry, Rolf Effert, Ansgar Kaupp, and Anrea Burhoff. Measurement of ocular alignment with photographic Purkinje I and IV reflection pattern evaluation. *Investigative Ophthalmology and Visual Science*, 35(13):4219–4235, December 1994a.

Jean-Cyrique Barry, Rolf Effert, Martin Reim, and D. Meyer-Ebrecht. Computational principles in purkinje i and iv reflection pattern evaluation for the assessment of ocular alignment. *Investigative Ophthalmology and Visual Science*, 35(13):4205–4218, December 1994b.

Peter Barten. The SQRI method: a new method for the evaluation of visible resolution on a display. *Proceedings of the SID*, 28:253–262, 1987.

Peter G. J. Barten. *Contrast Sensitivity of the Human Eye and Its Effect on Image Quality.* SPIE - Internation Society for Optical Engineering, September 1999.

M. W. Belin, J. L. Cambier, J. R. Nabors, and C. D. Ratliff. PAR corneal topography system (PAR CTS): The clinical application of close-range photogrammetry. *Optometry and Vision Science*, Vol.72:828 – 837, 1995.

M. W. Belin and P. Zloty. Accuracy of the PAR corneal topog a)hy system with spatial misalignment. *The CLAO Journal*, Vol.19:64 – 69, 1993.

A. G. Bennet. *Emsley and Swaines: Ophthalmic Lenses*, volume I. The Hatton Press Ltd., 1968.

Max Born and Emil Wolf. *Principles of Optics.* Cambridge University Press, third edition, 1965.

J. J. Camp, L. J. Maguire, B. M. Cameron, and R. A. Robb. A computer model for the evaluation of the effect of corneal topography on optical performance. *American Journal of Ophthalmology*, 109(4):379–386, April 1990a.

J. J. Camp, L. J. Maguire, and R. A. Robb. An efficient ray tracing algorithm for modeling visual performance from corneal topography. *First Conference on Visualization in Biomedical Computing*, pages 279 – 285, January 1990b.

F. W. Campbell and D. G. Green. Optical and retinal factors affecting visual resolution. *Journal of Physiology*, 181:576 – 593, 1965.

C.R. Carlson and R.W. Cohen. Visibility of displayed information: image descriptors for displays. *Report ONR-CR213-120-4F, Office of Naval Research, Arlington VA*, 1972.

L. Celikkol, D. Ahn, G. Celikkol, and S. T. Fedman. Calculating intraocular lens power in eyes with keratoconus using videokeratography. *Journal of Cataract and Refractive Surgery*, 22(4):497–500, May 1996.

W. N. Charman. *Optics of The Eye*, volume I, chapter 24, pages 34.1 – 34.26. McGraw Hill, Inc., 1995.

W. N. Charman and A. Olin. Image quality criteria for aerial camera systems. *Photographic Science and Engineering*, 9:385–397, 1965.

R. A. Clement, M. C. M Dunne, and D. A. Barnes. A method for raytracing through schematic eyes with off-axis components. *Ophthalmic Physiologic Optics*, Vol.7:149 - 152, 1987.

T. Dokken. Finding intersections of b-spline represented geometries using recursive subdivision techniques. *Computer Aided Geometric Design*, 2(1/3):189–195, 1995.

J. D. Doss, R. L. Hutson, J. J. Rowsey, and D. R. Brown. Method for calculation of corneal profile and power distribution. *Archives of Ophthalmology*, 99:1261–5, 1981.

Mark C. M. Dunne, Mohamed E. A. Elawad, and Derek A. Barnes. Measurement of astigmatism arising from the internal ocular surfaces. *Acta Ophthalmologica Scandinavica*, 74: 14–20, 1996.

Sami G. El Hage. The computerized corneal topographer (EH-270). In David J. Schanzlin and Jeffrey B. Robin, editors, *Corneal Topography: Measuring and Modifying the Cornea*, chapter 2. Springer-Verlag, 1992.

I Escudero-Sanz and Navarro R. Off-axis aberrations of a wide-angled schematic eye model. *Journal of the Optical Society of America*, 16(8):1881 - 1891, August 1999.

Thomas Euler. Biomedical Optics Group, Max-Planck-Institut for Medical Research. Last accessed, August 2001. URL `sun0.mpimf-heidelberg.mpg.de/~teuler/Pics/retina1.htm`.

Gerald E. Farin. *Curves and surfaces for computer aided geometric design.* Boston : Academic Press, 1988.

W. Fink, A. Frohn, U. Scheifer, E. W. Schmid, and N. Wendelsstein. A ray tracer for ophthalmological applications. *German Journal of Ophthalmology*, 5(2):118–25, March 1996a.

W. Fink, A. Frohn, U. Schiefer, E. W. Schmid, N. Wendelstein, and E. Zrenner. Visual images in high ametropia. Computer-assisted simulation with optic ray calculation. *Klin Monatsbl Augenheilkd*, 208(6):472–476, June 1996b.

N. Friedman. Glossary of the **CLEERE** website. Last accessed, March 2000. URL `www.spectacle.berkeley.edu/cleere`.

D. D. Garcia, B. A. Barsky, and S. A. Klein. *CWhatUC: A Visual Acuity Simulator.* PhD thesis, Department of Computer Science, University of of California, Berkeley Berkeley CA, May 15 2000.

Leon E. Garner and George Smith. Determination of the radius of curvature of the anterior lens surfaces from the purkinje images. *Ophthalmic Physiologic Optics*, 16(2):135–143, 1996.

N. Gerfelder and W. Miler. Quality aspects for computer-based video services. *SMPTE 1994 European Conference*, pages 44–67, 1994.

George A. Gescheider. *Psychophysics.* Hillsdale, N. J. : Erlbaum Associates, 2 edition, 1985.

P. E. Gill. *Practical Optimization.* London : Academic Press, June 1981.

R. C. Gonzalez and R. E. R. Woods. *Digital Image Processing.* Addison-Wesley, 1992.

E. M. Granger and K. N. Cupery. An optical merit function (SQF) which correlates with subjective image judgements. *Photographic Science and Engineering*, 16:221–230, 1972.

J. E. Greivenkamp, J. Schwiegerling, Miller J. M., and M. D. Mellinger. Visual acuity modeling using optical raytracing of schematic eyes. *American Journal of Opthalmology*, 120(5):227 - 240, August 1995a.

J. E. Greivenkamp, J. Schwiegerling, J. M. Miller, and M. D. Mellinger. Visual acuity modeling using optical raytracing of schematic eyes. *American Journal of Ophthalmology*, 120(2):227 - 240, August 1995b.

W. Haigis. IOL calculation according to haigis. Last accessed, March 2001. URL `www.augenklink.uniwuerzburg.de/uslab/ioltxt/haid.htm`.

Mark A. Halstead, Brian A. Barskey, Stanley A. Klein, and Robert B. Mandell. A spline surface algorithm for reconstruction of corneal topography from a videokeratographic reflection pattern. *Optometry and Vision Science*, 72(11):821–827, 1995a.

Mark A. Halstead, Brian A. Barskey, Stanley A. Klein, and Robert B. Mandell. *Reconstructing Curved Surfaces From Specular Reflection Patterns Using Spline Surface Fitting of Normals.* SPIE, 1996.

Mark A. Halstead, Brian A. Barsky, Stanley A. Klein, and Robert B. Mandell. Geometric modeling of the cornea using videokeratography. In M. Daehlen, T. Lyche, and L. L. Schumaker, editors, *Mathematical Methods in CAGD III*, pages 1–10. Academic Press, 1995b.

Pat Hanrahan. *An Introduction to Ray Tracing*, pages 81 - 105. Academic Press, 1997.

Eugene Hecht. *Optics.* Addison-Wesley, 1997.

P. S. Heckbert and P. Hanrahan. Beam tracing polygonal objects. *Computer Graphics (Siggraph '84)*, 18(3):119–127, July 1984.

Richard P. Hemenger, Alan Tomlinson, and Katherine Oliver. Corneal optics from videokeratographs. *Ophthalmic and Physioloigc Optics*, 15(1):63–68, 1995.

K. J. Hoffer. Intraocular lens power calculation for eyes after refractive keratotomy. *Journal Refractive Surgery*, 11(6):490–493, November 1995.

J. T. Holladay, T. C. Prager, T. Y. Chandler, K. H. Musgrove, J. W. Lewis, and R. S. Ruiz. A three-part system for refining intraocular lens power calculations. *Journal of Cataract and Refractive Surgery*, 14(1):17–24, January 1988.

S. E. Husain, T. Kohnen, R. Maturi, H. Er, and D. D. Koch. Computerized videokeratography and keratometry in determining intra-ocular lens calculations. *Journal of Cataract and Refractive Surgery*, 22(3):362–366, April 1996.

W. B. Jackson, M. R. Said, D. A. Jared, J. O. Larimer, J. L. Gille, and J. Lubin. Evalutaion of human vision models for predicting human-observer performance. In Harold L. Kundel, editor, *Medical Imaging 1997 : Image Perception*, volume 3036, pages 64–73. The International Society for Optical Engineering, SPIE, 1997.

Miles V. Klein. *Optics*. John Wiley and Sons, Inc., 1970.

S. A. Klein. A corneal topography algorithm that produces continuous curvature. *Journal of Optometry and Vision Science*, Vol.69:829 – 834, 1992.

S. A Klein. Axial curvature and the skew ray error in corneal topography. *Optometry and Vision Science*, Vol.74:931 – 944, 1997a.

S. A Klein. Corneal topography reconstruction algorithm that avoids the skew ray ambiguity and the skew ray error. *Journal of Optometry and Vision Science*, Vol.74:931 – 943, 1997b.

S. A. Klein and R. B. Mandell. Shape and refractive powers in corneal topography. *Investigative Ophthalmology and Visual Science*, Vol.36:2096 – 2109, 1995.

Stanley A. Klein and Daniel D. Garcia. Line of sight and alternative representations of aberrations of the eye. *Journal of Refractive Surgery*, 16(5):S630–5, Sep-Oct 2000.

Daniel Kleppner and Robert J. Kolenkow. *An Introduction to Mechanics*, chapter 7, pages 326–328. McGraw Hill International Book Company, 1984.

C. G. Klonos, J. Pallikaris, and F. W. Fitzke. A computer model for predicting image quality after photorefractive keratectomy. *Journal of Refractive Surgery*, 12(2):S280–S284, February 1996.

S. E. Klyce, S. D; Wilson. Imaging, reconstruction, and display of corneal topography. *SPIE*, Vol.1161:409 - 416, 1989.

A. C. Kooijman. Light distribution on the retina of a wide-angle theoretical eye. *Journal of the Optical Society of America*, 73(11):1544 - 1550, November 1983.

Jiri Korynta, Jiri Bok, Jiri Cendelin, and Kira Michalova. Computer modeling of visual impairment caused by intraocular lens misalignment. *Journal of Cataract and Refractive Surgery*, 25(1):100–105, January 1999.

A. J. Lang, V. Portney, and V. Lakshminarayanan. Estimation of the clinical significance of changes to the optics of the eye. In *Ophthalmic Lens Design and Fabrication II*, volume 2127, pages 44–53. SPIE, SPIE, 1994.

Yves Le Grand and Sami El Hage. *Physiological Optics*, volume 13 of *The Springer Series in Optical Sciences*. Springer-Verlag, 1980.

H. Liou and N. A. Brennan. Anatomically accurate, finite model eye for optical modeling. *Journal of the Optical Society of America*, 14(8):1684 - 1695, August 1997.

M Angeles Losada and Rafael Navarro. Point spread function of the human eye obtained by a dual double-pass method. *Pure Applied Optics*, 7(1):L7–L13, January 1998.

N.A. MacMillan and C.D. Creelman. *Detection Theory: A User's Guide*. Cambridge University Press, 1991.

Leo J. Maguire, Ralph W. Zabel, Paula Parker, and Richard L. Lindstrom. Topography and raytracing analysis of patients with excellent visual acuity 3 months after excimer laser photorefractive keratectomy for myopia. *Refractive and Corneal Surgery*, 7:122, March/April 1991.

Robert K. Maloney, Stephen J. Bogan, and George O. Waring III. Determination of corneal image-forming properties from corneal topography. *American Journal of Ophthalmology*, 115(1992):31–41, September 1993.

Mannos and Sakrison. The effects of a visual fidelity criterion on the encoding of images. *IEEE Transactions on Information theory*, 20:525–536, 1974.

Kresimir Matkovic. *Tone Mapping Techniaues and Color Image Difference in Global Illumination.* PhD thesis, Visualization and Animation Group, Vienna University of Technology, December 1997.

R. Mattioli and N. K Tripoli. Corneal geometry reconstruction with the keratron videokeratographer. *Optometry and Vision Science*, Vol.74:881 – 894, 1997.

G Modorati, L Pierro, and R Brancato. Preoperative astigmatic influence on the predictability of intraocular lens power calculation. *Journal of Cataract and refractive Surgery*, 16(5): 591–593, Septembe 1990.

K. Naeser. Intraocular lens power formula based on vergence calculation and lens design. *Journal of Cataract and Refractive Surgery*, 23(8):1200–1207, Octobet 1997.

NEI. National eye institute website, national institutes of health. bethesda, usa. Last accessed, August 2001. URL `www.nei.nih.gov`.

Donald C. O'Shea and Michael E. Harrigan. *Aberration Curves in Lens Design*, volume I, chapter 33, pages 34.1 – 34.26. McGraw Hill, Inc., 1995.

Thrasyvoulos Pappas and Robert J. Safranek. Perceptual criteria for image quality evaluation. accessed july 2000., March 1999. URL `citeseer.nj.nec.com/14738.html`.

P. Philips, J. Perez-Emmanuelli, H. D. Rosskothen, and C. J. Koester. Measurement of intraocular lens decentration and tilt in-vivo. *Journal of Cataract and Refractive Surgery*, 14:129–135, 1988.

William H. Press, Saul A. Teukolsky, William T. Vetterlin, and Brian P. Flannery. *Numerical Recipes in C: the Art of Scientific Computing*, chapter 16, pages 747–752. Cambridge Univerasity Press, second edition, 1992.

Michael W. Quick and Ronald G. Boothe. A photographic technique for measuring horizontal and vertical eye alignment throughout the field of gaze. *Investigative Ophthalmology and Visual Science*, 33(1):234–246, January 1992.

Richard H. Rand, Howard C. Howland, and Raymond A. Applegate. Mathematical model of a placido disk keratometer and its implications for recovery of corneal topography. *Optometry and Vision Science*, 74(11):927–930, November 1997.

R. H. Rengstorff. Corneal refraction : relative effects of each corneal component. *Journal of the American Optometric Association*, 56(3):218–9, March 1985.

J. A. Retzlaff, D. R. Sanders, and M. C. Kraff. Development of the SRK/T intraocular lens implant power calculation formula. *Journal of Cataract and Refractive Surgery*, 16(3): 333–340, May 1990.

C. Roberts. Characterization of the inherent error in a spherically-biased corneal topography system in mapping a radially aspheric system. *Refractive Corneal Surgery*, 10:113–4, 1994.

A. M. Rohaly, A. J. Ahumada, and A. B. Watson. A comparison of image quality models and metrics predicting object detection. *Society for Information Display Digest of Technical Papers*, 26:45–48, 1995.

A. R. Rudnicka, D. F. Edgar, and Bennett A. G. Construction of a model eye and its applications. *Ophthalmic Physiologic Optics*, Vol.12:485 - 490, 1992.

T. O. Salmon and D. G. Horner. Comparison of elevation, curvature, and power descriptions for corneal topographic mapping. *Optometry and Vision Science*, Vol. 72:800 - 808, 1995.

Thomas Salmon. *Corneal contribution to the wavefront aberrations of the eye.* PhD thesis, Indiana University, November 1999.

David J. Schanzlin and Jeffrey B. Robin. *Corneal Topography Measuring and Modifying the Cornea.* Springer Verlag, 1992.

Robert J. Schechter. *Optics of Intraocular Lenses*, volume 1, chapter 68, pages 5–6. Lippincott-Raven, revised edition edition, 1995.

Jim Schwiegerling. *OPTI 535X Visual Optics course notes.* University of Arizona, 2000.

Berthold Seitz and Achim Langenbucher. Intraocular lens power calculation in eyes after corneal refractive surgery. *Journal of Refractive Surgery*, 16:349–361, May/June 2000.

Andrei Sherstyuk. Fast ray tracing of implicit surfaces. *Computer Graphics Forum*, 18(2): 139–147, 1999.

Douglas C. Sinclair. *Optical Design Software*, volume I, chapter 34, pages 34.1 - 34.26. McGraw Hill, Inc., 1995.

George Smith and David A. Atchison. *The eye and visual optical instruments.* Cambridge Univeristy Press, 1997.

Warren J. Smith. *Modern Optical Engineering : The Design of Optical Systems.* McGraw Hill, 1966.

H. L. Snyder. *Image quality and observer performance.* Plenum Press, New York and London, 1973.

D.F. Specht. A generalized regression neural network. *IEEE Transactions on Neural Networks*, 2:568–576, November 1991.

Murray R Spiegel. Advanced calculus. In *Theory and Problems of Advanced Calculus*, chapter 4, page 61. McGraw Hill, 1988.

K. Takei, S. Hommura, and H. Okajima. Optimum form of posterior chamber intraocular lenses to minimize aberrational astigmatism. *Japanese Journal of Ophthalmology*, 39(4): 390–401, 1995.

Larry N. Thibos and Arthur Bradley. *Modeling the Refractive and Neuro-Sensor Systems of the Eye*, chapter 4, pages 101–159. McGraw-Hill Inc., New York, 1999.

N. K. Tripoli, K. L. Cohen, P. Obla, J. M. Coggins, and D. E. Holmgren. Height measurement of astigmatic test surfaces by a keratoscope that uses plane geometry surface reconstruction. *American Journal of Ophthalmology*, Vol.121:668 – 676, 1996.

H. K. Tuy and L. T. Tuy. Direct 2-D display of 3-D objects. *IEEE Computer Graphics and Applications*, 4(10):29–33, October 1984.

Unknown. Department of anatomy website, bristol university. Last accessed, April 2001. URL `www.bris.ac.uk/Depts/Anatomy/calnet/Visual1/page2.htm`.

A van Meeteren. *Visual aspects of image intensification.* PhD thesis, University of Utrecht, Utrecht, the Netherlands, 1973.

P. P. van Saarloos and I. J. Constable. Improved method for calculation of corneal topography for any photokeratoscope geometry. *Optometry and Vision Science*, 68:960–6, 1991.

J. Wang, D. Rice, and S. D. Klyce. A new reconstruction algorithm for improvement of corneal topogtraphical analysis. *Refractive Corneal Surgery*, 5:379–87, 1989.

A. B. Watson. The cortex transform: Rapid computation of simulated neural images. *Computer Vision, Graphics, and Image Processing*, 39:311 – 327, 1987.

A. B. Watson and Andrew E. Fitzhugh. Modelling character legibility. *Society for Information Display Digest of Technical Papers*, 20:360–363, 1989.